UNIVERSITY OF CALIFORNIA
SANTA CRUZ

STAR FORMATION SUPPRESSION AND FEEDBACK IN NEARBY QUIESCENT GALAXIES

A dissertation submitted in partial satisfaction of the
requirements for the degree of

DOCTOR OF PHILOSOPHY

in

ASTRONOMY & ASTROPHYSICS

by

Namrata Roy

June 2022

The Dissertation of Namrata Roy is approved:

Professor Puragra Guhathakurta, Chair

Professor Kevin Bundy

Professor Rachel Somerville

Peter F. Biehl
Vice Provost and Dean of Graduate Studies

Table of Contents

List of Figures

List of Tables

Abstract

Star formation suppression and feedback in nearby quiescent galaxies

by

Namrata Roy

Active galactic nuclei (AGN) driven feedback has been proposed to be one of the most efficient ways to quench star formation and help maintain quiescence in massive galaxies. However, direct evidence of feedback in typical quiescent galaxy populations has been restricted to only a handful of sources. This thesis presents a series of evidence that large-scale winds in a new (and relatively common) class of early-type galaxy, known as 'red geysers', may represent AGN radio mode feedback in action. The work is primarily based on integral field spectroscopic data from the SDSS IV- MaNGA survey that has completed observing 10,010 galaxies in the optical wavelength at $z < 0.1$. The main focus of this work is utilizing a multi-wavelength approach to understand the detailed physics of the red geyser galaxies and place them in the context of global quenching of star formation in typical red and dead galaxies.

Radio data from the combined surveys of Faint Images of the Radio sky at Twenty Centimeters (FIRST), VLA Sky survey (VLASS) and LOFAR Two Meter Sky Survey (LoTSS) reveal that red geysers preferentially host low luminosity radio mode AGNs with average radio luminosity $L_{1.4\ GHz} \sim 10^{21} - 10^{22}$ W Hz^{-1}. Red geysers exhibit a wide range of radio morphologies: from double-lobed large-scale jets to compact and moderately extended features with average radio sizes between 5 - 30 kpc. However,

the majority of the red geysers show a compact radio structure, closely resembling the 'FR0' radio galaxies, which are the low luminosity counterparts of the more luminous FRI/FRII sources and often host small scale jets. Optical long-slit spectroscopy from the Keck ESI instrument and resolved spectroscopy from the SDSS IV- MaNGA survey shows that the turbulent ionized gas kinematics with 'winged' emission line profiles are consistent with geometric projections through an outflowing broad conical wind.

In addition to the ample amount of ionized gas ($\sim 10^5 - 10^6$ $M_\odot$), a large fraction of red geysers also host a significant amount of cold gas reservoir in the interstellar medium. Traced by the Sodium doublet absorption line, the signature is particularly enhanced for the radio bright red geysers indicating some underlying connection between the gas supply and the AGN activity. A detailed stellar population modeling and subsequent extraction of absorption-line kinematics using a Markov Chain Monte Carlo (MCMC) framework show that a large part of this cool gas is infalling towards the galaxy, with an average velocity $\sim$ 60 km s^{-1}. The origin of this cool inflowing gas is predicted to be a combination of internal sources like stellar mass loss and external accretion events like minor mergers. The emerging hypothesis is that this gas is inflowing towards the center to possibly fuel the central radio-mode AGNs, which can then trigger the outflowing wind visible in the ionized phase. This hypothesis is in agreement with the observed duty cycle of the red geysers, which matches the minor merger frequency in the local universe (0.1 Gyr^{-1}). The minor mergers can provide the bulk of the multi-phase gas detected in these galaxies but cannot rejuvenate star formation, perhaps due to the feedback effect of the wind. The estimated kinetic energy

from the wind $\dot{E} \sim 10^{39}$ erg s^{-1} is energetically sufficient to suppress any residual star formation in the host galaxy. Red geysers are expected to be an episodic but short-lived phenomenon that possibly occurs in any red sequence galaxy. They can play an energetically important role in suppressing gas cooling and star formation at late times.

To my family for always believing in me...

Acknowledgments

I want to thank the folks who stood by me throughout my years of graduate school, encouraged me to pursue graduate studies in the first place, and showed me the path which eventually led to where I am today. The two years of the COVID-19 pandemic especially taught me that it is difficult to carry on without the supportive community around you. I always thought writing this section would be the hardest as I am blessed to have so many wonderful people in my life who cheered on for me and inspired me to be the best version of myself.

I come from a vibrant city called "Kolkata" in India, where I have stayed for the first 23 years of my life. When I first landed in Santa Cruz, California, in the beautiful Bay Area, I was excited, motivated, and also a little overwhelmed. I was thrilled to start the most significant chapter of my life but also anxious of the long academic journey lying ahead in a country halfway across the world from my hometown. It is impossible to explain the role my advisor Prof. Kevin Bundy played during these six years at UC Santa Cruz (UCSC). He shaped me into a mature, confident scientist and an independent thinker. He was a friend when I needed one, an advisor when I had to make important academic decisions and a guardian helping me find a house (and offering me his own) when my living situation collapsed. We used to have hours of discussions about my career, long-term plans, Indian cultures and, of course science. Thank you Kevin, for sharing your wisdom with me, encouraging me when I needed and teaching me Astronomy and life lessons that I will try to carry with me for the rest

of my life.

My transition from Kolkata to Santa Cruz would not have been possible without the support of Prof. Puragra Guhathakurta ("Raja" to us). I still remember the day I first met Raja in 86/1 College Street, Kolkata. We spent more than an hour chatting about science, observing using Keck, UCSC, SIP program, among other things, while sipping coffee at the Indian Coffee House. The coffee got better, and those discussions continued from Kolkata to California, with topics varying anywhere from Andromeda to art. Every time I stopped by Raja's office, I was always welcomed with a smile. When the disastrous California fire struck the Santa Cruz mountains in August 2020, Raja was the first person I called at 8 PM in the night. Thank you, Raja, for always being there for me.

I also want to wholeheartedly thank another member of my thesis committee – Dr. Rachel Somerville, for being an amazing collaborator and for serving on my committee. We had countless zoom hours discussing state-of-the-art simulations and how we can compare them to our observations. I hope to continue this wonderful collaboration in the upcoming years when I will be located on the east coast, closer to the Flatiron Institute. This acknowledgment piece will be incomplete without mentioning one of my greatest mentors, Prof. Sandra Faber (or "Sandy"). She has always been my role model, and I consider myself very lucky to be guided by her. Sandy has always been very enthusiastic about my academic success and personal growth. I remember one time over lunch, she casually asked me what project I was working on, and after I was done explaining, she replied "You are a wonderful speaker! I see great potential in you,

Namrata". I hope I can live up to your expectations, Sandy. I also want to thank Prof. Robert (Bob) Williams, former director of Space Telescope, for being another wonderful mentor. I will surely miss our long lunches and stimulating conversations about leadership roles in Astronomy. I am indebted to the Osterbrock leadership program for playing a big role in my graduate training.

A significant part of this thesis relied on optical spectroscopic data from MaNGA survey and follow-up radio data. I want to thank the entire MaNGA collaboration for being an incredibly supportive and collaborative group. I feel I have extended academic family members from almost all parts of the world. I especially want to thank Dr. Kyle Westfall for helping me with MaNGA and Keck data reduction and analyses used in Chapters 4, 5, and 6. I also thank Prof. Xavier Prochaska and Prof. Brad Holden for their advice on the Keck ESI data reduction. I want to thank Dr. Kate Rowlands for her help with some of the analyses performed in Chapter 5. Besides academic support, Kate has also given me great personal advice about living in Baltimore and working at Johns Hopkins University, where I will be heading for my first postdoctoral venture. For the radio analyses part of the thesis, especially Chapter 3, I would like to thank Dr. Emily Moravec and Prof. Martin Hardcastle. I especially want to thank Martin for his sharp insights about radio active galactic nuclei (AGN) population and for familiarizing me with the existing AGN literature via many emails (and zoom) conversations.

I also want to acknowledge my fellow graduate students in the Astronomy department at UCSC for always making me feel welcome and supporting me in every

possible way. Thank you Brittany, Zack, Grecco, Tiffany, Viraj, Sunil, Enia, Asher, and Platon for all the wonderful memories, and for being a part of my graduate school experience. I am grateful that I could meet so many amazing people along the journey. I also want to thank my officemate, Bruno, for sharing day-to-day gossips and small chats in between work hours. I want to specially mention graduate advisors Libby Severson and Lindsay Lauver for their constant support in various things. Finally, living at Santa Cruz wouldn't have been fun without having Geetanjali around. She was almost like an elder sister looking after me throughout my graduate school years. Our occasional trips to restaurants to get a taste of Kolkata in Santa Cruz, and our amateur cooking endeavors are some of the happiest memories I have of Santa Cruz.

I wouldn't have come to UCSC to pursue a Ph.D. in Astronomy without the mentorship of a few people back in India. I thank all the professors at the Physics department of Presidency University for teaching me to love Physics, but there are a few who deserves special mention. I am absolutely indebted to my undergraduate advisor and mentor, Prof. Ritaban Chatterjee (RC). Academic training and outstanding astrophysics classes aside (I particularly remember the stellar evolution class), he is the best possible mentor, and advisor one can ever have. I did my first Astrophysics research project with him, and he treated me with extreme patience and helped me think like a researcher. RC constantly encouraged me to do better — be it research, physics exams or life in general; and he still does. Without his guidance and advice, I would never consider going for an Astronomy Ph.D., let alone applying for graduate school abroad. I am really thankful for having an amazing friend, a well-wisher, and a teacher like you,

sir.

I would also like to thank Prof. Suchetana Chatterjee for her constant guidance and encouragement. She also played a big role in inspiring me to go beyond my comfort zone and take up bigger challenges in life. I remember she used to gift us chocolates for getting homework assignment problems correct in her quantum mechanics class and we all used to look forward to that! Her care for students and love for teaching greatly inspired me to pursue an academic career. I also like to thank a few other excellent professors in the Physics department, especially Profs. Soumyadeep Samui and Somak Roychoudhury, who inspired me to Astronomy in various ways. I am grateful to Prof. Durgesh Tripathi at IUCAA, India and Prof. Tapas Das at HRI, India for giving me a chance to work on various research projects with them. I learnt various specific skillsets, tools and understood the broad landscape of Astronomy research through their guidance.

I grew up in a family where education was given a lot of priority. Neither of my parents is from a science/teaching/research background, but they were extremely supportive when they heard about my interest in Physics. I share a very close bond with my mother who demands I acknowledge her as my best friend in this thesis. Jokes aside, she is the person I talk to every single day over the phone, giving details of every minuscule thing going on in my life. She is very supportive in everything I do, as long as that makes me happy. My father is always very proud of me and never forgets to remind me how hard I have worked to get to this day. No words will be enough to acknowledge their role. Being seven years older than me, my elder sister always acts like my mother

and scolds me over different excuses. But she is also the person who pampers me with gifts, love and affection throughout the year. I rely on my sister for everything other than Astronomy research. I am so glad to have a sibling who I can walk with until the last day. I also want to thank my brother-in-law who is always very excited about Astronomy and my three and a half years old nephew Rishabh (who already knows the names of all the planets in our solar system).

I want to end with the person without whom I would have quit during the COVID-19 pandemic, without whom I would not be here today. The person is Sagnick. When two years of complete isolation in a foreign land during the global pandemic pulled me into the dark, it was Sagnick who told me that there is light at the end of every tunnel. He gives me the right personal and professional advice, discusses astronomy with me, and constantly motivates me to do bigger and better things. He is the reason I never felt alone on this journey. His contribution to my life is truly immense. Sagnick, I am truly glad to have met you in my life, and I thank you from all my heart for making my life so much happier and more beautiful. I cannot wait for all the adventures that lie ahead of us!

Scientific Acknowledgments

A major part of this research was supported by the National Science Foundation under Award No. 1816388. I gratefully acknowledge support from the University of California Santa Cruz through the Chancellor's Dissertation year fellowship award. This work extensively uses Sloan Digital Sky Survey (SDSS) IV data. Funding for the Sloan

Digital Sky Survey IV has been provided by the Alfred P. Sloan Foundation, the U.S. Department of Energy Office of Science, and the Participating Institutions. SDSS-IV acknowledges support and resources from the Center for High-Performance Computing at the University of Utah. The SDSS web site is www.sdss.org.

SDSS-IV is managed by the Astrophysical Research Consortium for the Participating Institutions of the SDSS Collaboration including the Brazilian Participation Group, the Carnegie Institution for Science, Carnegie Mellon University, the Chilean Participation Group, the French Participation Group, Harvard-Smithsonian Center for Astrophysics, Instituto de Astrofísica de Canarias, The Johns Hopkins University, Kavli Institute for the Physics and Mathematics of the Universe (IPMU) / University of Tokyo, the Korean Participation Group, Lawrence Berkeley National Laboratory, Leibniz Institut für Astrophysik Potsdam (AIP), Max-Planck-Institut für Astronomie (MPIA Heidelberg), Max-Planck-Institut für Astrophysik (MPA Garching), Max-Planck-Institut für Extraterrestrische Physik (MPE), National Astronomical Observatories of China, New Mexico State University, New York University, University of Notre Dame, Observatário Nacional / MCTI, The Ohio State University, Pennsylvania State University, Shanghai Astronomical Observatory, United Kingdom Participation Group, Universidad Nacional Autónoma de México, University of Arizona, University of Colorado Boulder, University of Oxford, University of Portsmouth, University of Utah, University of Virginia, University of Washington, University of Wisconsin, Vanderbilt University, and Yale University.

This work has also used data from the Keck Telescope. I wish to acknowledge

the very significant cultural role and reverence that the summit of Mauna Kea has always had within the indigenous Hawaiian community. I am very fortunate to have the opportunity to conduct observations from this mountain.

Published Material

The text of this dissertation includes reprints of the following previously published material led by Roy, with the permission of the listed coauthors.

Chapter 2 was published in the literature as Roy et al. (2018). I was responsible for performing the analysis, writing the text, and creating the figures. I wish to thank my coauthors Kevin Bundy and Edmond Cheung for their generous support and feedback in the course of this research. Chapter 3 was published in the literature as Roy et al. (2021b). I was responsible for analyzing the data, creating the figures, interpretaing the results and writing the text. I wish to thank my coauthors Emily Moraviec and Martin Hardcastle for their help in giving me access to proprietary LOFAR data and also providing me with valuable feedback. Chapter 4 was published as Roy et al. (2021a). I have reduced the data, performed the analyses, developed the models and created the figures and text. I wish to thank Kevin Bundy for performing the telescope observations at Keck Telescope. Chapter 5 was published in the literature as Roy et al. (2021c). I was responsible for analyzing the data, writing the text and creating the figures. I want to sincerely thank Kate Rowlands for providing help with the data analyses. I gratefully acknowledge the support of Kevin Bundy and Kyle Westfall for providing valuable feedback in this research.

Thanks

Namrata Roy

Chapter 1

Introduction

The advent of a large number of ground and space-based telescopes in the last few decades has significantly improved our understanding of galaxy populations over cosmic time. Large photometric and spectroscopic surveys with better resolution, higher signal-to-noise and wider field of view have been instrumental in learning about the different physical processes involved in galaxy formation and evolution – an extremely complex topic with many unsolved problems. Especially utilizing the relatively new integral field spectroscopic (IFS) techniques, it is now possible to obtain spatially resolved information from different physical locations in a galaxy and thus gain a more detailed picture instead of an average integrated property. The primary challenge now is to efficiently utilize this huge database of information to connect the pieces of the puzzle together and build a coherent picture of galaxy evolution starting from the birth of galaxies when it is actively forming stars - all the way upto their death, when there is very little-to-no star formation activity. This thesis strives to better understand

the mechanism by which galaxies stop their active star forming state (often known as 'quenched' state), or more specifically, once they quench − how they preserve the passive quiescent state for a long period of time. Before diving into the specific unanswered questions and how the present work addresses them, it is important to discuss how our understanding of galaxy formation and evolution has matured over the years.

1.1 Star formation and quenching

Galaxies are the fundamental blocks of the universe. They come in many shapes, forms, and sizes. The current standard model of galaxy formation assumes that structure formation follows a hierarchical growth ("bottom up") scenario in the Λ cold dark matter (CDM) universe. This means that small primordial fluctuations of matter generated early-on during inflation collapsed first, and eventually grew into bigger clumps, called dark matter halos. Slowly, they started attracting baryons (gas) mixed in with the dark matter to accumulate near the center, preparing for future star formation episodes (Peebles 1982; Blumenthal et al. 1984).

The process of star formation is a crucial phenomenon which shapes the form and fate of a typical galaxy. Although the exact mechanism of star formation is still a subject of ongoing research, the process involves an abundant presence of cold dense gas. So, once the baryons fall inwards towards the center of the halo, gas density increases, ultimately leading to a collapse under its own gravity into a cloud. Then, the competition between radiative cooling and gravitational heating determines the fate of

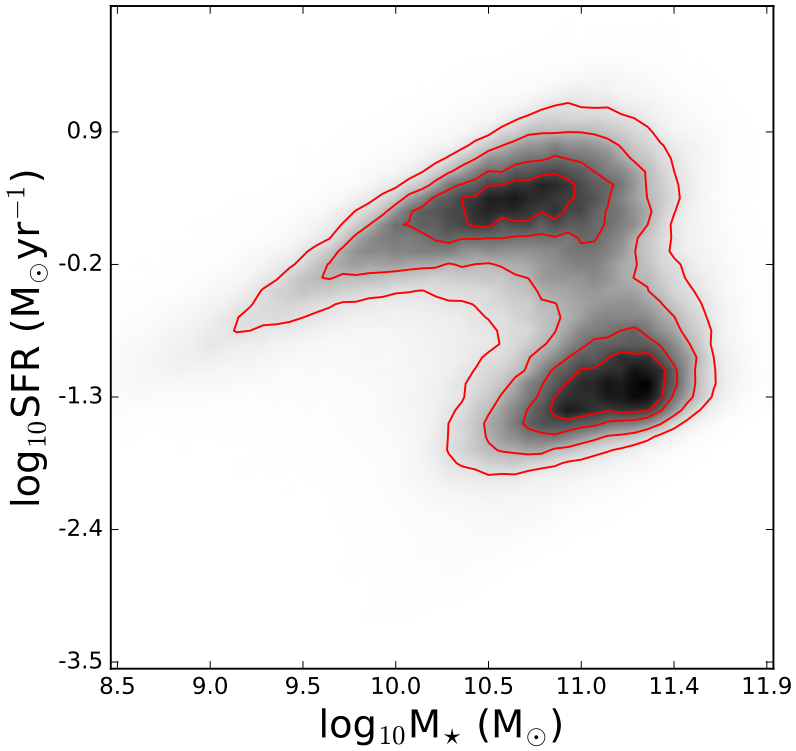

Figure 1.1: Star formation rate vs. stellar mass in log units for all MaNGA observed galaxies (with $0.01 < z < 0.1$) obtained from GALEX+SDSS+WISE catalog of Salim et al. (2016). This shows a clear bimodality with star forming blue cloud occupying the upper part of the diagram and quiescent red sequence galaxies lying in the bottom region.

the gas in these halos (Rees & Ostriker 1977; Binney 1977). If cooling is sufficient, these proto-stellar clouds will give birth to stars. During this star formation phase, galaxies continuously grow in stellar mass by forming stars and also by merging into larger structures. The accreted gas falling into the center eventually settles into a disk and forms spiral/disk star forming galaxies (Kereš et al. 2005; Dekel & Birnboim 2006; Fall & Efstathiou 1980).

When the stellar mass grows roughly above $> 10^{10}$ $M_{\odot}$ and becomes massive, heating dominates instead. Star formation activity also decreases considerably. Cool gas is no longer accreted from outside at a similar rate (Dekel & Birnboim 2006), thus considerably decreasing the supply of star forming fuel. Additional energy injection via feedback mechanisms (discussed in detail in the following paragraphs) quenches any residual star formation (Di Matteo et al. 2005; Somerville & Davé 2015; Hopkins et al. 2011; Weinberger et al. 2017b), marking the onset of the passive early-type galaxies (ETGs). The spheroidal/elliptical shape in the ETGs is formed hierarchically through mergers of pre-existing galaxies within a halo, which allows galaxies to grow even after gas accretion has ceased (e.g., White & Frenk 1991; Barnes 1992; Cole et al. 2000). This is the simplest evolutionary picture of a galaxy although the exact evolutionary path changes on a galaxy-by-galaxy basis. Recent work employing data from large surveys has shown that galaxy population today is indeed roughly bimodal with galaxies less massive than 10^{10} $M_{\odot}$ undergoing star formation and those above are predominantly quenched. This distinct division in the two populations is primarily observed in galaxy colour, morphology, star formation rate and stellar mass (Strateva et al. 2001; Baldry

et al. 2004; Balogh et al. 2004). Fig. 1.1 shows this clear bimodality arising in star formation rate and stellar mass for the low redshift (z<0.1) MaNGA observed galaxies, as measured from Salim et al. (2016) catalogue.

However there are several complexities. Particularly, understanding what causes the complete transition to the passive "red and dead" phase is quite challenging. Major surveys have now revealed that the ETGs are not completely devoid of cold gas, unlike what was believed previously (Binette et al. 1994; Buson et al. 1993; Demoulin-Ulrich et al. 1984). There are still ample source of gas supply from stellar mass loss, minor mergers and episodic accretion events which can cool down quickly and restart star formation activity. But that level of star formation is almost never observed. Once galaxies transition to the passive state, they remain quenched forever with very little rejuvenation, thus adding to the ETG population over time. This has been confirmed by the fact that the number of quiescent galaxies has been increasing steeply by a factor of almost ~ 25 since z$\sim$2 to present time (Bell et al. 2004; Bundy et al. 2006; Faber et al. 2007; Ilbert et al. 2010; Moustakas et al. 2013). This has been shown by Fig. 1.2 which depicts that the fractional contribution of the ETG population (in red symbols) to the total stellar mass has been increasing continuously from higher redshift towards present time, irrespective of the stellar mass interval considered. Additionally, the centers of the most massive galaxies in groups and clusters show very old stellar populations, with almost no signs of ongoing star formation episodes. Hence the primary questions in the puzzle are – how do galaxies halt their star formation initially? how do they maintain this passive state over long timescale?

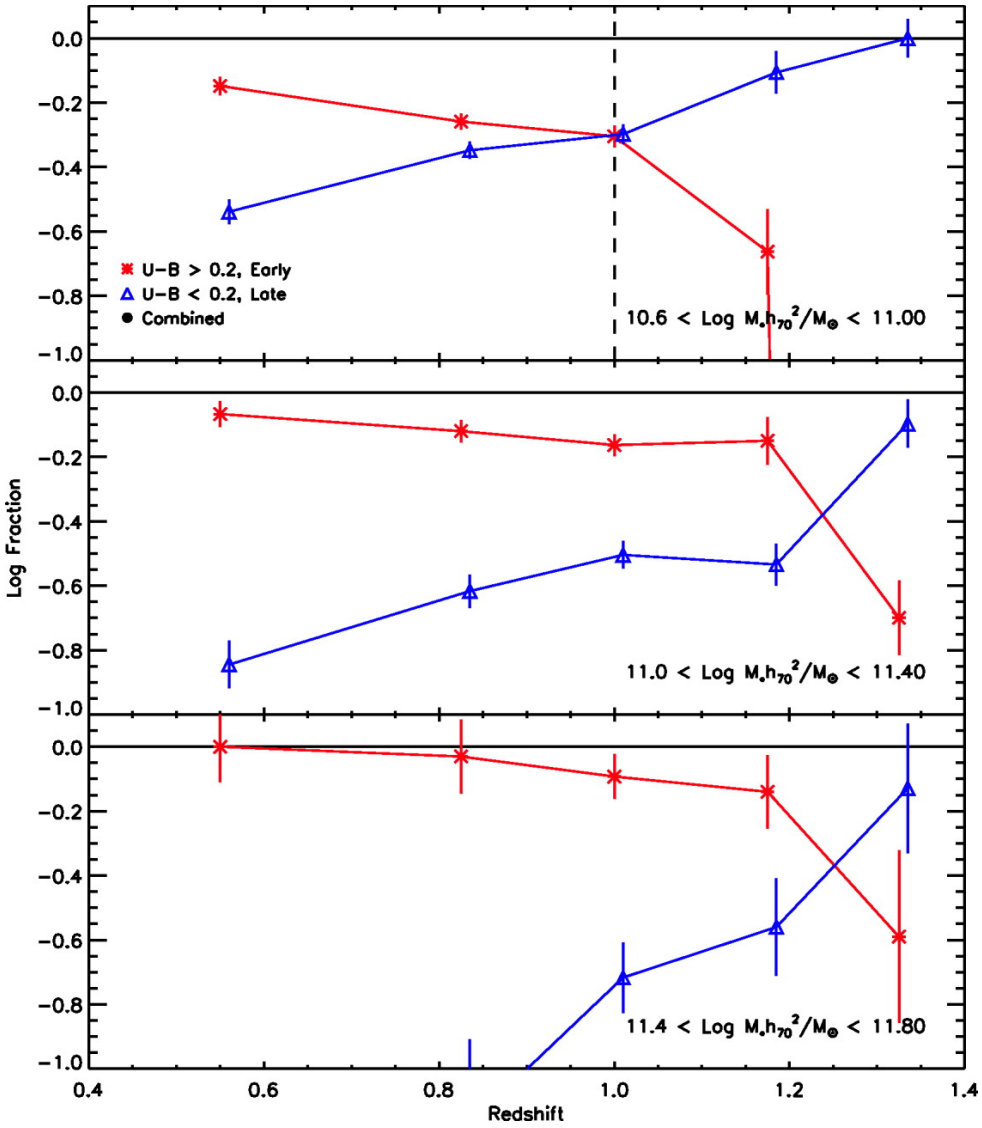

Figure 1.2: Fractional contribution in log units to the total mass function, divided into stellar mass bins and plotted as a function of redshift, reproduced from Bundy et al. (2006) (©AAS. Reproduced with Permission). Quiescent red and dead galaxies are shown by red symbols and late type star forming galaxies are denoted by blue. It is clear that the mass fraction of quenched galaxies is increasing monotonously from higher to lower redshift (i.e. present time). This indicates that the red sequence population is continuously growing since redshift 1.5 or beyond. The vertical dashed line in the top panel indicates the onset of incompleteness from the R-band limit, which occurs above the redshift indicated.

Galaxy formation models have proposed a range of feedback mechanisms ranging from gravitational torques induced by growing galaxy bulges, morphological quenching to ISM heating from fast-moving stars within galaxies (e.g., Martig et al. 2009; Conroy et al. 2015). However they are unable to quench the entire populations of galaxies in a manner consistent with observations (Su et al. 2019). Outflows from supernovae (SNe) and stellar winds are other possible explanations to prevent star formation. Although they indeed play a critical role in low mass dwarf galaxies, they turn out to be too low energetically to be effective in massive galaxies with deep potential wells (Dekel & Silk 1986; Bower et al. 2006; Hopkins et al. 2011; Conroy et al. 2015). A much more energetic and powerful feedback mechanism is required to halt star formation and then maintain it at a low level in massive galaxies. A promising candidate is energy released from the central supermassive black hole.

1.2 AGN feedback

One of the profound discoveries in the past two decades is that all massive galaxies host a super-massive black hole (SMBH) in their center. The black holes, with masses ranging from hundreds of thousands to billions of times than the sun ($\sim 10^5 - 10^{10}$ $M_\odot$), grow primarily through accretion of gas and can release a tremendous amount of energy of order $\sim 10^{61}$ erg (King & Pounds 2015; Harrison et al. 2018). The net energy emitted from the SMBH exceeds the binding energy of the host galaxies by two-three orders of magnitude. Even if a small fraction of this energy can be deposited

to the interstellar medium (ISM), it will be sufficient to heat up or expel the cold gas in the galaxies − thus regulating both the host galaxy star formation and the growth of the black hole itself. Schawinski et al. (2006) derived a critical SMBH mass of $M \sim 1.26 \times 10^8 (\frac{\sigma}{200})^{3.65}$ $M_\odot$ above which the feedback energy powered by the black hole is sufficient to prevent star formation even at the 1% level.

When the SMBH releases a massive amount of energy in the form of matter and/or radiation and becomes luminous across a large part of the electromagnetic spectrum, it is known as the active galactic nuclei (AGN). Depending on the accretion efficiency of the SMBH and the primary mechanism by which the AGN releases its energy, there are two separate modes of AGN feedback - quasar/radiative mode, and radio/ jet mode feedback. The radiative mode is associated with luminous AGNs (or quasars) which have a high accretion rate ($\sim 1 - 10\%$ of Eddington limit) into the SMBH. Triggered in some cases by a violent event such as a galaxy merger (Somerville et al. 2008; Hopkins et al. 2007), the quasar phase of intense accretion drives energy in the form of electromagnetic radiation (energetic photons) produced by efficient conversion of potential energy of the gas accretion (Di Matteo et al. 2005). The energetic photons are predicted to couple to the surrounding gas resulting in outflows within the inner kilo-parsec region, that have been identified in X-ray, ultraviolet and optical spectroscopy (Crenshaw et al. 2003; Ganguly & Brotherton 2008; Tombesi et al. 2010; Rupke et al. 2005; Dunn et al. 2010; Sturm et al. 2011; Fischer et al. 2010; Fabian 2012; Green et al. 2014; Wylezalek & Zakamska 2016). The primary mode of energy transfer is wide-angled, high velocity (> 1000 km s^{-1}) radiative winds driven close to

the accretion disk, which are detected via blueshifted absorption and emission lines in luminous AGNs, Seyferts and broad absorption line (BAL) quasars (Davies et al. 2009; Storchi-Bergmann et al. 2010; Greene et al. 2011; Feruglio et al. 2010; Allen et al. 2011). These winds have the capability to expel gas altogether from the galactic potential well and hence are often classified under the 'ejective feedback' category (Di Matteo et al. 2005; Cattaneo et al. 2009; Fabian 2012; King & Pounds 2015; Somerville & Davé 2015). Fig. 1.3, left panel, shows an illustration of this feedback mode. However, this mode is believed to act as an initial shut-down mechanism early-on in a galaxy's lifetime and is not deemed sufficient to hold off star formation over a long period of time (although see Choi et al. 2017, for a counter-argument). An additional mechanism is generally necessary in galaxy evolution models to successfully keep a galaxy in quenched and passive state over long timescales.

1.2.1 Radio/ jet-mode feedback

The second perhaps follow up mode of AGN feedback, known as the "radio-mode" or the "jet-mode" feedback, is associated with low to moderate luminosity AGNs with relatively low accretion rates ($< 1\%$ of Eddington limit). This AGN mode launches two-sided jets of magnetized plasma generally visible in radio wavelengths and inflates giant X-ray bubbles (Nesvadba et al. 2008; McNamara & Nulsen 2007; Gitti et al. 2012; Fabian 2012). It is believed that once star formation is initially shut down perhaps by the quasar phase, the radio mode feedback serves as an additional mechanism to maintain these galaxies in the passive 'red and dead' phase; hence this mode is often

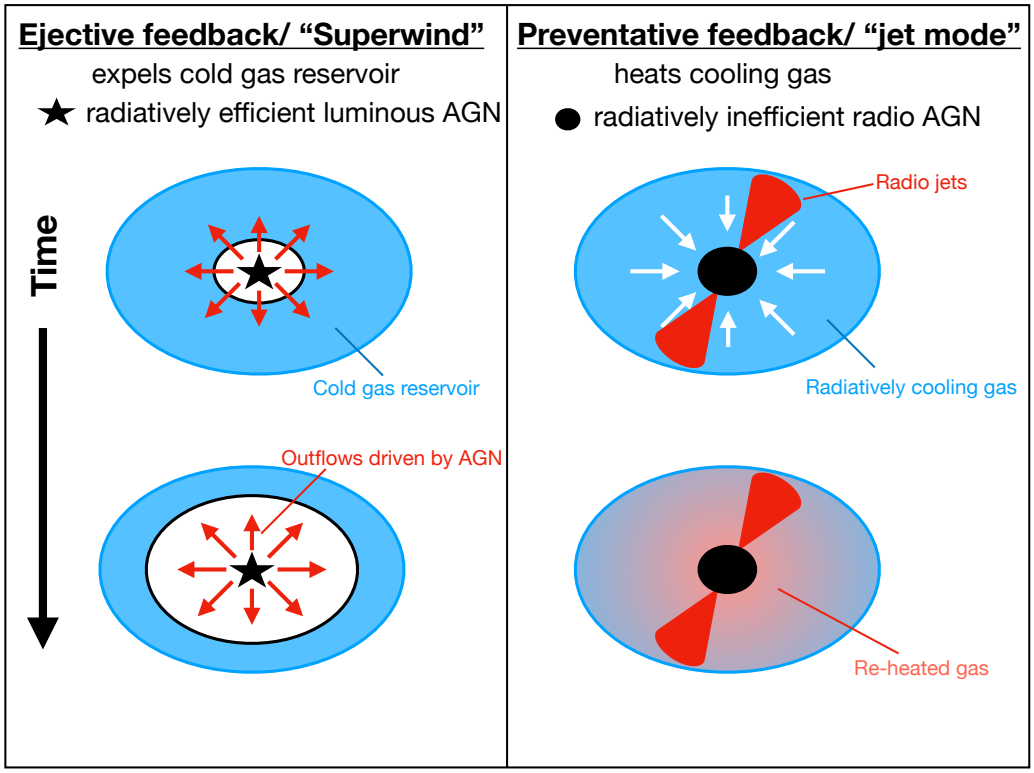

Figure 1.3: Schematic diagram to illustrate the two main modes of AGN feedback (motivated by Fig. 7 of Alexander & Hickox 2012). The 'ejective mode' is primarily associated with high velocity superwinds driven by radiatively efficient luminous AGNs and expels a large fraction of cold gas from the galaxy. The 'preventative mode' is dominated by galaxy-scale radio jets which reheats the cooling gas and maintain low level of star formation over long timescales.

referred to as the 'maintenance mode'. The primary energy transport in this mode occurs through the mechanical energy deposited by the jets/lobes and any associated low velocity gas outflows driven by these radio AGNs (Croton et al. 2006; Sijacki et al. 2007). Indeed, mechanically-driven AGNs are predominantly found in the most massive galaxies ($M_\star > 10^{11}$ $M_\odot$) with old stellar populations in the local universe (Heckman & Best 2014; Hickox et al. 2009). Incorporating a radio (mechanical) mode of feedback driven by radiatively inefficient AGNs in the semianalytic and hydrodynamical galaxy formation models improves the qualitative agreement with obervations of the quenched fraction and stellar mass function (Croton et al. 2006; Bower et al. 2006; Davé et al. 2012). In contrast to radiative winds extending barely to 100s of parsec scale, energetic feedback by radio jets can extend to large distances on the scales of the host galaxy. They are capable of counterbalancing the radiative cooling of hot gas supplied by the circumgalactic medium and recycled gas from old, evolved stars which can otherwise cool down and trigger star formation. This mode of feedback is 'preventative' in nature and by re-heating the atmosphere, it is capable of suppressing future star formation episodes over long timescales, as shown in Fig. 1.3 right panel (Somerville & Davé 2015; Alexander & Hickox 2012).

Even though this feedback mechanism is efficient, direct observational evidence is lacking, especially in typical massive galaxies. The only evidences that exist are in the centers of galaxy groups and clusters in the form of giant X-ray cavities forming near the radio jets (Rizza et al. 2000; McNamara & Nulsen 2007; Nesvadba et al. 2008; Cavagnolo et al. 2011; Gitti et al. 2012). Those cavities can be explained by the giant radio lobes

interacting with the surrounding medium and pushing the gas away. McNamara et al. (2000) pointed out that the cavity volumes (V) multiplied by their surrounding pressures (P) provide an estimate of the PV work (mechanical energy) expended as the cavities are inflated. This energy stored in the cavities is an order of magnitude higher than that required to balance radiative cooling of gas in the cluster center.

To search for similar evidence of radio mode feedback in typical early type galaxies (halo mass $< 10^{13}$ $M_{\odot}$), some studies have relied on indirect evidences based on correlation between star formation activity and the radio-loudness of the central AGN (Best & Heckman 2012). While those are meaningful in the statistical sense, finding direct proof of jet mode feedback will help us understand the quenching process better. Spatially resolved high quality observations of gas and stellar kinematics, stellar populations, and sensitive radio observations can help us search for the existence of jet-mode feedback. Finding signatures of radio/jet mode feedback in passive elliptical galaxies is the main focus of this thesis. Since the jet-mode feedback is primarily associated with mechanical energy deposition via jets, the radio luminosity, spatial extent of the jets and their environment may play a key role in the global energetics of the host galaxy and their subsequent effect on star formation. Thus to carry out this thesis, it is essential to review the diverse population of radio AGNs existing in the literature and their corresponding radio morphology.

1.2.2 Morphology of Radio AGNs and feedback via jets

From the first double lobed radio galaxies in the 3C catalogue to current low-frequency radio-galaxy samples, the general understanding of the diversity of radio-galaxy populations has evolved dramatically over the last seventy years. Fig. 1.4 shows the radio luminosity (at 1.4 GHz) vs. linear size of the different sub-populations of radio AGNs, as discussed in the next two subsections. AGN-driven jets can occur spanning a wide range in radio luminosity (nearly ten orders of magnitude), source size (six orders of magnitude) and morphology. The proposed jet-mode feedback can be immensely diverse based on these factors. In the next two subsections, the main morphological classes of radio galaxy that can be categorised primarily from radio observations are discussed.

1.2.2.1 Extended and resolved radio AGN:

The Fanaroff-Riley (FR) morphological class (Fanaroff & Riley 1974) is one of the earliest known radio galaxies exhibiting bright central radio emission and large scale radio jets. The FR class is further sub-divided into FRI and FRII morphology, based on the distinction between center-brightened and edge-brightened sources. The center-brightened FRI class objects are radio-loud according to the traditional Xu et al. (1999) criteria (average $L_{1.4\ \mathrm{GHz}} > 10^{23}$ W Hz^{-1}), with a bright central core and narrow, highly collimated relativistic jets that rapidly decelerate on kpc scales (Bicknell 1995; Tchekhovskoy & Bromberg 2016). The FRII sources, on the other hand, have jets which remain relativistic throughout the whole extent and they terminate in hotspots and

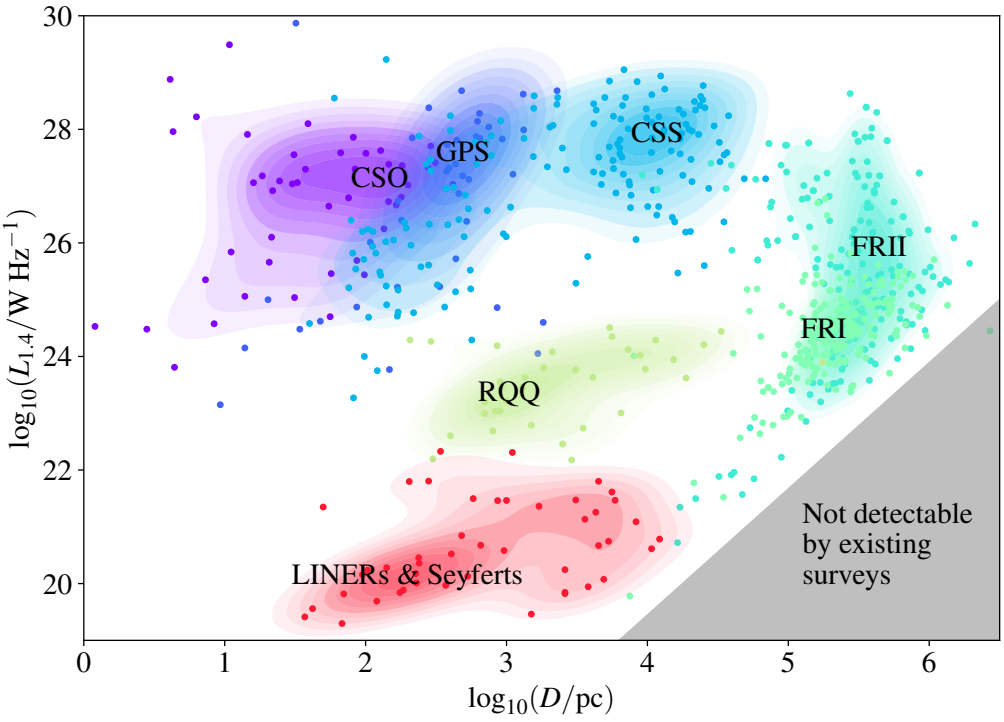

Figure 1.4: Radio luminosity versus linear radio size for large sample of radio AGN population compiled from the literature by Jarvis et al. (2019) and Hardcastle & Croston (2020). Points show individual objects and the colored contours represent source density. Seyfert and LINER galaxies are from Gallimore et al. (2006) and Baldi et al. (2018), while the radio-quiet quasars (RQQ) are from Jarvis et al. (2019) and Kukula et al. (1998). The rest of the objects, consisting of compact steep spectrum (CSS) sources, gigahertz peaked spectrum (GPS), compact symmetric objects (CSO) and Fanaroff-Riley class 1 and 2 are categorized by An & Baan (2012) and Mingo et al. (2019).

shocks at the edges. Hence, they are brighter at the two extreme edges. This structural difference is believed to originate from a combination of jet power and environmental density such that dense environments can rapidly decelerate the jet in the FRI class (Hardcastle & Croston 2020). Because of the large physical sizes of these jets, the FRI and FRII sources populate the right most region of the luminosity - radio size diagram in Fig. 1.4, with radio luminosities ranging between 10^{24} W Hz^{-1} $< L_{1.4GHz} <$ 10^{28} W Hz^{-1}. However, the luminosity function of radio-AGN is very steep with the abundance of luminous radio galaxies rapidly going down above $L_{1.4GHz} > 10^{24}$ W Hz^{-1} (see Best & Heckman 2012; Mauch & Sadler 2007). Hence the FRI and FRII sources are quite rare, especially in the local universe.

Recently with the advent of more sensitive radio surveys like the LOFAR-Two meter Sky survey (LoTSS; Shimwell et al. 2017), a population of low luminosity radio AGNs have emerged also showing extended lobes and FRI/II type morphology (Best 2009; Capetti et al. 2017; Mingo et al. 2019). This population was absent in earlier studies due to the lack of survey depth and sensitivity. Now they constitute the low-luminosity tail of the FR population in the luminosity-size diagram, extending all the way down to $L_{1.4GHz} \sim 10^{22}$ W Hz^{-1} (see Fig. 1.4). Mingo et al. (2019) has revealed the connection between the radio morphology, host galaxy properties and the local environments in these low-power FRII sources, displaying their similarity with their higher luminosity counterparts. Statistically, these low luminosity radio objects are quite common. However, their exact abundance is harder to estimate owing to the surface brightness limits of the radio observations.

1.2.2.2 Compact and unresolved AGN population

In addition to the extended radio galaxy population, compact radio sources also constitute a large fraction of the AGN population and have been studied for a long time. This includes compact symmetric objects (CSOs), gigahertz-peaked spectrum (GPS) sources, compact steep spectrum (CSS) sources and low power sources with small scale jets (O'Dea 1998; Baldi et al. 2015; Gürkan et al. 2018; Hardcastle et al. 2019). Among those, CSS and GPS sources are radio loud AGNs with very high luminosities ($L_{1.4GHz} > 10^{25}$ Watts Hz^{-1}) but with very small spatial extent (a few kpc). CSOs are even smaller radio sources with physical size less than few hundred parsecs. These sources lie in the upper left region in Fig. 1.4, with the highest luminosities but extremely compact structures. Historically, the CSS, CSO and GPS sources are associated with very high radio luminosities.

A new low-luminosity counterpart to these objects, known as the "radio-quiet quasars" (RQQ), has emerged which appear fairly compact in low resolution radio data but bear evidence of small scale (1-2 kpc) radio jets when viewed with sub-arcsecond resolution (Jarvis et al. 2019, 2021; Baldi et al. 2018). With about $\sim$ 100 discovered sources until now, they show similar physical sizes as the CSS sources but have radio luminosity three-four orders of magnitude lower, as evident from Fig. 1.4. Low luminosity kpc-scale jet structures have also been studied extensively in Seyfert galaxies, with jet sizes ranging anywhere between $1 - 25$ kpc (Gallimore et al. 2006; Croston et al. 2008; Mingo et al. 2011). Sometimes, these are classified as 'FR0' class, to describe the

unresolved low luminosity counterpart of the extended FRI/FRII class (e.g., Sadler et al. 2014; Baldi et al. 2015; Hardcastle et al. 2019).

The observed morphology depends largely on the resolving power of the observational setup, more specifically the beam size. However the relatively compact structure of these sources indicate two possible hypothesis. Either they host extremely small-scale 'frustrated jets' that cannot grow beyond a few hundred parsecs due to the surrounding dense environment (van Breugel et al. 1984). The other theory is that they are young sources with growing structures, which will eventually become traditional FRI/FRII sources with time (O'Dea 1998). Both scenarios could be simultaneously relevant for these compact FR0 class, since young objects commonly probe the densest part of the environments. These compact radio AGNs are an important population in the context of AGN feedback and understanding the lifeycle of radio galaxies. Their small scale jets confined within the inner kiloparsec region of the galaxy can be very efficient in depositing mechanical energy in the host galaxy (Wagner et al. 2012).

It is believed that radio jets (either compact or extended) play a significant role in driving turbulence in the surrounding medium and they often propel multi-phase gas outflows thereby inducing feedback (Whittle 1992; Tadhunter et al. 2003; Holt et al. 2008; Mukherjee et al. 2018). This section explained the various morphology of the radio AGNs and their jets. In the next section, we discuss about the detection of associated outflows via optical spectroscopic analyses.

1.3 Using spectroscopy to probe multi-phase gas outflows in radio AGN host galaxies

There is growing evidence that radio jets can be a dominant gaseous outflow driving mechanism and can have a broader impact than considered so far. This is based on statistical studies of hundreds of galaxies from large optical spectroscopic surveys like the Sloan Digital Sky survey (SDSS) and also from individual objects where outflows in the ionized gas phase and radio lobes show visible morphological connections on kpc scales (Mullaney et al. 2013; Tadhunter et al. 2014; Riffel et al. 2014; Husemann et al. 2019; Jarvis et al. 2019). As a potential channel for AGN feedback, outflows have been widely studied in local and high redshift AGNs using both optical emission and absorption lines as tracers (see Veilleux et al. 2005; Fabian 2012; Heckman & Best 2014). One widely used technique to trace outflows in ionized phase is observations of forbidden emission lines like [O III] λ5007. This forbidden line originates in relatively low density ($n \sim 10 - 10^5 cm^{-3}$) warm ($T \sim 10^4$ K) gas clouds. Measuring the doppler velocity of this line with respect to the systematic velocity of the galaxy gives an estimate of the motion of the ionized [OIII] emitting gas. Highly turbulent and disturbed gas with high velocities provide evidence for non-gravitational motions, thus indicating the presence of winds (Nesvadba et al. 2008; Greene et al. 2011; Cano-Díaz et al. 2012; Alexandroff et al. 2013; Liu et al. 2013; Rupke & Veilleux 2013; Harrison et al. 2014; Zakamska & Greene 2014). Presence of blue shifted asymmetry or excess broadening of the emission line profiles are additional characteristic signatures of high velocity outflows.

Single fiber and long slit spectroscopy have been widely used to detect these outflows from the presence of broad and extended emission line profiles (Harrison et al. 2012). However, due to the lack of spatial information from these 1D spectroscopic techniques, the outflow morphology, geometry and their direct association with radio jets couldn't be well constrained. With the recent advent of spatially resolved observations of optical emission lines (e.g. [OIII) λ 5007, Hα) from integral field spectroscopy, it is possible to map the 2D geometry and energetics of the outflows prevalent in the narrow line region of the AGNs and quasars (Storchi-Bergmann et al. 2010; Husemann et al. 2013; Rupke & Veilleux 2013; Harrison et al. 2014).

There have been many studies on the relationship between the observed properties of the radio AGNs and the presence of outflows. Traditional radio loud galaxies ($L_{1.4\ GHz} > 10^{24}$W Hz^{-1}) with strong FRI/FRII-like radio jets are observed to accelerate powerful outflows by pushing gas along their direction of propagation (Nesvadba et al. 2008; Vayner et al. 2017). But these luminous radio galaxies are quite rare. Recent works are revealing that similar incidence of outflows are seen in low power radio AGNs with compact morphology that are more commonly found in the local universe (Combes et al. 2014; Morganti et al. 2015; Harrison et al. 2015; Jarvis et al. 2019, 2021).

Majority of the compact radio sources are unresolved using typical 5″ resolution of FIRST survey. High resolution (sub-arcsecond) followup radio imaging from VLA, e-MERLIN, etc, has revealed small-scale extended radio jets in a majority of these unresolved compact radio galaxies, with jet sizes ranging between 1−25 kpc (Jarvis et al. 2019, 2021; Venturi et al. 2021; Husemann et al. 2019). These are moderate

luminosity sources ($L_{1.4\ GHz} < 10^{24}$ W Hz^{-1}) which are classified as 'radio-quiet' by traditional criteria (Xu et al. 1999). Using integral field spectroscopic observations, it has been possible to spatially resolve the gas kinematics of the host galaxies and identify the outflow regions.

AGNs displaying compact radio jets are commonly reported to have outflows that are spatially aligned with these jets (e.g., Tadhunter et al. 2003; Holt et al. 2006; Labiano 2008; Santoro et al. 2018; Husemann et al. 2019). There are also instances of gas outflows expanding parpendicular to the radio jets (Couto et al. 2013; Riffel et al. 2014; Venturi et al. 2021). The outflow regions are identified by broad emission lines and highly disturbed kinematics. These observations suggest an interaction between the low power jet and the cooler gas in the surrounding ISM, giving rise to highly turbulent motions very similar to the examples in radio loud FRI and FRII counterparts. For a statistically large sample of galaxies, gas outflows are observed to be preferentially present in those with a compact radio morphology than galaxies with large-scale radio jets (Mullaney et al. 2013). In addition to the radio morphology, radio power is also seen to be a strong driving factor to dictate the presence of outflows and hence the [OIII] λ 5007 profile (Zakamska & Greene 2014; Nesvadba et al. 2008). This is reflected in the fact that moderate radio luminosity objects ($23 < \log L_{1.4GHz}/\mathrm{W\ Hz^{-1}} < 25$), which are most commonly associated with compact FR0 sources, produce the strongest winds.

It is evident from these examples that low power FR0-type compact jets host the most extreme ionized gas kinematics and may play a more direct role in affecting

the host galaxy since the radio jets are confined within the ISM (Holt et al. 2008; Jarvis et al. 2019). These observations are consistent with model predictions which show that jets can increase the turbulence in the ISM and drive galactic-scale outflowing bubbles (Mukherjee et al. 2018; Weinberger et al. 2016; Weinberger et al. 2017a). These small-scale jets might be the dominant source of jet-mode feedback in kiloparsec scales (Wagner et al. 2012; Mukherjee et al. 2016; Bicknell et al. 2018).

Almost all the studies of radio jet driven feedback and outflows discussed in this section have been carried out in star forming Seyfert type galaxies, often with an active quasar ($L_{AGN} > 10^{45}$ erg/s) and high accretion rate. The host galaxies are not in a passive state yet and hence do not explicitly probe the 'jet-mode' feedback. Observational confirmation and a physical understanding of how this mode actually works are still urgently needed.

1.4 Red Geysers

A useful discovery was recently made in an effort to detect possible radio/jet mode feedback signatures in typical quiescent galaxies. Using z$\sim$0.05 spatially resolved spectroscopy from the SDSS-IV MaNGA survey (Mapping Nearby Galaxies at Apache Point Observatory; Bundy et al. 2015), Cheung et al. (2016) has revealed a new population of quenched early type galaxies, named 'red geysers', that host signatures of large scale ionized gas outflows. The prototypical red geyser 'Akira' studied in Cheung et al. (2016) also indicate the presence of a low luminosity radio AGN at the center

($L_{1.4GHz} \sim 10^{21}$ W Hz^{-1}), with enough mechanical output ($P_{mech} \sim 10^{41}$erg s^{-1}) to power the observed wind ($\dot{E}_{wind} \sim 10^{39}$ erg s^{-1}). Unlike the rare and extremely luminous bipolar jets found in traditional radio galaxies with FRI/FRII-like morphology, red geysers are present much more frequently in the local red sequence population at the rate of $5 - 10\%$.

From SDSS data, Akira looks like an ordinary elliptical galaxy with a moderate mass ($\log M_\star/M_\odot \sim 10.7$) and LINER-like optical spectra. However, MaNGA data displays a unique narrow bisymmetric feature in the resolved equivalent width (EW) map of strong emission lines (especially Hα), which is interpreted to be tracing the putative ionized wind cone. This ionized wind is estimated to have sufficient kinetic power to disrupt the cooling of cold gas and prevent rejuvenation of any further star formation activity. The level of star formation activity detected from multiband photometry is indeed very low (SFR $\sim 10^{-2}$ $M_\odot$/yr; Salim et al. 2016). This thesis strives to better understand the physics of the red geyser population and examine their role in suppressing star formation on the red sequence. Do they represent the long-sought maintenance-mode feedback? How do the winds inject energy into the ambient medium?

Before assessing the importance of red geysers as a possible feedback channel, a well-defined and robust selection procedure is required to ensure completeness of the sample and remove any false positives. As a first step of this thesis, we define a set of identification criteria to visually select the red geyser sample. The enhanced bisymmetric emission in spatially resolved maps of Hα and [OIII] λ5007 is one of the distinctive signatures of red geysers. §2.3.1.1 in Chapter 2 discusses the detailed features

used in the identification process. Initially in Roy et al. (2018), our red geyser population consisted of 84 sources from the SDSS data release 14 sample of $\sim$ 1100 red sequence galaxies. In Roy et al. (2021b), we have expanded the sample of red geysers to 140 galaxies based on the latest MaNGA sample available at the time.

Red geysers are quiescent galaxies, with red optical color (NUV $-$ r $>$ 5) and old stellar populations. The widespread presence of ionized gas detected throughout the integral field unit (IFU) field of view are thought to be ionized predominantly by evolved post-asymptotic giant branch stars, similar to the LI(N)ER like galaxies (Belfiore et al. 2016). Although the optical line ratios do not show any strong sign of AGN activity, our hypothesis is that the large scale centrally driven winds are possibly driven out by an AGN. Are these low luminosity AGNs not detected at optical wavelength but reveal themselves in radio frequency?

Data from the FIRST radio survey (Faint Images of the Radio Sky at Twenty centimeters; Becker et al. 1995) suggest that several within the red geyser sample are radio detected, although with a low flux level, and often hitting close to the detection limit ($\sim$ 1mJy). Using an exhaustive bootstrapping technique, we find that the red geysers show a FIRST detection rate at least $\sim$ 3 times higher than matched quiescent control galaxies. To consider the sources which might lie just below the FIRST detection threshold, we also perform a sample-wide stacking analysis and find that the average stacked flux in the red geysers is about $\sim 5\sigma$ greater than the control sample. Ruling out possible hidden star formation activity from WISE infrared data, this work described in Chapter 2 has confirmed that the red geysers preferentially host radio

AGNs compared to non red geyser quiescent galaxies, with an average radio luminosity $L_{1.4\ GHz} \sim 10^{22}$ W Hz^{-1} (Roy et al. 2018).

Almost all the red geyser sources appear compact or unresolved in the FIRST images. So, what are their radio morphology? In a followup study, we have obtained additional sensitive radio observations both at low frequency (144 MHz) from LOFAR Two meter sky survey (LoTSS) and at high frequency (2-4 GHz) from VLA Sky Survey (VLASS) to accompany the FIRST images. In Chapter 3, we show that the red geysers show an even higher radio detection rate in LoTSS compared to the earlier FIRST survey results. Moreover, the radio detected sources show a wide variety of interesting radio morphology - ranging from compact, slightly extended to large scale double-sided lobes that extend several tens of kpc outside the galaxy (Roy et al. 2021b). A majority of the sources still display a compact radio morphology with radio sizes varying between $5 - 25$ kpc. Their luminosity, spectral indices, and radio behaviour are consistent with the low power compact FR0 galaxies and the radio-quiet quasars (RQQ; see Fig. 1.4), which host small-scale AGN driven jets. Moreover, three red geysers present large radio lobes extending beyond 30 kpc and are classified as traditional FR-type radio galaxies.

The radio analysis presented in Chapter 2 is an important step in verifying the AGN presence which are capable of driving red geyser winds. We have developed several lines of evidence in support of the wind interpretation first proposed by Cheung et al. (2016) for the prototypical red geyser. One of the strongest arguments comes from the dynamical modelling of the gas kinematics using Jeans Axisymmetric Modeling (JAM). As shown in Appendix A.1, the optical surface brightness and the stellar kinematics

are used to constrain the galaxy's gravitational potential. This potential can predict a maximum velocity V_{rms} ($V_{rms} = \sqrt{V^2 + \sigma^2}$) of the gas arising from gravitationally bound orbits. However, the observed V_{rms} exceeds the JAM estimated value, indicating turbulent outflowing motion. The enhanced biconical pattern perceived in the emission map also roughly align with the gas kinematic major axis - as expected from the wind model, and they are marked by regions of high dispersion. Given high velocities and other common features shared among all the red geysers, outflowing winds emerge as a compelling interpretation.

Chapter 4 discusses these kinematic arguments and presents additional confirmation in support of the wind scenario using higher spectral resolution Keck Echelette spectra from the ESI instrument (R$\sim$ 8000 compared to MaNGA with R$\sim$ 2000; Roy et al. 2021a). Keck ESI data shows asymmetric emission lines with multi-component velocity structure along the bisymmetric enhanced EW regions, which were previously blended in the MaNGA resolution. Isolating the individual velocity components and quantifying the degree of asymmetry at different spatial locations in the targeted red geysers, we show that the systematic change in the 'winged' profile is only consistent with a broad conical outflow. As described in Chapter 4 in detail, we construct a toy wind and a disk model to try to reproduce the projected 2D kinematic maps observed by MaNGA, as well as the velocity profiles seen by Keck. The disk model fails to recreate the asymmetric emission line profiles and the broad line widths, clearly favoring the wind model over a rotating disk.

While the enhanced Hα line emission indicates an approximate mass of the

ionized gas to be $\sim 10^5$ $M_\odot$, red geysers likely host an even greater amount of cold gas, as seen by a strong presence of the sodium doublet absorption line (NaD) in the prototypical red geyser. Chapter 5 shows that this is certainly the case for the entire red geyser sample. Red geysers present widespread cool ($T \sim 100 - 1000$ K) but diffuse gas with an estimated mass of $M_{cool} \sim 10^8$ $M_\odot$. Curiously, the red geysers which are detected in radio surveys like FIRST and LoTSS possess the strongest NaD signatures with highest EW, indicating some underlying connection between the presence of cool gas reservoir and the activity of the central AGN (Roy et al. 2021c). Analyzing the absorption line kinematics in a Markov chain Monte Carlo framework, we find a large fraction of this gas to be inflowing towards the galaxy center. Our hypothesis is that the cool gas is infalling towards the center and fuelling the central SMBH, thus forming a mechanically powerful radio AGN which subsequently drive the red geyser winds. Despite the presence of ample amount of multi phase gas, these galaxies show very little star formation ($SFR < 0.02$ $M_\odot$ yr^{-1}), indicative of the ongoing feedback mechanism perhaps supplied by the wind and the radio jet.

These works show that red geysers emerge as an interesting population of AGN-host galaxies that possibly show signatures of maintenance mode feedback. However, questions still remain about the detailed mechanism of the underlying feedback process in action. Do the apparently compact radio AGNs host low power radio jets with physical sizes < 5 kpc? Do these radio jets drive the observed large scale gaseous outflows? How do the wind energy couple to the ISM leading to global suppression of star formation? To address these questions, higher spatial resolution data is required in

different wavelength windows to especially probe the central regions, where the AGN first encounters ambient gas. In Chapter 6, I have outlined ambitious projects using sub-arcsecond resolution radio data from upgraded LOFAR facilities and adaptive optics assisted infrared observations from Keck OSIRIS instrument that will vastly improve our understanding of this galaxy population.

Chapter 2

Detecting Radio-AGN Signatures in Red Geysers

A new class of quiescent galaxies named "red geysers" has been discovered using spatially resolved optical spectroscopy from the SDSS-IV MaNGA survey. They harbor emission and kinematic features signalling large scale ($\sim$ 10 kpc) centrally-driven winds that are predicted to play a role in suppressing star formation at late times. In this chapter, we test the hypothesis that AGN activity is ultimately responsible for this red geyser wind phenomenon. We compare the nuclear radio activity of the red geysers to a matched control sample with similar stellar mass, redshift, rest frame $NUV - r$ color, axis ratio and presence of ionized gas. We have used the 1.4 GHz radio continuum data from VLA FIRST survey to stack the radio flux from the red geyser and control samples. In addition to a 3 times higher FIRST detection rate, we find that red geysers have a 5σ higher level of average radio flux than control galaxies. After restricting to

rest-frame $NUV - r$ color > 5 and checking mid-IR WISE photometry, we rule out star formation contamination and conclude that red geysers are associated with more active AGN. Red geysers and a possibly-related class with disturbed Hα emission account for 40% of all radio-detected red galaxies with log ($M_\star/M_\odot$) < 11. Our results support a picture in which episodic AGN activity drives large-scale-relatively weak ionized winds that may provide a feedback mechanism for many early-type galaxies. [1]

2.1 Introduction

The level of star formation in galaxies is known to be bimodal (Blanton et al. 2003; Strateva et al. 2001; Kauffmann et al. 2003), with star–forming galaxies often referred to as the "blue cloud" and galaxies without significant star formation fall under the "red sequence" category. The latter is characterized by old stellar populations ($\geq$ 6 Gyr) and short star-formation timescales ($\sim$ 1 Gyr; Tinsley 1979; Worthey et al. 1992; Trager et al. 2000; Thomas et al. 2005; Graves & Schiavon 2008; Conroy et al. 2014; Worthey et al. 2014; Choi et al. 2014). The abundance of these quiescent galaxies has increased by several factors since z $\sim$ 2 (Bell et al. 2004; Bundy et al. 2006; Faber et al. 2007; Ilbert et al. 2010; Moustakas et al. 2013) which implies that more and more galaxies are transitioning to quiescence. The increase in the red-and-dead population indicates that once galaxies shut off their star formation by some mechanism, they must stay quenched for a long time.

[1]This chapter was previously published in the Astrophysical Journal as **Detecting Radio AGN Signatures in Red Geysers**, Roy, N., Bundy, K., Cheung, E. et al. 2018, ApJ, 869, 117, DOI:10.3847/1538-4357/aaee72.

A permanent shut down of star formation is hard to explain, because the quiescent population is not devoid of gas and is also capable of accreting new gas to eventually start forming stars again. Major surveys have shown an abundance of gas in quiescent galaxies (Binette et al. 1994; Buson et al. 1993; Demoulin-Ulrich et al. 1984), which if left to itself, should ultimately cool and form stars. This gas comes from a variety of sources like stellar mass loss from evolved stars (e.g., Mathews & Brighenti 2003; Ciotti & Ostriker 2007) or minor mergers. If all this gas formed stars, we would expect the global stellar mass density to be larger by factors of a few than the observed at z = 0. This implies that an additional feedback mechanism is required to maintain the suppression of star formation in galaxies on the red sequence (Benson et al. 2003).

While a number of feedback mechanisms have been proposed, including inter-stellar medium (ISM) heating from stellar winds (Conroy et al. 2015) and gravitational effects induced by galaxy bulges (Martig et al. 2009), the most popular explanation has been active galactic nuclei (AGN) feedback (Binney & Tabor 1995; Ciotti & Ostriker 2001; Croton et al. 2006; Fabian 2012; Yuan & Narayan 2014; Heckman & Best 2014). It states that the energy released from the central AGN in the host galaxy in the form of winds, outflows or jets can significantly effect the evolution of the galaxy by feedback mechanism which can take place via two different ways (Fabian 2012; Morganti 2017). The "quasar" or "radiative" mode feedback, mostly associated with luminous AGN or massive quasar, release huge amount of energy to their surroundings by radiation from the accretion disk and drive powerful gas outflows, which remove gas altogether from the galactic potential well (Cattaneo et al. 2009; Fabian 2012). The "radio-mode", on

the other hand, is prevalent mostly in low to moderate luminosity AGN where the black hole accretes at a lower rate and the radio AGN present in the center of the galaxy deposits energy into the surrounding gas via jets or winds, heating it and suppressing star formation (Binney & Tabor 1995; Ciotti & Ostriker 2001; Croton et al. 2006; Bower et al. 2006; Ciotti & Ostriker 2007; Ciotti et al. 2010; McNamara & Nulsen 2007; Cattaneo et al. 2009; Fabian 2012; Yuan & Narayan 2014; Heckman & Best 2014). Direct observational evidence for this low-luminosity radio-mode or "maintenance mode" feedback is limited to several nearby clusters (Cattaneo et al. 2009; Dunn & Fabian 2006; Fabian 1994, 2012; Fabian et al. 2006; McNamara & Nulsen 2007). Evidence for this mechanism in more typical galaxies remain elusive.

Recently, Cheung et al. (2016) discovered a new class of quiescent galaxies, referred to as "red geysers", that show distinctive emission line patterns showing gas outflows from the center and kinematic properties (explained in detail in §2.3.1.1) which may signal AGN maintenance-mode feedback in action. Based on spatially resolved information from Sloan Digital Sky Survey-IV (SDSS-IV) Mapping Nearby Galaxies at Apache Point Observatory (MaNGA) survey (Bundy et al. 2015), this class of quiescent galaxies appears to host large scale winds of ionized gas that align with bi-symmetric enhancements in the spatial distribution of strong emission lines like Hα. Ionized emission extends throughout the entire galaxy with line ratios similar to LIER-like (low ionization emission region) galaxies (Belfiore et al. 2016). In addition to their enhanced bisymmetric line emission, the red geysers also exhibit gas kinematics consistent with outflowing winds. The gradient of the gas velocity field aligns with the position angle

of the emission pattern, but is largely misaligned with the major or minor axes derived from the stellar velocity field. The gas velocity values can reach ~ 300 km s^{-1}, a value that is difficult to explain by orbital motion from the galaxy's gravitational potential, considering the mass range of the galaxies.

Early-type galaxies with accreted disks, as studied by Chen et al. (2016) and Lagos et al. (2015), can show similar kinematic features as red geysers, but those features are formed due to a completely different phenomena. The accreted gas coming in from random directions will gradually align itself with either major or minor axis through gravitational torques generated by the galaxy's potential well. Hence, while a misalignment in the velocity gradient of stars and gas can occur for these galaxies too, often the misalignment angle is 90° or 0°/ 180° depending on whether a polar disk or co-rotating/ counter rotating disk is formed. Some galaxies with accreted disks might show similar Hα equivalent width (EW) distributions as red geysers. Cheung et al. (2016) rejected the disk interpretation through detailed Jeans Anisotropic modeling (JAM; Cappellari 2008) of the prototypical red geyser with 99% confidence which demonstrated that the gas velocity in this source is too high (difference between observed gas velocity and expected velocity from modeling being $\sim$ 100 km s^{-1}) to be described by the orbital motion. Given similar high velocities and other common features shared among all the red geysers, outflowing winds emerge as a compelling interpretation (Bundy et al. in preparation), making the question of whether AGNs are capable of driving these winds particularly important.

A critical first step is to test the hypothesis that the red geyser population is

more likely to host an active AGN compared to quiescent galaxies with similar global galaxy properties. For the prototypical red geyser named "Akira", Cheung et al. (2016) showed that the host galaxy has a weakly and/or radiatively-inefficient supermassive black hole with very low Eddington ratio ($\lambda = 3.9 \times 10^{-4}$), accreting mass from a low-mass companion galaxy. It was detected as a central radio point source.

The goal of this work is to search for radio-mode AGNs in the entire red geyser sample. We analyze stacked radio flux from Very Large Array (VLA) Faint Images of the Radio Sky at Twenty-Centimeters (FIRST) survey and find a higher value of radio flux from the red geyser candidates than the comparison sample of quiescent galaxies. We have excluded possible star formation contamination and/or galaxies with embedded disks from our sample by using optical and infrared photometry. §2.2 describes the optical, infrared and radio data that we have used in this work. In §2.3.1, we discuss in detail, the red geysers and the control sample chosen from the MaNGA local quiescent population. The technical details of radio aperture photometry and the stacking analysis have been narrated in §2.3.2. The results thus obtained from the stacked radio flux are described in §2.4. The implication of the results are given in §2.5.

Throughout this paper, we assume a flat cosmological model with $H_0 = 70$ km s^{-1} Mpc^{-1}, $\Omega_m = 0.30$, and $\Omega_\Lambda = 0.70$, and all magnitudes are given in the AB magnitude system.

2.2 Data

2.2.1 The MaNGA survey

Our sample comes from the ongoing SDSS-IV MaNGA survey (Blanton et al. 2017; Bundy et al. 2015; Drory et al. 2015; Law et al. 2015; Yan et al. 2016; Albareti et al. 2017). MaNGA is an integral field spectroscopic survey that provides spatially resolved spectroscopy for nearby galaxies (z $\sim$ 0.03) with an effective spatial resolution of 2.5″ (full width at half-maximum; FWHM). The MaNGA survey uses the SDSS 2.5 meter telescope in spectroscopic mode (Gunn et al. 2006) and the two dual-channel BOSS spectrographs (Smee et al. 2013) that provide continuous wavelength coverage from the near-UV to the near-IR: $3,600 - 10,000$ Å. The spectral resolution varies from R $\sim$ 1400 at 4000 Å to R $\sim$ 2600 at 9000 Å. An r-band signal-to-noise (SN) of $4 - 8$ Å^{-1} is achieved in the outskirts (i.e., $1 - 2$ R$_e$) of target galaxies with an integration time of approximately 3-hr. MaNGA will observe roughly 10,000 galaxies with log (M$_*$/M$_\odot$) $\geq$ 9 across $\sim$ 2700 deg^2 over its 6 yr duration. In order to balance radial coverage versus spatial resolution, MaNGA observes two thirds of its galaxy sample to $\sim$ 1.5 R$_e$ and one third to 2.5 R$_e$. The MaNGA target selection is described in detail in Wake et al. (2017).

The raw data are processed with the MaNGA Data Reduction Pipeline (DRP; Law et al. 2016). An individual row-by-row algorithm is used to extract the fiber flux and derive inverse variance spectra from each exposure, which are then wavelength calibrated, flat-fielded and sky subtracted. We use the MaNGA sample and data products

drawn from the MaNGA Product Launch-5 (MPL-5) and Data Release 13. The data products are identical to those released as part of the SDSS Data Release 14 (DR14; Abolfathi et al. 2018). We use spectral measurements and other analyses carried out by a preliminary version of the MaNGA Data Analysis Pipeline (DAP), specifically version 2.0.2.[2] In brief, the data we use here are based on DAP analysis of each spaxel in the MaNGA datacubes. The DAP first fits the stellar continuum of each spaxel to determine the stellar kinematics using the Penalised Pixel-fitting algorithm `pPXF` (Cappellari & Emsellem 2004; Cappellari 2017) and templates based on the MILES stellar library (Falcón-Barroso et al. 2011). The templates are a hierarchically clustered distillation of the full MILES stellar library into 49 templates. This small set of templates provide statistically equivalent fits to those that use the full library of 985 spectra in the MILES stellar library. The emission-line regions are masked during this fit. The DAP then subtracts the result of the stellar continuum modeling to provide a (nearly) continuum-free spectrum that is used to fit the nebular emission lines. This version of the DAP treated each line independently, fitting each for its flux, Doppler shift, and width, assuming a Gaussian profile shape. This is different from the approach used by the DAP for DR15, which is to tie the velocities of all lines to a single value and to impose fixed flux ratios for the [OI], [OIII], and [NII] line doublets. A detailed comparison of the results from the DR15 and MPL-5 versions of the DAP show that the different approach taken by the latter, and used for our analysis, has a negligible influence on our results. The final

[2]This version of the code has been made public in the SDSS Data Release 15 (DR15; Aguado et al. 2019). An overview of the DAP used for DR15 and its products is described by Westfall et al. (2019), and assessments of its emission-line fitting approach is described by Belfiore et al. (2019)

output from the DAP are gas and stellar kinematics, emission line properties and stellar absorption indices.

We use ancillary data drawn from the NASA-Sloan Atlas[3] (NSA) catalog which reanalyzes images and derives morphological parameters for local galaxies observed in Sloan Digital Sky Survey imaging. It compiles spectroscopic redshifts, UV photometry (from GALEX; Martin et al. 2005), stellar masses, and structural parameters. We have specifically used spectroscopic redshifts and stellar masses from the NSA catalog.

2.2.2 The FIRST survey

The radio data studied in this paper comes from the VLA Faint Images of the Radio Sky at Twenty Centimeters (FIRST; Becker et al. 1995) survey, which obtained data at frequency channels centered at 1.36 GHz and 1.4 GHz over 10,000 square degrees in the North and South Galactic Caps. The source detection threshold is $\sim$ 1 mJy, corresponding to a source density of $\sim$ 90 sources deg^{-2}. FIRST images have 1.8$''$ pixels with a resolution of $\sim 5''$ and typical rms of 0.15 mJy. The astrometric accuracy of each source is $0.5 - 1''$ at the source detection threshold. Since FIRST survey area was designed to overlap with the Sloan Digital Sky Survey (SDSS; York et al. 2000; Abazajian et al. 2009), most MaNGA targets have FIRST data coverage. For our sample of interest, 93% of the red geysers have FIRST coverage. However, the 1 mJy threshold results in non detections for most MaNGA galaxies.

For each pointing center, there are twelve adjacent single-field pointings that

[3] http://www.nsatlas.org

are co-added to produce the final FIRST image. Sources are extracted from the co-added reduced images and fit by two dimensional Gaussians to derive peak flux, integrated flux densities and size information. The current FIRST catalog is accessible from the FIRST search page[4].

2.2.3 SDSS+WISE star formation rates

In order to assess possible contamination from obscured star formation, we have used the Chang et al. (2015) catalog to obtain infrared (IR)-based star formation rates (SFR). The catalog contains 858,365 galaxies within the SDSS spectroscopic sample as compiled in the New York University Value-added Galaxy Catalog (NYU-VAGC; Blanton et al. 2005; Adelman-McCarthy et al. 2008; Padmanabhan et al. 2008) and cross-matched with the ALLWISE (Wide Field Infrared Survey Explorer) source catalog. Unlike optical emission line SFR estimates, Chang et al. (2015) utilized mid-IR data from full WISE photometry and employed an SED fitting technique to estimate stellar mass and star formation rates. Their modeling is based on the MAGPHYS library [5] (MAGPHYS contains 50,000 stellar population template spectra and 50,000 PAH+dust emission template spectra) and is applied to all $z < 0.2$ galaxies with good WISE photometry (FLAG_W = 1 or 2), and good-quality SED fits (FLAG_CHI2 = 1). None of the objects in our sample features AGN-like WISE colors, hence it is unlikely that AGN contamination may be significantly biasing the SED-based SFR estimates. We

[4] http://sundog.stsci.edu/cgi-bin/searchfirst. The full images are available in ftp://archive.stsci.edu/pub/vla_first/data

[5] http://www.iap.fr/magphys/

have used the public Chang et al. (2015) catalogs [6]. Details are given in Chang et al. (2015).

2.3 Method

The identification of red geysers is based on the optical resolved spectroscopic data from MaNGA. Sub-section §2.3.1.1 describes the conditions and criteria that have been used to select our sample. Matched control sample galaxies have been selected from the full galaxy sample via the method discussed in §2.3.1.2. A third category of galaxies, which we call the "Hα-disturbed" class as described in detail in §2.3.1.3, consists of galaxies that are not classified as geysers due to the absence of the characteristic bi-symmetric pattern in resolved optical emission map, but they show kinematic and emission line properties that are quite different from typical quiescent galaxies. They have distinct regions of enhancements in Hα-equivalent width map, along with high spatially resolved gas velocity values in comparison to stellar velocity. The Hα-disturbed class forms a separate category, distinct from both the red geyser and control samples. We perform aperture photometry (described in detail in §2.3.2) on the FIRST radio cutouts for all galaxies using an aperture size of $10''$ diameter, to obtain radio flux values and the associated photometric errors. The galaxies which satisfy the condition $S/N > 3$ are classified as radio-detected with a confidence level of 3σ. Since the detection threshold of the VLA FIRST survey is shallow ($\sim$1 mJy), many galaxies might lie below the sensitivity limit. Section §2.3.2 describes the stacking analysis that allows us

[6] http://irfu.cea.fr/Pisp/yu-yen.chang/sw.html

to constrain the average radio flux for samples of galaxies that are undetected individually. The median-stacked FIRST images for our sample provide greater signal-to-noise with typical rms ≈ 10 μJy.

2.3.1 Sample Selection

In this section we describe the identification of red geysers, the selection of matched control sample galaxies and characterization of the Hα-disturbed galaxies.

2.3.1.1 Red geysers

Red geysers are visually selected based on their characteristic features, as described in Cheung et al. (2016). Red geysers are red galaxies defined by rest frame color $NUV - r > 5$ (Fig 2.2). The specified UV-optical color cut selects predominantly quiescent galaxies (Salim et al. 2005, 2007, 2009). In MPL-5, 40% of all the targets fall in the quiescent category by the specific color cut. The SFR estimate derived from full SED fitting from optical to mid infrared data (Chang et al. 2015) are small for the red geysers (96% of the sample has log SFR [$M_\odot$/yr] < -2, shown later in Fig 2.8) to ensure quiescence and remove possible obscured star formation. Additionally, the spatially resolved map of EW of the Dn4000 absorption feature are high, roughly > 1.4 Å, thus ensuring the absence of young stars in the galaxy. The red geysers show narrow bi-symmetric patterns in the ionized gas emission as observed in the EW maps of strong emission lines like Hα and [OIII]. These patterns line up approximately with the gaseous kinematic axis and show a misalignment with the stellar kinematic axis,

but we pay close attention to cases where the mis-alignment of the stellar and gas velocity field is 0°, 180° or 90° in order to exclude embedded co-rotating, counter-rotating and polar gas disks. Another important defining property of the red geysers is that they have high spatially resolved gas velocities which can reach a maximum value of $\sim 250 - 300$ km s^{-1}, much higher compared to stellar velocities; as well as high gas velocity dispersion values (maximum ~ 200 km s^{-1}). Hence the observed second moment of the velocity ($V_{\rm rms} \equiv \sqrt{V^2 + \sigma^2}$) of the ionized gas typically exceed the second velocity moments of the stars by $80 - 100$ km/s, suggesting that the ionized gas kinematics in these galaxies cannot be explained by gravitationally-bound orbits alone. For the prototype red geyser, Cheung et al. (2016) performed detailed Jeans Anisotropic Modeling (JAM) and used the dynamically constrained potential to get a rough estimate of escape velocity, $V_{\rm esc} \sim 400 \pm 50$ km/s. They found that roughly 15-20% of the gas would exceed the escape velocity. A typical example of a red geyser is shown in Fig 2.1. Further details of the selection procedure will be described in Bundy at al. (in prep).

Accreted gas disks in early type galaxies (e.g., Chen et al. 2016) can sometimes produce similar gas velocity gradients like the red geysers, due to rotation of the gaseous material in the disk. A few edge-on disks show a bisymmetric pattern in EW map similar to the red geysers. Hence, we include a few steps in our visual identification, to exclude galaxies with a visible disk component or dust lanes apparent in the optical SDSS image. We discard edge-on galaxies with axis ratio b/a < 0.3. We also checked the galaxy specific stellar angular momentum (λ_{Re}) and ellipticity (ϵ) from the extensive catalog in Graham et al. (2018). Convincingly, we find that 95% of the red geysers are

fast rotator early-type galaxies. Our control sample galaxies are of similar nature, 97% of which are fast rotators according to Graham et al. (2018). Since the fast rotators have stellar disks and are axisymmetric, this implies that a gas disk cannot be in equilibrium if it is misaligned with the stellar kinematic position angle (PA), thus ruling out the possibility of disks to be the source of the observed misalignment in the red geysers. Additionally, to avoid galaxies with rotating disk from being included in the red geyser sample, any galaxy showing a very low value of average gas velocity dispersion through out the galaxy (< 60 km s^{-1} which is roughly the average dispersion value observed in polar disks), has been discarded from our red geyser sample completely, even if it shows other convincing features of a red geyser.

As described in Cheung et al. (2016), the gas velocity fields of the red geysers are poorly fit by flexible disk rotation models. The error-weighted average residual, characterizing the goodness-of-fit, place the red geysers among the worst 5% of fitted MaNGA galaxies with disk-like kinematics. The resolved spectral line ratios land predominantly in the LINER region in the Baldwin, Phillips & Telervich (BPT) diagram, predicting that the ionizing source is mostly post-asymptotic giant branch (AGB) stars and/or AGN.

To summarize, the red geysers in our chosen sample have the following characteristic features:

- Quiescent nature with rest frame color $NUV - r > 5$.
- Bi-symmetric emission feature in Hα-EW resolved map.

- Rough alignment of the bi-symmetric feature with the ionized gas kinematic axis, but misalignment with stellar kinematic axis.
- High spatially resolved gas velocity values, typically reaching a maximum of $\pm$ 300 km/s, which are greater than the stellar velocity values by at least a few factors.
- Very low star formation rate with typical value of log SFR [$M_\odot$/yr] < -2.

Currently, our sample has 84 red geysers, which accounts for $\approx 8\%$ of quiescent MaNGA galaxies (defined as $NUV - r > 5$, see Section §2.3.1.2).

2.3.1.2 Control Sample

We create a control sample of quiescent galaxies with $NUV - r > 5$ (shown in Fig 2.2), which are matched in global properties but do not show the resolved geyser-like features described in §2.3.1.1.

For each red geyser, we match up to five unique quiescent galaxies with the following criteria:

- $|\log\ M_{*,\text{ red geyser}}/M_{*,\text{ control}}| < 0.2$ dex
- $|z_{\text{red geyser}} - z_{\text{control}}| < 0.01$
- $|b/a_{\text{red geyser}} - b/a_{\text{control}}| < 0.1$,

where M_* is the stellar mass, z is the spectroscopic redshift, and b/a is the axis ratio from the NSA catalog. Stellar mass and redshift have been shown to correlate with radio

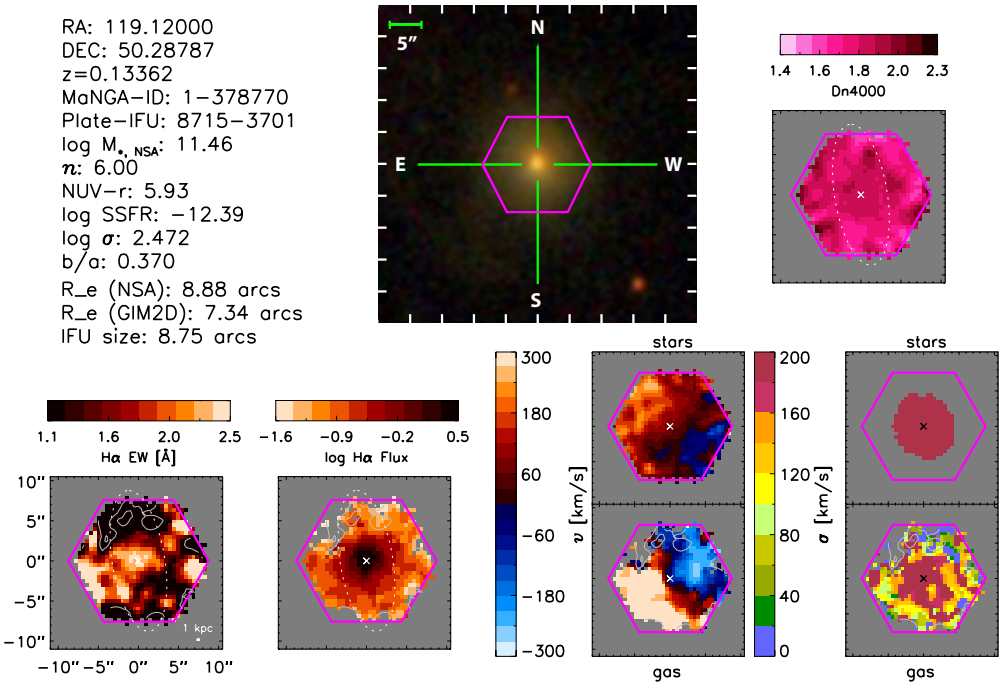

Figure 2.1: A typical red geyser included in our sample. The data has been obtained from MaNGA Integral Field spectroscopic observations. The panel on the center shows the optical image of the galaxy (MaNGA-ID: 1-634825).The magenta hexagon marked in the image is the extent of the MaNGA fiber bundle. In the other panels, as labelled, we have shown the Hα-flux map, Equivalent width map, Dn4000 absorption map, the velocity maps of gas and the stars along with their dispersion. This galaxy satisfies all the conditions that we use to classify an object as red geyser. Specially notable is the bi-symmetric pattern in the equivalent width map of Hα and the kinematic axis align perfectly with the gas velocity field.

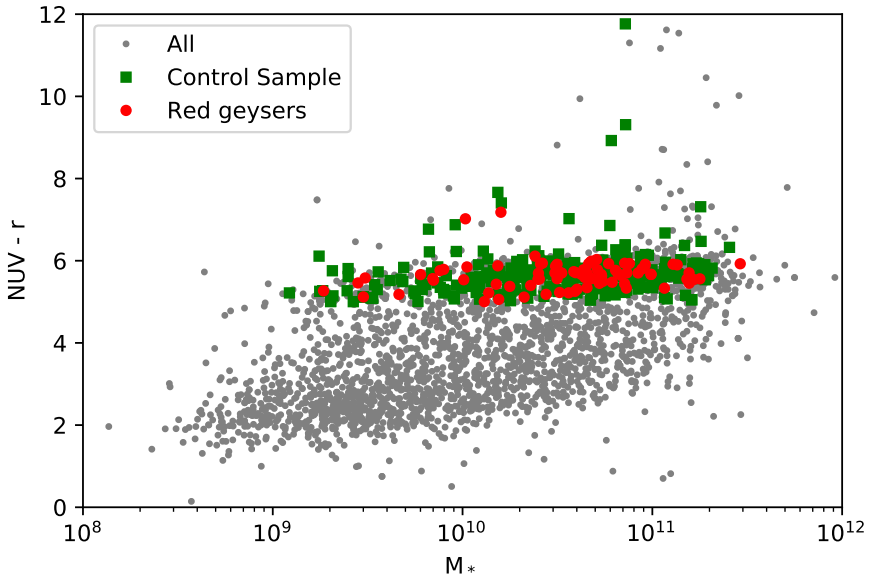

Figure 2.2: The rest-frame $NUV - r$ color vs. stellar mass (log M_*) diagram of the MaNGA sample, with the red geysers in red circles and the control galaxies in green squares. Quiescent galaxies are clustered in the upper part of the NUV − r distribution; we define NUV − r > 5 as a conservative boundary of quiescent galaxies. Galaxies with NUV − r > 8 are undetected in the NUV data.

emission and thus must be controlled for (e.g., Condon 1984; Dunlop & Peacock 1990; Best et al. 2005). We also control for axis ratio so that we do not compare potentially dust-reddened edge-on galaxies with the relatively face-on red geyser galaxies. This matching technique results in 260 unique control galaxies. Fig 2.3 shows an example of a typical quiescent galaxy from the control sample.

Fig. 2.4 compares the global galaxy properties of the control sample and the red geysers. The red geysers (red) and the control sample (blue) are well-matched in all four parameters– stellar mass, redshift, color and axis ratio as expected.

2.3.1.3 Hα-Disturbed Galaxies

During the course of visual inspection, we have discovered another category of galaxies which we will hereby refer to as "H$\alpha-$disturbed". Fig 2.5 shows an example. The gas content of these galaxies is comparable to the red geysers (median Hα EW value > 0.5 Å similar to ~ 0.8 Å in the red geysers) but the Hα equivalent width maps do not show the clear bisymmetric patterns of a red geyser. They show twisted, disturbed Hα EW maps, sometimes with individual blobs of gas that are found throughout the galaxy. 90% of the sample have spatially resolved gas velocity values reaching a maximum of $\sim$ 250 km/s, which are high compared to the stellar velocities which lie within $\pm$ 60 km/s. Some of them have high gas velocity dispersion, upwards of ~ 200 km s^{-1} as seen in red geyser population. We found 60 such H$\alpha-$disturbed candidates from $\sim$ 900 MaNGA quiescent population, and we treat them as a separate third category different from both the red geyser and control samples.

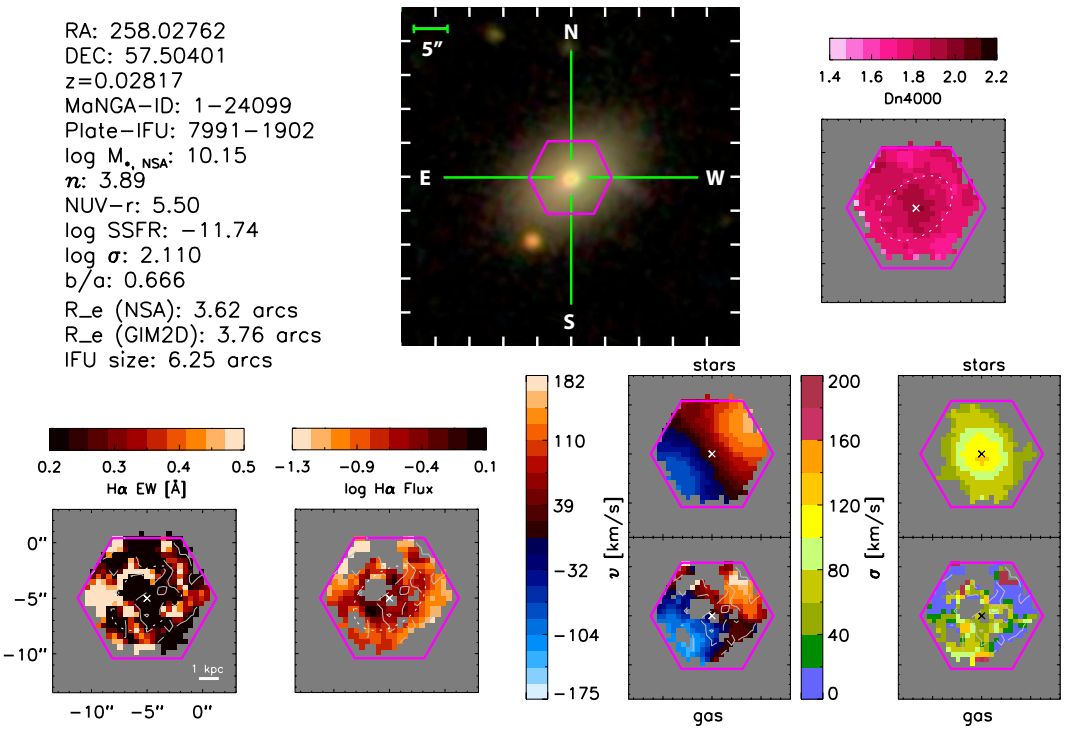

Figure 2.3: A typical control galaxy chosen in our sample. The data has been obtained from MaNGA Integral Field spectroscopic observations. The panel on the center shows the optical image of the galaxy (MaNGA-ID: 1-24099). The magenta hexagon marked in the image is the extent of the MaNGA fiber bundle. In the other panels, as labelled, we have shown the Hα-flux map, Equivalent width map, Dn4000 absorption map, the velocity maps of gas and the stars along with their dispersion. As described in §2.3.1.2, this galaxy is red with NUV-r $>$ 5, has a very low value of star formation and it is relatively face-on with b/a $>$ 0.3. This galaxy is clearly not a red geyser as it does not satisfy any of the red geyser features described in §2.3.1.1, so it can safely be included in the control sample.

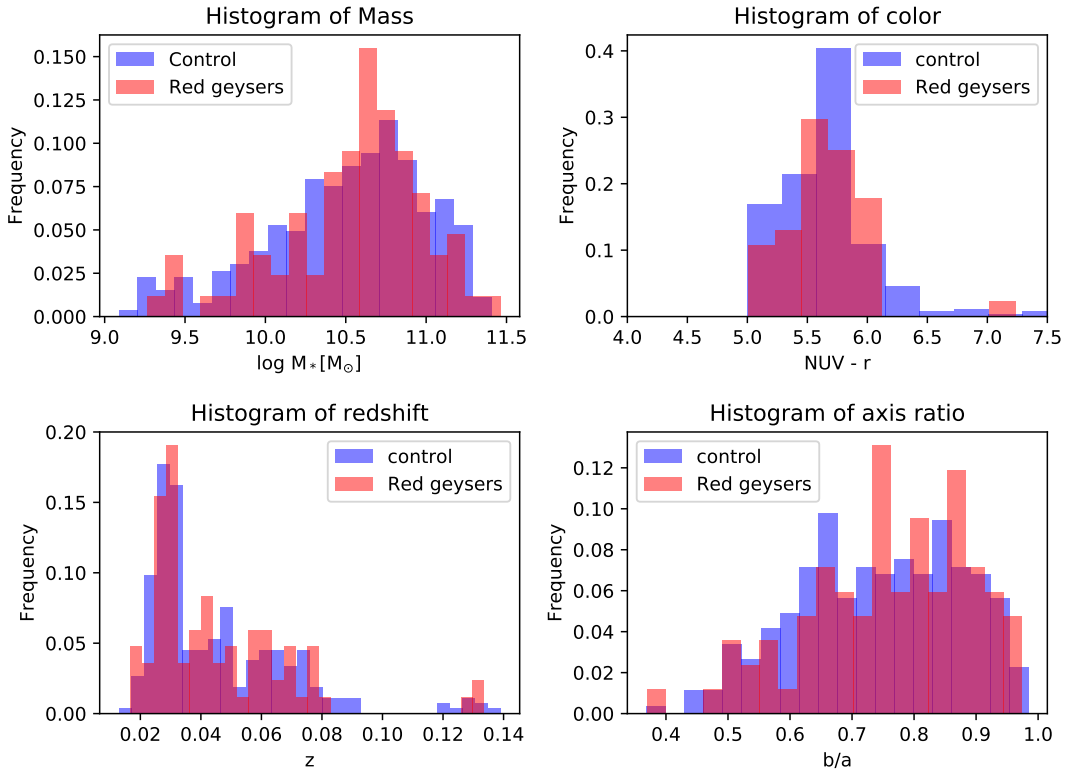

Figure 2.4: Comparison of global properties of red geysers with our chosen control sample. Normalized histograms of the red geysers and control galaxies in: stellar mass (log M_*), rest-frame $NUV - r$ color, redshift (z), and axis ratio (b/a). The red geyser sample distribution are shown in red, while the control sample properties are shown in blue. We see similar distribution for red geysers and control sample properties, as expected from our method of selection of control sample.

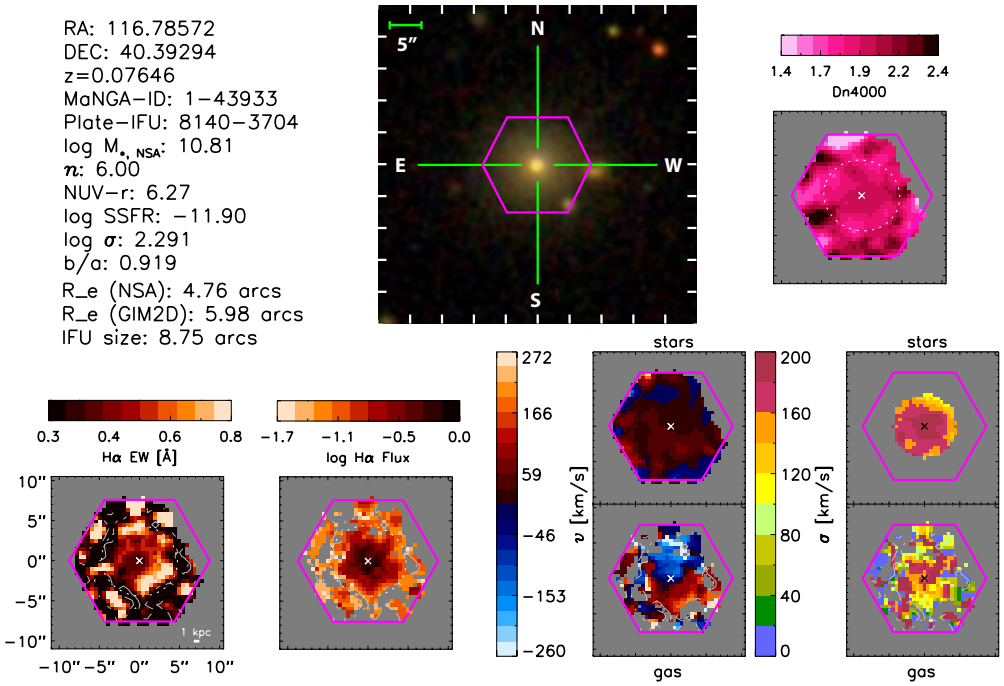

Figure 2.5: A typical disturbed galaxy as described in §2.3.1.3. The data has been obtained from MaNGA Integral Field spectroscopic observations. The panel on the center shows the optical image of the galaxy (MaNGA-ID: 1-43933). The magenta hexagon marked in the image is the extent of the MaNGA fiber bundle. In the other panels, as labelled, we have shown the Hα-flux map, Equivalent width map, Dn4000 absorption map, the velocity maps of gas and the stars along with their dispersion. As described in §2.3.1.3, this galaxy cannot be called a promising geyser candidate because of the lack of the signature bisymmetric pattern, but the kinematics indicate a difference from ordinary control sample. It has been classified as a third "Hα-disturbed" category to separate from the geyser and the control sample population

2.3.2 FIRST Radio Photometry and Stacking

To obtain the radio flux, we perform aperture photometry on the FIRST cutouts for 78 out of 84 red geysers, 260 control galaxies and 57 out of 60 Hα-disturbed galaxies which have FIRST coverage. We first determine which FIRST tile (of dimension $34.5' \times 46.5'$) a specific galaxy falls on. If a galaxy is located too close to the FIRST tile edge (less than $10''$), that galaxy is discarded. We extract a small cutout 50×50 pixels wide (each pixel is $1.8''$) centered on the galaxy of interest. We use a circular aperture of $10''$ diameter centered on the galaxy and sum the radio flux values within. For our target galaxies which are located roughly at redshift ~ 0.03, $10''$ aperture corresponds to 6 Kiloparsec (Kpc) on the sky and hence is a reasonable choice as aperture size. We have defined the criteria for radio detection to be $S/N > 3$. We then perform a median stack of the FIRST images associated with the three samples described in §2.3.1. To ensure that our results are not biased by a few radio bright sources, we have made separate stacks of radio flux with the individually radio detected sources removed.

We have also tested that our stacked radio signal is not an artifact of faulty FIRST tiles by median stacking random cutouts within a radius of $75''$ in the same FIRST tile where the galaxy is located. We would expect these "blank" stacks to have pure white noise with no radio signal.

Fig. 2.6 shows the images of the median stacked flux of these four samples — (1) the red geysers, (2) the control sample, (3) the non-radio-detected red geysers, and (4) the non-radio-detected control sample. The rightmost panel in both the rows show

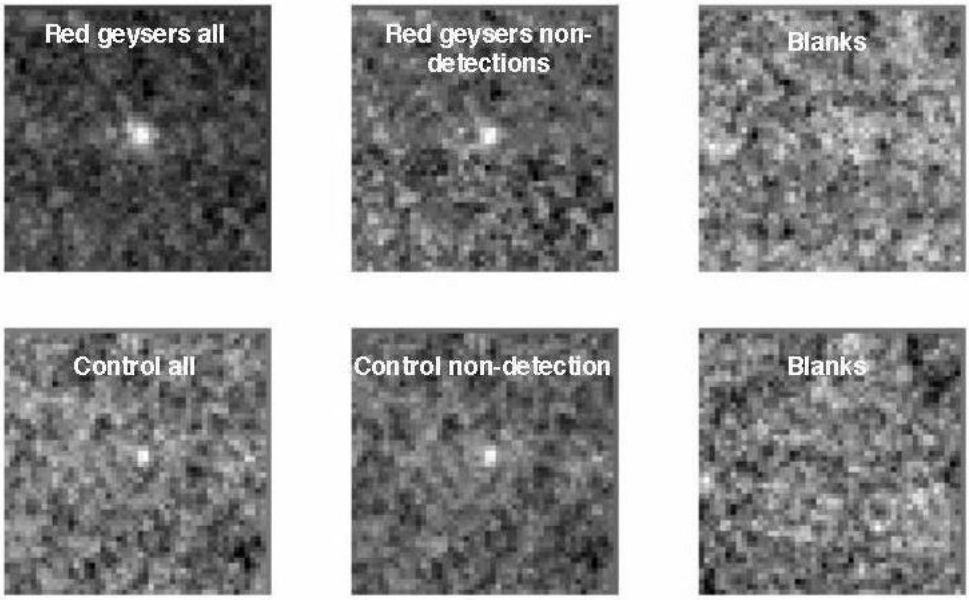

Figure 2.6: The median stacked images of red geysers (top) and control sample (bottom). The middle panels show the non-radio detected stacked images for the red geysers (middle) and the control (bottom middle), where all radio detected sources have been excluded. The blank stacks are shown in (top right) and (bottom right) panels.

the blank stacks. Reassuringly, the blank stacks show no signal.

We perform additional separate stacks controlling for ionized gas content and star formation rates in the control galaxies to see their effect on the radio output. Details of our findings are given in §2.4.

In order to account for the photometric error as well as the systematic error due to sample construction, we perform a bootstrap analysis on all our samples. We construct 1000 random samples with replacement with the same size as each sample and compute the stacked radio flux as before. We take the standard deviation of the resulting flux distributions (σ) to be the estimate of the error on the stacked flux measurements.

2.4 Results

2.4.1 Radio detection of red geysers vs. control sample

We have crossmatched FIRST radio detections with our sample of red geysers and control galaxies. 12 ± 3 out of 78 red geysers ($\sim\ 15\% \pm 4\%$) are found to be radio-detected, where quoted errors are obtained from standard Poisson statistics. Among the control sample, 14 ± 4 out of 260 are radio detected with a detection fraction $\sim 5\% \pm 1.5\%$. Red geysers show a 3 times higher radio detection rate compared to our control sample with a significance level of 5σ. We also find that the radio detected red geysers make up an appreciable fraction ($\sim 10\%$) of the red MaNGA galaxies which are radio-detected by FIRST survey. This fraction increases to $\sim 20\%$ when the Hα-disturbed category galaxies are included along with the red geyser population. If we limit our sample to log $(M_\star/M_\odot) < 11$, the detection rate of red geysers and Hα-disturbed goes up to 40%.

2.4.2 Stacked radio activity of red geysers vs. the control sample

Fig 2.7 shows the first main result of our analysis. We compare the median-stacked radio fluxes of the red geysers (red circles) with that of the control sample (blue squares). Data points in the column marked "All" indicate the median fluxes when the entire sample of geysers and control samples are included in the stack. In the column labelled "Radio non-detection" we have excluded radio bright red geysers and control galaxies. We see that for both these cases, the red geyser radio fluxes, obtained from

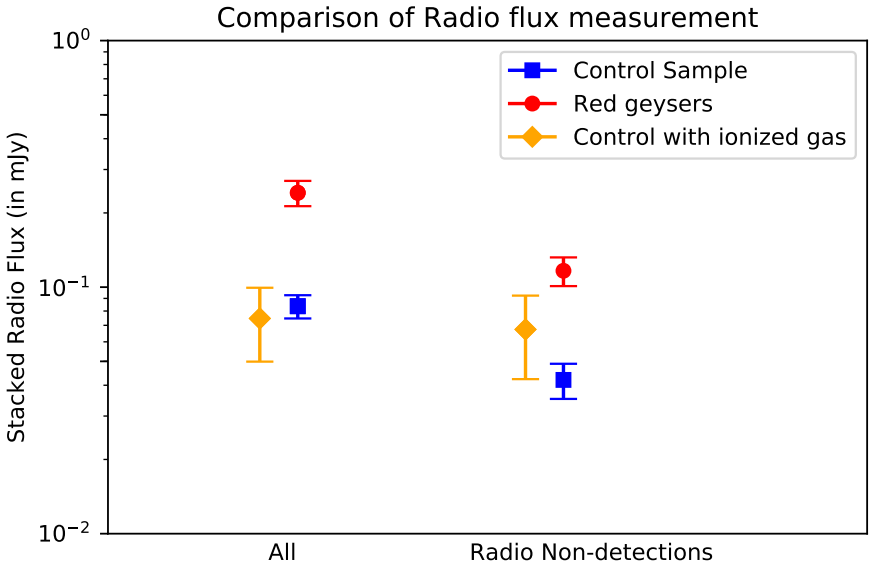

Figure 2.7: The median stacked radio flux obtained from the stacked sample of red geysers (shown in red circles) and control sample (blue squares). "All" represents the stacks where the entire sample has been included for both red geysers and control, while "Radio Non-detections" indicate the stacks where the individually radio-detected sources have been removed. The condition of radio detection of a source has been defined as SN > 3. "Control with gas"– marked in yellow diamonds– shows a specific subset of control galaxies when we additionally controlled for ionized gas (described in §2.4 in details). The red geyser sample show an enhanced radio flux compared to control sample galaxies and the presence of higher amount of ionized gas in the control sample does not necessarily affect the radio-detection rate. The spaxel by spaxel equivalent width information have been obtained from the MaNGA DAP (Data analysis Pipeline) and they have been averaged over the spatial extent of 1.5 effective radii to obtain the mean EW value for a particular galaxy.

median stacking, are 3 times higher than the control sample at greater than 99.99% confidence ($> 5\sigma$).

We additionally control for the presence of ionized gas in our sample. We obtain Hα equivalent width (EW) measurements from the MaNGA DAP. The mean value obtained by averaging the EW (Hα) values of all spaxels in a particular galaxy within 1.5 effective radii is used as the mean EW value, and a proxy for ionized gas content. The control galaxies show an average value of 0.3 Å, somewhat lower than the corresponding 0.8 Å seen in the red geyser sample. To compare against galaxies with similar equivalent width values, we select an additional control sample with EW > 0.5 Å (stacks marked with yellow diamond points). We see that even the radio stack of control galaxies having a comparable level of ionized gas, has a value about 3 times less than that of the red geyser stack. In addition to that, the stacked radio flux for the control galaxies with ionized gas does not show much difference for "All" and "Radio Non-detections" sample, which implies that presence of higher amount of ionized gas in the control sample does not necessarily affect the radio-detection rate.

The detailed implications of these findings are summarized in §2.5.

2.4.3 Dusty star-formation

As described in §2.3.1.1, we set a color cut of rest frame $NUV - r > 5$, and exclude edge on galaxies with b/a < 0.3 to avoid possible radio contamination by star formation to the radio flux. However, UV wavelengths are susceptible to dust attenuation and may not reveal heavily obscured star formation (e.g., Calzetti 2001).

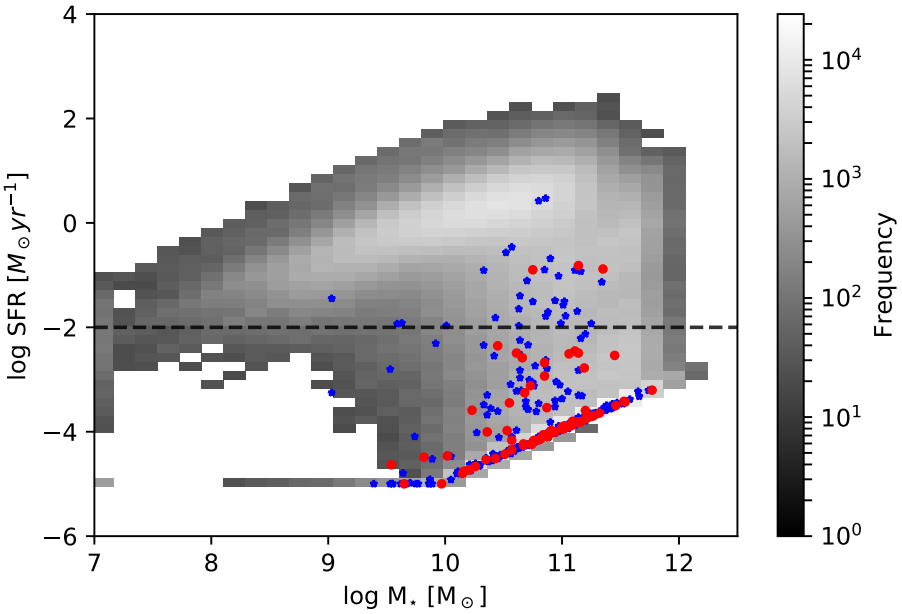

Figure 2.8: The figure shows the log SFR vs log $M_\star$ as obtained from SDSS+WISE catalog of Chang et al. (2015). The gray 2D histogram shows all the galaxies in the catalog with $0.01 < z < 0.1$. The red circles and blue stars signifies red geyser and control sample galaxies respectively. Most of the galaxies in our chosen sample have a low log SFR value, < -2 M$\odot$/yr.

Here we use the SDSS+WISE Chang et al. (2015) catalog for obtaining star formation rates (SFR) based on IR fluxes that are sensitive to dusty star formation. Chang et al. (2015) has utilized the full WISE photometry to model the spectral energy distribution (SED) in optical through mid-IR bands and obtained updated measures of mass and SFR.

Fig 2.8 show the log SFR vs log $M_\star$ diagram of the galaxies from the Chang et al. (2015) catalog. We see that the majority of red geyser and control galaxies lie in the non-star forming region, with low values of SFR. To ensure that our result is not

affected by radio contamination from dusty star formation, we have redone the stacking analysis after excluding galaxies that have log SFR [$M_\odot$/yr] > -2. This cut removes 3 red geysers and 30 control sample galaxies. Fig 2.9 shows the median stacked radio flux in the column labelled "Non-Starforming". We conclude that our results are not affected by contamination from dusty star formation.

WISE colors can be used to detect strong nuclear heating associated with bright AGNs or quasars at the center of the host galaxy. According to Yan et al. (2013), W1 (3.4μm) − W2 (4.6μm) > 0.8 presents an efficient mid-IR color based selection criteria for luminous AGN and quasars. Most of the red geysers and control sample have $0.6 <$ W1 − W2 < 0.7 with very few (1 or 2) having a value > 0.8. This lends confidence to the ability of the WISE data to constrain obscured star formation in these galaxies, as there is no AGN contamination present in the SEDs of these galaxies. We trust the SED-based SFRs from Chang et al. (2015).

2.4.4 Stacked flux of Hα−Disturbed category

In Fig 2.9, the stacked flux for the galaxies in the disturbed category is shown in green star symbol. Remarkably these galaxies show a slightly higher value of median stacked radio flux than the red geysers. The disturbed EW maps and high gas velocity dispersions revealed by MaNGA data correlate with enhanced radio flux. We will discuss the implication of this finding in Section §2.5.

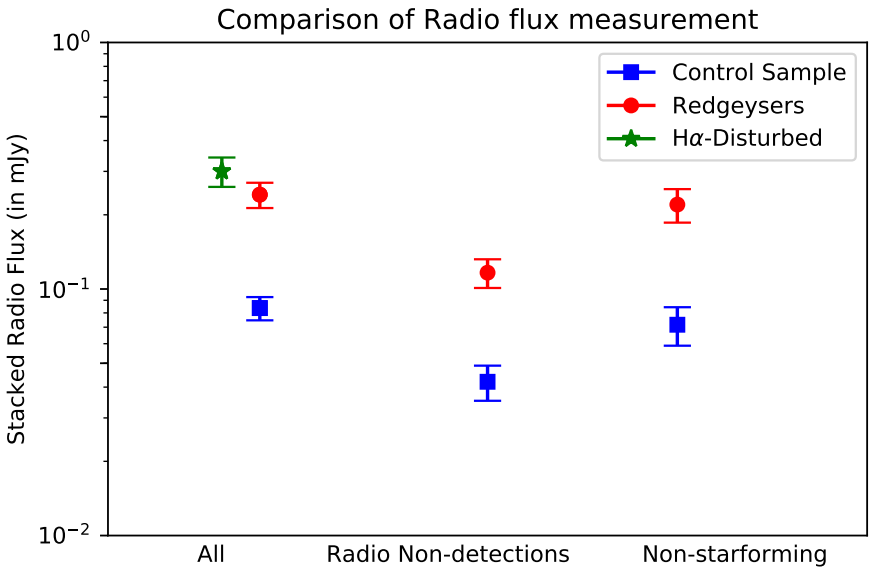

Figure 2.9: The median stacked radio flux obtained from the stacked sample of red geysers (shown in red), Hα-disturbed (pink) and control sample (blue). The leftmost panel shows the stacks for the entire sample of red geysers (shown in red circles), control sample (shown in blue squares) and the Hα-disturbed category (shown in green star). "Radio Non-detections" panel shows the stacked radio flux for the geysers and the control sample where the individually radio-bright ones, satisfying the criteria S/N > 3, have been removed. The red geyser and the control sample have been cross-matched with SDSS+WISE catalog of Chang et al. (2015). Galaxies with log SFR $> -2 M\odot$/yr have been removed and re-stacked. They constitute the "Non-Starforming" category shown in the rightmost panel of the plot. In all the cases, the median stacked radio flux is higher for the red geyser sample compared to the control sample by $> 5\sigma$.

2.5 Discussions & Conclusion

We have performed a radio stacking analysis of 78 red geysers selected from the MaNGA survey which have FIRST coverage and have compared their median radio flux with a sample of quiescent galaxies matched in global integrated properties but are not classified as red geysers. The red geyser galaxies show significantly higher radio

fluxes than the control galaxies, despite the fact that the red geyser selection is based on optical data alone. This suggests a physical link between the optical features that identify red geysers and the presence of enhanced AGN activity, lending further support to the argument that AGN-driven winds are responsible.

We have made several subdivisions based on different physical criteria, to check our results:

- We have performed the stacking for all galaxies both in the red geyser and control samples.
- We have performed the stacking for samples in which the radio detected sources are removed so that a few bright sources do not dominate the median stacked radio flux value.
- We have performed the stacking for galaxies with similar levels of ionized gas by imposing a cut on EW (Hα) value.
- We have performed the stacking for samples that exclude galaxies which show a high value of star formation from SDSS+WISE.

In all cases red geysers exhibit elevated radio flux values.

Given our conservative $NUV - r$ color cut, the use of WISE mid-IR data (§2.4.3) and absence of star forming HII regions from resolved BPT diagrams, we can rule out star formation as the explanation for this enhanced radio flux. The other most likely sources are AGN activity or Supernova remnants. SN Ia remnants can induce

radio synchrotron emission from shock-accelerated cosmic rays. However in our case, they are unlikely to be responsible for the increased radio signal in red geyser sample because our selection criteria do not involve any factors that may enhance or suppress the SN Ia rate. We have controlled primarily for the M_*, rest-frame $NUV - r$ color and age of the galaxy respectively. Thus there should be no difference in the frequency of SN Ia remnants between the red geysers and the control sample.

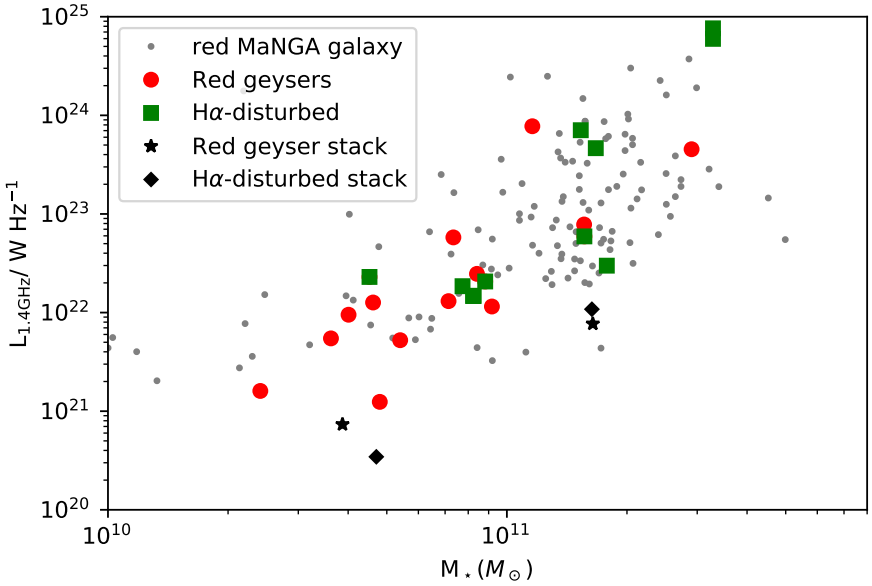

Figure 2.10: The figure shows the 1.4GHz radio luminosity versus stellar mass of radio detected red geysers (shown in red big circles), Hα-disturbed (shown in green squares) and the red (NUV − r > 5) MaNGA galaxies (in gray small circles). This plot shows that the radio AGN population occupies two distinct regions in the luminosity stellar-mass space depending on the types of host quiescent galaxies. The lower mass regime (log M$_\star$ < 11) is occupied by quiescent galaxies with optical emission line features (red geysers and Hα-disturbed) while in the higher mass region, we mainly find galaxies without detectable emission line features (similar to our control sample). The black stars and diamonds show the stacked radio luminosities from the entire sample (which includes both radio-detected and non-detected ones) of red geyser and Hα-disturbed galaxies respectively, in two mass bins.

We conclude that the enhanced radio emission of red geysers is due to the presence of radio-mode AGNs. To confirm this statement, we compare the expected SFR from the average radio luminosity from the entire red geysers sample with the observed SFR derived from full SED fitting of optical mid-infrared data from Chang et al. (2015) catalog. The mean radio luminosity density ($L_{1.4GHz}$) obtained from the stacked integrated flux density is $L_{1.4GHz} \sim 2 \times 10^{21}$ W Hz^{-1} (obtained by averaging the values of radio luminosity of the red geysers in two mass bins shown by two black filled-stars in Fig 2.10). From the best-fit relation between 1.4 GHz radio continuum luminosity and the Balmer decrement corrected Hα (Brown et al. 2017), we obtain a corresponding Hα luminosity $\sim 1.3 \times 10^{41}$ erg s^{-1}. Using the known relation between SFR and Hα luminosity (Kennicutt et al. 2009; Brown et al. 2017) assuming a Kroupa intial mass function (IMF) (Kroupa & Weidner 2003), we obtain an expected SFR from this radio emission $\sim 1 M_\odot$ yr^{-1}. However, the observed mean SFR from the sample, as shown in Fig 2.8, is $\sim 10^{-3} M_\odot$ yr^{-1}, which is much lower than expected, thus confirming AGN to be the primary source of radio emission rather than star formation in the red geysers. The AGN feedback can induce radio emission through their radio jets (Zensus 1997; Falcke & Biermann 1999), their advection-dominated accretion flows (ADAFs; Narayan et al. 1995, 2000), and/or their winds (Jiang et al. 2010).

It stands to reason that the AGNs in the red geysers may act as the central powerhouse driving the ionized gas winds that signal the red geyser phenomenon.

It is interesting to consider how the Hα-disturbed galaxies fit in this context. These galaxies show a comparable (within uncertainty) or a slightly higher value of

stacked radio flux compared to the red geysers. All of them show significant gas blobs in the Hα EW maps. Some of them can be potential geyser candidates or relics from mergers or tidal interactions with other galaxies. The complex gas morphology might be a product of a multi-phase and clumpy interstellar medium, ionized by the central AGN. These blobs may form out of the geyser wind material after the central engine shuts down. They may also result from a less stable accreting source. Given the uncollimated and chaotic distribution of ionized gas, it seems unlikely that cool inflowing of material from a galactic encounter is responsible. There is also no indication that that Hα-disturbed galaxies have recently undergone a merger or interaction. Clearly more work is needed to understand them.

We would also like to highlight the handful of control galaxies with clear radio detections that are not classified as red geysers or as Hα-disturbed. These galaxies likely host a central active nucleus and exhibit significant emission line flux. They may mean any of the following:

- Our red geyser sample based on visual inspection is not a complete sample of AGN-driven ionized winds. Red geysers may be a special type of AGN wind phenomena.

- The AGNs in the control sample are too weak too drive out sufficient gas for detection at large radii.

- A time lag may exist between AGN triggering and the development of a large-scale wind. Those AGN hosted control galaxies may not be in the red geyser phase at

the current epoch, but may have passed through this phase in the past, or might in the future.

Fig 2.10 shows the variation of radio luminosity ($L_{1.4GHz}$) with stellar mass ($M_\star$) for all the FIRST radio-detected quiescent galaxies in MaNGA sample. We see that radio-AGN population occupies two distinct regions in the plot depending on the properties of host quiescent galaxies. Radio-AGN in the galaxies showing optical emission line features (red geysers and Hα-disturbed) are found mostly at log $(M_\star/M_\odot) < 11$ (low mass end of the typical quiescent galaxy population) while the radio detection rate overall is higher for log $(M_\star/M_\odot) > 11$ by almost a factor of 1.4, compared to the lower mass galaxies. One possibility is that red geysers and "radio galaxies" represent different AGN populations with different associated accretion histories and fueling mechanisms. Alternatively, the declining presence of wide-scale ionized gas at higher stellar mass (Belfiore et al. 2016) may simply hide the existence of AGN-driven winds at higher masses.

We can gain further insight by considering the average luminosities from our stacked samples in two stellar mass bins. Using the median redshift in each mass bin, we overplot the average luminosity of red geysers and Hα-disturbed galaxies on Fig 2.10 (shown in black filled-stars and diamonds respectively). The average luminosity has been obtained from the stacked radio flux that includes both radio-detected and non-detected sources. While radio-detected sources show a strong mass dependence, the average radio luminosity associated with red geysers show a slightly weaker dependence

with stellar mass. This suggests that a different kind of accretion physics may be at play.

Considering the two red geyser mass bins in Fig 2.10, we see that the typical radio power of the red geysers is $\sim$ 10^{21} W Hz^{-1}(shown in Fig 2.10 by the two black filled stars). From the best-fit linear relation between jet mechanical energy and the radio power from Heckman & Best (2014), we get an estimate of the jet kinetic energy to be 3 $\times 10^{41}$ erg/s. The AGNs in the red geysers are low-luminosity sources and their mechanical energy will be confined predominantly to size-scales of the host galaxy halo. Also, according to our interpretation, the short-lived geyser phase possibly occur in any red-sequence galaxy, hence the "duty cycle" represents the number of galaxies with an active red geyser phase in the present. Hence, if we assume that the observed fraction of red geysers represents their duty cycle, then these phenomena are present 10% of the time (higher, if we consider log ($M_\star/M_\odot$) < 11). Multiplying this duty cycle by the typical jet kinetic power yields $\sim$ 3×10^{40}erg/s, an estimate of the AGN power averaged over long time scales. We can compare this to the cooling rate implied from the X-ray gas in this stellar mass range (Best et al. 2006; O'Sullivan et al. 2001), which is similar, $\sim$ 10^{40}erg/s. This similarity provides further evidence that red geysers may play an energetically interesting role in the suppression of gas cooling and star formation at late times.

Chapter 3

Radio Morphology of Red Geysers

We present 150 MHz, 1.4 GHz, and 3 GHz radio imaging (LoTSS, FIRST and VLASS) and spatially resolved ionized gas characteristics (SDSS IV-MaNGA) for 140 local ($z < 0.1$) early-type red geyser galaxies. In this chapter, we confirm that red geysers host low-luminosity radio sources ($L_{1.4\ \mathrm{GHz}} \sim 10^{22}$ W Hz^{-1}). Out of 42 radio-detected red geysers, 32 are spatially resolved in LoTSS and FIRST, with radio sizes varying between $\sim$ 5 - 25 kpc. Three sources have radio sizes exceeding 40 kpc. A majority display a compact radio morphology and are consistent with either low-power compact radio sources ("FR0" galaxies) or "radio-quiet quasars". They may be powered by small-scale AGN-driven jets which remain unresolved at the current $5''$ resolution of radio data. The extended radio sources, not belonging to the 'compact' morphological class, exhibit steeper spectra with a median spectral index of -0.67 indicating the dominance of lobed components. The red geysers hosting extended radio sources also have the lowest specific star formation rates, suggesting they either have a greater impact on

the surrounding interstellar medium or are found in more massive halos on average. The degree of alignment of the ionized wind cone and the extended radio features are either 0° or 90°, indicating possible interaction between the interstellar medium and the central radio AGN. [1]

3.1 Introduction

Active galactic nucleus (AGN) feedback has been proposed to be one of the most efficient ways to quench star formation and help maintain quiescence in massive galaxies and evoked to explain the enormous increase in the number of red galaxies since $z \sim 2$. AGN feedback is often described as occurring in two different modes: "quasar" or "radiative" mode and "maintenance" or "radio" mode (Fabian 2012; Morganti 2017; Harrison et al. 2018). The "quasar" mode feedback, ushering in a rapid quenching phase during the early stage of a galaxy's lifetime, is associated with radiatively efficient luminous AGN or massive quasars. They release enormous amounts of energy to their surroundings via radiation from the accretion disk and drive powerful gas outflows that may remove gas altogether from the galactic potential well (Cattaneo et al. 2009; Fabian 2012). On the other hand, the "radio" mode feedback, predominant during the late stages of evolution, is thought to be powered by low to moderate luminosity AGN which are radiatively inefficient and accreting at a low rate. They deposit most of their energy to the surrounding medium via radio jets or winds, heating the gas and

[1] This chapter was previously published in the Astrophysical Journal as **Radio Morphology of Red Geysers**, Roy, N., Moravec, E., Bundy, K. et al. 2021, ApJ, 922, 230, DOI:10.3847/1538-4357/ac24a0.

suppressing star formation (Binney & Tabor 1995; Ciotti & Ostriker 2001; Croton et al. 2006; Bower et al. 2006; Ciotti & Ostriker 2007; Ciotti et al. 2010; McNamara & Nulsen 2007; Cattaneo et al. 2009; Fabian 2012; Heckman & Best 2014). The radio mode feedback process has been directly observed in galaxy groups and clusters (McNamara & Nulsen 2012). Evidence for maintenance mode feedback in typical passive quenched galaxies (halo mass $< 10^{13}$ $M_{\odot}$) have been rare. A few large-scale statistical studies of the local radio AGN population (Hardcastle et al. 2019) and studies of individual galaxies showing radio AGN-driven outflows (Morganti et al. 2005; Nesvadba et al. 2008) seem to suggest that the jet mechanical energy derived from the radio luminosity is enough to counterbalance the radiative loss of the hot gas and prevent cooling.

Low redshift integral field spectroscopy from the Sloan Digital Sky Survey-IV (SDSS-IV) Mapping Nearby Galaxies at Apache Point Observatory (MaNGA) survey (Bundy et al. 2015) has recently revealed an interesting population of moderate mass ($\log M_{\star}/M_{\odot} \sim 10.5$), red and quenched ($NUV - r > 5$) galaxies that may be useful in this regard. Known as "red geysers", these passive early-type galaxies possess unique optical emission and kinematic properties signalling galactic scale centrally-driven outflows (Cheung et al. 2016; Roy et al. 2021a). The large scale winds of ionized gas, evident from the spatially resolved gas kinematics (Roy et al. 2021a), aligns with a distinctive bi-symmetric enhancement in the spatial distribution of ionized gas, i.e. in Hα, [OIII] and [NII]. The observed ionized gas, traced by emission lines, is possibly ionized by post asymptotic giant branch (AGB) stars with some contribution from shocks, as evident from a combination of low ionization nuclear emission line regions (LINER) and

Seyfert-like line ratios in spatially resolved BPT (Baldwin, Phillips & Terlevich; Baldwin et al. 1981) diagrams (Cheung et al. 2016; Roy et al. 2021a). Using the Keck Echelette Spectrograph and Imager (ESI) instrument, we obtained high spectral resolution observations (R $\sim$ 8000 compared to 2000 in MaNGA) in two representative red geysers and found a systematic variation in the asymmetry of the emission line profiles. Roy et al. (2021a) showed that the observed nature and the magnitude of asymmetry along with increased gas velocity dispersion are consistent with line-of-sight projections through a broad conical outflow. In addition, Cheung et al. (2016) performed detailed dynamical modeling of gas and stellar kinematics and concluded that the observed ionized gas velocities are too high to be in gravitationally bound orbits and can only be explained by an outflowing wind. These galaxies show very low star formation activity with average log SFR ($M_\odot$/yr) ~ -2 using simultaneous SED fitting of GALEX+SDSS+WISE (Salim et al. 2016) and present no visible signatures of dust lanes from ground based imaging.

For a prototypical red geyser, Cheung et al. (2016) showed that the host galaxy has a radiatively-inefficient supermassive black hole which was detected as a central radio point source. Roy et al. (2018) extended that analysis and used the Very large Array (VLA) Faint Images of the Radio Sky at Twenty-Centimeters (FIRST, Becker et al. 1995) survey to measure stacked 1.4 GHz radio continuum flux from the entire red geyser sample. The study revealed that red geysers have significantly higher ($> 5\sigma$) radio continuum flux (in the stacked sample) and a three times higher radio-detection rate compared to the control samples. Roy et al. (2018) concluded that the red geysers

host low-luminosity radio AGNs ($L_{1.4GHz} \sim 10^{22} - 10^{23}$ W/Hz) which are energetically capable of driving sub-relativistic winds consistent with the MaNGA observations. Additionally Roy et al. (2021a), discovered a significant amount of cool gas (average $M_{cool} \sim 10^8$ $M_\odot$) traced by sodium doublet absorption (NaD) in the red geyser sample, especially in those which are radio-detected according to FIRST. The spatial distribution of the cool gas lies spatially offset from the warm ionized gas component, as traced by Hα. The absorption line kinematics are observed to be redshifted on average ($\sim 40 - 50$ km s^{-1}) in about 86% of the radio red geysers, implying that the detected cool gas is inflowing into the galaxy and is possibly associated with fuelling the central radio AGN. The lack of any detectable star formation, the association with low luminosity radio-mode active galactic nuclei (Roy et al. 2018), signatures of large scale ($\sim$ 10 kpc) ionized wind (Roy et al. 2021a) and their relatively high occurrence rate on the red sequence (5-10 %, Cheung et al. 2016), make the red geysers a promising candidate for "maintenance" or "radio-mode" feedback in typical quiescent galaxies.

While feedback from high luminosity radio-loud AGN, radio galaxies and radio Mpc-scaled jets have been extensively discussed and studied, feedback from low-luminosity radio AGN is less well understood. However recently, there have been a growing number of studies of the radio properties and morphology of "radio-quiet" sources and their relation with radio-mode AGNs hosting small scale jets that do not extend beyond the host galaxy. For example, Jarvis et al. (2019) presented 1-7 GHz high resolution radio imaging (VLA and e-MERLIN) for ten z<0.2 type-2 quasars which host ionized outflows based on broad [OIII] emission-line components. These "radio-

quiet quasars" (RQQ) have low-to-moderate radio luminosities ($\log[L_{1.4GHz}/W\ Hz^{-1}] \leq 24.5$), exhibit extended radio structures in the scale of $1-25$ kpc, and are consistent with being low power compact radio galaxies. The small-scale radio jets seem to be associated with ionized gas outflowing regions, indicating jet-interstellar medium (ISM) interaction on galactic scales (similar to Venturi et al. 2021).

Capetti et al. (2019), on the other hand, explored the low-frequency (150 MHz) radio properties of similar compact low-luminosity ($\log[L_{150MHz}/\ W\ Hz^{-1}] \leq 22.5$) radio AGN sources, known as Fanaroff-Riley class 0 (FR0), associated with nearby ($z < 0.05$) massive early-type galaxies. FR0 sources are typically unresolved with sizes $< 3-6$ kpc and a few outliers showing a jetted morphology extending beyond 20 kpc. This class of sources represents the low end in size and radio power of small-scale AGN-jet population. Another set of "galaxy-scale jets" (GSJ) from 195 radio galaxies has been discovered by Webster et al. (2021) using LOFAR Two Metre Sky Survey (LoTSS, Shimwell et al. 2019). The radio emission from the GSJs extends to no larger than 80 kpc and are small enough to be directly influencing the evolution of the host galaxies. Baldi et al. (2018, 2021) studied high resolution ($< 0.2''$) 1.5 GHz radio images for local active (LINERs and Seyferts) and inactive (HII and Absorption line galaxies) galaxies using e-MERLIN array. Investigating their radio morphology, they observed mostly radio cores with about one third of the detected sample featuring $\sim$ 1 kpc-scale radio jets. They concluded that the galaxies with LINER nuclei harbor radio sources which are scaled-down version of the FRI radio galaxies. Finally Panessa et al. (2019) has explored a wide range of possible mechanisms to understand the driver of the radio-quiet sources, starting from

star formation, AGN driven winds to free-free emission from photo-ionized gas and the innermost accretion disc coronal activity.

Red geysers emerge as an interesting class of ETGs to study in the context of AGN-jet ISM interaction because they host low luminosity radio sources, exhibit suppressed star formation and show signatures of centrally driven outflows in ionized gas signatures. In this work we present the multi-frequency radio observations of 42 radio detected red geyser galaxies with 3 GHz using Very Large Array Sky Survey (VLASS), 1.4 GHz using FIRST and 150 MHz using LoTSS survey. Using a combination of radio and optical observations, we confirm that the observed radio emission is associated with radio mode AGN rather than star formation. We also investigate the spatial extent, morphology and spectral index of the radio emission from red geysers and explore the radio – ionized outflow connection. In §3.2, we report the red geyser sample and its unique identifying features. In §3.3 we describe the radio and optical surveys used in this analyses. In §3.4, 3.5 and 3.6 we present our results, which we then discuss in §3.7. We summarise our conclusions in §3.8.

Throughout this paper, we assume a flat cosmological model with $H_0 = 70$ km s^{-1} Mpc^{-1}, $\Omega_m = 0.30$, and $\Omega_\Lambda = 0.70$, and all magnitudes are given in the AB magnitude system.

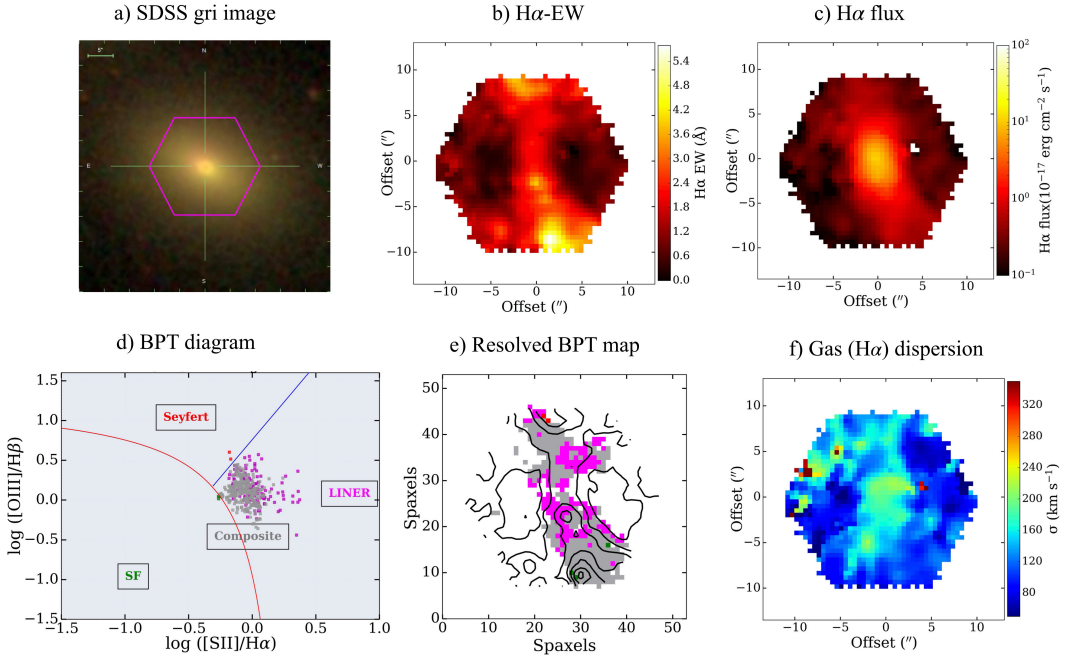

Figure 3.1: The spatially resolved emission and kinematic properties of an example red geyser (MaNGAID: 1-595166) as observed from SDSSIV-MaNGA. The upper left panel (a) shows the optical image of the galaxy from SDSS with the MaNGA IFU overlaid on top in magenta. In the other panels, we show the spatial distribution of Hα equivalent width (b) and Hα flux (c). The lower left panel (d) shows the spatially resolved [SII] BPT diagram showing spaxels with signal to noise > 3. The spaxels are color-coded by the classification based on both the [NII] and [SII] BPT diagram. Almost all spaxels fall into the LINER/shock category (magenta color) while some spaxels are classified as "composite" from the [NII] BPT diagram (grey color). The lower middle panel (e) shows the spatial position of the BPT classified spaxels, with Hα EW contours in black. The lower right panel (f) shows the gas velocity dispersion. The characteristic bi-symmetric pattern in Hα-EW map is particularly apparent.

3.2 Sample selection: Red Geysers

This study of red geyser galaxies builds upon a series of papers in which we presented observations from radio (FIRST) and spatially resolved optical spectroscopic data (from SDSS-IV MaNGA survey and Keck ESI instrument) for a smaller sample of 84 red geysers. Cheung et al. (2016); Roy et al. (2018, 2021a) and Roy et al. (2021c) have shown that the red geysers are passive ETGs lying in the red sequence (NUV $-$ r $>$ 5) with ample amount of ionized and neutral gas present and they exhibit signatures of kpc-scale ionized winds driven out by a centrally located low-luminosity AGN. These galaxies show the widespread presence of ionized gas, traced by elevated flux of strong emission lines (e.g., Hα, [NII] and [OIII]) compared to other passive quenched galaxies, but with little ongoing star formation activity ($\sim$ 0.01 $M_{\odot}$ yr^{-1}). In this work we expand on Roy et al. (2018) by investigating the radio-detection of our updated sample of 140 red geysers and focus on the radio properties on three different radio bands $-$ 3 GHz, 1.4 GHz and 150 MHz.

The red geyser sample is visually selected from the SDSS IV-MaNGA survey (description of the survey in §3.3.1) and has the following characteristic features (see Cheung et al. 2016; Roy et al. 2018, 2021a,c, for details):

- Spheroidal galaxies (sersic index $>$ 3) with no visible disk component or dust lanes as observed by SDSS, red optical color (NUV $-$ r $>$ 5) and low star formation rate (average SFR $\sim 10^{-2}$ $M_{\odot}$ yr^{-1}). Edge-on galaxies with axis ratio b/a $<$ 0.3 are discarded.

- Bi-symmetric/bi-conical feature in spatially resolved EW map of Hα, [NII] and [OIII] emission lines.

- Rough alignment (within $\pm 10^{\circ}$) of the bi-symmetric feature with the ionized gas kinematic axis, but strong misalignment with stellar kinematic axis with the constraint that misalignment angle is not 90°, 0° or 180°.

- High spatially resolved gas velocity values, typically reaching a maximum of $\pm$ 300 km s^{-1}, which are greater than the stellar velocity values by at least a factor of $4-5$.

- High gas velocity dispersion values, reaching about $\sim 220-250$ km s^{-1} in distinct parts of the galaxy.

- Showing LINER or Seyfert type line ratios in the integrated BPT diagrams.

An example red geyser is shown in Fig. 3.1. The optical image (panel a) from SDSS shows spheroidal morphologies typical of these galaxies. The upper middle panel (b) shows the characteristic bi-symmetric feature in the Hα EW map. The upper right panel (c) shows the Hα flux distribution which is extended in nature and shows enhanced values surpassing 5×10^{-16} erg cm^{-2} s^{-1}, a value quite high compared to typical passive galaxies. The regions of elevated Hα flux coincides with the bi-symmetric EW pattern. This observed feature, which aligns with the gas velocity field, is believed to be tracing the putative wind cone. Panel d shows the spatially resolved [SII] BPT diagram for this red geyser in which only spaxels with signal to noise > 3 are plotted. The lower

middle panel (e) shows the spatial position of the spaxels in the spatially resolved BPT diagram, colored by their classification based on both the [NII] and [SII] BPT diagram (Kewley et al. 2006). Almost all spaxels fall into the LINER/shock category (magenta color) while some spaxels are classified as "composite" from the [NII] BPT diagram (grey color). The lower right panel (f) show the gas velocity dispersion map, traced by Hα, which is clumpy with values going up to ~ 250 km s^{-1}.

The sample of red geysers used in this work is derived from MaNGA Product Launch 9 (MPL-9) and consists of 140 galaxies, which account for $\approx 6-8\%$ of the local quiescent galaxy population observed by MaNGA.

3.3 Data Acquisition

3.3.1 MaNGA survey

We use optical data primarily from the recently completed SDSS-IV MaNGA survey (Blanton et al. 2017; Bundy et al. 2015; Drory et al. 2015; Law et al. 2015; Yan et al. 2016; Albareti et al. 2017). MaNGA is an integral field spectroscopic survey that provides spatially resolved spectroscopy for nearby galaxies ($z \sim 0.03$) with an effective spatial resolution of $2.5''$ (full width at half-maximum; FWHM). The MaNGA survey uses the SDSS 2.5 meter telescope in spectroscopic mode (Gunn et al. 2006) and the two dual-channel BOSS spectrographs (Smee et al. 2013) that provide continuous wavelength coverage from the near-UV to the near-IR: $3,600 - 10,000$ Å. The spectral resolution varies from R $\sim$ 1400 at 4000 Å to R $\sim$ 2600 at 9000 Å. An r-band signal-to-noise

(S/N) of $4-8$ Å^{-1} is achieved in the outskirts (i.e., $1-2$ R$_e$) of target galaxies with an integration time of approximately 3-hr. MaNGA has observed more than 10,000 galaxies with log $(M_\star/M_\odot) \geq 8$ across ~ 2700 deg^2 over its 6 yr duration. In order to balance radial coverge versus spatial resolution, MaNGA observes two thirds of its galaxy sample to ~ 1.5 R$_e$ and one third to 2.5 R$_e$. The MaNGA target selection is described in detail in Wake et al. (2017).

The raw data are processed with the MaNGA Data Reduction Pipeline (DRP, Law et al. 2016). In this work, we use the MaNGA sample and data products drawn from the MaNGA Product Launch-9 (MPL-9) and Data Release 16 (DR16, Ahumada et al. 2020). We use spectral measurements and other analyses carried out by MaNGA Data Analysis Pipeline (DAP), specifically version 2.3.0. The data we use in this work are based on DAP analysis of each spaxel in the MaNGA datacubes. The DAP first fits the stellar continuum of each spaxel to determine the stellar kinematics using the Penalised Pixel-fitting algorithm `pPXF` (Cappellari & Emsellem 2004; Cappellari 2017) and templates based on the MILES stellar library (Falcón-Barroso et al. 2011). The templates are a hierarchically clustered distillation of the full MILES stellar library into 49 templates. This small set of templates provide statistically equivalent fits to those that use the full library of 985 spectra in the MILES stellar library. The emission-line regions are masked during this fit. The DAP then subtracts the result of the stellar continuum modeling to provide a (nearly) continuum-free spectrum that is used to fit the nebular emission lines. This version of the DAP treated each line independently, fitting each for its flux, Doppler shift, and width, assuming a Gaussian profile shape.

The final output from the DAP are gas and stellar kinematics, emission line properties and stellar absorption indices. All the spatially resolved 2D maps shown in the paper are outputs from the DAP with hybrid binning scheme. An overview of the DAP used for DR15 and its products is described by Westfall et al. (2019), and assessments of its emission-line fitting approach is described by Belfiore et al. (2019). All the integrated quantities reported in this paper are signal-to-noise weighted average taken over one effective radius.

We use ancillary data drawn from the NASA-Sloan Atlas[2] (NSA) catalog which reanalyzes images and derives morphological parameters for local galaxies observed in Sloan Digital Sky Survey imaging. It compiles spectroscopic redshifts, UV photometry (from GALEX, Martin et al. 2005), stellar masses, and structural parameters. We have specifically used spectroscopic redshifts and stellar masses from the NSA catalog. The star formation rates are derived from Salim et al. (2016), which utilizes GALEX-SDSS and WISE to perform UV-optical-IR spectral energy distribution (SED) fitting.

3.3.2 LoTSS

The LOFAR Two-metre Sky Survey (LoTSS, Shimwell et al. 2017, 2019) is an ongoing sensitive, high-resolution survey which will cover the whole northern sky with 3168 pointings in the frequency range between 120 and 168 MHz. The LoTSS first data release (DR1, Shimwell et al. 2019) covers 424 square degrees centred in the Hobby Eberly Telescope Dark Energy Experiment (HETDEX; Hill et al. 2008) Spring

[2] http://www.nsatlas.org

Field region (right ascension 10h45m00s to 15h30m00s and declination 45°00′00″ to 57°00′00″) and contains over 300,000 sources with SNR > 5. The median sensitivity is ~ 71 μJy/beam and 95% of the area in the DR1 release has an rms noise level below 150 μJy/beam. The angular resolution is 6″ and the positional accuracy is within 0.2″ for high signal-to-noise sources; the positional accuracy increases to $\sim 0.5''$ for the faintest sources with a flux density of less than 0.6 mJy. The source density is a factor of ∼10 higher than the most sensitive existing very wide-area radio-continuum surveys such as the NRAO VLA Sky Survey (NVSS, Condon et al. 1998), Faint Images of the Radio Sky at Twenty-Centimeters (FIRST, Becker et al. 1995), Sydney University Molonglo Sky Survey (SUMSS, Bock et al. 1999; Mauch et al. 2003), and WEsterbork Northern Sky Survey (WENSS, Rengelink et al. 1997).

The second LoTSS data release (DR2), to be released publicly in 2021, consists of two contiguous fields at high Galactic latitude centered around 0h and 13h and covering approximately 5,700 square degrees (Shimwell et al. in preparation). DR2 provides fully calibrated mosaics at the same 6″ resolution as DR1, and images can also be obtained from individual LoTSS pointings, outside the DR2 area. For the red geysers in the existing LoTSS coverage, including fields not part of the DR2 release, we obtain the fluxes and sizes from either (a) the internally released catalog (Shimwell et al. in prep) or (b) similarly generated catalogues for small areas of individual pointings around our target objects. In both cases, the flux scale correction described by Hardcastle et al. (2021) and Shimwell et al. (in prep) is applied to the data so that flux densities are as close as possible to the flux scale of Roger et al. (1973). The residual flux scale

uncertainty lies between 5 and 10% for the DR2 area (Hardcastle et al. 2021) and is likely to be $\sim 10\%$ for individual fields.

The total number of red geysers with currently available LoTSS data is 103 which is about 74% of the parent 140 red geyser sample. The list of LOFAR detected red geysers is presented in Table 3.1.

3.3.3 FIRST survey

The Very Large Array (VLA) Faint Images of the Radio Sky at Twenty Centimeters (FIRST, Becker et al. 1995) survey is a systematic survey over 10,000 square degrees of the North and South Galactic Caps at frequency channels centered at 1.36 GHz and 1.4 GHz. FIRST uses the VLA in B-configuration and achieves an angular resolution of $5''$ and the survey is insensitive to structures larger than $\sim 60''$ as it is carried out in the VLA's B configuration. The source detection threshold is ~ 1 mJy corresponding to a source density of ~ 90 sources deg^{-2}. The astrometric accuracy of each source is 0.5 - $1''$ at the source detection threshold. Since FIRST survey area was designed to overlap with the Sloan Digital Sky Survey (SDSS, York et al. 2000; Abazajian et al. 2009), most MaNGA targets have FIRST data coverage. However, the 1 mJy threshold results in non-detections for most MaNGA galaxies. For each pointing center, there are twelve adjacent single field pointings that are co-added to produce the final FIRST image. Sources are extracted from co-added reduced images and fit by two dimensional Gaussians to derive peak flux, integrated flux densities, and size information (Becker et al. 1995). The current FIRST catalog is accessible from the FIRST search page. The

full images are available from ftp://archive.stsci.edu/pub/vla_first/data.

3.3.4 VLASS

The Very Large Array Sky Survey (VLASS, Lacy et al. 2020) is a community-driven initiative to carry out a synoptic radio sky survey using the Karl G. Jansky Very Large Array (VLA). VLASS will eventually use $\sim$ 5500 hours to cover the whole sky visible at the VLA ($\delta > -40$ deg) observing a total of 33,885 deg^2 at angular resolution of $\sim 2.5''$. The data will be acquired in three epochs and will cover the frequency range 2–4 GHz in 2 MHz channels, with calibrated polarimetry in Stokes I, Q and U, providing wideband spectral and polarimetric data for a myriad of targets and source types. The angular resolution is $\sim$ 2.5 arcsec and the survey is insensitive to structures larger than $\sim 30''$ as it is carried out in the VLA's B configuration. The 1 σ sensitivity goal for a single pass is 120 μJy while it is 69 μJy when all three epochs are combined. Thus the VLASS is an all-sky radio sky survey with a unique combination of high angular resolution, high sensitivity, full linear Stokes polarimetry, time domain coverage, and wide bandwidth. Observing began in September 2017 and the survey will finish observing in 2024.

3.4 Radio Detection and Characterization

3.4.1 Percentage of radio detection

LoTSS DR2 footprint contains 93 of the parent sample of 140 red geyser galaxies. Additionally, ten more sources are contained within individual LoTSS pointings outside the DR2 area. Thus the total number of red geysers with currently available LOFAR data is 103, which is about 75% of the complete red geyser sample. 34 ± 6 out of those 103 sources ($33\% \pm 5.5\%$) are found to be radio-detected at the frequencies observed by LOFAR ($\sim$ 150 MHz), where quoted errors are obtained from standard Poisson statistics.

We cross-matched the FIRST catalog with our red geyser sample with a cross-matching radius of $10''$. For visibly extended radio sources in the FIRST image, we extend the cross-matching radius up to a maximum of $1'$, but restricting the central component of the detected source to lie within $< 10''$ of the galaxy center. We find that 29 ± 5 out of 140 red geyser galaxies are detected at 1.4 GHz frequency with a detection fraction of $21\% \pm 3.5\%$. This FIRST detection rate is roughly in agreement with our previous work (Roy et al. 2018) which noted a 15% radio detection rate from the FIRST survey. However Roy et al. (2018) used a preliminary red geyser sample of 84 sources drawn from an earlier MaNGA data release − MPL-5. The current updated red geyser sample from MPL-9 has increased the total number of red geysers by 56 sources which results in an additional 17 FIRST detections for this work.

Lastly, we cross-matched the parent red geyser sample with VLASS (3 GHz)

survey using the same cross-matching radius as the FIRST survey and found 29 radio detections, which is a similar detection rate to FIRST. There are 13 red geysers which are detected in LOFAR but not in VLASS and FIRST. On the other hand, there are eight sources which are detected in FIRST and VLASS but are not within the LoTSS field of view. 21 ± 4 out of 140 red geysers ($\sim 15\% \pm 4\%$) have simultaneous radio detections from all three surveys, which are used for calculation of spectral indices (discussed in §3.5.3). 42 ± 6 red geysers ($30\% \pm 4\%$) are detected in at least one of LoTSS, FIRST or VLASS surveys, and these are listed in Table 3.1.

In order to understand how, if at all, the radio-detected red geyser galaxies intrinsically differ from those which are non-detected, we compare the host galaxy properties of the respective samples of interest. Fig. 3.2 shows the histograms of SDSS I-band magnitude (upper left), Hα luminosity (upper right), stellar mass (lower left) and star formation rate (lower right) of non-radio detected red geysers (in blue) and 42 radio-detected red geysers (in salmon) − detected in at least one of the LoTSS, FIRST or VLASS surveys. The SFR estimates are obtained from Salim et al. (2016) catalog, while the magnitude and the stellar mass reported here are acquired from the NSA catalog. We notice that the distributions of I-band magnitude, Hα luminosity and stellar mass are quite different between the radio-detected and non detected sample. This is statistically confirmed by a Kolmogorov-Smirnov (KS) test which rejects the null hypothesis that the radio-detected and non-detected samples show similar distributions. This is shown by extremely small p values of 1.48×10^{-6}, 1.84×10^{-6}, and 1.05×10^{-6} for I-band magnitude, Hα luminosity and stellar mass distributions respectively. How-

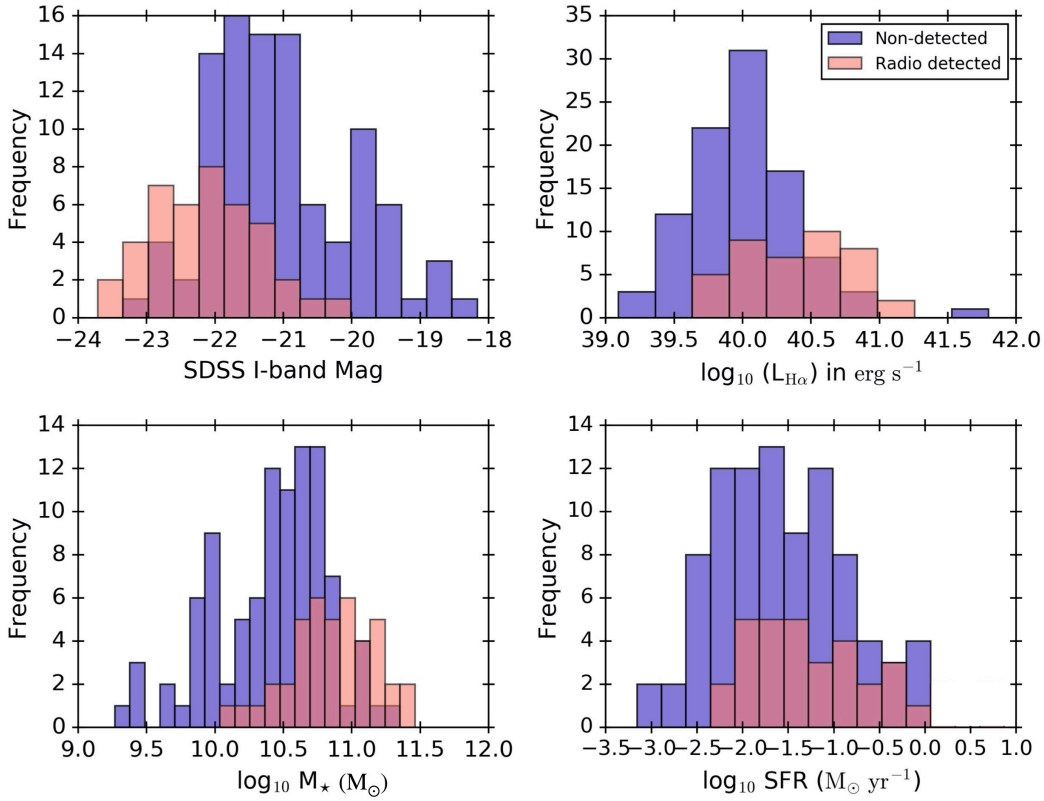

Figure 3.2: Comparison of global properties of radio-detected red geysers in salmon (detected in any of LOFAR, FIRST or VLASS survey) with non-radio detected red geysers (in blue). Histograms are shown for SDSS I-band magnitude, integrated Hα luminosity, stellar mass and star formation rate. We see similar distributions of star formation rate but a substantial difference in the rest of the properties.

ever, for the SFR distributions, we cannot reject the null hypothesis at a level $< 1\%$ ($p = 0.06$), signifying similar distributions of radio and non-radio detected galaxies. The radio detected sources are in general brighter in the SDSS I-band (mean $M_I = -22.5$) and more massive (mean $\log_{10}$ $M_\star \sim 11$ $M_\odot$) than the non-radio detected galaxies (mean $M_I = -21$ and $\log_{10}$ $M_\star \sim 10.5$ $M_\odot$). The Hα luminosity in the radio-detected sample also tend to be higher on average (mean $\log_{10}$ $L_{H\alpha} = 40.5$ erg s^{-1}) than the non-radio detected sample ($\log_{10}$ $L_{H\alpha} = 40$ erg s^{-1}), possibly implying that the galaxies with higher amount of ionized gas and thus a more prominent Hα bi-symmetric pattern are more likely to have enhanced radio emission. The SFR distribution, however, is unchanged irrespective of radio-detection indicating no underlying correlation between them.

3.4.2 Radio loudness

Fig. 3.3 shows the radio luminosities at 1.4 GHz vs. the observed total [OIII] luminosities extracted from the central 3″ as observed by the SDSS fiber, of the 42 radio-detected red geysers (in black). Since LOFAR is most sensitive to fainter and extended radio emissions, it provides a more accurate estimate of the total flux density than FIRST. Hence we convert flux densities (S) measured at 144 MHz from LoTSS to 1.4 GHz for the LOFAR detected sources in order to compare to existing literature, assuming a spectral index (α) of -0.7 using $S_\nu \sim \nu^\alpha$ (Condon et al. 2002). We use FIRST measured flux densities for the eight sources outside the LoTSS footprint. The radio luminosities thus obtained are compared to the Mullaney et al. (2013) $z < 0.2$

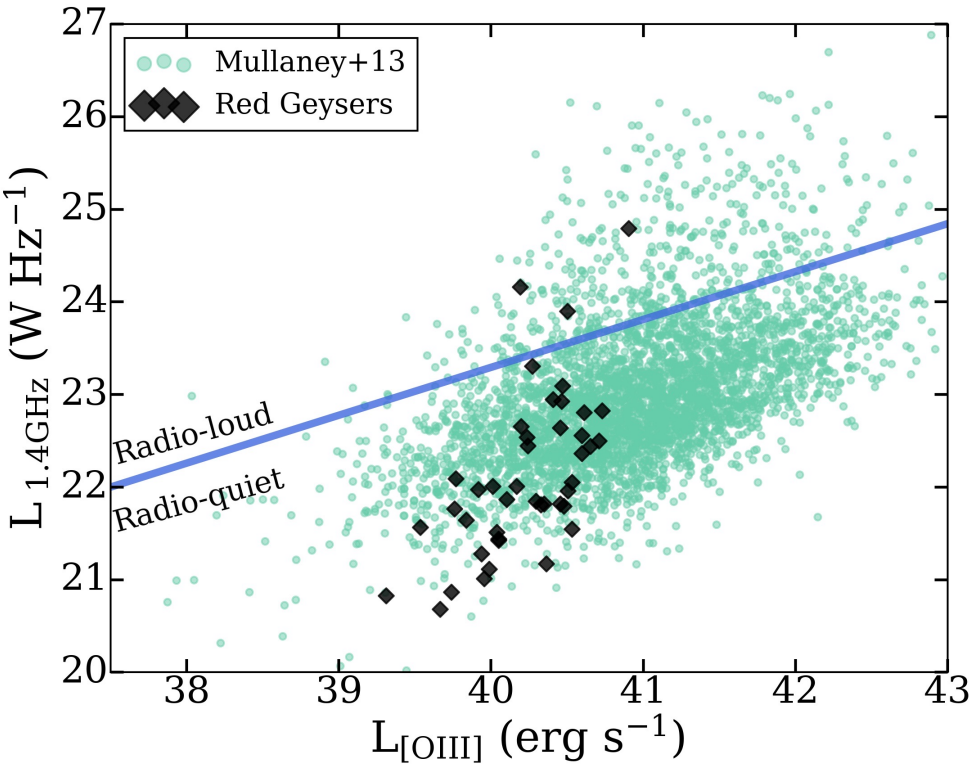

Figure 3.3: Radio luminosity measured at 1.4 GHz frequency vs. integrated [OIII] luminosity within central 3″ of red geyser galaxies (in black) and $z < 0.2$ AGN sample of Mullaney et al. (2013) (in green). The blue line divides the sample into 'radio-loud' and 'radio-quiet' according to Xu et al. (1999). A large fraction of the red geysers are radio-quiet sources by this definition.

AGN population, plotted as green circles. The blue line marks the division between "radio-loud" and "radio-quiet" sources from Xu et al. (1999). A majority of our radio red geyser sample are classified as "radio-quiet" according to this definition with only three galaxies lying in the "radio-loud" regime. If we assume $L_{1.4GHz} \sim L^{\beta}_{[OIII]}$ similar to Xu et al. (1999), β range from 0.53 to 0.60 in the red geyser sample with a mean value of 0.56. This is consistent with $\beta \sim 0.5$ as reported in Xu et al. (1999).

In addition to using the criterion of Xu et al. (1999), we compute the commonly

used radio-loudness parameter R, the ratio of radio to optical brightness (Kellermann et al. 1989), to differentiate between "radio-loud" and "radio-quiet" sources in our sample. Similar to Ivezić et al. (2002) and Jarvis et al. (2021), we calculate R using the radio flux density at 1.4 GHz calculated in a similar way as mentioned above, and the SDSS i-band apparent magnitude using the following equation:

$$R = 0.4(m_i - t) \tag{3.1}$$

Here m_i is the Petrosian i-band apparent magnitude from SDSS DR16 (Ahumada et al. 2020). The Petrosian magnitudes used here recover essentially all of the flux of an exponential galaxy profile and about 80% of the flux for a de Vaucouleurs profile. Here, t is the "AB radio magnitude" defined as

$$t = -2.5 \log \left(\frac{S_{1.4GHz}}{3631Jy} \right) \tag{3.2}$$

where $S_{1.4GHz}$ is the radio flux density (in Jy) measured at 1.4 GHz. We find that according to the R parameter criterion, four out of 42 radio-detected red geysers would be classified as "radio-loud" with $R > 1$. This includes the three galaxies which were identified as radio-loud according to Xu et al. (1999) and a fourth galaxy which was a borderline case − lying just below the division line separating "radio-loud" and "radio-quiet" population (see Fig. 3.3). Although the R parameter criterion is generally implemented in quasars with typical R values for radio-loud sources going up to 2.8 (Ivezić et al. 2002), the R values reported here simply quantifies the relative contribution of the

radio luminosity over optical light. 93% of the radio-detected red geysers are radio-quiet according to both criteria. This is consistent with Roy et al. (2018) which stated that the radio detected red geysers occupy the low-luminosity end ($L_{1.4GHz} < 10^{23}$ W Hz^{-1}) of the radio population in the MaNGA quiescent galaxy sample.

The next section is dedicated to understanding the dominant mechanism responsible for the observed radio emission in these sources via physically motivated tests.

3.4.3 Source of the radio flux: radio AGN or SF?

In Fig. 3.3 we see that 39 out of 42 radio-detected red geysers in our sample would be classified as "radio-quiet" by the Xu et al. (1999) criterion. An important and significantly challenging follow-up question to address is whether the observed radio emission is associated with the central radio AGN or star formation. Although, we have predicted in Roy et al. (2018) that the radio continuum emission in red geysers is generally associated with central low-luminosity, radiatively inefficient radio-mode AGN, it is important to verify that interpretation in the light of other observations and in our increased sample of 42 radio detected red geysers. Star-forming galaxies (SFGs) emit at radio wavelengths primarily due to synchrotron emission from shocks associated with supernovae (Klein et al. 2018), and hence their radio luminosity is expected to correlate broadly with the SFR. They generally display a diffuse clumpy radio emission not extending beyond the host galaxy with a steep spectral slope (Webster et al. 2021; Jarvis et al. 2019). On the other hand, radio emissions in the radio AGNs are primarily dominated by a jet originating from the central supermassive black hole. Unlike Mpc-

scale radio jets in the centers of massive clusters and giant radio galaxies, the jets in low-luminosity AGN hosts are small scaled and confined near the very central region of the host galaxy (Jarvis et al. 2019; Venturi et al. 2021; Capetti et al. 2020; Webster et al. 2021) which often remains unresolved due to the low spatial resolution of various radio observations. This gives rise to compact or slightly extended radio sources with no visible lobes/ jets which are hard to distinguish from star forming galaxies.

In order to consider the possibility of star formation giving rise to the detected radio emission ($\sim 10^{22}$ W Hz^{-1}, Fig. 3.3), we need to detect a significant amount of star formation ($\sim 1-5$ M$_{\odot}$) (Brown et al. 2017) in the red geyser galaxies. If similar level of SF is not detected, we can rule out SF and attribute the observed radio emission to be from the central radio AGN. We consider three diagnostic plots to classify the radio-detected sources as either starforming or non-starforming galaxies:

- Identification based on WISE colors, particularly in W3–W2 (Yan et al. 2013). Star forming galaxies possess W3 $-$ W2 > 0.3.

- Using emission line diagnostics, in particular the ratio of [OIII] 5007 and Hβ line fluxes, and that of [NII] 6584 and Hα (Baldwin et al. 1981), referred to as the 'BPT' method. Galaxies with $\log([\mathrm{OIII}]/\mathrm{H}\beta) < 0.5$ and $\log([\mathrm{NII}]/\mathrm{H}\alpha) < -0.3$ lying under the Kauffmann et al. (2003) curve are star forming galaxies.

- Using the relationship between the 4000 Å break strength and radio luminosity per stellar mass (Best et al. 2005), hereafter referred to as the 'D4000 vs L$_{\mathrm{rad}}$/M' method. Galaxies with D4000$\leq$ 1.6 are dominated by young stellar populations

and hence constitute star forming galaxies.

Specific WISE mid-infrared colors can be used to separate galaxies with and without star formation. Thus, star-forming galaxies separate from the typical hosts of radio AGN in their WISE colours, particularly in W2–W3 (4.6 to 12 micron color, Yan et al. 2013). Fig. 3.4 upper left (panel a) shows a plot of W1–W2 versus W2–W3 mid-infrared WISE colors for 42 red geysers which are radio-detected in at least one of the LoTSS, VLASS or FIRST surveys (in black). The background orange contours represents the WISE colors for all galaxies in SDSS-MaNGA DR16 sample. The contour clearly indicates a bimodal distribution in the color space representing the star forming and quenched galaxy population. Star forming galaxies mostly occupy regions with $0.3 < \mathrm{W3} - \mathrm{W2} < 0.9$, while the quenched population has $-0.6 < \mathrm{W3} - \mathrm{W2} < 0.0$. The radio-detected red geysers lie in the quenched part of the diagram which confirms the passive nature of these galaxies.

Since our red geyser targets possess strong emission lines, a common and useful method to separate SFG from AGN-hosts is through the ionization of the gas via Baldwin-Phillips-Terlevich diagram (BPT, Baldwin et al. 1981). By observing the relative strengths of four emission lines, namely [OIII]/Hβ and [NII]/Hα, we can separate SFG and AGN-host galaxies based on the hardness of their ionizing spectrum, that in turn, drives the relative fluxes of different emission lines. This leads to the AGN-host galaxies to occupy a separate region in the diagram from the SF galaxies with the Kewley et al. (2006) and Kauffmann et al. (2003) demarcation lines in between. Fig. 3.4 upper right (panel b) shows the BPT diagram of all galaxies from MaNGA Data Release

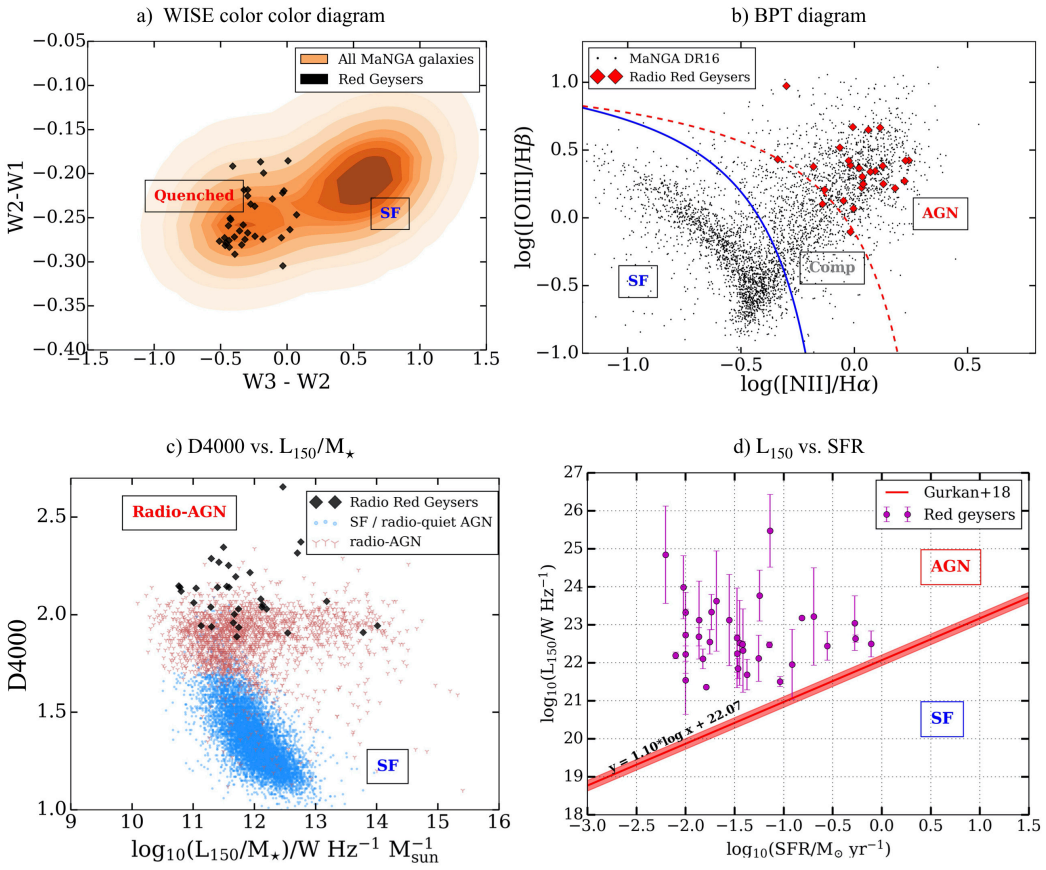

Figure 3.4: Location of the radio-detected red geyser sources on the different diagnostic plots used to separate the radio AGN from those galaxies where the radio emission is powered by SF. [Panel a] WISE W2-W1 vs W3–W2 colour-colour diagnostic diagram. The radio detected red geysers are shown in black diamonds, while the orange contours are the wise-detected MaNGA galaxies. [Panel b] The [OIII]/Hβ versus [NII]/Hα emission line ratio diagnostic diagram from Baldwin et al. (1981), known as the 'BPT-diagram', for the radio-detected red geysers (in red) and MaNGA galaxies from data release 16 (in black). [Panel c] The 'D4000 versus $L_{150MHz/M_\star}$' method, developed by Best et al. (2005), for the radio-detected red geysers (in black). They are compared to the SF (blue) and AGN population (red) from the LoTSS (DR1) detected SDSS (DR7) galaxies by Sabater et al. (2019). [Panel d] Radio luminosities vs. star formation rate for the LoTSS-detected red geysers (magenta) compared to the Gürkan et al. (2018) measured low frequency radio luminosity - star formation relation (red). All the red geysers lie above the said line, indicating that the radio emission observed in the red geysers are too high to be explained from the amount of star formation detected in these galaxies.

16 in black. The red diamonds indicate the radio detected red geysers (detected in at least one radio band). The red geysers land in either the LINER or AGN regions of the BPT diagram and show no indication of SF activity. The absence of SF through the BPT diagram provides an useful diagnostic, as this confirms and re-iterates the quiescent "red and dead" nature of the galaxies and indicates that the possible source of the radio emission is an AGN.

The 'D4000 vs L_{rad}/M' method for identifying radio AGN was developed by Best et al. (2005). The parameter D4000 is the strength of the 4000 Å break in the galaxy spectrum, and $L_{rad}/M_{\star}$ is the ratio of radio luminosity (measured in a specific radio band) to stellar mass. This identification process is constructed on the basis that SFGs with a wide range of star formation histories occupy the same region in this plane since both L_{rad}/M and D4000 depend broadly on the specific star formation rate of the galaxy. On the other hand, radio-loud AGN have enhanced values of L_{rad} and are thus separable on this plane. Among the low-luminosity radio sources, low D4000 value would distinguish galaxies with active star formation which would possibly be the dominant cause behind the observed radio emission in those sources. This identification method, later implemented with slight modifications by Kauffmann et al. (2008) and Sabater et al. (2019), has been generally successful with few cases of mis-classification.

In Fig. 3.4 lower left panel (c), we plot D4000 vs. $L_{150}/M_{\star}$ for the radio-detected red geysers in black. We use only the 34 LOFAR-detected sources in this analyses utilizing the flux measurements from the 150 MHz band, which are then compared with existing sources from the literature. We overplot the radio sources from SDSS

DR7 from Sabater et al. (2019) in the background. The data points are color-coded in blue circles and red arrows which represents SFG and radio AGN respectively, classified using a combination of diagnostics (see Sabater et al. 2019). In general, sources with average D4000 value exceeding $\sim$ 1.7 do not exhibit enough active star formation to show substantial radio emission due to supernovae/ stellar activity. Hence radio sources with $L_{150}/M_{\star} > 11$ W Hz^{-1} $M_{\odot}^{-1}$ and D4000 > 1.7 are predominantly radio AGN. All the red geysers in our sample land in the radio AGN portion of the diagram, as they have a relatively old stellar population with D4000 exceeding 2.0.

In addition to these three diagnostic plots, we also show the relation between radio luminosity (from LOFAR at $\sim$150 MHz) and SFR (panel d) for the LOFAR-detected red geysers sample (in magenta). As mentioned previously, star formation rate is expected to correlate with radio luminosity in star forming galaxies, due to synchrotron emission from supernovae shocks. Gürkan et al. (2018) studied low frequency radio luminosity - SFR relation on a large sample of SDSS galaxies and found the best fit (single power law) relation to be:

$$\log_{10}(L_{150}) = 1.07 \pm 0.01 \times \log_{10}(\mathrm{SFR}) + 22.07 \pm 0.01 \tag{3.3}$$

The above relation is shown as a red line in Fig. 3.4. Any galaxy lying above this relation posses an excess amount of radio emission, too high to be produced from the corresponding level of SF. We find that all the red geysers lie above the Gürkan et al. (2018) relation, which indicates that the radio emission is consistent with galaxies hosting radio AGNs.

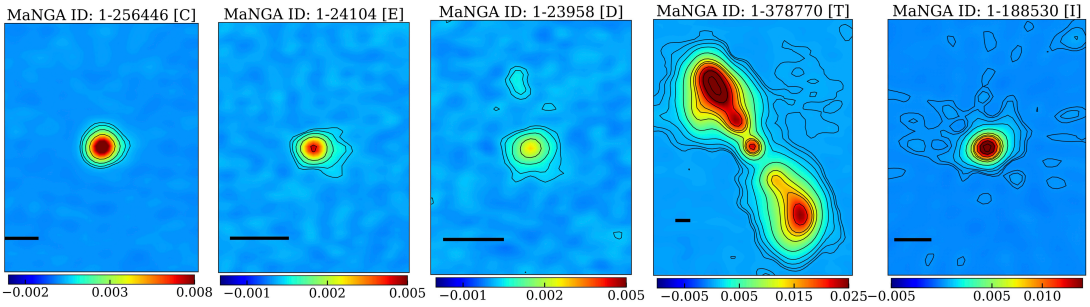

Figure 3.5: The LoTSS images of five example red geysers, classified in different radio morphology classes as mentioned in square brackets. Galaxy with MaNGAID: 1-256446 is classified as "compact" source, 1-24104 as "extended", 1-23958 as "double", 1-378770 as "triple" and 1-188530 as "irregular" source. The black horizontal scale bar in each panel indicates 20 kpc length scale.

3.5 Radio Morphology

3.5.1 Classification based on morphology

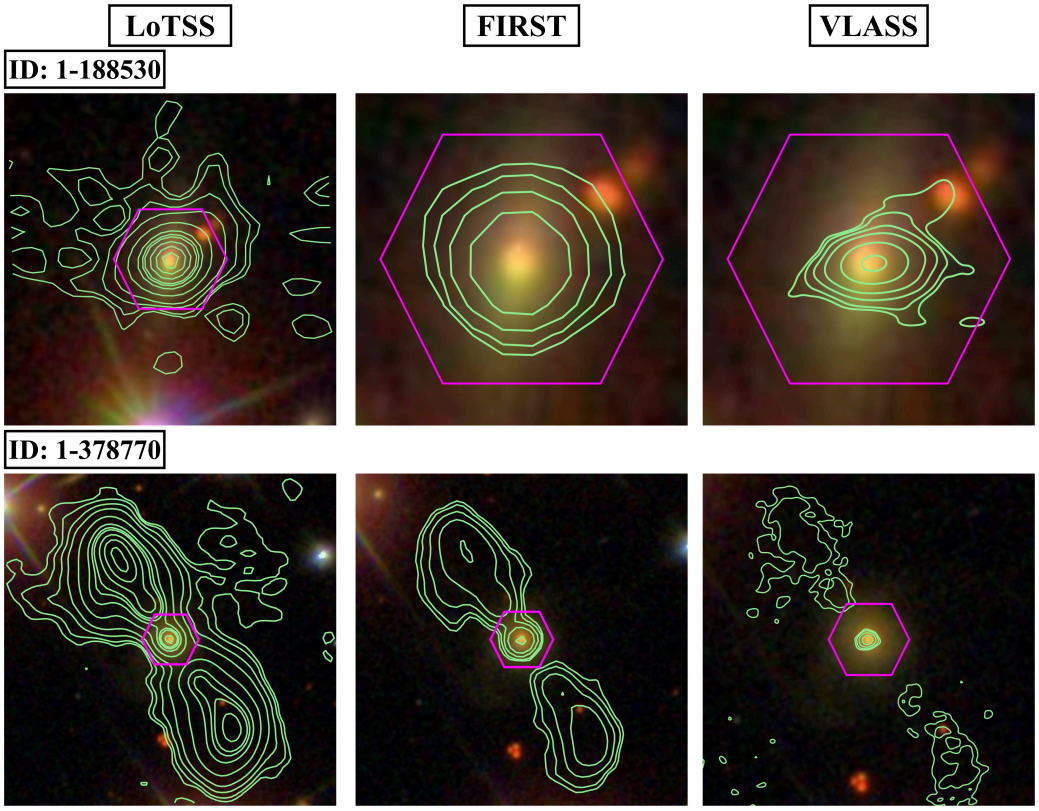

Figure 3.6: The LOFAR (left column), FIRST (middle column) and VLASS radio contours (right column) on top of optical images from SDSS for two red geysers with MaNGAID: 1-188530 (first row), 1-378770 (second row). The magenta hexagon signifies the MaNGA field of view.

Table 3.1: Summary of the radio properties for the red geyser sample. 1) MaNGA ID: identification of the galaxies. 2) z: SDSS measured redshift. 3) L_{150MHz}: radio luminosity measured from LoTSS survey. 4) $L_{1.4GHz}$: radio luminosity measured from FIRST survey, 5) Radio size: The largest of the linear sizes (see §3.5.2 for details) measured from LoTSS and FIRST surveys. For sources with no available LOFAR data, the FIRST measured sizes are reported as lower limits. 6) α: Spectral index measured from radio flux from LoTSS, FIRST and VLASS surveys at frequencies of 144 MHz, 1.4 GHz and 3 GHz. 7) Morphology: The different radio morphology class from LoTSS images, as stated in §3.5.1. C, D, E, I, T indicates compact, double, extended, irregular and triple class respectively. U means unresolved sources. For sources with no available LOFAR data, the morphology from FIRST images are indicated in square brackets.

MaNGA ID	z	L_{150MHz} [LoTSS] [10^{22} W Hz^{-1}]	$L_{1.4GHz}$ [FIRST] [10^{22} W Hz^{-1}]	Radio Size [kpc]	α	Morph
1-575668	0.060	1.71±0.17	–	6.24±0.70	–	C

1-273933	0.044	13.36±0.12	2.67±0.06	2.74±0.02	-0.712	U
1-217324	0.024	1.75±0.02	–	10.50±1.2	–	D
1-48084	0.031	0.23±0.04	–	6.96±0.88	–	E
1-279073	0.032	0.49±0.04	0.59±0.03	3.92±0.76	-0.019	C
1-198182	0.036	3.35±0.06	1.41±0.04	2.45±0.06	-0.494	U
1-44418	0.031	0.33±0.05	–	4.16±0.72	–	C
1-198180	0.037	3.53±0.20	–	21.41±02.3	–	D
1-217022	0.024	0.92±0.03	0.17±0.02	2.99±0.09	-0.616	C
1-256446	0.058	13.24±0.29	2.58±0.01	5.05±0.06	-0.748	C
1-245451	0.078	42.15±0.53	6.25±0.24	8.86±0.06	-0.870	C
1-256234	0.075	4.34±0.94	–	23.96±4.43	–	E
1-352569	0.079	11.07±1.58	9.51±0.23	7.81±0.246	-0.163	C
1-322336	0.135	20.99±0.70	6.09±0.69	8.51±0.35	-0.496	C
1-374549	0.086	2.98±0.61	–	9.7±2.08	–	E
1-321221	0.036	1.31±0.08	0.27±0.04	3.84±0.25	-0.132	C
1-268789	0.059	16.53±0.29	7.04±0.12	4.13±0.05	-0.416	U
1-595166	0.044	58.92±0.65	5.41±0.07	44.09±2.7	-1.06	T
1-575742	0.061	3.15±0.19	–	6.78±0.67		C
1-209772	0.041	96.92±0.16	25.78±0.07	20.31±2.1	-0.628	I
1-627331	0.027	4.51±0.14	0.11±0.02	2.52±0.06	-0.741	C
1-188530	0.055	21.24±0.23	9.06±0.11	25.59±3.33	-0.283	I

1-605515	0.096	5.37±0.54	–	1.2±0.09	–	U
1-150792	0.066	0.71±0.16	–	8.41±2.04	–	C
1-218116	0.047	4.86±0.12	2.23±0.08	10.35±2.87	-0.312	E
1-634825	0.030	4.84±0.20	1.36±0.03	5.36±0.06	-0.306	C
1-378770	0.13	2984.26±10.57	615.10±7.2	233.07±7.2	-0.847	T
1-94168	0.03	2.79±0.03	0.98±0.03	20.96±1.87	-0.746	D
1-567948	0.13	15.08±1.00	–	11.40±2.56	–	C
1-289864	0.049	695.26±15.26	8.38±0.09	157.184±3.04	-0.900	T
1-23958	0.029	1.27±0.03	0.34±0.03	16.15±1.8	-0.621	D
1-218764	0.068	3.08±0.12	–	2.15±1.8	–	U
1-584723	0.015	0.35±0.06	–	1.59±0.1	–	U
1-24104	0.029	1.56±0.07	0.39±0.03	6.55±1.2	-0.612	E
1-113668	0.129	–	6.39±0.06	>0.33±0.02	–	[U]
1-550578	0.076	–	8.44±0.22	>1.68±0.62	–	[C]
1-37036	0.0283	–	0.13±0.02	> 0.58±0.7	–	[U]
1-43718	0.041	–	1.24±0.06	> 0.85±0.52	–	[U]
1-209926	0.095	–	3.63±0.03	> 13.04±3.5	–	[E]
1-210863	0.03	–	1.02±0.06	> 10.17±0.03	–	[E]
1-96290	0.130	–	6.72±0.66	> 11.64±3.98	–	[C]

1-37440	0.0136	–	0.66±0.06	$> 0.78 \pm 0.34$	–	[U]

We primarily use data from the LoTSS survey to analyze the radio morphology of the red geysers for the following reasons. First, the LoTSS data is most sensitive to extended fainter radio emissions amongst the interferometers used in this work as it has shorter interferometric baselines than the VLA surveys. Second, the low frequency ($\sim$ 150 MHz) radio continuum emission reflects the oldest and the lowest energy emission from the plasma which helps in characterizing the full extent of the structure and enables a robust classification. As mentioned in §3.4.1, 34 out of 103 red geysers with LOFAR observations are detected at 150 MHz. Six of them are unresolved with deconvolved major axis $< 5''$ (i.e. $<$ 3 kpc at median z = 0.03) and are thus physically contained within the central region of the galaxy. There are 28 LOFAR-detected red geysers which are resolved compared to the beam size. We visually classify the morphology of these 28 sources into five types based on the LOFAR images, roughly following Baldi et al. (2018); Kimball et al. (2011); Jarvis et al. (2021):

1. Compact (C): if the source shows no visibly spatially-resolved features (i.e. has the appearance of a single two-dimensional Gaussian) and is constrained within the host galaxy. These sources have sizes larger than the beam size and may be elongated intrinsically but higher resolution is needed to confirm this.

2. Extended Jet (E): if the source is visibly spatially extended in one direction but composed of one contiguous feature, i.e., one distinct peak in the radio emission.

3. Double (D): if the source shows two distinct peaks in the radio emission.

4. Triple (T) : if the source shows three distinct peaks in the resolved radio image, typically consisting of two jets and one core.

5. Irregular (I): sources generally with one distinct peak in the radio emission but with unique spatially extended (irregular) radio morphologies that do not fit within the above categories.

The most common morphology is the "compact" class, found in 14 out of 28 sources. The object with MaNGAID 1-256446 in Fig. 3.5 belongs to this class of sources. In five sources, we see a comparatively extended morphology stretching in one direction, which we define as "extended jet". It is to be noted that this term is used to describe the morphology only and might not be physically associated with an AGN-jet. Four sources show a double-peaked radio emission (classified under "double"). They generally consist of a radio core and a one-sided bubble/tail which may or may not be directly attached to the central component. MaNGAID 1-23958 (Fig. 3.5) is one such example. In three sources, we see three or more distinct peaks in radio emission. Two of them show a central core emission with large scale double-sided lobes on either side, extending > 40 kpc. The third source shows an extended morphology which consist of several distinct radio peaks with $> 50\sigma$. These belong to the "triple" category. The galaxy with MaNGAID 1-378770 in Fig. 3.5 is an example with double-sided jets. Finally, MaNGAID 1-188530 represents the irregular morphological class; in this case the LOFAR image looks quite peculiar, resembling a jelly-fish, with a bright central core superimposed on a large scale structure of diffuse radio emission.

Although we perform our morphological classification primarily using LOFAR images there are eight FIRST-detected red geysers which are not covered by the LOFAR observations. We similarly categorize these sources using FIRST data into the five classes described above. Out of those eight sources, four are unresolved with a deconvolved major axis $< 2.5''$. The rest belong to either the compact or extended jet classes.

Table 3.1 shows the classification type of each LOFAR-detected red geyser along with the additional eight FIRST-detected sources which do not have corresponding LOFAR images (indicated by square brackets).

Fig. 3.6 shows the morphological comparison of the LoTSS images (left panel) with images from the FIRST (middle panel) and VLASS surveys (right panel) of two example red geysers out of the five sources from Fig. 3.5. The radio-detected red geysers, depending on the morphological class, exhibit spatially diffuse extended features which are often only visible with LOFAR data. In most cases, the corresponding VLASS and FIRST images look rather compact.

3.5.2 Radio size

The actual physical sizes of the radio sources are independent of the frequency of observations. However, the apparent linear size, as measured from different radio bands - i.e., using FIRST, VLASS and LoTSS data, can be different (as evident from Fig. 3.6) for several reasons. First, the FIRST/VLASS data are at higher frequencies and hence less sensitive than LOFAR to structures of typical spectral index which can

lead to a smaller estimated size. Second, FIRST and VLASS lack short interferometric baselines which makes observations of extended structures above a certain size difficult in these surveys. Surface brightness sensitivity, on the other hand, can limit LOFAR sizes as well. Hence, we estimate sizes from both LoTSS and FIRST surveys, and report the larger of the two as our best estimate of the physical size of the radio source. In almost all cases, the size estimate obtained from LOFAR is greater than that from FIRST by at least a few factors. So in cases where only FIRST data is available, we report the FIRST-measured size as a lower limit. Our method of determination of size depends on the nature of the radio morphology.

For the sources under the label 'double' and 'triple', which show two and three distinct radio features in LOFAR images respectively, the linear size in the 150 MHz is calculated as the distance between the peak emission of the two farthest morphological features detected within 10 σ contours. For sources having contiguous, extended (E) and irregular morphology (I) with closely blended components, we measure the end-to-end linear size of the radio structure detected within $> 10\ \sigma$. For the cases where the source is featureless and has only one primary morphological feature (classified as compact 'C'), we use the major axis size, de-convolved from the beam, as listed in the LOFAR catalogue.

Depending on the specific structure of the FIRST image, the linear size in 1.4 GHz is also calculated in a similar way. The FIRST catalogue also provides major axis measurements (FWHM in arcsec) from the elliptical Gaussian model for the source which are then deconvolved to remove blurring by the elliptical Gaussian point-spread

function. As mentioned above, we consider the larger of the measured sizes from LOFAR and FIRST to be the "largest linear size" or simply the radio size. Table 3.1 lists the measured sizes of the radio sources along with 1σ uncertainty. For the compact and unresolved sources, the errors are derived from the respective catalogue which reports 1σ uncertainty in the de-convolved major axes, derived from the Gaussian models of the sources. For resolved objects showing spatially extended morphologies, we assume the uncertainty to be the linear size (in kpc) corresponding to half the beam-width, i.e. $3''$ for LOFAR. The uncertainty in size from the FIRST band is obtained from the relation: $\sigma_{\rm Size} = 10'' * (1/{\rm SNR} + 1/75)$ [3], where SNR is the signal-to-noise, given by: ${\rm SNR} = ({\rm F_{peak}} - 0.25)/{\rm RMS}$. $\rm F_{peak}$ and RMS signifies the peak flux and the root mean square deviation measured from the catalogue respectively.

Table 3.1 shows the radio sizes along with radio luminosities of the radio detected red geysers in both the LOFAR and FIRST radio bands. Fig. 3.7 shows the radio-luminosity (at 1.4 GHz) vs. linear size of the radio-detected red geysers, detected in at least one of the radio bands (in black stars), over-plotted along with different classes of radio sources from the literature in different colored contours. For the red geysers with available LoTSS counterpart, we convert measured 144 MHz flux from LOFAR to 1.4 GHz, assuming a spectral index of -0.7 in order to calculate the desired luminosity (Condon et al. 2002). This is preferred over using FIRST flux that misses extended emission. However for those without LOFAR data, corresponding FIRST luminosities are used. The different colored contours in the figure, as indicated, represent

[3] http://sundog.stsci.edu/first/catalogs/readme.html

compact symmetric objects (CSO), gigahertz peaked spectrum (GPS), compact steep spectrum sources (CSS), Fanaroff-Riley class 1 (FRI), Fanaroff-Riley class 2 (FRII), radio-quiet quasars (RQQ) and Seyferts. The data for these radio-detected AGNs have been compiled by Jarvis et al. (2019) from a variety of studies of radio AGN population, namely An & Baan (2012); Gallimore et al. (2006); Kukula et al. (1998); Baldi et al. (2018); Mingo et al. (2019). Most of the radio-detected red geyser sources, marked as black stars, overlap with the LINER/Seyfert type classification and with the tail of the distribution of radio-quiet quasars. There are two sources which lie on the FRI part of the diagram, both of which are categorized as "triple" according to morphology classification. Our sources are in general consistent with having similar small scale low-luminosity jetted morphologies as observed in the radio-quiet quasars in Jarvis et al. (2019) or with FR0 sources which remain classified as "compact" unless higher resolution observations are available to resolve the sources, as in Baldi et al. (2015); Capetti et al. (2019); Hardcastle et al. (2019).

3.5.3 Spectral Index

In this section, we study the spectral indices for our sample of 21 red geysers which have simultaneous radio detection from LOFAR, FIRST and VLASS data (See §3.4.1 for more details). The radio-continuum spectrum is generally dominated by non-thermal synchrotron emission with the characteristic power-law, $S_\nu \propto \nu^\alpha$, where α is the spectral index, ν is the frequency of radio emission and S_ν is the flux density measured at frequency ν. In star-forming galaxies there may also be some additional contribution

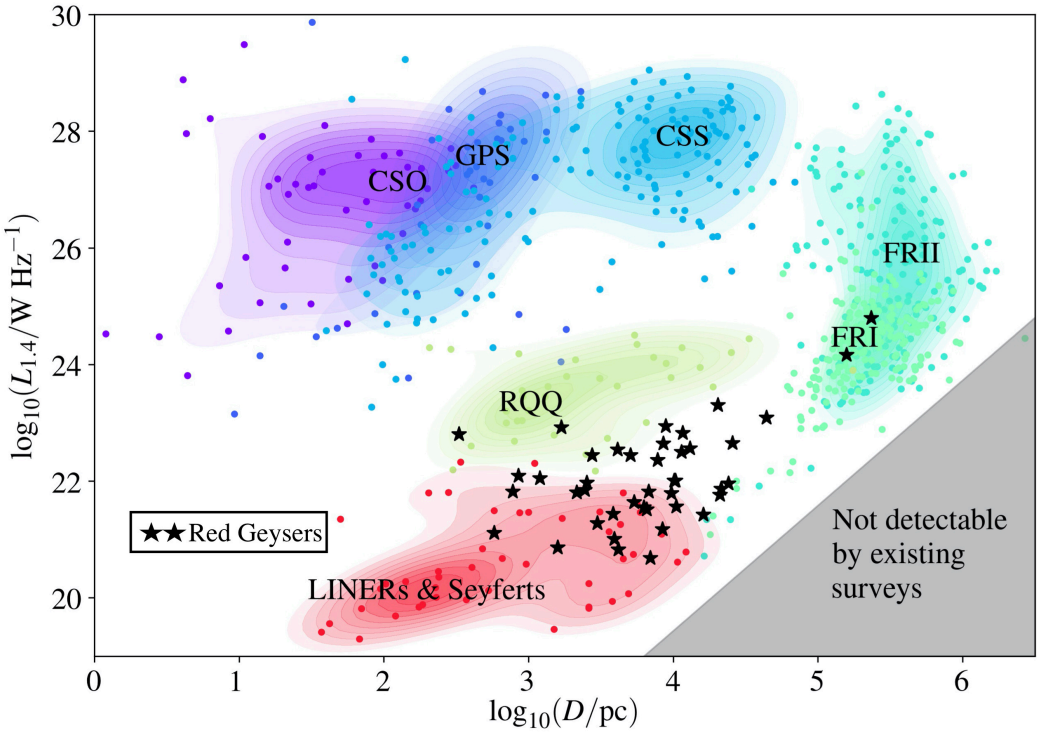

Figure 3.7: Radio luminosity versus linear size for our red geyser sample (black stars) compared to a sample of radio AGN population compiled from the literature by Jarvis et al. (2019) and Hardcastle & Croston (2020). Points show individual objects and the colored contours represent source density. Seyfert and LINER galaxies are from Gallimore et al. (2006) and Baldi et al. (2018), while the radio-quiet quasars (RQQ) are from Jarvis et al. (2019) and Kukula et al. (1998). The rest of the objects, consisting of compact steep spectrum (CSS) sources, gigahertz peaked spectrum (GPS), compact symmetric objects (CSO) and Fanaroff-Riley class 1 and 2 are categorized by An & Baan (2012); Mingo et al. (2019).

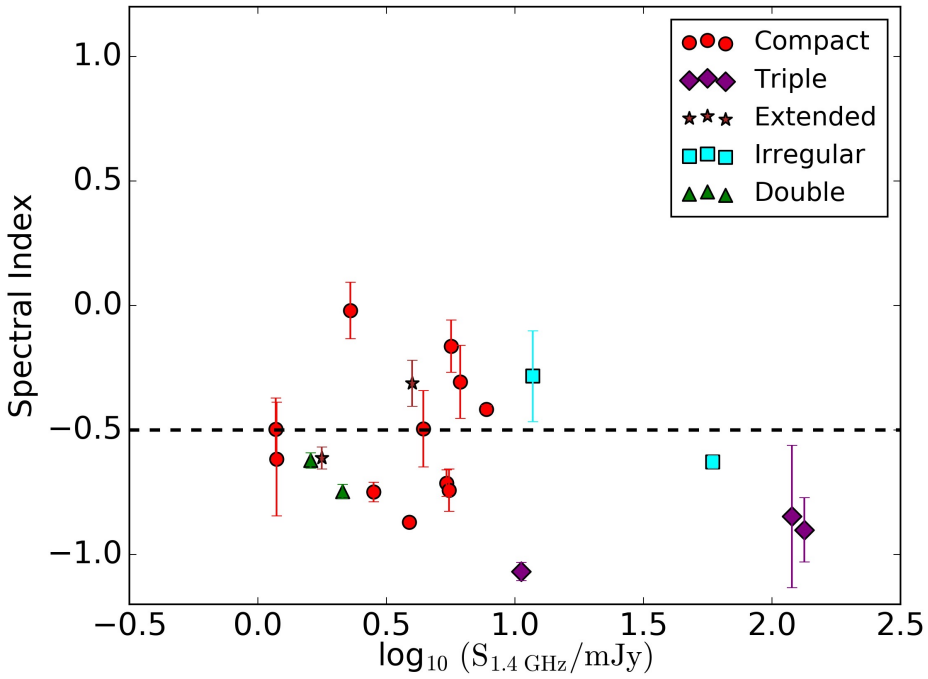

Figure 3.8: The spectral index vs. radio flux density at 1.4 GHz frequency for the 21 red geysers which are simultaneously detected in LOFAR, FIRST and VLASS. The galaxies are color-coded by radio morphology classification, as defined in §3.5.1. Note, for this figure, the unresolved galaxies are also marked as "compact" along with the actual compact class.

from the thermal bremsstrahlung (free-free) emission (Duric et al. 1998; Gioia et al. 1982), but that is irrelevant here.

The spectral index of a radio galaxy can provide information about the relative contributions of the core and the extended lobed structure in the total radio emission. Core-dominated emission and any compact source typically have flat ($\alpha > -0.5$) spectrum due to the effects of synchrotron self absorption and free-free absorption (e.g., O'Dea & Saikia 2021). The extended lobes, on the other hand, tend to have steep spectra ($\alpha \leq -0.5$) because the predominant emission mechanism is optically-thin synchrotron. Thus, radio sources which are more core-dominated therefore tend to have flatter spectra than those dominated by extended emission. This is confirmed from the observation of a high-core dominance in FR0s, owing to their compact nature, based on high resolution images (Baldi et al. 2018).

As can be seen in Fig. 3.5 and Table 3.1, our sources exhibit a range of radio morphologies from LOFAR data. We use the integrated flux densities and uncertainties from the LoTSS, FIRST and VLASS catalogs for our analyses (See Table 3.1 for the flux densities and uncertainties for each source). For sources having more than one component/ region, we visually identify all the individual components detected at a significance of $> 5\sigma$ which are associated with the source and add the flux densities from these components together. We define the radio spectral index, α, using $S_\nu \propto \nu^\alpha$ and measure α by fitting the flux densities measured at three different frequencies (1.4 GHz, 3 GHz and 150 MHz) with the said function for each source. The errors are obtained from the uncertainties in flux densities via simple error propagation. Table 3.1

lists the spectral indices with 1σ uncertainty of the 21 red geyser galaxies.

The red geysers show a large spread in spectral indices, ranging from -1.0 to 0.0 with a median value of -0.62 (see Table. 3.1 and Fig. 3.8). The extended radio sources, which do not belong to the "compact" morphological class, exhibit steeper spectra on average with a mean spectral index $\alpha = -0.67$. The fraction of sources with a steep spectrum ($\alpha < -0.5$) is $\sim 57\%$ indicating the presence of extended emission or dominance of lobed components in those radio sources. This automatically implies that 43% of our sample of 21 red geysers (i.e., eight sources) have a flatter spectrum, with core-dominated compact structures. This agrees well with our morphological classifications, in that a fairly large fraction of red geysers have compact radio morphologies confined within the host galaxy. The bright nuclear radio component with a moderately flat spectral index (i.e.,$\alpha > -0.5$) may indicate a contribution from radio emission associated directly with an AGN 'core' / unresolved base of the jet (Padovani 2016).

Fig. 3.8 shows the variation of the spectral index with 1.4 GHz flux density as measured from FIRST. Galaxies are color-coded by the morphological class, as given in Table 3.1. Note, for this figure, the unresolved sources are also color-coded as the "compact" class. All three galaxies classified as "triple" have steep spectral indices indicating that those sources have more extended lobes with predominantly optically thin synchrotron emission. With an exception of two galaxies, almost all the red geysers which are not-compact (any color except red) have a steep spectrum and lie below the dashed line. The two sources showing flat spectrum might be due to the result of a combination of underlying biases in the measured fluxes and puzzling morphology

leading to an incorrect classification. On the other hand, half of the sources labelled "compact" show flat spectrum while the other half exhibit a steep spectral index. We do not see any significant correlation of spectral indices with radio flux density. The implications of these results are discussed in §3.7.

3.6 Radio jet and connection with galactic outflows

Here we explore the connection between the radio emission, its morphology, and the ionized gas properties in our sample.

3.6.1 Integrated properties

Traditionally, for compact radio-loud sources (CSS/GPS), a weak positive trend has been observed between the luminosity of strong emission lines and radio size (O'Dea & Saikia 2021). Larger radio sources are found to be more commonly associated with higher [OIII] luminosities (O'Dea 1998). A similar correlation has also been observed in radio-quiet sources using SDSS-measured [OIII] luminosities (Jarvis et al. 2021). Here we investigate whether similar correlation exists in red geyser galaxies. Here we use Hα as a tracer of ionized gas instead of the traditional [OIII] line, since the characteristic bi-symmetric pattern identifying a red geyser is most prominently observed in the spatial distribution of Hα.

Fig. 3.9 shows the the Hα luminosity, integrated over one effective radius as observed by MaNGA, vs. the linear size of the radio emission of the 42 radio detected red geysers. The data are color-coded by the radio luminosity at 1.4 GHz. The radio

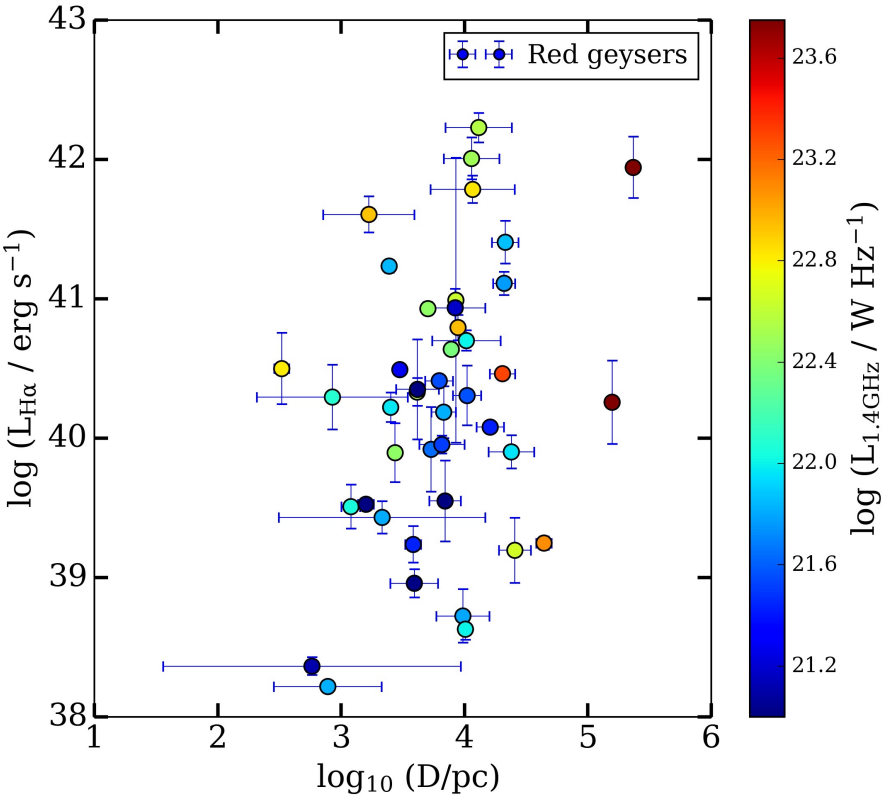

Figure 3.9: Hα luminosity integrated over one effective radius aperture vs. radio size (as given in Table 3.1) for 42 radio detected red geysers, color coded by radio luminosity at 1.4 GHz. For the 34 LOFAR detected sources, L_{150MHz} has been converted to $L_{1.4GHz}$ assuming a spectral index of -0.7. For the remaining eight galaxies outside LOFAR footprint, FIRST measured luminosities have been used. A moderate positive correlation between Hα luminosities and radio size is detected.

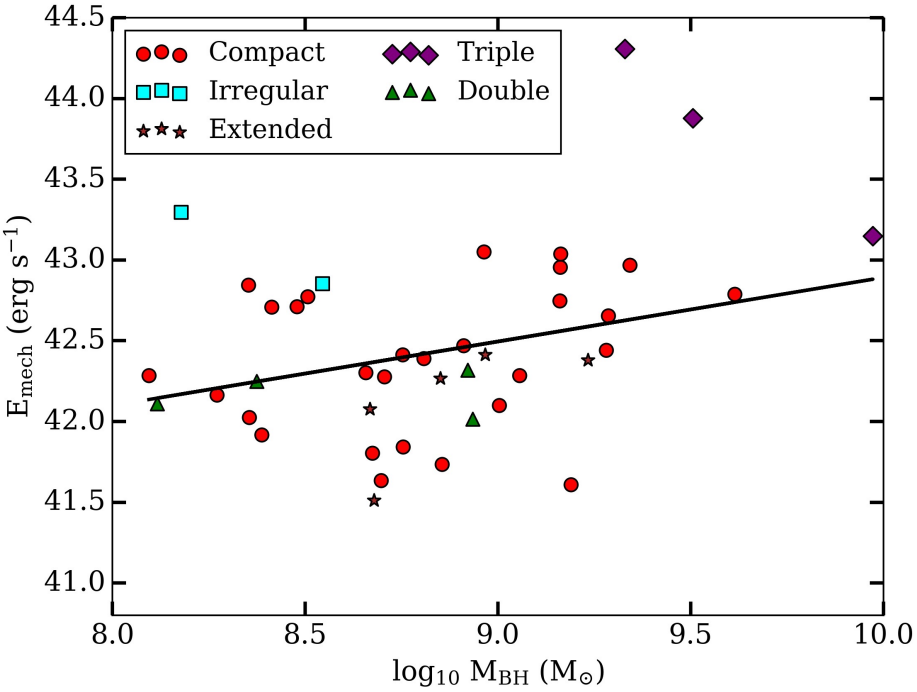

Figure 3.10: Jet mechanical energy, estimated from radio luminosity vs. supermassive black hole mass for 42 radio detected red geysers color coded by morphological class. A clear positive trend is seen, implying that the observed radio emission is linked to the nuclear SMBH.The black solid line shows the best fit relation obtained by least square optimization.

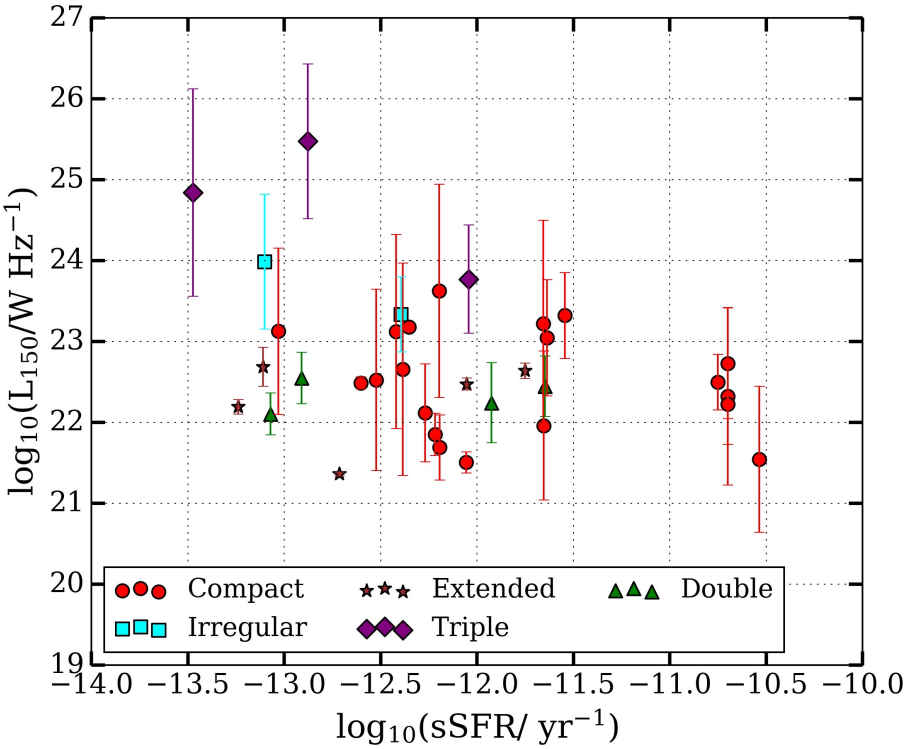

Figure 3.11: Radio luminosity (L_{150MHz}) vs. specific star formation rate for the radio detected red geysers, color coded by morphological class. Galaxies which are not classified as "compact" and possess extended radio structures show low SFR for their stellar mass. This implies large radio sources are more efficient in quenching red geyser galaxies.

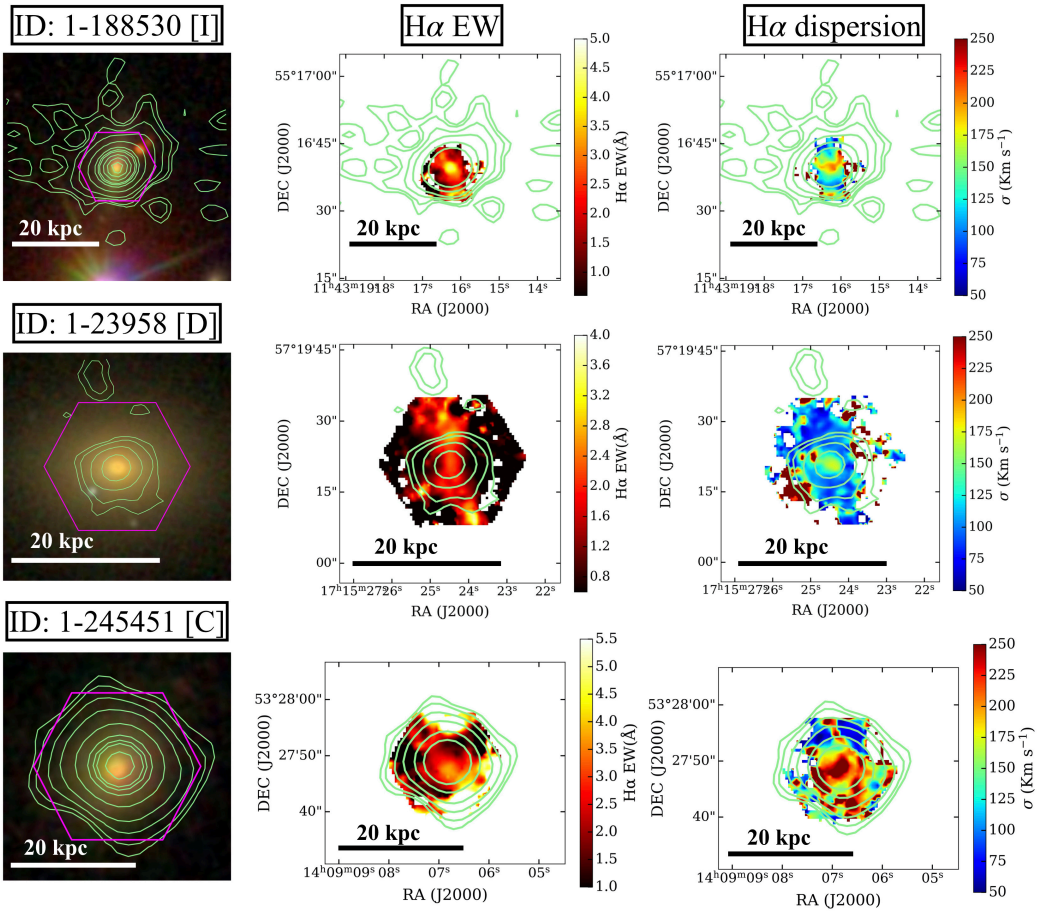

Figure 3.12: SDSS optical image (left column), MaNGA Hα EW map (middle column) and Hα velocity dispersion (right column) shown for three red geyser galaxies with LOFAR radio contours overplotted in green. Each row represent a red geyser galaxy. Galaxy with ID: 1-188530 (top row) belongs to the irregular morphology class, 1-23958 (middle row) has a double morphology and 1-245451 (bottom row) shows compact radio structure.

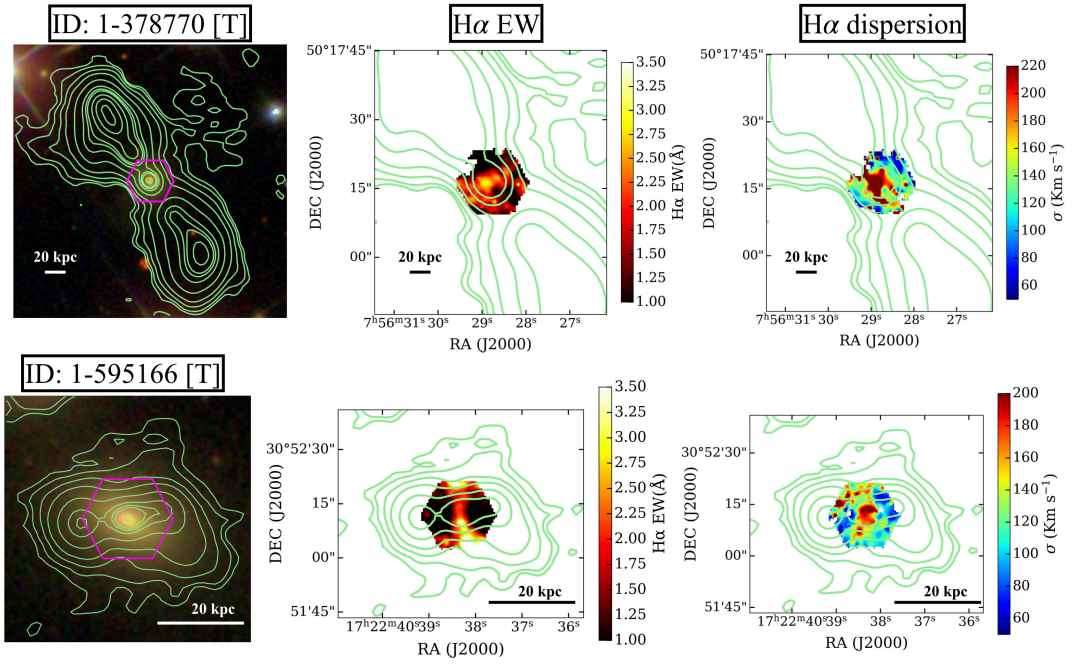

Figure 3.13: SDSS optical image (left column), MaNGA Hα EW map (middle column) and Hα velocity dispersion (right column) shown for two red geyser galaxies with LOFAR radio contours overplotted in green. Each row represent a red geyser galaxy. Both galaxies belong to the "triple" morphology class showing large scale radio lobes.

luminosities are derived by converting L_{150MHz} to $L_{1.4GHz}$ assuming a spectral index of -0.7, as before. Our data show a positive correlation that is consistent with what has been observed in radio-loud compact sources and in some recently studied radio-quiet sources. Liao & Gu (2020) showed that for the radio-loud population, the [OIII] bright sources (with $L[OIII] > 10^{42}$ erg s^{-1}) have radio sizes > 0.75 kpc. This is consistent with our result since the red geysers show radio sizes > 10 kpc for similar $L_{H\alpha}$. The existence of this positive correlation in the red geysers is strongly supported by a Spearman rank correlation coefficient of 0.6. Fig. 3.9 also shows that the radio luminosity generally shows a higher value ($\sim 10^{23}$ W Hz^{-1}) for larger radio size and higher Hα luminosities (i.e. towards the upper right portion of the figure). On the other hand, as $L_{1.4GHz}$ drops to $10^{21.5}$ W Hz^{-1} for $L_{[OIII]} < 10^{40}$ erg s^{-1} the radio size decreases to $<$ 5kpc. This is expected because of the first order dependence of the morphology of the radio sources with radio power. Large scale radio structures are found to be generally more abundant in radio-loud sources, although this correlation is not so apparent in radio quiet sources (Morganti 2021). In the case of red geysers, this possibly implies that larger radio sources with greater radio luminosity hosts greater amount of ionized gas.

In previous studies, similar relations between the strength of an ionized gas outflow tracer and the size of the radio source has been explained by considering the interaction between an embedded, AGN-driven radio jet and the ISM. Regardless of size and structure of the radio jet—which is unlikely to be resolved owing to spatial resolution in this case—the important parameter to quantify the impact on the surrounding ISM is jet energy. Although there have been several methods to estimate the jet power, the

method presented by Willott et al. (1999) based on the synchrotron properties of the radio sources has been shown to be particularly effective. They proposed the following conversion between the jet mechanical energy and the radio luminosity:

$$E_{mech} = 2.8 \times 10^{37} \left(\frac{L_{1.4GHz}}{10^{25} \text{ W Hz}^{-1}} \right)^{0.68} \text{ W} \tag{3.4}$$

This expression is used in this work, although there are limitations of this approach, as discussed in Hardcastle & Krause (2013); Croston et al. (2018). We find that red geysers show a large range in E_{mech}, spanning three orders of magnitude, within $10^{41.5} - 10^{44.5}$ erg s^{-1}. In order to re-affirm the hypothesis that the source of this estimated energy is the central radio AGN, we also calculate the corresponding supermassive black hole mass (SMBH) of our sources. The SMBH mass and the jet mechanical energy are typically connected in an AGN. A radio AGN tends to be more radio loud and is associated with more energy as the black hole becomes more massive (Best et al. 2005). However, these two quantities are not expected to show any correlation for radio sources associated with other astrophysical phenomenon. We estimate the black hole mass, M_{BH}, using the following relation (McConnell & Ma 2013; Cheung et al. 2016):

$$\log_{10} (M_{BH}/M_{\odot}) = 8.32 + 5.64 \log_{10}[\sigma_{\star}/(200 \text{ kms}^{-1})] \tag{3.5}$$

where $\sigma_{\star}$ is the velocity dispersion of the stars, extracted from the central 2″ radius aperture. Fig. 3.10 shows the the jet mechanical energy vs. SMBH mass in the radio detected red geysers, color coded by their respective morphological class. We find that they are moderately correlated. We fit the data points with a linear function using

least square optimization technique and find a relation in the form: $\log_{10}$ (E_{mech}) = [$\log_{10}$ (M_{BH})]$^{0.39}$ + 38.925, with a Spearman's correlation coefficient (r-value) of 0.4. This positive trend implies that the central AGN, with possibly unresolved small-scale radio jets, is driving the radio emission seen in these galaxies.

In order to estimate the possible contribution of this jet energy to the quenching of star formation, Fig. 3.11 shows the radio luminosity at 150 MHz vs specific star formation rate (sSFR) for the LOFAR detected sources, color coded by their morphological classification. Similar to Fig. 3.8, the unresolved sources are also indicated as "compact". We find that the radio sources which are non-compact and belongs to either one of extended, irregular, double or triple class, have much lower sSFR with average $\log_{10}$ sSFR = -13 yr^{-1}, compared to the compact sources with average $\log_{10}$ sSFR = -11.75 yr^{-1}. This implies that the radio sources showing more extended radio morphology are either more effective in quenching or reside in a larger halo with greater stellar mass, bringing the total sSFR down by several factors. A weak negative correlation is also visible between radio luminosity and sSFR, although this apparent trend can be due to the low sample size and driven predominantly by a few large and extended radio sources which are generally more radio-loud on average. This seems to be the case here since the three sources under the "triple" category and one "irregular" source, which are solely responsible for driving the negative trend, have radio luminosity (L_{150MHz}) at least an order of magnitude more than the average luminosity of the rest of the sources.

3.6.2 Spatially resolved properties

In addition to the integrated properties discussed above, we now compare the spatially resolved ionized gas flux and kinematic maps with radio image morphology.

While every galaxy in the red geyser sample shows signatures of ionized gas outflows via extended bi-symmetric pattern in equivalent width map, there is a distinct lack of extended visible radio lobes on a similar scale in these galaxies as observed from a combination of LoTSS, FIRST and VLASS survey. As reported in §3.5.1, 14 out of 28 ($\sim$ 50%) sources showing resolved radio emission in LOFAR observations display a compact radio morphology. Although similar radio-quiet compact sources hosting radio AGN have been observed to host small-scale ($\sim$ 1 kpc) radio jets in higher spatial resolution ($< 1''$) radio observations in previous studies (Jarvis et al. 2019, 2021; Venturi et al. 2021; Panessa et al. 2019; Baldi et al. 2018; Webster et al. 2021), the presence of resolved radio jets in the red geyser sample is observed to be quite rare with the current $5''$ resolution.

For the red geysers belonging to the "compact" or "extended" class, the spatial correlation between ionized wind cone and the radio jets is difficult to infer. However, the sources belonging to the "double" or "triple" category provide the most insight. In two out of three red geysers belonging to the "triple" class (MaNGAID: 1-378770 and 1-595166), the radio lobes align perpendicular to the direction of the ionized wind cone. On the other hand, for the rest of the sources which are resolved but not "compact" (four "double", one "triple" and two "irregular"), the elongation axis in the radio images

roughly aligns with the direction of the ionized wind cone.

We choose five prototypical galaxies representing the compact, irregular, double and triple morphological class to explore the detailed ionized gas-radio interaction using spatially resolved maps.

MaNGAID: 1-245451 in Fig. 3.12 shows an example of a radio detected red geyser belonging to the "compact" radio morphology class. The three columns in the figure correspond to SDSS optical image (first row), Hα-EW (second row) and velocity dispersion (third row) extracted from the Hα emission line. The LOFAR radio contours (in green) are over-plotted on top of each map. The on-sky diameter of the MaNGA fiber bundles (overplotted in magenta hexagon in the optical image) generally ranges between $17''$ - $32''$, corresponding to a physical size of $10 - 30$ kpc at median redshift of MaNGA observations ($z \sim 0.03$). The bi-symmetric pattern in the Hα EW map traces the ionized wind cone. The absence of structures in the radio image makes it hard to associate the radio properties with any specific ionized features. However, we note very high gas dispersion within the inner radio contours detected with $> 20\sigma$, indicating extreme ionized outflow kinematics there.

For the red geyser with MaNGA ID $-$ 1-188530 (belonging to the "irregular" morphology class), the LOFAR image has an unusual extended morphology spanning a distance of ~ 30 kpc, with a central radio core and a plateau of diffuse emission. Interestingly, the radio structure is spatially extended in the direction of the Hα enhancement in the EW map, similar to the other sources in the "irregular" class. Additionally, we note that the galaxy shows an elongated region of enhanced line width (> 200 km s^{-1}),

spanning about >7 kpc.

In red geyser with MaNGA ID: 1-23958, the radio image show a one-sided low surface brightness bubble, detached from the central bright core. Similar to the previous example, the direction of the radio bubble roughly aligns with the bi-symmetric pattern in the Hα emission line map. This is the case for all sources classified as "double".

Finally, as already mentioned, double-lobes and distinct jets are observed to be quite rare in the red geyser sample using the current $\sim 5''$ resolution of the radio images. Out of the three sources classified in the "triple" morphological category, two of them (Fig. 3.12, MaNGA ID: 1-378770 and 1-595166) have radio jets lying perpendicular to the ionized gas traced by the Hα EW map (Fig. 3.13). This is unlike what is observed in the above cases. The gas velocity dispersion is enhanced perpendicular to the Hα bi-symmetric feature in 1-378770, but is aligned in 1-595166. The implications of these findings are discussed in more detail in §3.7.

3.7 Discussion

We have presented 150 MHz, 1.4 GHz and 3 GHz radio imaging from the LoTSS, FIRST and VLASS surveys, together with spatially resolved optical spectroscopy from the SDSS IV- MaNGA survey, for 42 radio detected red geyser sub-sample out of the total 140 $z < 0.1$ red geyser galaxies. 103 out of those 140 galaxies have available LOFAR imaging data with 34 of them ($\sim 33\%$) being radio-detected. 29 out of 140 ($\sim 21\%$) galaxies are detected in FIRST and 29 are detected in VLASS. There are 21

sources ($\sim 15\%$) which have simultaneous radio detection from all three surveys and 42 sources which are detected in at least one of them. The radio properties are summarized in table 3.1.

The FIRST detection rate is roughly in agreement with our previous work (Roy et al. 2018) which established that the red geysers, that show signatures of kpc-scale winds in warm ionized gas tracers, have a higher incidence of radio continuum emission than typical early type galaxies without such signatures. Thus, Hα, one of the primary tracers of putative ionized winds in the red geysers, was seen to be associated with increased radio emission. Indeed, even within the red geyser sample, we have shown in Fig. 3.2 (upper right) that a radio-detection indicates a greater amount of ionized gas. The mean of the distribution of luminosity of Hα ($L_{H\alpha}$) in radio detected red geyser sample is $10^{40.5}$ erg s^{-1}, about four-five times higher than the non-radio detected sample.

39 out of 42 radio-detected galaxies in our sample are classified as being 'radio-quiet' based on standard criteria of Xu et al. (1999) (Fig. 3.3), while 38 out of 42 sources are radio-quiet from R parameter value (Ivezić et al. 2002). R values in the three radio loud cases are fairly moderate, with R<1.5, compared to the typical R value of 2.8 for radio-loud sources from Ivezić et al. (2002). Thus, the red geyser galaxies are largely low-luminosity sources and belongs to the "radio-quiet" group of objects (see Kellermann et al. 1989; Morganti 2021, for detailed discussions).

3.7.1 Origin of the detected radio emission

Although the radio emission in "radio-quiet" sources is often attributed to being dominated by star formation processes, red geyser targets have very little star formation activity (log SFR $< 10^{-2} M_{\odot}$ yr^{-1} Roy et al. 2021a, and Fig. 3.2). §3.4 shows the quiescent nature of these galaxies via WISE infra red colors, confirms complete lack of star formation and presence of old stellar population through the 'D4000 vs. $L_{rad}/M_{\star}$' method and show the lack of ionization from young stars via the BPT diagram. Indeed, in Cheung et al. (2016), the central radio continuum emission in the prototypical red geyser was from a low-luminosity radio AGN ($L_{1.4GHz} \sim 10^{21}$ W Hz^{-1}) with low Eddington ratio ($\lambda \sim 10^{-4}$). Roy et al. (2018) showed that the expected SFR ($\sim$ 1 $M_{\odot}$ yr^{-1}) derived from the average radio luminosity from the red geysers sample exceeds the observed SFR, derived from ultra-violet to infrared SED fitting, by two to three orders of magnitude. If we perform a similar calculation on our current sample of 29 FIRST-detected sources, we obtain an average radio luminosity $L_{1.4GHz} \sim 5 \times 10^{22}$ W Hz^{-1} (Fig. 3.7). From the best-fit relation between 1.4 GHz radio continuum luminosity and the Balmer decrement corrected Hα (Brown et al. 2017), we obtain a corresponding Hα luminosity $\sim 2.5 \times 10^{42}$ erg s^{-1}. Using the known relation between SFR and Hα luminosity (Kennicutt et al. 2009; Brown et al. 2017) assuming a Kroupa initial mass function (IMF) (Kroupa & Weidner 2003), we obtain an expected star formation rate exceeding $5 - 10$ $M_{\odot}$ yr^{-1}, which is not observed in our galaxy sample. This is further confirmed by Fig. 3.4 (panel d) which shows that our objects lie above

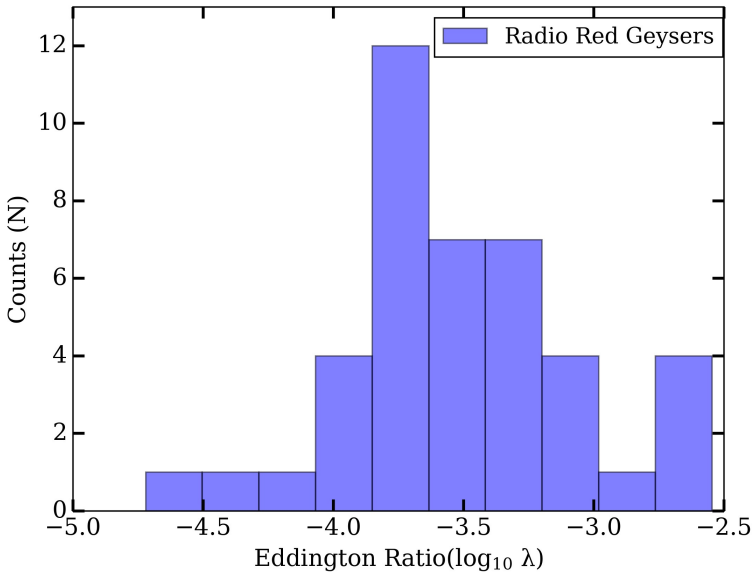

Figure 3.14: The distribution of Eddington ratios for the 42 radio detected red geysers. The Eddington scaled accretion rate (λ) values are $< 10^{-3}$ for the majority of the sources, implying that the red geysers are in general radiatively inefficient.

the low frequency radio luminosity - star formation rate relation from Gürkan et al. (2018). This implies that the observed radio luminosity can not be explained by the detected very low amount of star formation and is consistent with radio emission from central radio AGN.

Another widely discussed source of the radio emission in radio-quiet sources is radiatively-driven accretion disc winds which result in synchrotron emitting shocks through the inter-stellar medium (Zakamska & Greene 2014; Nims et al. 2015; Zakamska et al. 2016). However, these are generally associated with quasars with bolometric luminosity $L_{AGN} \sim 10^{45}$ erg s^{-1} where outflow velocities of $\sim$ 1000 km s^{-1} interact with the ISM and can produce radio luminosities similar to our sources ($L_{1.4GHz} \sim$

$10^{22} - 10^{23}$ W Hz^{-1}). However, the red geysers show typical gas velocities $\sim$ 300 km s^{-1} (Fig. 3.1) with no signature of quasar-like broad emission lines. A rough estimation of bolometric radiative luminosity from the [OIII] λ 5007 Å emission line flux (within the central 2″ radius aperture), using the relation $L_{rad} = 3500 L_{[OIII]}$ (Heckman et al. 2004), yields $L_{rad} \sim 10^{43}$ erg s^{-1}. We calculate the classical eddington limit with $L_{Edd} = 3.3 \times 10^4$ M_{BH}, where M_{BH} has been calculated in §3.6.1 (Eq. 3.5). Inserting the jet mechanical energy E_{mech}(Eq. 3.4), radiative luminosity L_{rad} and eddington luminosity L_{Edd}, we calculate the eddington radio $\lambda = (E_{mech} + L_{rad})/L_{Edd}$. Fig. 3.14 shows the distribution of Eddington ratios for the radio red geysers, which spans primarily between $\sim 10^{-4} - 10^{-3}$. These fairly low eddington ratios implies that these are radiatively inefficient sources that cannot be formed due to radiative accretion disk winds.

Low-luminosity jets from radio-quiet AGN are the most plausible explanation for the observed low power radio emission in our red geyser targets. Sufficiently deep and high resolution radio observations have been able to identify small-scale radio jets in several "radio-quiet" quasars and Seyfert galaxies (Gallimore et al. 2006; Baldi et al. 2018; Jarvis et al. 2019, 2021; Venturi et al. 2021). Our sample of radio-quiet red geysers have many properties in common with jetted compact radio galaxies similar to those in Kimball et al. (2011); Baldi et al. (2018); Jarvis et al. (2019).

3.7.2 Radio red geysers in the context of other radio-quiet sources in the literature

At the frequencies of interest in this work, the radio continuum emission is dominated by non-thermal synchrotron emission. In the absence of a constant energy injection source, the replenishment of fresh electrons ceases and the radio spectrum is dominated by radiative loss. Since the energy loss rate is directly proportional to the frequency, the energy loss rate at lower frequencies ($\leq$ 1.4GHz) is lower which enables the original injection index of the electrons to be retained for much longer. Thus, the lower frequency emission generally is more extended, characterizing emission from older plasma where injection took place longer ago. Additionally, LOFAR is more sensitive to extended emission than the FIRST and VLASS surveys. This is consistent with our findings (Fig. 3.6) which shows that the LOFAR measured sizes are roughly two-three times more spatially extended than the FIRST and VLASS images, sometimes revealing intriguing structures not visible in higher frequency images.

We observe a range of radio morphologies from LOFAR observations in our red geyser targets. From Table 3.1, we see that 16 out of 42 radio-detected sources exhibit resolved but compact morphology, with the spatial extent ranging between 3$-$7 kpc in 150 MHz frequency band. They can be represented by a two dimensional gaussian with no particular feature in their radio images. On the other hand, 16 other sources show extended features ($\geq$ 9 kpc), with contiguous one-sided morphology, bubbles and double-lobes (belonging to "extended", "irregular", "double" and "triple" morphology

class). The remaining ten sources are unresolved in the typical resolution of LOFAR and FIRST. Thus, $\sim 38\%$ of the radio-detected sources show spatially extended features extending to scales of more than ten kpc. This is consistent with the results of Pierce et al. (2020), who have studied similar moderate luminosity radio AGN population, although with a greater radio luminosity range ($22.5 < L_{1.4GHz} < 25.$) than the red geysers. However, among those 38%, the seven galaxies classified as "extended" also do not show any resolved radio jets although they show elongation in a specific direction, indicating some underlying radio structures remaining unresolved at the current spatial resolution.

To quantitatively compare the radio morphologies of our sample to the traditional radio AGN population, we investigate the radio size versus radio luminosity plane for the red geysers compared to the literature compilation of radio selected AGN from An & Baan (2012); Gallimore et al. (2006); Kukula et al. (1998); Mingo et al. (2019); Jarvis et al. (2019) in Fig. 3.7. In terms of linear size, most of the red geyser sources are similar to the compact steep spectrum sources (spanning $\sim 1-25$ kpc in 1.4 GHz radio image) with a few showing even more compact structures with no structures resolvable beyond the nuclear component, similar to the gigahertz peaked spectrum sources (typically < 1 kpc, O'Dea 1998). However, unlike the red geysers, the CSS and GPS sources are powerful radio-loud AGN ($L_{1.4GHz} > 10^{25}$ W Hz^{-1}). Hence, our sources would be excluded from these samples due to a much lower radio-luminosity. The red geysers are more aligned with the "radio-quiet quasars" from Jarvis et al. (2019) and also from the LINER and Seyfert radio sources from the LeMMINGs survey (Baldi et al. 2018, 2021)

according to the radio luminosity- size diagram. A few are consistent with the lowest luminosity AGN in the sample of Gallimore et al. (2006).

As noted by Jarvis et al. (2019, 2021), objects in the radio-quiet quasar (RQQ) category possess small-scale jets when observed in higher resolution (sub-arcsec scale) VLA and e-MERLIN images, but exhibit compact or slightly extended kpc-scale structures when observed in low spatial resolution ($> 3''$). They have similar radio morphology, spectral index and radio size as the red geysers. Considering the stark similarities of the radio properties of the red geyser sources with the RQQ sample, it seems plausible that our sources also possess small-scale jets which are blurred in the current resolution. These could resemble 'frustrated' jets, which are small and contained within the inner 1 kpc central region of the galaxy, occurring due to the surrounding dense environments that doesn't enable the jet to grow to a large size (van Breugel et al. 1984). Two of our targets overlap with the Fanaroff-Riley class I (FRI; Fanaroff & Riley 1974) galaxies in the luminosity–size plane but the majority of our targets do not fit within the traditional FRI and FRII radio classifications. Due to the abundance of compact and featureless radio morphology in our red geyser galaxies, these sources can also be classified as 'FR0' galaxies (e.g. Baldi et al. 2015; Capetti et al. 2020). However, higher spatial resolution data may reveal more complex morphologies, jets, hot-spots on smaller scales (see discussion in Hardcastle & Croston 2020).

3.7.3 Interaction between radio and ionized gas

We have previously identified kpc-scale outflows in ionized gas in the red geyser galaxies (Cheung et al. 2016; Roy et al. 2021a), which are marked by the bi-symmetric extended pattern in the Hα EW map (Fig 3.1). Our study of red geysers complements several other studies that have aimed to characterize the drivers of ionised outflows by investigating the radio properties of the central radio AGN. For example, there are many spatially-resolved studies of multiphase gas outflows driven by local galaxies hosting low power AGN (Mingozzi et al. 2019; Wylezalek et al. 2020; Venturi et al. 2021). Specifically, Capetti et al. (2019, 2020) have studied FR0 galaxies showing similar compact radio structures detected with LOFAR observations and their effect on the galaxy environments, while Webster et al. (2021) has discovered galaxy scale jets and their interaction with the interstellar medium of the host galaxy. There have been numerous studies at high redshift as well, but they primarily focus on powerful radio galaxies and luminous AGN (Nesvadba et al. 2017; Circosta et al. 2018; Perna et al. 2015; Zakamska et al. 2016) where the impact of quasars are dominant (Hopkins et al. 2007). The faint radio emission from radio-quiet AGN are difficult to detect, although a growing number of studies are being done in recent times to study the interaction between the radio emission from the AGN and the ionized gas outflows (Al Yazeedi et al. 2021). However, high signal-to-noise and high spatial resolution radio data (e.g., Jarvis et al. 2019; Venturi et al. 2018) are required to resolve the small-scale radio jets and morphologies to establish further connection with the ionized outflows.

Fig. 3.9 aims to establish the connection between ionized gas and radio emission in the red geysers via integrated Hα luminosity with radio sizes. We show that our results are consistent with Jarvis et al. (2021) studying similar radio-quiet ($L_{150MHz} < 10^{24}$ W Hz^{-1}) compact (generally < 10 kpc) AGN sources from the "Quasar-feedback survey", which states that ionized gas tracers are correlated with the central radio AGN. Additionally, radio detected red geysers not classified as "compact", possessing large radio sizes, are shown to have relatively lower sSFR ($\log_{10}$ sSFR ~ -13.0 yr^{-1}) than the compact ones (Fig. 3.11). Assuming these compact objects have similar star formation history as the extended, lobed & irregular ones, large radio sources having lower SFR for a given stellar mass might be implying more efficient quenching due to the presence of jets than the compact ones. The other possibility is that the extended radio sources are generally found in more massive and evolved sources with higher stellar mass, perhaps even massive central galaxies in large halos. Extended or "lobed" radio sources may be the evolved form of compact "FR0" galaxies in such environments. This idea is consistent with the theory that compact FR0 radio galaxies are younger and will eventually evolve to form the traditional FRI or FRII galaxies (O'Dea 1998). Thus the range of radio morphologies observed in the red geysers could represent the various stages of transition of FR0 class of objects to the traditional FRI/ FRII sources.

Fig. 3.12 and 3.13 compare the spatially resolved equivalent width and kinematics of ionized gas, traced by Hα, compared to the distribution of radio emission for five example red geysers belonging to different radio morphological class. We find that for the galaxies in the "irregular" and "double" class, elongation along a specific

direction or presence of one-sided bubbles in the radio emission (MaNGAID: 1-188530 and 1-23958, Fig. 3.12) roughly aligns with the ionized gas features, marked by high gas dispersion. Such observations indicate that the large scale ionized outflows, stretching to > 10 kpc, are possibly driven by small scale radio jets, unresolved at the current LOFAR resolution. Often in these cases, the velocity dispersion map is clumpy and shows high values in distinct parts of the galaxy, and also in some cases, perpendicular to the bi-symmetric Hα feature. This is similar to the observation by Venturi et al. (2021) who found that increased line widths were perpendicular to small-scale radio jets. They interpreted this to be due to the low-power jet strongly interacting with the ISM in the galaxy, releasing energy and giving rise to highly turbulent motions in the perpendicular direction. Similar characteristics have been seen in a few other local seyfert galaxies as well (see Riffel et al. 2014, 2015; Lena et al. 2015; Freitas et al. 2018).

However, among the three rare cases (classified as "triple") where we detect clear evidence of large scale radio jets and lobes, particularly notable are the galaxies with MaNGAID: 1-378770 and 1-595166 where we find that the radio jets, shown by LOFAR radio contours, and ionized wind, traced by the Hα emission map, lie perpendicular to each other (Fig. 3.13).

There can be several possible explanations for the perpendicular incidence of the radio jet and ionized broad angled wind.

- Changing orientation of the magnetic field, as proposed by Mehdipour & Costantini (2019).

- The formation of an expanding cocoon structure described in simulations of jet-driven feedback (Begelman et al. 1984).
- A precessing accretion disk due to a misalignment between the orientation of the disk and the spin of the black hole (Riffel et al. 2019).
- Radiation driven midplane wind (Proga & Kallman 2004).

In a sample of 16 radio loud Seyfert-1 AGN galaxies, Mehdipour & Costantini (2019) showed an inverse correlation between the column density of the ionized wind and the radio loudness parameter (R) of the jet observed mis-aligned with the wind. They argued that this indicates a wind-jet bimodality in radio loud AGNs with the AGN alternating between powering a radio jet and an un-collimated broad wind. They proposed that the magnetic field is the primary driving mechanism for the observed accretion-disk wind and the change in the magnetic field configuration from toroidal to poloidal cause this switch. This bi-modality can explain the low incidence of radio jets and high prevalence of ionized wind in the red geyser sample along with a 90° mis-alignment between the jet and the wind. However, if the magnetic driving mechanism can work equally efficiently on low power radio-quiet AGNs is still open to questioning.

Wagner & Bicknell (2011), Wagner et al. (2012), Mukherjee et al. (2016) and Mukherjee et al. (2018) have studied the interaction between radio-jet and multi phase ISM using detailed 3D hydro-dynamical simulations. They find that when a radio jet propagates through an inhomogenous ISM, they not only impact the ISM along the radio-jet axis but also create a spherical bubble which drives gas clouds outwards in all

directions. This leads to outflowing gas traveling at a modest speed mostly in the path of least resistance. Although this mechanism can not lead to extreme velocity outflows escaping the galaxy altogether, it can impart enough energy and turbulence to heat the gas and sufficiently inhibit star formation. Since we observe similar modest outflowing gas velocities ($\sim$ 300 km s^{-1}) accompanied by turbulent high velocity dispersions (exceeding $\sim$ 220 km s^{-1}) in specific regions of the galaxy in red geysers with very little star formation activity, this phenomenon might be the primary mechanism to explain the perpendicularity between radio jets and winds observed in the two red geysers.

A third possibility is due to the precession in the accretion disk, as proposed by Riffel et al. (2019). They suggested that if there is a misalignment between the orientation of the accretion disk and the spin of the black hole, it can create a torque leading to a constant precession. This mechanism, in turn, can lead to a small scale jet, contained within the central part near the nucleus to be mis-aligned with the large scale ionized wind observed in MaNGA. Riffel et al. (2019) has successfully implemented this model to the prototypical red geyser to explain the misalignment observed between the direction of the ionized wind in small ($1 - 2$kpc) and large (> 10 kpc) scale spatially resolved Hα map. A similar procedure can possibly explain the large scale radio jet and ionized wind mis-alignment, although further work is needed to confirm whether the small-scale precession near the black hole can be implemented in a larger spatial scale > 20 kpc.

The final proposed mechanism exploring the radiation driven mid-plane disk wind has been proposed by Proga & Kallman (2004). However, as discussed in §3.7.1,

the red geysers do not seem to harbor radiatively-driven accretion disk winds owing to low eddington ratios between $10^{-4} - 10^{-3}$ and absence of extreme outflow velocities of ~ 1000 km s^{-1}.

Finally, while there is a body of evidence that supports the interpretation of red geyser kinematics as the result of outflowing winds, this interpretation may be wrong in some cases. It is tempting to associate the perpendicular orientation of the major kinematic axis with a diffuse accretion disk, giving rise to extended, bipolar radio jets. While difficult to rule out, this explanation is unlikely because it implies that a black hole accretion disk on sub-parcsec scales would remain aligned to a galaxy-scale gaseous disk on kpc scales. In simulations and observations, such an alignment is extremely rare.

3.8 Conclusion

We have studied the 150 MHz, 1.4 GHz and 3 GHz radio images from LoTSS, FIRST and VLASS surveys ($6'', 5''$and $2.5''$ resolution respectively) along with integral field spectroscopic observations of a sample of red geyser galaxies. Red geysers are low redshift (z<0.1) passive early-type galaxies that host ionized gas outflows on scales of $\sim$10 kpc (Cheung et al. 2016; Roy et al. 2021a). The parent sample of 140 red geysers are selected from SDSS IV-MaNGA MPL-9 data. 42 out of the total 140 red geysers are detected in at least one of the three radio surveys while 21 sources are detected in all three surveys. We present the radio characteristics, morphology, size of the radio-

detected red geysers and explore the connection of the radio emission with ionized gas. Our main conclusions are:

- Only 3-4 of the 42 radio detected red geysers are radio-loud according to two traditional criteria (Xu et al. 1999; Kellermann et al. 1989). Red geysers are largely low luminosity sources and are classified as "radio-quiet" objects.

- Although these are radio-quiet, the source of the detected radio emission is the central radio AGN and not star formation. We use a series of four diagnostic diagrams (see Fig. 3.4) to show the absence of sufficient star formation to explain the observed radio luminosity. The association with the central radio AGN is confirmed by Fig. 3.10 which shows a moderately tight correlation of the jet mechanical energy derived from radio luminosity with the SMBH mass.

- 16 out of 42 sources show extended radio structures with a diverse range of morphologies, with radio sizes spanning a large range 9 kpc $<$ size $<$ 200 kpc. Two sources are classified as "FRI" sources. The remaining 26 sources are either unresolved or exhibit resolved but compact structure with size $<$ 9 kpc. The compact sources have no particular feature in their radio image.

- Based on their radio luminosity-size relationship, spectral index and the observed radio morphology, these galaxies are consistent with "radio-quiet" quasars (Jarvis et al. 2019), low power compact radio galaxies called the "FR0" sources (Baldi et al. 2015; Capetti et al. 2020) and the radio emitting LINERs and Seyfert class (Gallimore et al. 2006; Baldi et al. 2021). Higher resolution ($< 1''$) radio images

are required to detect small scale "frustrated" radio jets within these compact sources, if there are any.

- We show that there are indications of interaction between the radio structures and the ionized gas (traced by Hα). Specifically, Hα luminous sources tend to have more extended radio emission, in general (Fig. 3.9).

- We find evidence that compact radio red geysers show a higher specific star formation rate on average than those possessing large extended radio structures (Fig. 3.10). This could mean larger radio sources with visible lobes and jets are more efficient in quenching than the compact ones and thus having less SFR. This could also mean that the extended radio sources are generally found in more massive and evolved sources with higher stellar mass, causing them to have the lowest sSFR. The later possibility could imply that the compact 'FR0' galaxies would eventually evolve to transition towards jetted FRI/FRII sources. Thus, the range of radio morphologies observed in the red geysers represent the various stages of this transition.

- From spatially resolved maps, the ionized gas and the radio structures are mostly co-spatial with distinct kinematic components. However, in two out of the three objects where we detected large scale radio lobes, the ionized wind and the radio lobes are perpendicular to each other. These can arise from the jet-ISM interaction via different mechanisms (see §3.7).

In this work we provide evidence that the compact radio structures are a

common characteristic feature of red geyser galaxies. In order to test the presence of small scale radio jets within the compact morphology and to study the detailed radio jet-ISM interaction, further higher-resolution (sub-arcsecond) radio imaging from VLA and upcoming more sensitive and powerful radio and optical telescopes like Next Generation Very Large Array (ngVLA), Square Kilometer Array (SKA) and Vera C. Rubin Observatory will be essential.

Chapter 4

Evidence of Wind Signatures in the Gas Velocity Profiles of Red Geysers

Red geysers host low luminosity radio active galactic nuclei and are characterized by narrow extended bisymmetric patterns in ionized gas extending across the whole galaxy. This emission features possibly trace large scale AGN-driven winds. Given their potential importance in maintaining low level of star formation at late times, additional evidence confirming that winds are responsible for the red geyser wind phenomenon is critical. In this work, we present follow-up observations with the Echellette Spectrograph and Imager (ESI) at the Keck telescope of two red geysers (z<0.1) using multiple long slit positions to sample different regions of each galaxy. Our ESI data with a spectral resolution (R) $\sim$ 8000 improves upon MaNGA's resolution by a factor of four, allowing us to resolve the ionized gas velocity profiles along the putative wind cone with an instrumental resolution of σ = 16kms^{-1}. The line profiles of Hα and [NII]λ6584

show asymmetric shapes that depend systematically on location − extended blue wings on the red-shifted side of the galaxy and red wings on the opposite side. We construct a simple wind model and show that our results are consistent with geometric projections through an outflowing conical wind oriented at an angle towards the line of sight. An alternative hypothesis that assigns the asymmetric pattern to "beam-smearing" of a rotating, ionized gas disk does a poor job matching the line asymmetry profiles. While our study features just two sources, it lends further support to the notion that red geysers are the result of galaxy-scale winds. [1]

4.1 Introduction

"Maintenance" or "radio" mode feedback resulting from low to moderate luminosity active galactic nuclei (AGN) has been proposed as a means for maintaining low levels of star formation (log SFR < -2 $M_\odot$ yr^{-1}) at late times, thereby explaining the massive increase in the number of red galaxies since $z \sim 2$ (Croton et al. 2006; Bell et al. 2004; Bundy et al. 2006; Faber et al. 2007; Ilbert et al. 2010; Moustakas et al. 2013). These radio AGNs are thought to be radiatively inefficient, accreting at low rates and depositing most of their energy to the surroundings via momentum driven winds or radio jets (Binney & Tabor 1995; Ciotti & Ostriker 2001; Croton et al. 2006; Bower et al. 2006; Ciotti & Ostriker 2007; Ciotti et al. 2010; McNamara & Nulsen 2007; Cattaneo et al. 2009; Fabian 2012; Yuan & Narayan 2014; Heckman & Best 2014). This

[1] This chapter was previously published in the Astrophysical Journal as **Evidence of wind signatures in the gas velocity profiles of Red geysers**, Roy, N., Bundy, K., Nevin. R., et al. 2021, ApJ, 913, 33, DOI:10.3847/1538-4357/abf1e6. ©AAS. Reproduced with Permission.

input energy heats ambient gas that might otherwise cool and form stars, thus maintaining quenched galaxies in a passive state. Although evidence for radio mode AGN feedback has been observed in the form of large bubbles of ionized gas and radio jets in the centers of massive clusters and giant radio galaxies (Cattaneo et al. 2009; Dunn & Fabian 2006; Fabian 1994, 2012; Fabian et al. 2006; McNamara & Nulsen 2007), it has been difficult to find evidence for this mechanism operating in lower mass halos that host typical quiescent galaxies (halo mass $< 10^{12}$ $M_{\odot}$).

We have been studying a population of moderate mass ($\log M_{\star}/M_{\odot} \sim 10.5$) red quiescent galaxies ($NUV - r > 5$), known as "red geysers" (Cheung et al. 2016; Roy et al. 2018) that may hold clues in this regard. Identified in low redshift integral field spectroscopy from the Sloan Digital Sky Survey-IV (SDSS-IV) Mapping Nearby Galaxies at Apache Point Observatory (MaNGA) survey (Bundy et al. 2015), these galaxies are characterized by bisymmetric equivalent width (EW) maps of strong emission lines like Hα, [NII]$\lambda\lambda$6548,84 and [OIII]$\lambda\lambda$4959,5007 which appear to be tracing large scale ionized gas outflows. This distinctive emission pattern roughly aligns with the gas kinematic axis but is strongly misaligned with the stellar velocity gradient. The gas velocity values reach $\sim$300 km s^{-1} compared to less than 40 km s^{-1} in the stars. These galaxies lack star formation with average $\log$ SFR [$M_{\odot}$/yr] < -2 (using GALEX+SDSS+WISE, Salim et al. 2016). They additionally show a high value of the 4000-Å break index (D4000) with an average value > 2.0, thus providing further evidence that young stars are absent in the galaxy. Spatially resolved Baldwin-Phillips-Terlevich diagrams (BPT, Baldwin et al. 1981) indicate wide-spread ionization with line ratios consistent with a

combination of LINERs (Low Ionization Nuclear Emission Region) and Seyfert values. The morphology of these galaxies are spheroidal with a high sersic index (n $\geq$ 3).

Although the observed characteristics of the red geysers can be explained by a centrally driven wind, early type galaxies with accreted gas disks (Chen et al. 2016; Sarzi et al. 2006; Davis et al. 2013; Bryant et al. 2019; Lagos et al. 2014, 2015; Starkenburg et al. 2019; Duckworth et al. 2020) can also show similar kinematic misalignment and emission features due to rotation of the gaseous material in the disk. However, 95% of the red geyser sample are fast rotator early-type galaxies from the Graham et al. (2018) catalog (Roy et al. 2018) and it is considerably difficult for a gas disk to be in equilibrium if it is misaligned with the stellar kinematic axis because of the axisymmetric nature of the fast rotators (although see van de Voort et al. 2015; Davis & Bureau 2016). The red geysers are also selected to have axis ratio b/a $>$ 0.4 (Roy et al. 2018) with no visible dust lanes, as seen from SDSS imaging, in order to exclude any edge-on disks in the sample. A disturbed disk with a chaotic accretion scenario is still possible and further investigation is therefore needed to confirm otherwise.

In Roy et al. (2018) we reported evidence for the presence of faint radio AGNs in the red geyser galaxies. Stacked 1.4 GHz radio flux from very large array (VLA) Faint Images of the Radio Sky at Twenty-Centimeters (FIRST) survey shows significantly ($> 5\sigma$) higher radio flux in red geysers than a matched control sample. Red geysers also show a three times higher radio detection rate than the control. Roy et al. (2018) shows that this radio emission indicates low-luminosity radio AGNs ($L_{1.4GHz} \sim 10^{22} - 10^{23}$ W/Hz) with radiatively inefficient accretion (Eddington scaled

accretion rate $\lambda \sim 10^{-4}$). Recently Duckworth et al. (2020) has indicated a tentative correlation between enhanced AGN activity and misaligned gas disks in low mass galaxies (log M < 10.2 $M_{\odot}$) using IllustrisTNG simulations. However no such trend has been found in high mass quenched population having similar mass as the red geyser sample. Hence the enhancement in radio-AGN activity seen in the red geysers cannot be immediately attributed to the phenomena of misaligned gas disks. Riffel et al. (2019) studied the launching of these proposed winds with Gemini GMOS (Gemini Multi Object Spectrograph) observations of the prototypical red geyser in Cheung et al. (2016) to constrain the gas kinematics in the nuclear region. They observed the emission line flux distributions and gas kinematics within the inner $1''$ to be distinct and misaligned from that of the outer regions, $5''$ away from center, a result that may indicate precession of the accretion disk.

Cheung et al. (2016) presented a variety of evidence including dynamical modeling and geometric arguments that lend support for an interpretation of red geysers as an AGN-driven wind phenomenon (see also Gomes et al. 2016). However, it is important to seek out additional lines of evidence to distinguish outflows from rotation. In this work, we examine further evidence for the wind interpretation through followup Keck spectroscopy of red geyser galaxies with higher spectral resolution (R$\sim$ 8000) than the original MaNGA data (R$\sim$ 2000). The improved resolution allows us to search for detailed kinematic signatures of outflowing winds which are blurred at MaNGA's instrumental resolution. We detect asymmetric emission lines that vary in a systematic manner along the kinematic major axis which likely indicate the specific geometry of

the wind along the line of sight. For the two red geysers (MaNGA ID: 1-217022 and 1-145922) studied here with the Keck Echellette Spectrograph and Imager (ESI) instrument, we find results consistent with our simple wind model. An alternative hypothesis that assigns the asymmetric pattern to "beam-smearing" of a rotating, ionized gas disk is not favored by our data.

Throughout this paper, we assume a flat cosmological model with $H_0 = 70$ km s^{-1} Mpc^{-1}, $\Omega_m = 0.30$, and $\Omega_\Lambda = 0.70$, and all magnitudes are given in the AB magnitude system.

4.2 Observation and Data acquisition

4.2.1 The MaNGA survey

We use observations from the SDSS-IV MaNGA survey (Bundy et al. 2015; Drory et al. 2015; Law et al. 2015; Yan et al. 2016; Albareti et al. 2017; Blanton et al. 2017). MaNGA is an integral field spectroscopic survey that provides spatially resolved spectroscopy for nearby galaxies (z $\sim$ 0.03) with an effective spatial resolution of 2.4″ (full width at half-maximum; FWHM). The MaNGA survey uses the SDSS 2.5 meter telescope in spectroscopic mode (Gunn et al. 2006) and the two dual-channel BOSS spectrographs (Smee et al. 2013) that provide continuous wavelength coverage from the near-UV to the near-IR: $3,600-10,000$ Å. The spectral resolution varies from R $\sim$ 1400 at 4000 Å to R $\sim$ 2600 at 9000 Å. An r-band signal-to-noise (SN) of $4-8$ Å^{-1} is achieved in the outskirts (i.e., $1-2$ R$_e$) of target galaxies with an integration time of

approximately 3-hr. MaNGA has observed roughly 10,000 galaxies with log $(M_*/M_\odot) \geq 9$ across $\sim$ 2700 deg^2 over its 6 yr duration. In order to balance radial coverge versus spatial resolution, MaNGA observes two thirds of its galaxy sample to $\sim$ 1.5 R_e and one third to 2.5 R_e. The MaNGA target selection is described in detail in Wake et al. (2017).

The raw data are processed with the MaNGA Data Reduction Pipeline (DRP, Law et al. 2016; Yan et al. 2016). An individual row-by-row algorithm is used to extract the fiber flux and derive inverse variance spectra from each exposure, which are then wavelength calibrated, flat-fielded and sky subtracted. We use the MaNGA sample and data products drawn from the MaNGA Product Launch-8 (MPL-8, Table 1 from Law et al. 2021). We use spectral measurements and other analyses carried out by version 2.3.0 of the MaNGA Data Analysis Pipeline (DAP). The data we use here are based on DAP analysis of each spaxel in the MaNGA datacubes. The final output from the DAP are gas and stellar kinematics, emission line properties and stellar absorption indices. All the spatially resolved 2D maps shown in the paper are outputs from the DAP. An overview of the DAP used for DR15 and its products is described by Westfall et al. (2019), and assessments of its emission-line fitting approach is described by Belfiore et al. (2019).

We use ancillary data drawn from the NASA-Sloan Atlas[2] (NSA) catalog which reanalyzes images and derives morphological parameters for local galaxies observed in Sloan Digital Sky Survey imaging (Blanton et al. 2011). It compiles spectroscopic

[2] http://www.nsatlas.org

redshifts, UV photometry (from GALEX; Martin et al. 2005), stellar masses (Blanton & Roweis 2007), and structural parameters.

4.2.2 Keck ESI data

ESI is a visible-wavelength, faint-object, imager and single-slit spectrograph in operation at the Cassegrain focus of the Keck II telescope since 1999. ESI has three modes of observations: echellete mode, low dispersion mode and direct imaging mode. The mode of operation used here is the echellette mode which provides cross-dispersed spectroscopy mode at a resolving power of up to R = 13,000. Slits are 20 arcseconds in length and are available with widths of 0.3, 0.5, 0.75, 1.0, 1.25 and 6.0 arcseconds with varying spatial scales and velocity resolution.The echellete mode disperses the light into ten orders with a dispersion ranging from $\sim$ 0.30 Å/pixel in order six (red) to $\sim$ 0.16 Å/pixel in order 15 (blue), while maintaining a roughly constant dispersion of 11.5 $\mathrm{kms}^{-1}\mathrm{pixel}^{-1}$ in velocity across all orders. The orders are curved due to the distortion within the prisms. ESI has a wide spectral coverage spanning from 0.39 to 1.1 micrometer in a single exposure and a velocity resolution as low as 22 km s^{-1} FWHM (using the 0.3 arcsec wide echellette slit). An Epps refracting camera and a single 2K×4K detector are used for all three modes.

Utilizing two half nights in February 2017, we followed up 2 red geysers from our MaNGA sample. These targets completely fill ESI's 20″ slit. We were able to observe both targets with multiple slit positions to map out different parts of the galaxy. For the first target galaxy with ID 1-217022, which is the prototypical red geyser "Akira"

from Cheung et al. (2016), we observed 3 slit positions while for the second target (ID 1-145922), we observed 2 slit positions. For each slit position, we integrated for 1.5−2 hours (in source and sky combined), nodding to sky positions every 5 minutes to enable quality sky subtraction. However, for the second slit for the second target, a combination of high clouds and a lower integration time resulted in an unacceptably low signal-to-noise spectra. Hence, we discarded that slit for our present analyses. We took measurements of the standard star G191b2b at the beginning of each night with the same instrumental setting with an exposure of three minutes to perform flux calibration. The width of the slit for all observations was $0.5''$ yielding a velocity resolution $\sim$ 37 km s^{-1} or R $\sim$ 8000. The median seeing FWHM over the course of the observations was $0.9''$. This should be compared to MaNGA's R $\sim$ 2000 spectral resolution and its effective spatial resolution of $2.4''$.

Fig. 4.1 and 4.2 show the slit positions for the two galaxies respectively, overlaid on their optical image (left panel) and on their MaNGA ionized gas velocity fields with Hα EW contours on top (right panel). In the first target, slit 1 was placed at an angle of 40° from North to East tracing the bi-symmetric emission feature. Slit 2 was placed at an angle of 110° from North to East to sample the central parts of the galaxy and intersect with slit 1 at the center. Slit 3 ran parallel to slit 1 at an offset of $\sim 4.9''$ in the South-East direction. In the second galaxy, the slit was placed at an angle of 320° from North to East along its biconical pattern.

We used routines from the ESIRedux package, developed by Jason X. Prochaska to aid in reducing the ESI data. This package was primarily built in IDL and is publicly

available [3]. Our primary goal is to extract spatially resolved spectra along the multiple slits of our targets, whose angular extent on the sky fills the slit ($\sim 20''$). This requires some steps in addition to the ESIRedux pipeline. The detailed description of the data reduction steps is given in the next section.

4.2.3 ESI data Reduction

We begin by using ESIRedux to perform bias subtraction, flat field correction and wavelength calibration. Several dome flats are taken at the beginning of each night with the same instrument setup as the target observations. In the first step, the routine identifies and combines the bias and flat frames separately to create a median bias and a median flat frame. The median bias is subtracted from the image. The bias subtracted image is then normalized by the median flat. The resulting image is then run through the wavelength calibration routine in the pipeline.

We utilize python routines to do the rest of the reduction steps. Since all the targets fill the $20''$ ESI slit, object detection and sky spectra extraction can't be performed with ESIRedux routines. Separate sky observations were taken near the target during observations roughly $\sim 50\%$ of the time, alternatively switching between the sky and the targets. Sky subtraction is done by directly subtracting the sky image from the science image taken closest in time. We also account for small telescope pointing offsets that may arise between different exposures by cross-correlating and shifting the spectra from different exposure frames with respect to each other in order to

[3] https://www2.keck.hawaii.edu/inst/esi/ESIRedux/

be aligned perfectly. A 3σ clipping routine is then applied to the sky subtracted science images to remove cosmic rays. Finally the individual exposures are added together to form a combined 2D image. Using the 2D wavelength solution obtained from wavelength calibration and the co-added 2D science image, we extract 1D spectra from each spatial pixel along the slit for each individual echellete order. Finally we stitch all ten echelette orders together to form a continuous spectrum over the entire wavelength range. To improve the signal-to-noise (SN) and ensure a minimum SN > 1 over the entire extent of the slit, the spectra are binned spatially with a binsize of $1''$.

The final step of the data reduction is flux calibration. Standard star (G191b2b) observations taken at the beginning of each night have been used to calibrate the spectra to first order. Flux Calibration corrects initially for two effects: the blaze effect caused by the instrument response of the echelle grating and the conversion from photon counts to flux density in physical units. Both effects are corrected using standard star observations by comparing the absolute flux of the standard star to the observed counts sampled at the same wavelength. However, the science spectra, which have been flux-calibrated in this manner, show a systematic difference in flux values with that of the MaNGA spectra by non-negligible amount. The possible reason behind this mismatch maybe inaccurate blaze function removal, non-photometric conditions or variations along the slit. Since we already possess MaNGA spectra for our targets, with flux calibration accuracy to a few % (Yan et al. 2016), we use the MaNGA spectra as a reference to correct for residual inaccuracies in the flux calibrated Keck spectra.

To perform this second step flux calibration, we obtain the sky positions of each

of the $1''$ Keck ESI spatial bins (hereafter, spaxels) on the target galaxy. We then find the MaNGA spaxels which overlap in sky position, yielding 1-1 spatial mapping between the MaNGA spaxels (of size $\sim 0.5''$) and ESI binned spaxels ($1''$). Next, for each ESI spaxel, we take the corresponding MaNGA spectrum (from the spatial mapping) and smooth it using a Gaussian filter. The smoothing uses a fairly large spectral window size while disregarding emission lines and other sharp spectral features. The smoothed MaNGA spectrum is then fit with a Chebyshev polynomial, the fit being given by the calibration vector, P_{MaNGA}. On the other hand, the corresponding ESI spectra is also smoothed by a gaussian filter, but using a window size almost 3 times as large, owing to the higher spectral resolution. The smoothed ESI spectrum is fit similarly with a Chebyshev polynomial which gives P_{ESI}. The final corrected flux calibrated ESI spectrum (ESI_{final}) is then obtained by scaling the original ESI spectrum ($\mathrm{ESI}_{original}$) by the formula:

$$ESI_{final} = ESI_{original}\frac{P_{MaNGA}}{P_{ESI}}$$

The above process is repeated for all spectra along each ESI slit. An example of a reduced ESI spectrum is shown in Fig. 4.3.

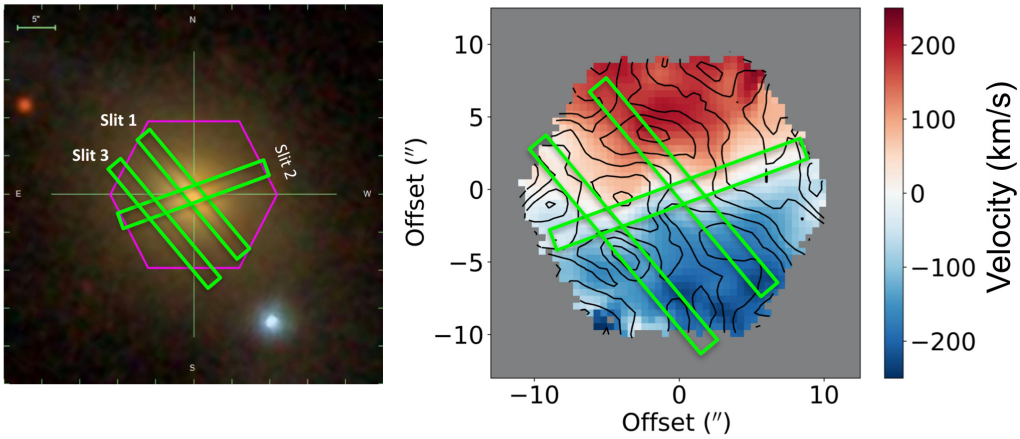

Figure 4.1: The Keck ESI slit positions for the first target galaxy (MaNGA-ID: 1-217022). The left and the right panels show the three slit positions overlaid on the SDSS optical image and the MaNGA ionized gas velocity map respectively. The black contours in the velocity map shows the Hα equivalent width (EW). Slit 1, placed at an angle of 40° from North to East, traces the bi-symmetric emission feature. Slit 2 is placed at an angle of 110° from North to East, sampling the central parts of the galaxy. Slit 3 is placed parallel to slit 1 with an offset of $\sim 4.9''$.

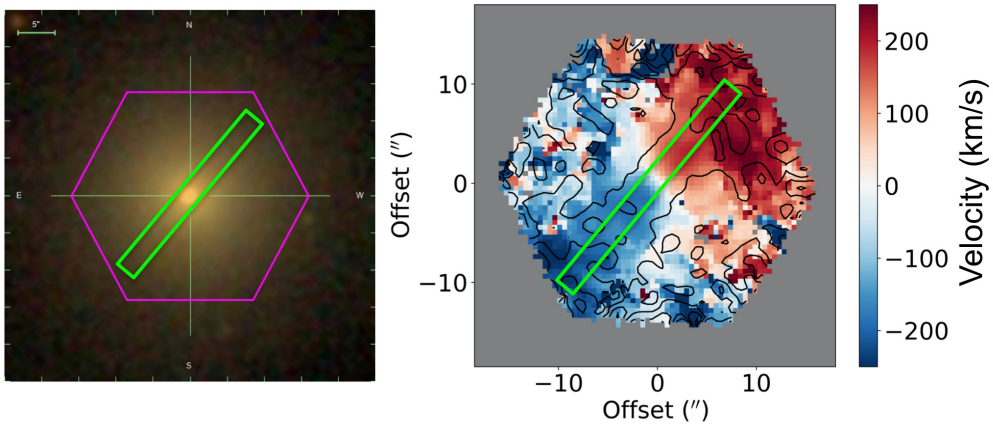

Figure 4.2: The ESI slit positions for the second target (MaNGA-ID: 1-145922). The left and the right panel show the slit position on the optical image and the MaNGA gas velocity map respectively. The black contours in the velocity map shows the Hα EW. The slit is placed at an angle of 320° from North to East, tracing the bi-conical emission feature.

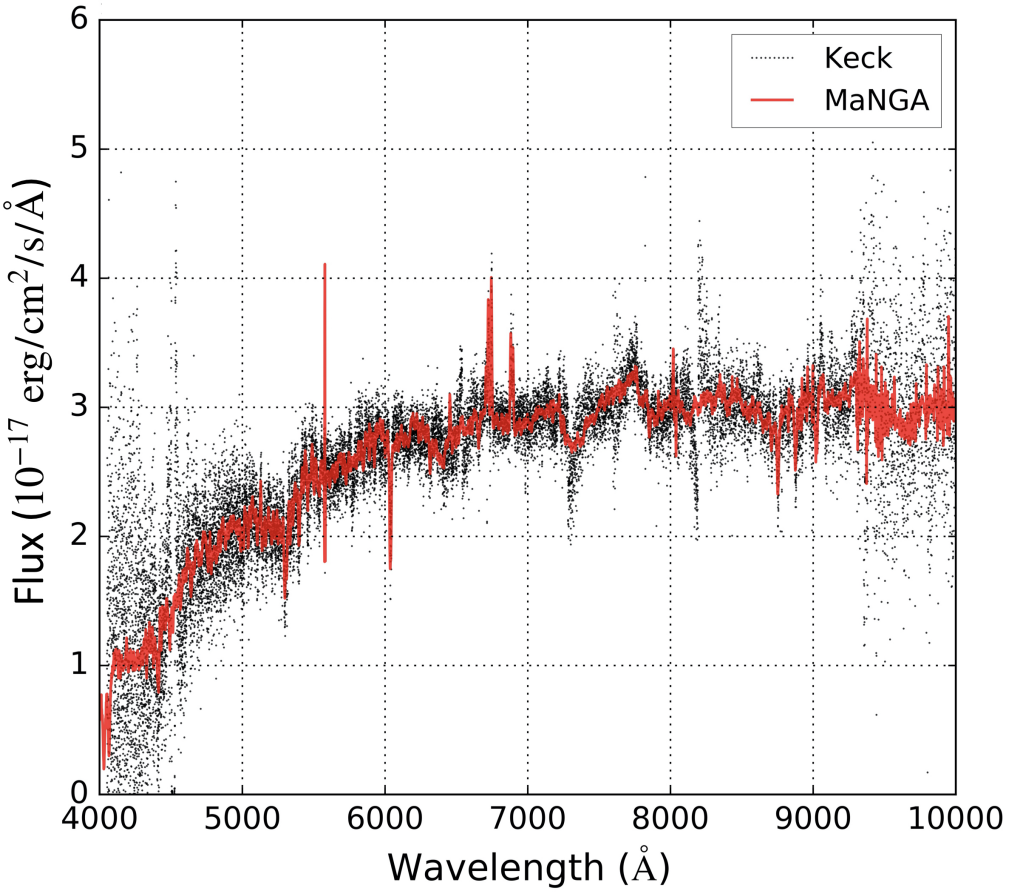

Figure 4.3: Example of a reduced Keck ESI spectrum (in black) in an 1″ spatial bin along the ESI slit. MaNGA spectra from the spaxel corresponding to the same physical position on the sky is overplotted in red.

4.3 Method & Analysis

4.3.1 Sample Selection

Our parent sample of red geysers consists of 84 galaxies which accounts for $\approx 8\%$ of the quiescent MaNGA population (Roy et al. 2018). The red geyser sample is visually selected based on the following characteristic features:

- Very low star formation rate with typical value of log SFR $[M_\odot/yr] \sim -3$, measured by optical-IR SED fitting (Chang et al. 2015; Salim et al. 2016), and rest frame color $NUV - r > 5$.
- Bi-symmetric emission feature in spatially resolved Hα-EW 2-dimensional map.
- Rough alignment of the bi-symmetric feature with the ionized gas kinematic axis, but misalignment with stellar kinematic axis.
- High spatially resolved gas velocity values, typically reaching a maximum of 300 km s^{-1}, which are greater than the stellar velocity values by a few factors.

Further details about the full sample are given in Roy et al. (2018).

The two red geyser candidates selected for the Keck ESI followup represent a range of different values of Hα flux, EW, ionized gas velocity, misalignment angle and radio flux while having sky positions amenable to the allocated Keck observing time. Hence they are good representations of the entire parent sample. The two chosen targets are shown in Fig. 4.4 and 4.5. The first galaxy (ID: 1-217022) is the prototypical red geyser (Cheung et al. 2016) which shows all the characteristics mentioned above and was

among the first ones discovered in MaNGA. Its relevant characteristics are highlighted in Fig. 4.4. The top leftmost panel in the figure shows the Hα flux distribution, which is extended in nature and shows a high value compared to other passive quenched galaxies, surpassing $\sim 5 \times 10^{-16}$ erg cm^{-2} s^{-1} . The galaxy has a clear bi-symmetric pattern in the Hα EW map with an average EW $\sim$4.5 Å (bottom left panel). The top and bottom middle panels show the stellar and gas velocity maps respectively. Cheung et al. (2016) performed detailed dynamical modeling of the gas and stellar kinematics in this galaxy to conclude that a centrally driven outflow is the likely explanation for the high ($\sim$ 300 km s^{-1}) gas velocity values. The spatially resolved BPT diagrams (rightmost panels) show LINER-like line ratios through out the galaxy. This galaxy has a central radio source detected in FIRST and Jansky Very Large Array (JVLA) 1.4 GHz continuum emission (Cheung et al. 2016), which indicates a low-luminosity radio AGN with low Eddington ratio ($\lambda \sim 10^{-4}$). The presence of ionized gas is evident in the strong detection of Balmer lines and forbidden emission lines like Hα, [NII] and [OIII].

The second red geyser target (ID: 1-145922) also shows a clear bi-symmetric EW pattern (Fig. 4.5), but with a much lower Hα EW value $\sim$ 1 − 2.5 Å (bottom left panel). LINER-like line ratios are observed through most of the galaxy while AGN/Seyfert line ratios appear in the center (right panels), with $\log([\mathrm{NII}]/\mathrm{H}\alpha) > -0.4$. Unlike the first target, this galaxy doesn't show systematic rotation in the stellar kinematics (upper middle panel) and hence the exact misalignment angle between the gas and stellar velocity field is unclear. However, the estimated average second velocity moment ($V_{\mathrm{rms}} \equiv \sqrt{V^2 + \sigma^2}$) of the ionized gas and stars are similar to the first target.

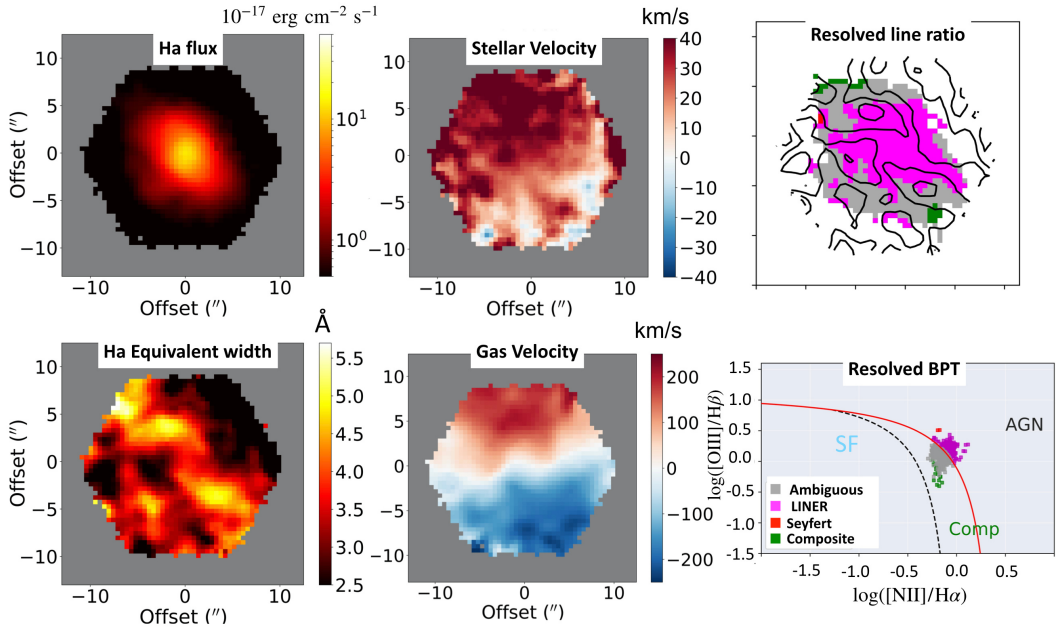

Figure 4.4: The spatially resolved emission line and kinematic properties of the first target red geyser galaxy from SDSS IV-MaNGA (MaNGA-ID: 1-217022). The on-sky diameter of this particular IFU fiber bundle is 22″ which corresponds to a physical size of 11 Kpc. The upper left panel shows the spatial distribution of Hα flux. In the other panels, as labelled, we show the Hα-EW map (lower left), the 2D stellar velocity field (upper middle) and the ionized gas velocity traced by Hα (lower middle). The lower right panel show the spatially resolved BPT diagram showing spaxels with signal to noise > 3. The upper right panel shows the spatial position of those spaxels, colored by their classification based on the BPT diagram. Characteristic red geyser features such as the bi-symmetric emission feature in Hα and its alignment with the gas kinematics axis are particularly apparent.

This galaxy is not radio detected in the FIRST survey and has not been followed up with JVLA. Both galaxies have spheroidal morphology as observed from SDSS ground based imaging.

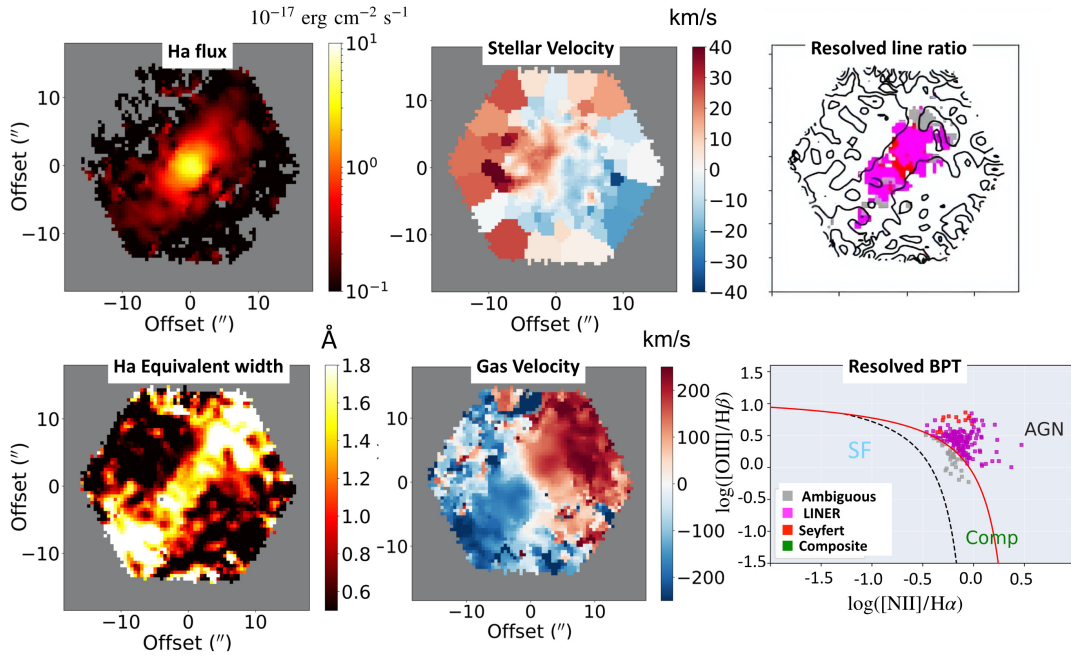

Figure 4.5: The spatially resolved emission line and kinematic properties of the second target red geyser galaxy from SDSS IV-MaNGA (MaNGA-ID: 1-145922). The on-sky diameter of this particular IFU fiber bundle is 32″ which corresponds to a physical size of 18 Kpc. The different panels are the same as in Fig 4.4.

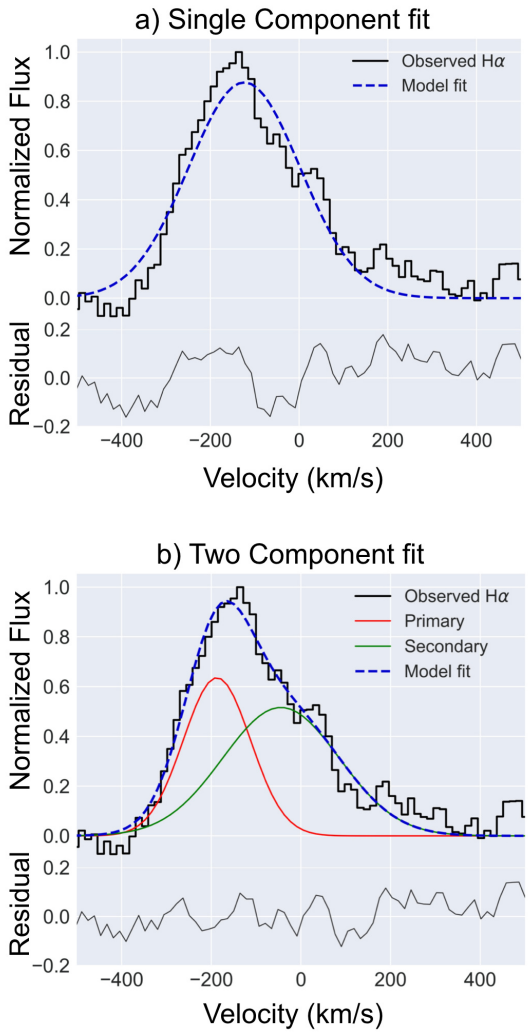

Figure 4.6: [Top panel] An example of a single gaussian fit to the continuum subtracted Hα emission line from ESI at a particular 1″ spaxel. Single component model (shown in blue) leaves huge residual of about $\pm$15% as shown in the residual panel. [Bottom panel] A two-component model fit to the same spectrum as above is shown. The model consist of a double gaussian, with the "Primary" component shown in red measuring the bulk velocity of the gas, and the "Secondary" component shown in green which shows the wings and departures from single component model. This model greatly reduces the residual to only about $\pm$5% and is favored.

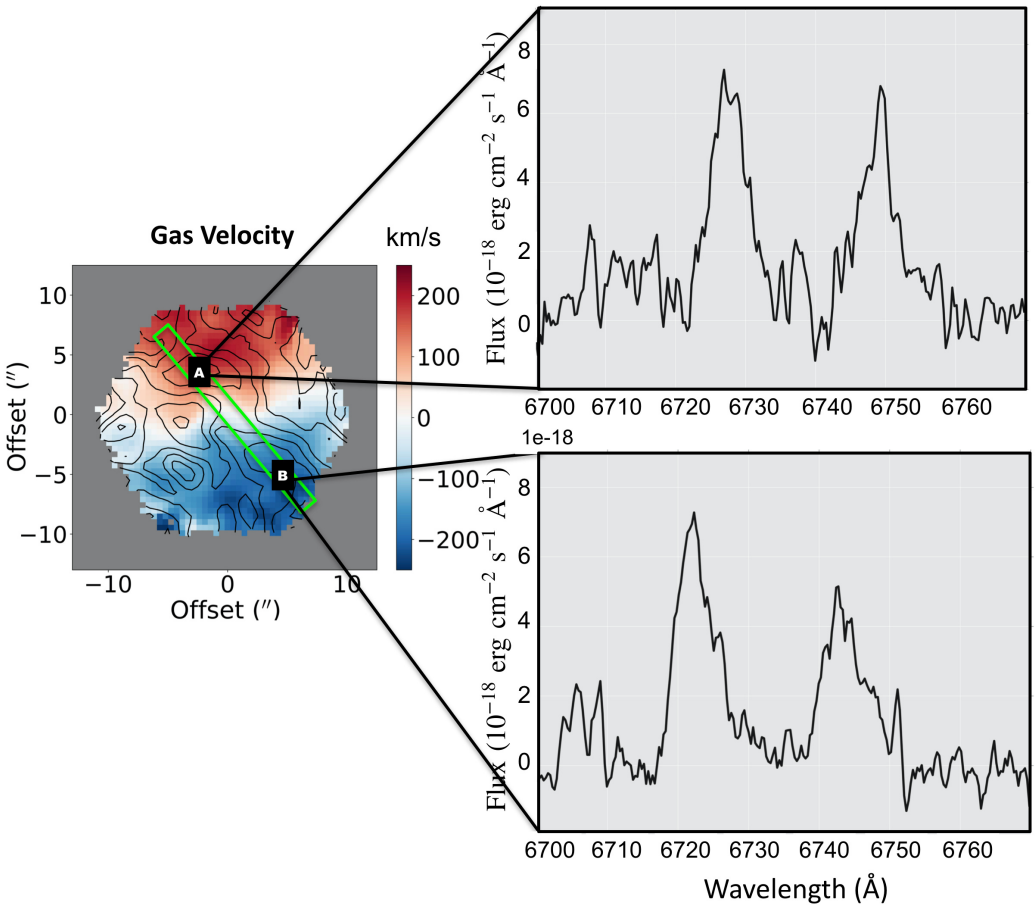

Figure 4.7: [Left panel] The 2D gas velocity field of the first target galaxy obtained from MaNGA data with Hα-EW contours overplotted in black. [Right panel] Hα and [NII]λ6584 emission line profiles obtained from Keck ESI at two separate locations in the galaxy indicated A and B in the left panel. The emission line profiles reveal complex velocity structure likely resulting from multiple components. Extended wings in the emission lines switch from the blue side at position A to the red side at position B.

4.3.2 Line profile fitting

An important aspect of accurately measuring emission lines is properly accounting for the stellar continuum. This is particularly important for the Balmer lines since underlying stellar absorption can lead to incorrect emission line flux and equivalent width estimation. We apply MaNGA's data analysis pipeline (DAP), version 2.3.0 (Westfall et al. 2019) on the fully reduced Keck data for accurate modeling of the stellar continuum throughout the galaxy. First, we run DAP modules on each spaxel in the MaNGA datacube of the target galaxy. The DAP masks $\pm$750 km s^{-1} surrounding each of the expected emission line regions at the galaxy systemic redshift and fits the stellar continuum using the Penalized Pixel fitting algorithm `pPXF` (Cappellari & Emsellem 2004; Cappellari 2017). It uses a combination of 49 templates based on the MILES stellar library, known as MILES-HC library (Falcó n-Barroso et al. 2011), which provides statistically equivalent fits to those that use the full library of 985 spectra in the MILES stellar library (Westfall et al. 2019). Once the DAP fits the continuum and obtains the optimal stellar template for a particular MaNGA spaxel, we use that same template to fit the continuum of the Keck spectra for the corresponding Keck spaxel, again using `pPXF`. The best fit stellar continuum is then subtracted from the observed spectrum before we analyze the emission lines.

We treat Hα and [NII]λ 6584 Å emission lines independently, fitting for their flux, velocity and dispersion. At first we model both the Hα line and [NII]λ 6584 Å line as single Gaussian profiles. After binning the ESI slit data into spatial bins of size 1″,

we constrain the velocity within each bin to be within ± 350 km s^{-1} of the systemic velocity. This is done to prevent the module from fitting spurious peaks. We also require the dispersion to be less than 500 km s^{-1}. In order to sample the entire parameter space and to obtain an unbiased estimate of the uncertainties in the fitted values, we wrap our fitting procedure in a Markov Chain Monte Carlo (MCMC) framework with Dynamical Nested Sampling algorithm (Higson et al. 2019) using the Python package `dynesty` (Speagle 2020). The nested sampling method (Skilling 2004) is used to estimate both the Bayesian evidence and posterior distribution in an iterative fashion until the convergence criteria is met. However, the single Gaussian model results in large residuals for most of the spatial bins (or spaxels). Fig. 4.6 panel a (top) shows the single Gaussian fit of the spectrum around Hα emission line for a particular ESI spaxel in the first target galaxy (MaNGA-ID: 1-217022). It is clear from the figure that the emission line show large departure (± 15%) from the model. We therefore proceed to fit a double Gaussian model to the emission lines, keeping the velocity of the first Gaussian component within ± 50 km s^{-1} of the velocity estimate obtained from single component fitting. This "primary component" is constrained to have a greater flux than the "secondary component". The dispersion in the primary component is constrained to be < 200 km s^{-1} while no restriction is imposed on the secondary component. This is done to make sure that the primary component, or the "narrow" component, represents the bulk velocity of the gas while the secondary component is sensitive to broad wings and other departures from the primary. Fig. 4.6, panel b (bottom) shows the double Gaussian fit of the same spectrum, with primary component shown in red and secondary

component in green. The resulting fit (blue dashed line) shows that the flux residuals are less than 5% of the median flux.

To determine which of the two models is preferred for each spaxel, we use a Bayesian Information Criterion (BIC) which uses the likelihood to determine the optimum model but penalizes for additional free parameters. It is defined as :

$$\mathrm{BIC} = -2\mathcal{L} + \mathrm{k}\ \log(\mathrm{N}) \tag{4.1}$$

where $\mathcal{L}$ is the log-likelihood, k is the number of free parameters and N is the number of data points that get fit. The model with the lower BIC value is the preferred model and the final fit is selected accordingly. For example in Fig. 4.6, the double Gaussian model is preferred over the other.

4.4 Results

With emission line velocity profiles extracted from the higher resolution Keck ESI data and fit with single or double Gaussian model depending on the BIC criterion, we are ready to investigate systematic patterns in the profile shape emerging in different parts of the galaxy. An example of Hα and [NII] emission line profiles in two opposite ends of the galaxy is shown in Fig. 4.7. This detailed line profile information may inform or refute our earlier wind model interpretation of red geyser gas kinematics that was based on MaNGA data alone. We begin by presenting all the Ha and [NII] velocity profiles derived from the ESI data at different slit positions for both of the

target galaxies.

4.4.1 Target 1-217022

For the first target, slit 1 is placed at a position angle of 40° from North to East along the bi-symmetric emission feature. The observed spectra are shown in Fig. 4.8. The top panel shows the MaNGA 2D ionized gas velocity field of the target, with Hα EW contours overplotted in black. The slit position is overlaid on top with white filled circles indicating the different spaxels of $1''$ where reduced spectra have been extracted. In the bottom panel, the different rows indicate those reduced spectra with Hα (emission line on the left side) and [NII]λ6584 (on the right) lines shown for each $1''$ spaxel of physical size of 0.51 kpc along the slit. The spectra are color coded by the velocity estimate obtained by fitting single Gaussian model to the Hα emission line. The spectra are then shifted along the wavelength axis so that the emission lines from the different spaxels are roughly aligned. This is done to enable easy visual comparison of the shapes and asymmetry of the emission lines.

The gas velocity amplitude rises steeply from the center outwards both on the red and blue-shifted side. The details in the emission line profiles are shown in Fig. 4.9 via Gaussian model fits of Hα and [NII] lines at different spaxels (spaxel number shown in the upper right or left corner in each subplot). The primary velocity component reflects the bulk velocity of the ionized gas. If the double Gaussian model is preferred (according to the BIC criterion as mentioned in §4.3.2), the line profile is asymmetric and wings or any departures from the bulk velocity is then reflected in the secondary

velocity component. The best fit parameters for all spaxels are given in Appendix A.2.

We find that the primary velocity component (shown in red for the 2-component model and in blue for the one component model, Fig. 4.9) goes from blue-shift ~ -250 km s^{-1} from one end of the slit to a redshift of $\sim$ 250 km s^{-1} in the other closely matching the values observed from the MaNGA velocity map (Fig. 4.8, top panel). The secondary fainter component (in green) varies widely in full-width half maxima (FWHM; $2.355{\cdot}\sigma$) ranging from $\sim 150 - 600$ km s^{-1}, with broad wings near the center and the red-shifted side of the galaxy. On average, emission lines with a blue-shifted primary velocity component show a secondary component shifted redward. The secondary component switches to the bluer side when the primary velocity component is red-shifted. In other words we see a "red" wing on the blue side of the galaxy and a "blue" wing on the red side. Infact, for this particular slit position, the secondary component in certain spaxels have shifted so much relative to the primary that its velocity relative to the systemic velocity have opposite signs compared to the primary component. That means, on the red-shifted side, the blue wing is actually blue-shifted relative to the systemic velocity of the galaxy and vice versa on the other side of the galaxy. The line profiles show mostly symmetric profiles near the galaxy center where a single Gaussian model is preferred. The implication of these findings are discussed in §4.5.

For the second slit configuration (Fig. 4.10), the slit lies almost perpendicular to the bi-symmetric feature, at an angle of 110° from North to East. From the Hα-EW 2D map, it is clear that the EW of the ionized emission is enhanced along the

bi-symmetric feature, hence there is comparatively less signal perpendicular to it. The spectra extracted in different spaxels along the second slit is shown in the bottom panel of Fig. 4.10. Near the edges of the slit, line-fitting becomes unsuccessful owing to low signal-to-noise. The bulk velocity in slit 2 varies from ~ 50 km s^{-1} to ~ -50 km s^{-1} (Fig. 4.11). The emission lines along this slit are substantially broad, with FWHM $>$ 250 km s^{-1} going up to ~ 600 km s^{-1}, similar to a few cases in slit 1. The average FWHM of [NII] lines is higher than that of Hα and broad lines (with FWHM > 300 km s^{-1}) are observed reaching a distance of ~ 1 kpc from the center along the slit. The observed emission lines are generally symmetric across slit 2. Very slight asymmetry occasionally arises near the edges.

The third slit (Fig. 4.12) is placed parallel to the first slit, i.e. parallel to the bi-symmetric feature, but slightly off-centered at a distance of ~ 2.5 kpc in the South-East direction. Owing to the decrease of ionized emission in the outskirts of the galaxy, the signal to noise of the spectra drops overall, compared to the first slit. Nevertheless, the line profile clearly shows a red wing on the blue side of the galaxy and a blue wing on the red side similar to slit 1 (Fig. 4.13). The degree of asymmetry is less, but the primary velocity component goes from blue-shift ~ -200 km s^{-1} on one end of the slit to a redshift of ~ 250 km s^{-1} on the other. Just like slit 1, there is a significant velocity offset ($\sim 100 - 150$ km s^{-1}) between primary and secondary components. We note that in the MaNGA Hα-EW contour map, there is an additional Hα enhanced region ~ 2.9 kpc south east of the center. The overlapping ESI spectra in the 3rd row from the bottom (Fig. 4.12, bottom panel) shows broader Hα and [NII] lines possibly due to a

distinct velocity component associated with this region.

4.4.2 Target 1-145922

The second target has only one slit observation (Fig. 4.14) with sufficient signal-to-noise spectra (a minimum SN $>$ 1 across the slit). The slit is oriented along the bi-symmetric feature, at a position angle of 320° from North to East. Despite the lower signal-to-noise, the fitting procedure was successful in extracting individual velocity components (Fig. 4.15). The bulk velocity varies from ~ -250 km s^{-1} to about $\sim$ 300 km s^{-1}. The average FWHM is lower compared to the first target with an average value between $\sim 150-200$ km s^{-1}, but it reaches a maximum value of over ~ 600 km s^{-1} near the center. The blue-shifted part of the galaxy exhibits a secondary component with a velocity $\sim 150 - 200$ km s^{-1} redder than the primary velocity. This component provides an obvious "red" wing on the blue side. The profiles become symmetric towards the center before showing a blue wing in the red-shifted side.

4.4.3 Measured velocity asymmetries

In order to measure the observed asymmetry of the emission lines, we fit the emission lines with a Gauss-Hermite polynomial of the form:

$$\mathrm{f(x)} = \mathrm{Ae}^{\frac{-\mathrm{g}^2}{2}}[1 + \mathrm{h}_3(-\sqrt{3}\mathrm{g} + \frac{2}{\sqrt{3}}\mathrm{g}^3) + \mathrm{h}_4(\frac{\sqrt{6}}{4} - \sqrt{6}\mathrm{g}^2 + \frac{\sqrt{6}}{3}\mathrm{g}^4)] \tag{4.2}$$

where $g = \frac{x-x_c}{\sigma}$. Here A is the flux, x_c is the peak wavelength and σ is the velocity dispersion. Departures from symmetry are quantified by the coefficient h_3, which is a proxy for the skewness parameter (k). A positive k parameter indicates the presence of a "red" wing. Similarly blue-winged components have a negative k value. $k = 0$ signifies a perfectly symmetric profile. To estimate the errors on the measured skewness, we perform MCMC simulations of the above model fit for every spaxel. We construct one hundred realizations of each spectrum by adding Gaussian noise with amplitude comparable to the noise measured in the original spectrum and quote the standard deviation of the k parameter distribution, thus obtained, as the $1-\sigma$ uncertainty on the measured skewness.

In Fig. 4.16, the k parameters obtained from Hα and [NII] λ6584 Å emission lines for all four slit observations from the two galaxies are plotted against spaxel number, which maps to locations in the slit as shown in Fig. 4.8−4.14. We can see that, for slit 1 for the first target galaxy and the only slit for the second galaxy, which sample the bi-symmetric feature in the Hα EW map, the k parameter values clearly transition from positive to negative as we move from the blue-shifted side (low spaxel number) towards the red-shifted side (high spaxel number) of the galaxy. This reaffirms the finding that the line profiles show a "red" wing on the blue-shifted side of the galaxy and a "blue" wing on the red-shifted side. The 2nd slit of the first galaxy shows almost a flat asymmetry parameter distribution with values oscillating close to 0. This particular slit samples the central regions of the first galaxy galaxy and reveals mostly symmetric profiles. For the 3rd slit, the k parameter values again show a transition from positive

to negative values similar to slit 1. This slit traces the outskirts of the galaxy parallel to the bi-symmetric feature.

4.5 Discussion

The main result of our observations is the systematic asymmetry of line profiles, i.e. a red wing on the blue-shifted side of the galaxy and a blue wing on the red-shifted side with symmetric profile near the center, which is observed along the bi-symmetric emission feature in both the target red geysers. Before we discuss possible interpretations in detail, we summarize our Keck ESI data using the skewness parameter k (§4.4.3) measured as a function of distance from the galaxy center along the slit (Fig. 4.16, also shown later in Fig. 4.20).

We will consider two physical interpretations that can give rise to our observations: ionized gas in rotation and a wide-angle outflowing wind driven by an AGN.

4.5.1 Gas in rotation scenario: Disk model

In the case of a rotating disk, because the portion of the disk intersected by the line-of-sight is constant due to symmetry, there is no intrinsic velocity asymmetry. Instead, asymmetry profiles mainly arise from beam smearing from the PSF and the spatial binning of the data, sometimes producing a similar red wing in the blue-shifted side of the galaxy and vice-versa, with the strength of asymmetry roughly proportional to the velocity gradient. Beam smearing can also inflate the FWHM of the lines especially along the regions where the projected line-of-sight velocity gradient is maximum

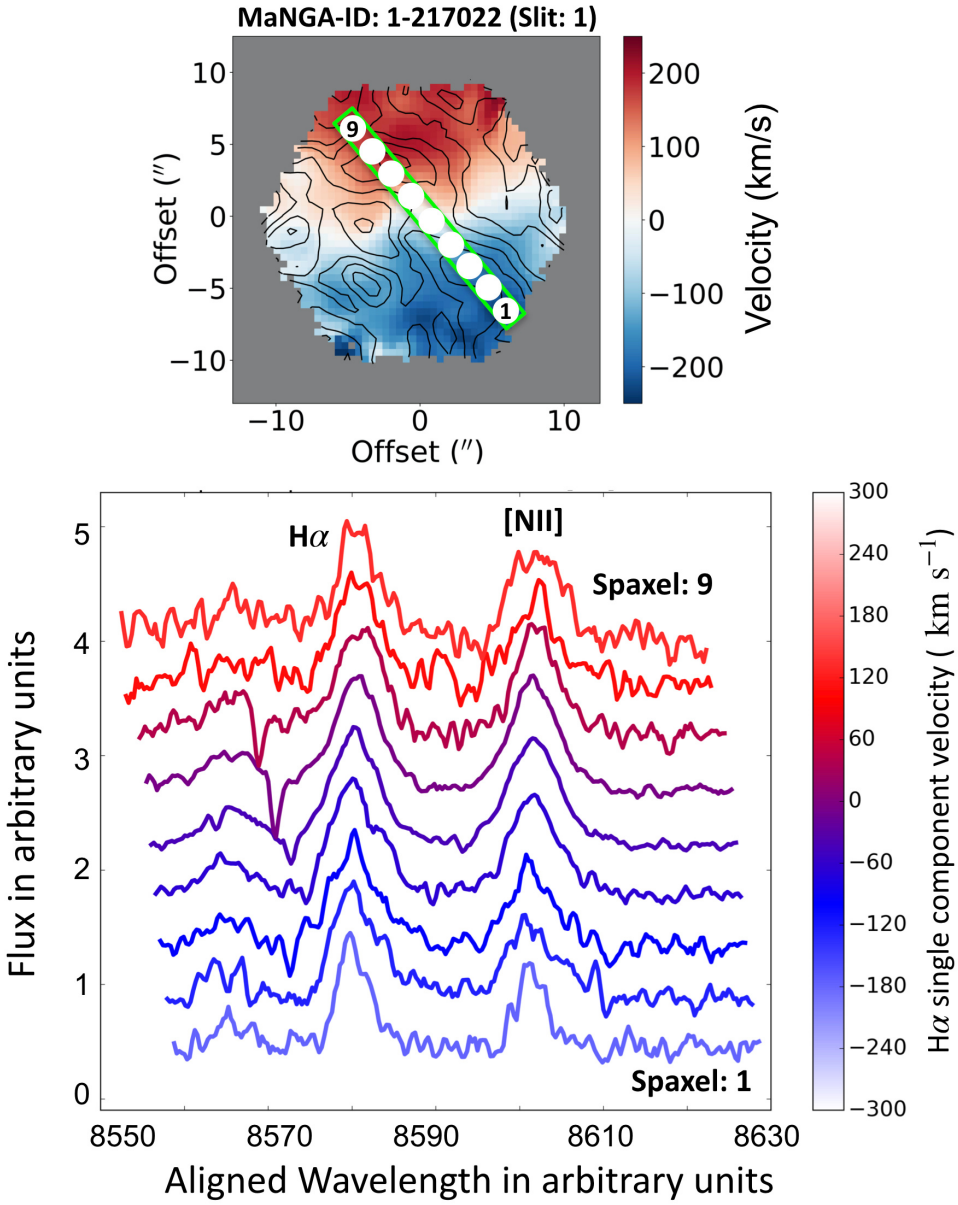

Figure 4.8: [Top panel] The 2D ionized gas velocity field of the first target galaxy obtained from MaNGA data with the Hα EW contours overplotted in black. The first slit position with different spatial bins ($\sim 1''$) is overlaid on top to map the physical location of the extracted spectra on the slit. [Bottom panel] The different rows indicate the observed spectra from Keck ESI around the spectral window of Hα, [NII]λ6584 extracted from different spatial bins (or spaxels) as marked in the top panel. The spectra are registered to the same wavelength and color coded by gas velocity.

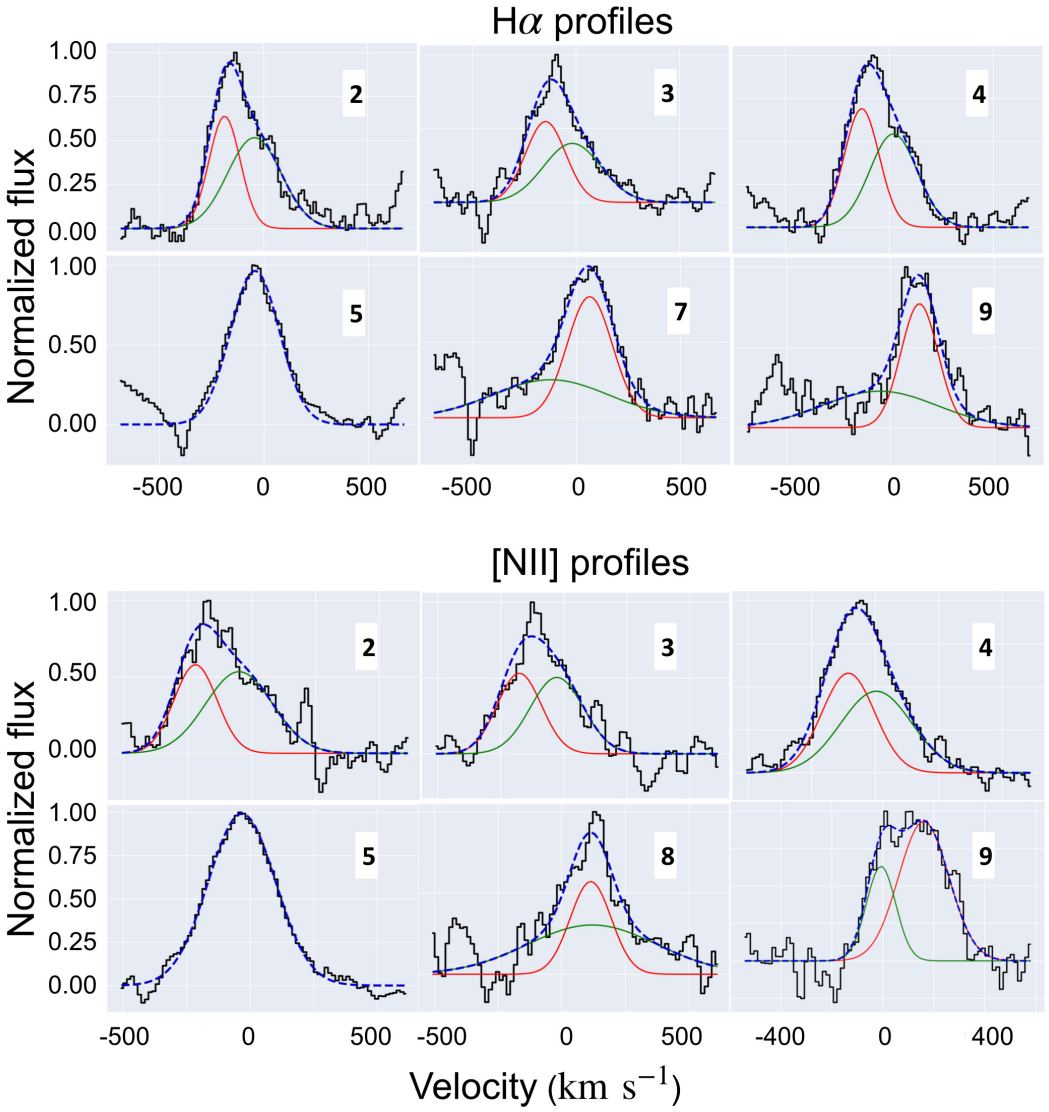

Figure 4.9: [Top panel] The Hα emission lines from ESI for slit 1 position of the first target galaxy are shown for different spaxels along the slit in different panels. A single or a double Gaussian model, as favored by the Bayesian Information criterion (BIC), is used to model the emission lines. For a single component model the model is shown in blue. For two component models, the primary component is shown in red and secondary in green. The modelled line profile in blue shows the total model fit to the data (which is in black). [Bottom panel] The [NII]λ6584 emission line profiles in black with their model fits over-plotted in blue, similar to the sub-panel above.

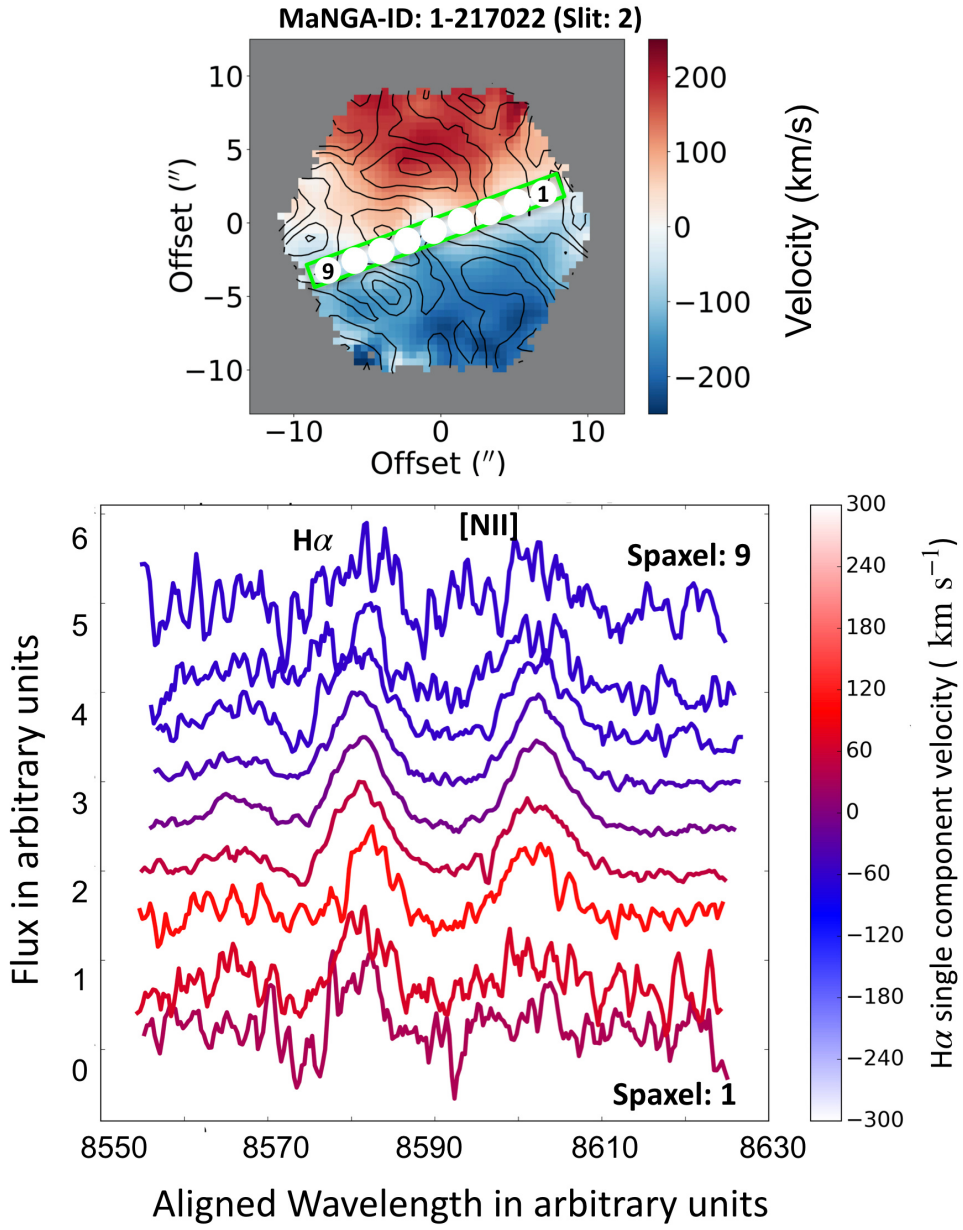

Figure 4.10: [Top panel] The MaNGA ionized gas velocity field with Hα EW contours overplotted in black, similar to Fig. 4.8. The second slit position with different spaxels ($\sim 1''$) are overlaid on top. [Bottom panel] The different rows indicate the observed spectra from Keck ESI around the spectral window of Hα, [NII]λ6584 extracted from different spaxels as marked in the top panel. The spectra are registered to the same wavelength and color coded by gas velocity.

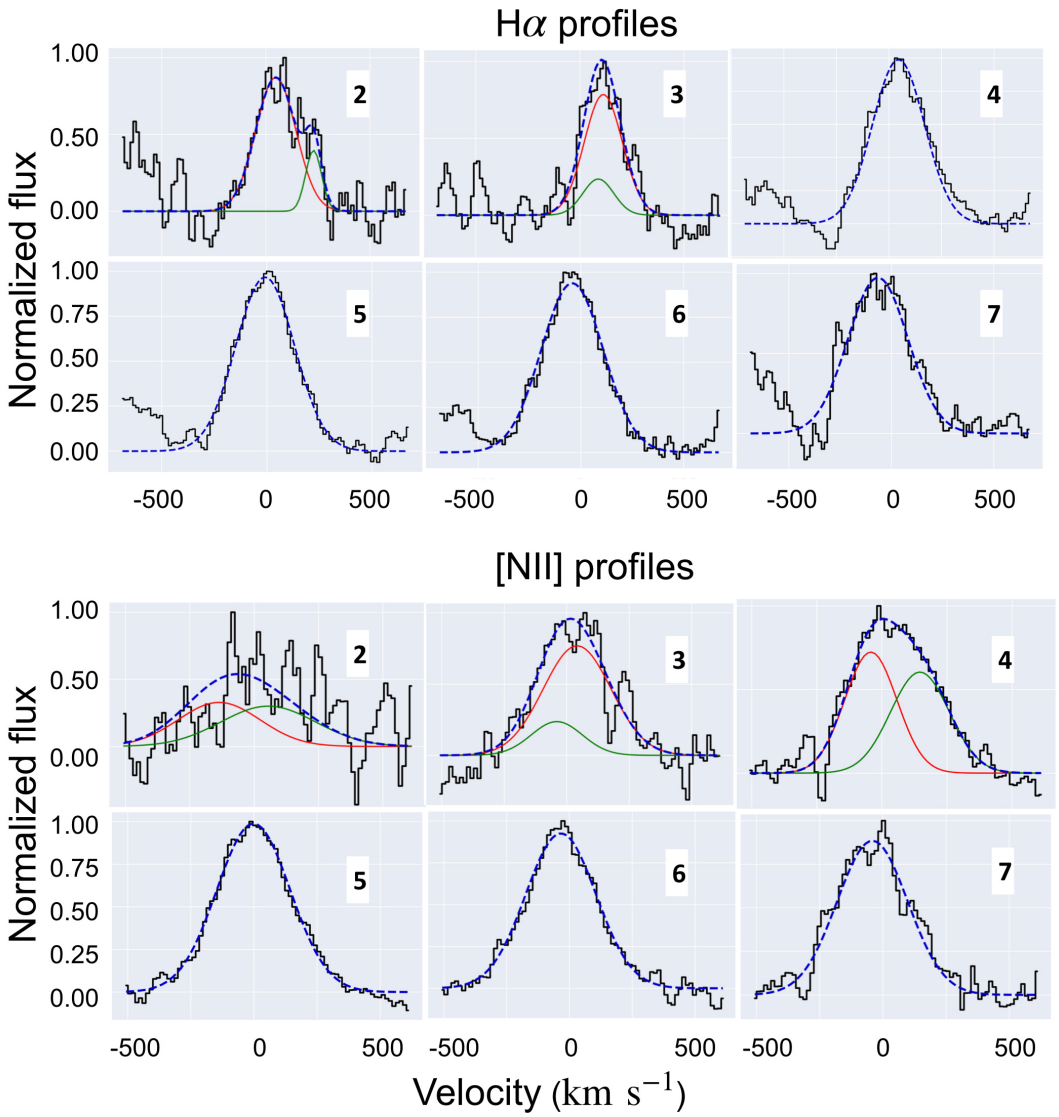

Figure 4.11: [Top panel] The Hα emission lines from ESI for slit 2 position of the first target galaxy are shown for different spaxels along the slit in different panels. A one or two component Gaussian model is used to model the emission lines similar to Fig. 4.9. The modelled line profile in blue shows the total model fit to the data (which is in black). [Bottom panel] Model fit for [NII]λ6584 emission line profiles, similar to the sub-panel above.

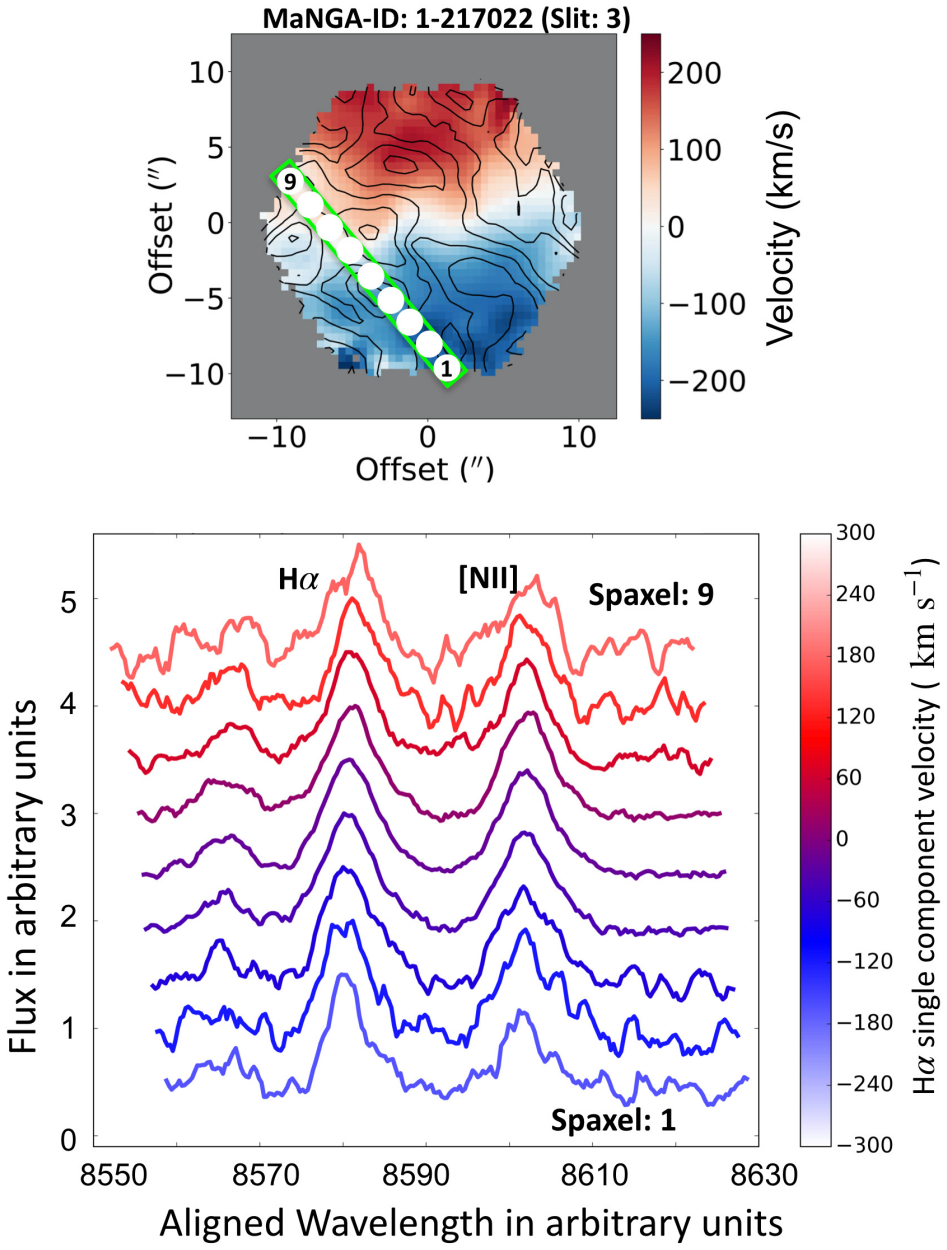

Figure 4.12: [Top panel] The MaNGA ionized gas velocity field with Hα EW contours overplotted in black, similar to Fig. 4.8 & 4.10 for the third slit position. This slit is parallel to but offset to the bi-symmetric feature, hence traces the edge of the putative wind cone. [Bottom panel] The different rows indicate the observed Hα, [NII]λ6584 emission lines from Keck ESI extracted from the spaxels marked in the top panel. The spectra are registered to the same wavelength and color coded by gas velocity.

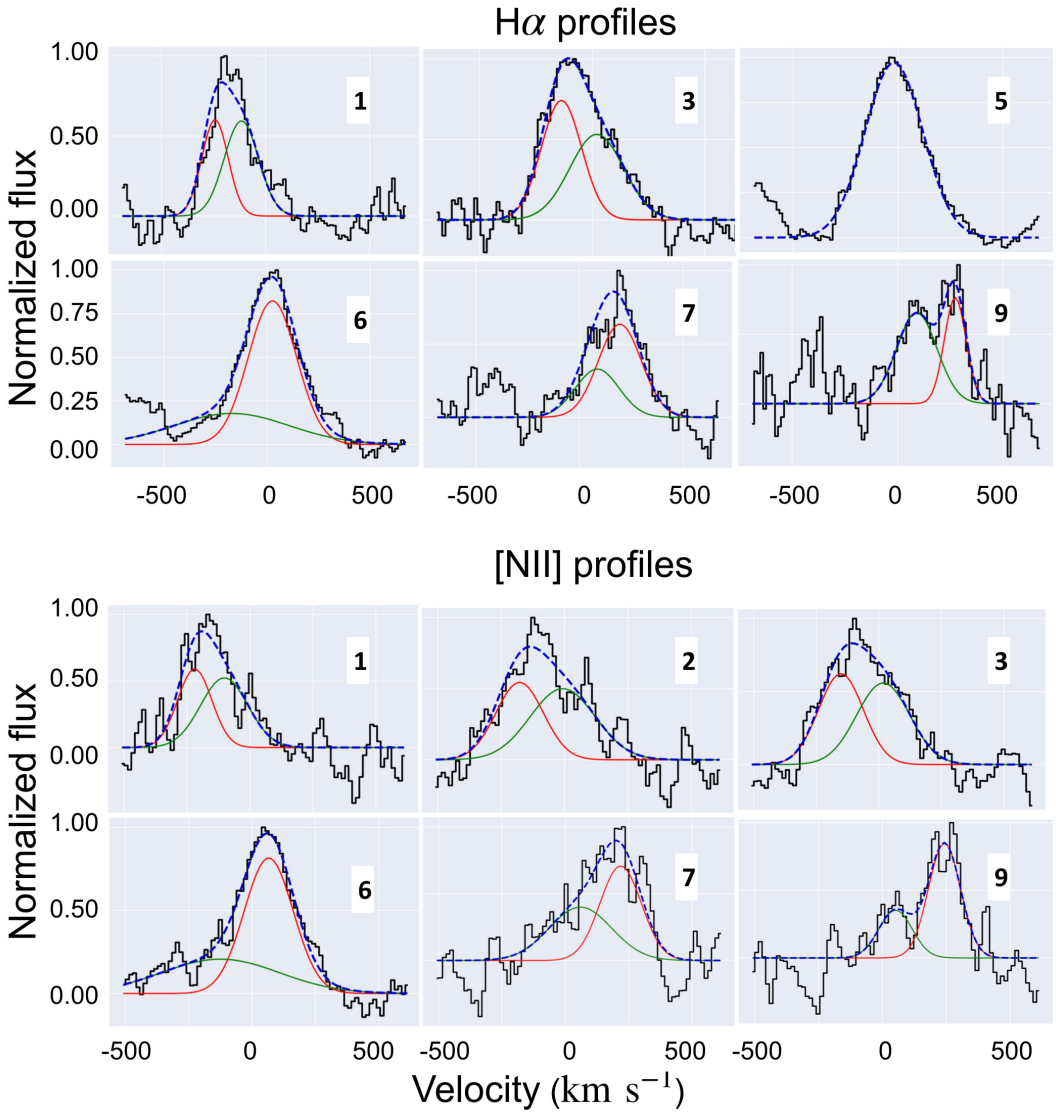

Figure 4.13: [Top panel] The Hα emission lines from ESI for slit 3 position of the first target galaxy are shown for different spaxels along the slit in different panels. A one or two component Gaussian model is used to model the emission lines similar to Fig. 4.9. The modelled line profile in blue shows the total model fit to the data (which is in black). [Bottom panel] Model fit for [NII]λ6584 emission line profiles, similar to the sub-panel above.

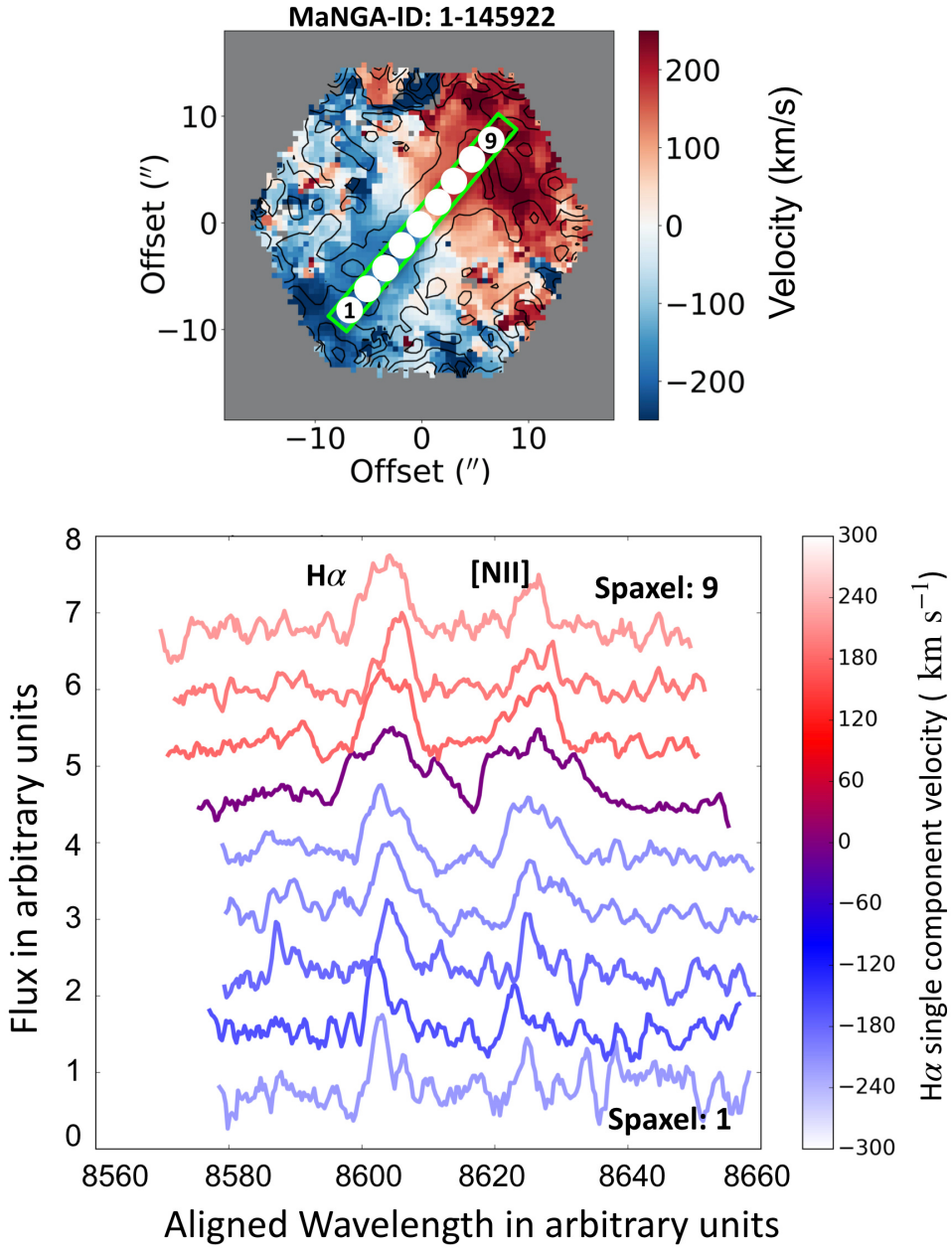

Figure 4.14: [Top panel] The MaNGA ionized gas velocity field of the second target galaxy with the Hα EW contours overplotted in black. The only slit observation with reasonable S/N taken for this galaxy is overlaid on top with different spatial bins ($\sim 1''$) indicated with circles to map the physical location of the extracted spectra on the slit. [Bottom panel] The different rows indicate the observed ESI spectra extracted from different spaxels as marked in the top panel. The spectra are registered to the same wavelength and color coded by gas velocity. The spectra are lower signal to noise in general compared to the first target galaxy.

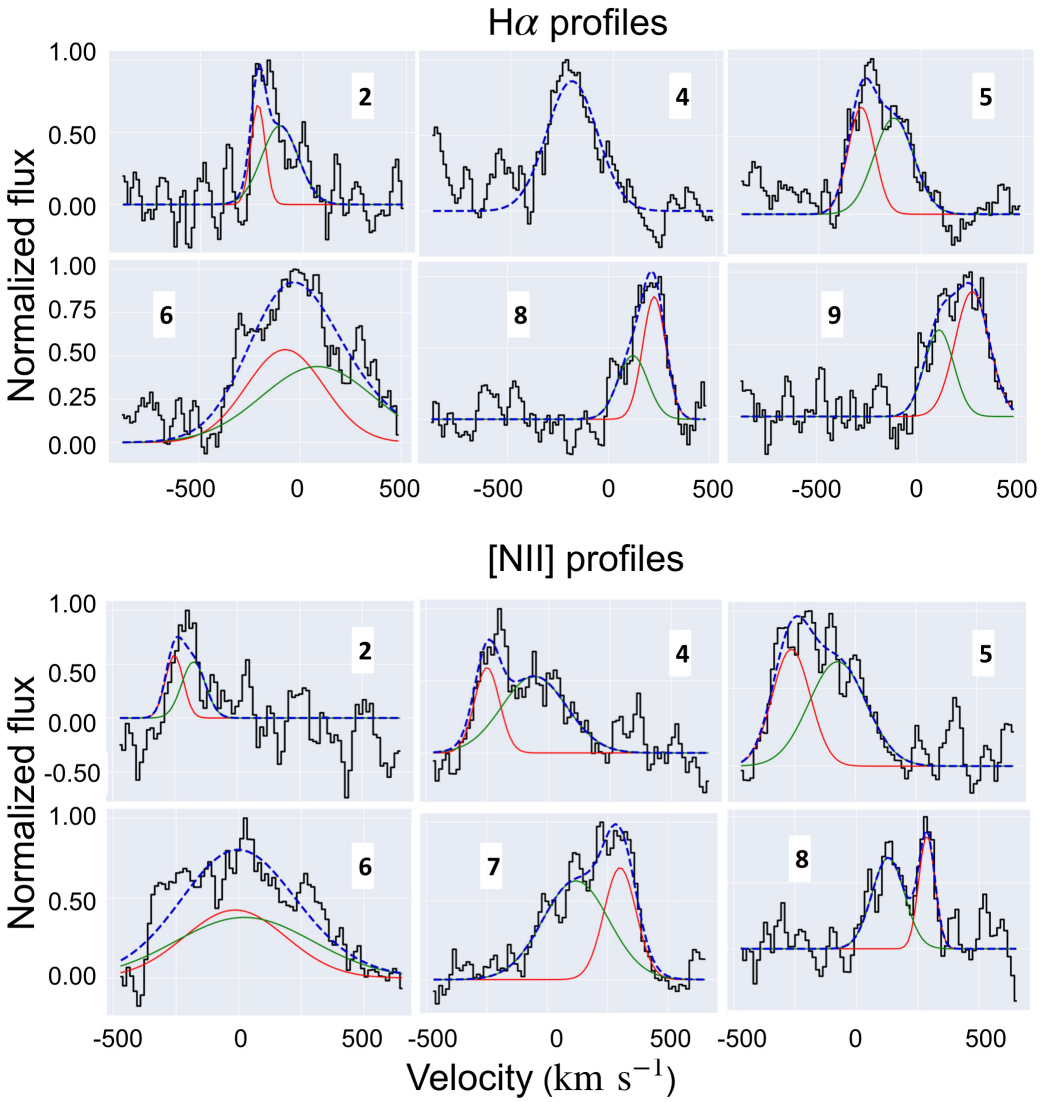

Figure 4.15: [Top panel] The Hα emission lines from ESI for the only slit in the second target galaxy are shown for different spaxels along the slit in different panels. A one or two component Gaussian model is used to model the emission lines similar to Fig. 4.9. The modelled line profile in blue shows the total model fit to the data (which is in black). [Bottom panel] Model fit for [NII]λ6584 emission line profiles, similar to the sub-panel above.

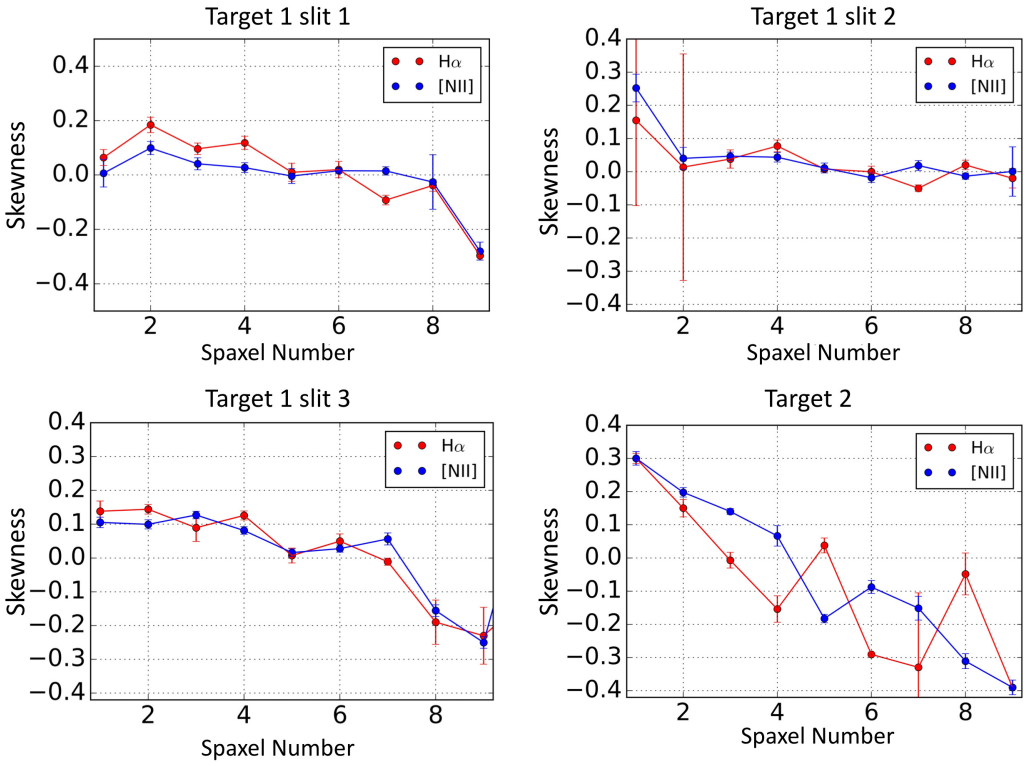

Figure 4.16: The observed Gauss-Hermite skewness of the Hα (in red) and [NII] (in blue) lines for each slit positon of the two target galaxies. The skewness or the asymmetry parameter k, described in §4.4.3, quantifies the asymmetric nature of the line profiles. k $>$ 0 indicates a red wing and k $<$ 0 indicates blue wing. The spaxel number maps to the spatial locations in the slit as indicated in Fig. 4.8 - 4.14. Low spaxel number indicates blue-shifted part of the galaxy while high spaxel number indicates red-shifted side.

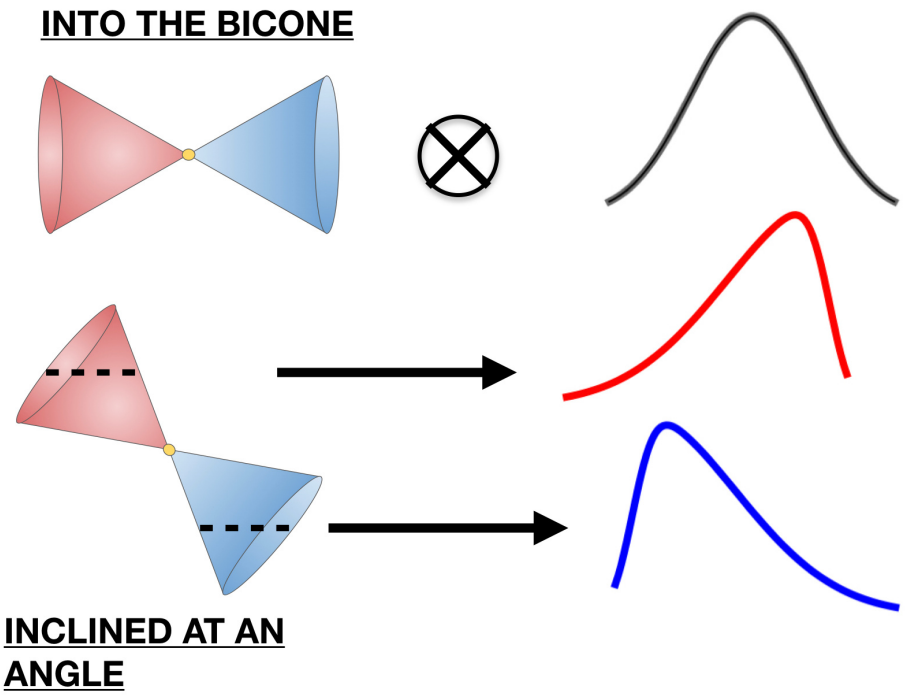

Figure 4.17: A schematic diagram showing how emission line profiles integrated along the line of sight of a conical wind are expected to produce asymmetric lines with a "blue" wing on the red side and vice versa. This behavior is evident in the emission line profiles from Keck ESI data.

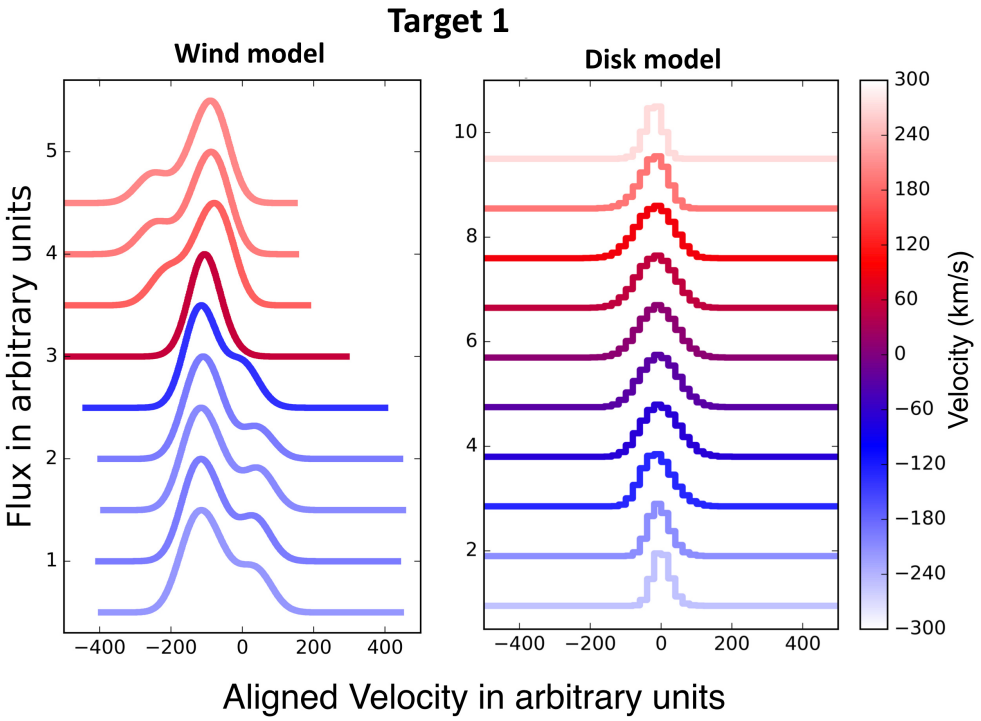

Figure 4.18: Left panel shows the mock spectra obtained from wind modelling of the first galaxy. Right panel shows the spectra obtained from the disk model. Each row in the plot represents the line-of-sight integrated spectra co-added inside each spatial bin sampling the same locations as ESI spaxels along the bi-symmetric feature in Fig. 4.8. All the emission lines are registered to common velocity and the velocity information is encoded in the color scheme.

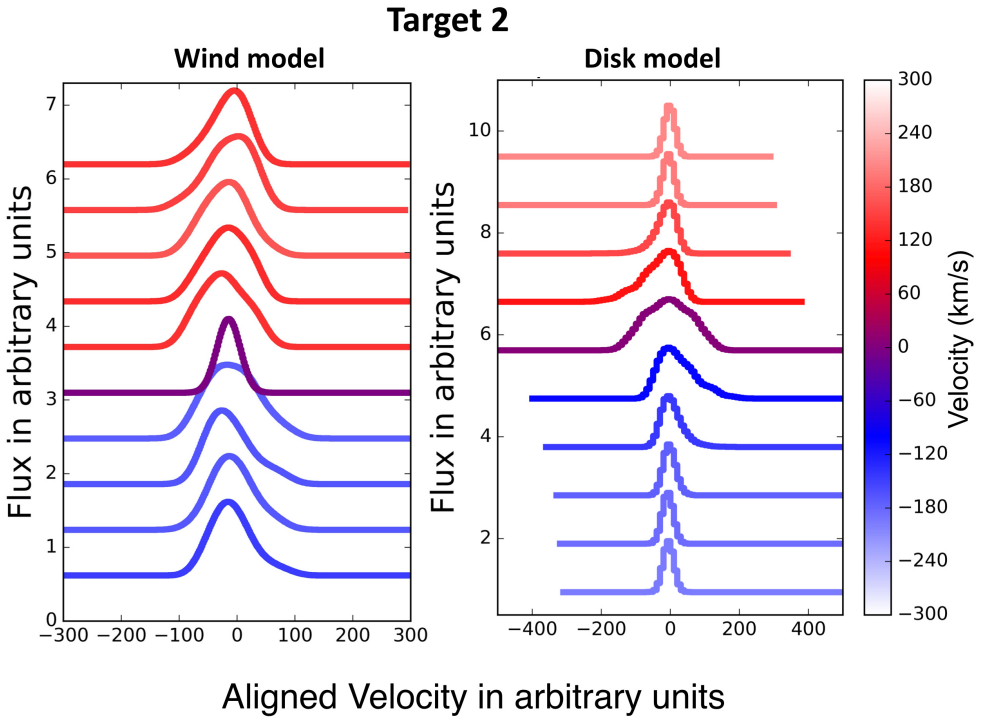

Figure 4.19: Left panel shows the mock spectra obtained from wind modelling of the second galaxy. Right panel shows that obtained from the disk model. Each row in the plot represents the the line-of-sight integrated spectra co-added inside each spatial bin sampling same locations as ESI spaxels along the bi-symmetric feature in Fig. 4.14. All the emission lines are registered to common velocity and the velocity information is encoded in the color scheme.

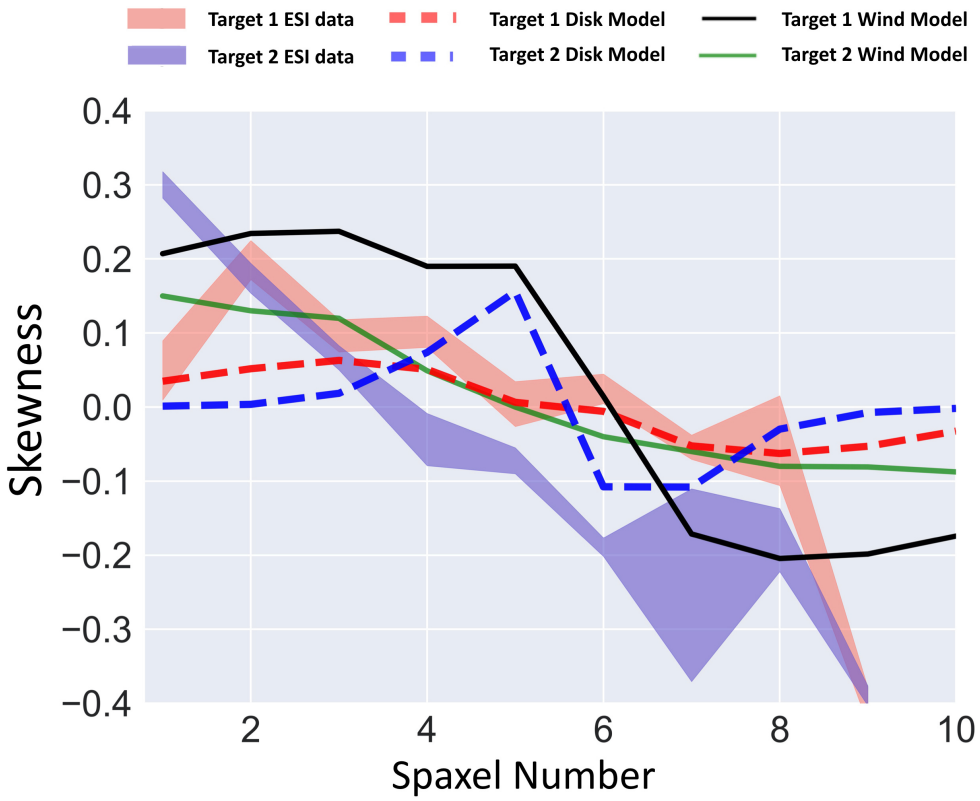

Figure 4.20: Comparison of the variation of asymmetry parameter obtained from ESI line profiles with predictions from different models. The salmon and blue shaded regions show the variation of the asymmetry parameter computed by averaging over k values from $H\alpha$ and [NII] lines along the presumed wind cone for both galaxies. The asymmetry parameter obtained from the disk models (shown in dashed lines) and wind models (in solid lines) for the two galaxies are overplotted on top.

(Epinat et al. 2010; Davis et al. 2013; Green et al. 2014; Burkert et al. 2016).

Although the red geysers show multiple characteristics that argue against the disk hypothesis (see Cheung et al. 2016), it is important to address whether the Keck ESI data provides additional insight. Therefore, we construct a symmetric disk model. We use the python version of the KINMS package (KINematic Molecular Simulation, Davis et al. 2013)[4] to construct the disk model. The major advantage of using KINMS is that it self-consistently accounts for beam smearing by mocking observations of a disk defined by the rotation curve and surface brightness profile. We assume a thin disk inclined at an angle from the observer, with velocity given by the following formula:

$$V(r, \theta) = \frac{2\ V_{max}}{\pi}\ \tan^{-1}(r/r_{turn}) \tag{4.3}$$

Here, V_{max} is the maximum velocity across the galaxy, and r_{turn} is the turnover radius for the rotation curve.

We assign an Hα surface brightness distribution to our disk models that reproduces the MaNGA Hα flux maps for our two galaxies, as determined by fitting an exponentially declining function of the form $\Sigma(r) \propto e^{-\frac{r}{d_{scale}}}$, where d_{scale} is the scale radius determined by the model fit. We experiment with different choices for the input parameters to find the best match between the modeled rotation curve and the position velocity curve observed from the ESI data for both the targets (see Appendix A.3). The chosen set of disk model parameters for the first galaxy are: inclination = 35°, turnover radius = 9″ and maximum velocity = 715 km s^{-1}. The spatial scale and extent of the model grid are chosen from the ESI data. For the second galaxy, the values are: incli-

[4]https://github.com/TimothyADavis/KinMSpy

nation = 40°, turnover radius = 1″ and maximum velocity = 350 km s^{-1}. We provide the point spread function (PSF) of FWHM ∼ 0.9″, which roughly corresponds to the median seeing of Keck, as the "beam-size" for the computation of beam smearing. We extract the projected velocity fields and line profiles at each keck "spaxel". We then calculate the asymmetry parameter (k) of the extracted line profiles in a similar way as the data (described in §4.4.3). The mock spectra extracted from the disk model along the major axis for both targets at the spatial locations of the keck spaxels are shown in Fig. 4.18 and 4.19.

We find that while the disk models can produce considerable asymmetry in the line profiles because of the beam smearing effect, the nature of the resulting asymmetry does not match the data. For the first galaxy, the observed position velocity curve from ESI data is almost linear with a gentle slope (Appendix A.3, Fig. A.2). This results in the skewness parameter due to beam smearing of the disk (which approximately varies according to the line-of-sight velocity gradient) to rise and decline gently with less asymmetry overall compared to the data. For the second galaxy, the observed velocity curve has a sharp gradient near the center with considerable flattening at the edges (Appendix A.3, Fig. A.2). Hence the skewness from the disk model is greater near the center compared to the outskirts. These findings are in accordance with other similar studies of beam smearing on star forming disk galaxies (Green et al. 2014). Thus, the increasing asymmetry towards the outskirts of the galaxies along the kinematic axis, as observed from ESI spectra, can not be captured by the disk model. The trend of asymmetries that we obtain from the disk model for both galaxies along the major axis

of the disk are shown by (red and blue) dashed lines in Fig. 4.20.

We see in §4.4.1 and Fig. 4.13 that the third ESI slit, sampling locations offset to the bi-symmetric feature in the first galaxy, also shows considerable asymmetry in the observed ESI spectra with similar trend as locations along the bi-symmetric feature (Fig. 4.16). This level of asymmetry is however not seen at similar spatial locations from the disk model, which shows a skewness value oscillating around ~ 0. This is because the velocity gradient declines rapidly as we move parallel to major axis of the disk away towards the outskirts. Thus this model struggles to reproduce both the trend and the magnitude of the skewness parameter for locations offset to the kinematic major axis.

We find that the FWHM of the secondary velocity component in the observed spectra at several locations in both galaxies exceed $500 - 600$ km s^{-1}, a value which is quite high and is typically attributed to ionized gas outflows in numerous studies (Arribas et al. 2014; Fischer et al. 2017; Humire et al. 2018; Couto et al. 2017; Soto-Pinto et al. 2019). The mock spectra extracted from the disk model for our target galaxies show an average enhancement of the velocity dispersion of about $40 - 50$ km s^{-1} (or FWHM upto 100 km s^{-1}) due to beam smearing effect, far below what we observe from data. Fig. 4.18 and 4.19 (right panels) demonstrate that apart from the central spaxel that shows the FWHM value to be much higher than average, exceeding ~ 150 km s^{-1}, the modelled spectral lines from beam smeared disks are quite narrow in the outskirts. On the other hand, the ESI spectra for both galaxies show significantly high FWHM near the center as well as in the outskirts of the galaxies, in locations along, offset or perpendicular to the bi-symmetric feature. In other words, the enhanced dispersion

doesn't necessarily follow the velocity field gradient which implies that beam smearing effect is not the primary reason behind the observed broad lines.

4.5.2 Outflowing gas scenario: Wind model

Let us now consider the scenario of radially outflowing motion of gas particles in a filled bi-cone geometry. We use a simple wind model to test our interpretation of the ESI emission line velocity profiles. A 3D cartesian grid of points is populated with tracer particles with uniform density that are weighted by a Hernquist profile (Hernquist 1990). The outflowing wind is assumed to be a filled wide angle bi-cone centered on the galaxy. Each gas particle in the bicone is given a constant radially outward velocity directed away from the center. Those outside the bicone are given zero velocity and zero weight. The model is motivated by our observation that the dominant ionization in the red geysers is extended LI(N)ER-like (Fig. 4.4 & 4.5) and hence the assumption that the strong emission lines (e.g., Hα, [NII]) are ionized mainly by the radiation field of evolved post-AGB stars present around it (Yan & Blanton 2012; Belfiore et al. 2016). Although shocks can also contribute to the ionization, the smooth components of the Hα flux distribution in red geysers typically fall off roughly proportional to the stellar surface brightness supporting a stellar origin for the observed LIER ionization. Moreover, the exact nature of the ionization source should not impact the model-predicted velocity profiles to first order as both models are constrained by the observed Hα flux distribution. The warm ionized gas clouds entrained by the wind trace the observed kinematics and emit emission line flux due to the assumed ionization.

Hence the projected velocity field is a convolution of the wind geometry along the line of sight and the galaxy's 3D luminosity profile. The projected line-of-sight component of the wind velocity at each point inside the bicone is weighted by its Hernquist profile value. In order to construct the luminosity distribution which gives rise to the wide-spread ionization of the observed gas, imaging and dynamical constraints on the stellar component, obtained from Jeans Anisotropic Modeling (JAM, Cappellari 2008) are used for both target galaxies in the model. We use JAM analyses to find intrinsic (3D) axis ratio and inclination of the galaxy, while the projected major axis effective radius and sky position angle are obtained from the Nasa Sloan Atlas (NSA) catalogue. For target 1-217022, we have taken the axis ratio to be 0.4, galaxy inclination as 50°, a projected major-axis effective radius to be 7″, and an on-sky PA as 53° (see Methods: Dynamical modeling evidence against the presence of disks, Cheung et al. 2016). For the second galaxy (target 1-145922), the intrinsic axis ratio is taken to be 0.5, inclination as 20°, a projected major-axis effective radius to be 9″ , and an on-sky PA as -73°. The detailed description of the JAM parameters for the second galaxy is presented in Appendix A.1. The wind parameters like the opening angle, length, intrinsic velocity and the inclination of the wind cone are varied manually until the best qualitative match is obtained between the modeled and the observed MaNGA 2D gas kinematics. For the first target galaxy, the best match is found for wind opening angle = 80°, inclination = 75°, position angle = 55° and velocity = 300 km s^{-1}. For the second galaxy, the wind parametrs are opening angle = 40°, inclination = −55°, PA = 135°, and velocity = 200 km s^{-1}.

We construct a data cube consisting of spatial and spectral dimensions from the

model. We assign single Gaussian emission line profiles to model gas particles throughout the 3D volume of the cone and convolve the flux distribution with a Gaussian of FWHM = $0.9''$ along each spatial dimension to capture the effect of beam smearing on the simulated data cube. The velocity dispersion is taken to be the instrumental dispersion (16 km s^{-1}). Finally, we construct spatial bins following the same slit orientation as the Keck ESI data and integrate the line profiles along lines of sight to produce mock spectra that can be compared to the ESI data.

Due to the radially outward velocity of the gas particles inside the cone, material with the greatest line-of-sight velocity component contributes the most in observed velocity and flux. Since the velocity components are integrated along the line of sight, this leads to a series of fainter components with velocities changing slightly in a systematic manner and they add up together to give a "winged" emission line profile near the two ends of the cone (Fig. 4.17).

Moving closer towards the center of the galaxy, the volume inside the cone decreases. This leads to less gas to integrate along the line of sight. The velocity variation is also comparatively less because of a much tighter configuration and there is lesser variation in the angle of the velocity vector to the observer. Consequently, we expect a rather symmetric profile near the central part of the galaxies. Parallel to the axis of the cone and towards the outskirts of the galaxy, we trace the edge of the cone according to the wind hypothesis. Although the volume of the cone and the number of gas particles present towards the edge is smaller compared to that of the axis, similar asymmetries are expected though of lesser extent.

We have extracted mock spectra from the simple outflowing wind model we constructed for both our targets along the spatial positions that match the orientation of our slits and have color-coded them by their respective observed velocity (Fig. 4.18 and 4.19). The model spectra, after properly accounting for beam smearing (as we did in the disk model), have been binned spatially to match the ESI extractions. The extracted spectra in different spatial bins are plotted in different rows after being registered to a common wavelength. As in the real data, we see a clear blue-wing in the red-shifted side and a red wing on the blue side for the first galaxy thus agreeing to the wind cone hypothesis for this galaxy. An additional observation from the ESI slit sampling the bi-symmetric feature is that the "blue" wing in the red-shifted side (and vice versa on the other side) has such a big offset from the primary component that it actually lands in the blue-shifted side relative to the systematic velocity. In other words, the velocity offset between the primary and secondary component sometimes exceeds ~ 250 km s^{-1} leading to primary and secondary components to be on opposite sides of the systemic velocity. This has also been reproduced by the wind model and possibly suggests that the cone opening half-angle could be larger than the inclination and it covers the plane of the sky.

For the wind modelling of the second galaxy, although extended wings and the systematic variation across the slit are observed, the amplitude of asymmetry is found to be weaker than the first galaxy. This might be due to the fact that the velocity field obtained from the toy wind model for the second galaxy did not fit the data as well. Further, the emission signal of the second galaxy drops considerably towards the

outskirts, which makes model comparison more difficult.

We compute the asymmetry parameter k as discussed in §4.4.3 for the wind models and compare the k profiles from these simulated spectra to the ESI data and the previously discussed disk models in Fig. 4.20. The salmon and blue shaded regions show the average asymmetry parameter variation, computed by averaging the k values of both Hα and [NII] λ6584 Å emission lines as observed from ESI data, along the bi-symmetric feature for the two target galaxies. The asymmetry parameters obtained from the disk models for those two galaxies are overplotted in dashed lines, while that from the wind model are shown in solid lines. Clearly in either targets, neither the rotating disk nor outflowing wind models fully reproduce the observed asymmetry profiles. Both models are able to reach typical values we observe for k ($\pm 0.2 - 0.25$), but the disk models only achieve these asymmetries near the center, where beam smearing of a strong velocity gradient reaches a maximum. In the galaxy outskirts, the disk model asymmetries nearly vanish while the observed k magnitudes continue to increase. Both wind models reproduce this increased asymmetry in the outskirts, although they fail to match the observed magnitude of k, especially for Target 2. This might be explained generally in the wind interpretation by a clumpy or turbulent outflowing medium. It is harder to explain with a rotating disk which requires a degree of dynamical stability in order to maintain its apparent velocity structure.

4.6 Conclusion

We have performed an analysis of the emission line velocity profiles of Hα and [NII] λ6584 of two red geyser galaxies using high spectral resolution (R$\sim$8000) Keck-ESI observations. Our observations of the first target (MaNGAID: 1-217022) include three slit orientations that sample different parts of the galaxy, namely, the bi-symmetric feature, the regions around the center and the outskirts. The second target (MaNGAID: 1-145922) includes only one slit observation along its bi-symmetric feature. The slits that align with the bi-conical axis for both galaxies show strong asymmetry in the emission lines. The slit that lie parallel to the bi-symmetric feature with an offset for the first galaxy also shows similar asymmetry. The shape of the emission lines, which can be decomposed into primary and secondary velocity components, exhibit a red wing on the blue-shifted part of the galaxy and a blue wing on the red side, with a symmetric profile near the center. This has been quantified by an asymmetry parameter that changes systematically from positive to negative values (Fig. 4.16 and 4.20). A bi-cone geometry of the gas with a radially outward motion can better explain the observed features than a rotating gas disk.

The presence of low-luminosity radio mode AGNs in the red geysers (Roy et al. 2018) along with the confirmation of an outflowing wind scenario obtained from MaNGA data and the current observations from Keck ESI, lead to the evidence of AGN-driven winds in the red geyser galaxies.

Chapter 5

Signatures of inflowing gas in red geyser galaxies hosting radio-AGN

We study cool neutral gas traced by NaD absorption in 140 local ($z < 0.1$) early-type red geyser galaxies. These galaxies show unique signatures in spatially-resolved strong-line emission maps that have been interpreted as large-scale active galactic nuclei driven ionized winds. To investigate the possible fuel source for these winds, we examine the abundance and kinematics of cool gas ($T \sim 100 - 1000K$) inferred from Na I D absorption in red geysers and matched control samples drawn from SDSS-IV MaNGA. We find that red geysers host greater amounts of NaD-associated material. Substantial cool gas components are detected in more than 50% of red geysers (compared to 25% of the control sample) going up to 78% for radio-detected red geysers. Our key result is that cool gas in red geysers is predominantly infalling. Among our 30 radio-detected red geysers, 86% show receding NaD absorption velocities (with respect

to the systemic velocity) between $40 - 50$ km s^{-1}. We verify this result by stacking NaD profiles across each sample which confirms the presence of infalling NaD velocities within red geysers (~ 40 km s^{-1}) with no velocity offsets detected in the control samples. Interpreting our observations as signatures of inflowing cool neutral clouds, we derive an approximate mass inflow rate of $\dot{M}_{in} \sim 0.1 M_{\odot} yr^{-1}$, similar to that expected from minor merging and internal recycling. Some red geysers show much higher rates ($\dot{M}_{in} \sim 5 M_{\odot} yr^{-1}$) that may indicate an ongoing accretion event. [1]

5.1 Introduction

Low-redshift ($z < 0.1$) integral field unit (IFU) spectroscopy from the Sloan Digital Sky Survey-IV (SDSS-IV) Mapping Nearby Galaxies at Apache Point Observatory (MaNGA) survey (Bundy et al. 2015) has revealed a population of moderate mass ($\log M_{\star}/M_{\odot} \sim 10.5$) passive red galaxies ($NUV - r > 5$), known as "red geysers" (Cheung et al. 2016; Roy et al. 2018). These galaxies possess unique emission and kinematic properties that may be signatures of galactic scale (~ 10 kpc), centrally-driven outflows (Cheung et al. 2016; Roy et al. 2021a). The lack of any detectable star-formation (average $\log$ SFR $(M_{\odot}/yr) < -2$, using GALEX+SDSS+WISE from Salim et al. 2016, see Fig. 5.1), the association with low luminosity radio-mode active galactic nuclei (AGN, Roy et al. 2018), and their relatively high occurrence rate on the red sequence (5–10%, see Cheung et al. 2016), makes red geysers a candidate for supplying "maintenance (or

[1] This chapter was previously published in the Astrophysical Journal as **Signatures of inflowing gas in Red geyser galaxies hosting radio-AGN**, Roy, N., Bundy, K., Rubin, K.H.R. et al. 2021, ApJ, 919, 145, DOI:10.3847/1538-4357/ac0f74.

radio)-mode" feedback by low luminosity AGN. While such a feedback process has been widely proposed and studied as a way to suppress star formation at late times (Binney & Tabor 1995; Ciotti & Ostriker 2001; Croton et al. 2006; Bower et al. 2006; Faber et al. 2007; Ciotti et al. 2010; Yuan & Narayan 2014), direct observational evidence in typical quiescent galaxies has remained elusive.

Red geysers are characterized by a distinctive bisymmetric pattern in spatially resolved equivalent width (EW) maps of strong emission lines (Hα, [NII], [OII]). These features extend to $\sim$ 10 kpc, up to the edge of the MaNGA fiber bundle. The emission line flux distributions are also widespread and significantly elevated ($\sim 5-10$ times) along the bi-symmetric feature. The observed gas is possibly ionized by post asymptotic giant branch (AGB) stars with some contribution from shocks, as evident from a combination of LI(N)ER and Seyfert like line ratios in spatially resolved BPT (Baldwin, Phillips & Terlevich, Baldwin et al. 1981) diagrams in these galaxies (Cheung et al. 2016; Roy et al. 2021a). This enhanced emission roughly aligns with the gas kinematic major axis but is strongly misaligned with the stellar velocity gradient.

Accreted gas disks in early type galaxies (Chen et al. 2016; Lagos et al. 2014, 2015; Sarzi et al. 2006; Davis et al. 2013; Bryant et al. 2019; Duckworth et al. 2020) can produce similar misaligned stellar and gas velocity fields so it is important to test the hypothesis that red geysers signal the presence of outflows. Cheung et al. (2016) presented detailed dynamical modeling to conclude that the observed ionized gas velocities in the prototypical red geyser were too high to be in gravitationally bound orbits. More recently, our group used the Keck Echellette Spectrograph and Imager (ESI) to obtain

higher spectral resolution observations (R $\sim$ 8000 compared to R $\sim$ 2000 in MaNGA) of two representative red geysers to find a systematic variation in the asymmetry of the emission line profiles with radius (Roy et al. 2021a). The observed magnitude and nature of the asymmetry along with an increased velocity dispersion (exceeding $\sim$ 230 km s^{-1}) are consistent with line-of-sight projections through a broad conical outflow. The alternative scenario of a puffy, rotating gas disk is unable to fit the data.

An additional set of tests involve the mechanism driving the putative wind. Riffel et al. (2019) studied the nuclear region of the prototypical red geyser in Cheung et al. (2016) with Gemini GMOS (Gemini Multi Object Spectrograph). By comparing the emission line flux distributions and gas kinematics from the inner parts (within 1″) with that of the outer regions (5″ away from center), they concluded that the observed red geyser show signatures of precession. Roy et al. (2018), meanwhile, used the Very large Array (VLA) Faint Images of the Radio Sky at Twenty-Centimeters (FIRST) survey to measure significantly higher ($> 5\sigma$) radio continuum flux in stacked red geyser samples and a three times higher radio detection rate compared to control samples. The study concluded that the red geysers host low luminosity radio AGNs ($L_{1.4GHz} \sim 10^{22} - 10^{23}$ W/Hz) with radiatively inefficient accretion (Eddington scaled accretion rate $\lambda \sim 10^{-4}$). These AGNs are energetically capable, however, of driving sub-relativistic winds consistent with the MaNGA observations.

What is the fuel source for this AGN activity? The presence of warm ionized gas suggests the possibility that red geysers also host cooler gas reservoirs in the interstellar medium (ISM). Cool gas in the form of outflows are routinely observed in

ultra luminous infrared galaxies, star forming and post-starburst galaxies (Cazzoli et al. 2016; Rubin et al. 2012, 2014; Weiner et al. 2009; Alatalo et al. 2016; Martin et al. 2005; Chen et al. 2010; Yesuf et al. 2017; Roberts-Borsani & Saintonge 2019; Coil et al. 2011; Rupke 2018; Veilleux et al. 2020). Indeed, Cheung et al. (2016) studied signatures of cool material traced by NaD absorption in their prototypical red geyser. With a mass estimated at $M_{cool} \sim 10^8$ $M_\odot$, the NaD component occupied one side of the galaxy, kinematically and spatially distinct from the ionized gas and apparently inflowing at ~ 60 km s^{-1} towards the center. An idealized merger simulation run by these authors suggested that the cool gas was being accreted from a companion galaxy.

Detecting gaseous inflows across the galaxy population in general has garnered significant attention, but definitive inflow signatures have been hard to detect (although see Sato et al. 2009; Krug et al. 2010; Rubin et al. 2012; Zheng et al. 2017; Sarzi et al. 2016). The advent of IFU surveys is revolutionizing this field with the measurement of spatially resolved absorption line kinematics in large samples of galaxies (Rupke et al. 2021, Rowlands et al in prep.). Here, the kinematics of cool gas are computed by estimating the doppler shifts of the suitable lines with respect to the systemic velocity after carefully accounting for the stellar continuum (down-the-barrel technique, Roberts-Borsani & Saintonge 2019). This method involves probing the gas lying in front of the galaxy, with the continuum arising due to the illumination by the background stellar light of the galaxy. Redshifted absorption indicates inflows, i.e., the motion of the gas towards the galaxy (or away from the observer along the line-of-sight). Similarly, a blueshifted component suggests outflows. Different tracers are available in

rest-frame UV or optical wavelengths (e.g., Fe II $\lambda\lambda$2586,2600, Mg II $\lambda\lambda$2796,2803, Na I D $\lambda\lambda$5891,5897; Chen et al. 2010; Rubin et al. 2012, 2014; Rupke 2018; Veilleux et al. 2020). In this work we use the resonant Na I absorption doublet at 5891 Å and 5897 Å (referred to as NaD) which traces cool (T $\sim$ 100–1000 K), metal-enriched gas.

An important aspect of measuring the NaD-associated gas kinematics correctly is subtracting the stellar continuum with an appropriate accuracy. This is especially important in early type galaxies, since the evolved K-M type stars present throughout the galaxy can contribute a significant fraction to sodium absorption in the spectrum, thus contaminating the signal from the ISM. There exists several stellar population model libraries (theoretical and empirical) which can be used to estimate the stellar component of NaD absorption generally within a variation of $\sim 10-30\%$. This difference in the continuum estimate due to the specific choice of the stellar model can affect the estimated properties of the ISM gas. Spatially resolved spectra from MaNGA can aid this process significantly by revealing irregularities in the 2D morphology of the NaD absorption. When these spatial irregularities have no correspondence with the stellar velocity and the surface brightness distribution, we can be more confident that they are associated with the ISM.

The goal of this work is to address how frequent the cool gas as traced by NaD is within the red geyser sample and whether these cooler gas reservoirs are associated with inflows towards the center, similar to the prototypical red geyser, or with the outflowing wind triggered by the AGN. We will also study if there exists any possible correlation between radio properties and the presence of cool gas, by conducting our analyses on

samples split by radio detection. We analyze the spatially resolved, globally integrated and stacked kinematics of NaD from the red geyser sample and compare them with a matched control sample. We find that the red geysers, specially those which are detected in FIRST, have higher NaD EW on average and 78% of the sample show detectable ISM gas over a projected spatial extent > 5 kpc. This fraction is many times higher compared to the radio-detected control (41%) and non radio detected control (25%) galaxies. The kinematics is observed to be redshifted on average ($\sim 40 - 50$ km s^{-1}) in about $\sim 86\%$ of radio-detected red geysers, implying that most of the gas is inflowing into the galaxy possibly fuelling the central active black hole.

§5.2.1 give a brief overview of the optical data from MaNGA that we have used in this work and in §5.2.2 we describe the sample selection process of the red geyser and control galaxy samples from the MaNGA quiescent population. The technical details of the stellar continuum modeling, equivalent width estimation, absorption line fitting and kinematics calculation are narrated in sub-sections §5.3.1, §5.3.2 and §5.3.3. The results of the analyses are described in §5.4 and the implications and concluding remarks are discussed in §5.5 and §5.6. Throughout this paper, we assume a flat cosmological model with $H_0 = 70$ km s^{-1} Mpc^{-1}, $\Omega_m = 0.30$, and $\Omega_\Lambda = 0.70$, and all magnitudes are given in the AB magnitude system.

5.2 Data Acquisition and Sample Definitions

5.2.1 The MaNGA survey

We use data primarily from the recently completed SDSS-IV MaNGA survey (Blanton et al. 2017; Bundy et al. 2015; Drory et al. 2015; Law et al. 2015; Yan et al. 2016; Albareti et al. 2017). MaNGA is an integral field spectroscopic survey that provides spatially resolved spectroscopy for nearby galaxies (z $\sim$ 0.03) with an effective spatial resolution of 2.5″ (full width at half-maximum; FWHM). The MaNGA survey uses the SDSS 2.5 meter telescope in spectroscopic mode (Gunn et al. 2006) and the two dual-channel BOSS spectrographs (Smee et al. 2013) that provide continuous wavelength coverage from the near-UV to the near-IR: $3,600 - 10,000$ Å. The spectral resolution varies from R $\sim$ 1400 at 4000 Å to R $\sim$ 2600 at 9000 Å. An r-band signal-to-noise (S/N) of $4 - 8$ Å^{-1} is achieved in the outskirts (i.e., $1 - 2$ R$_e$) of target galaxies with an integration time of approximately 3-hr. MaNGA has observed more than 10,000 galaxies with log $(M_*/M_\odot) \geq 9$ across $\sim$ 2700 deg^2 over its 6 yr duration. In order to balance radial coverge versus spatial resolution, MaNGA observes two thirds of its galaxy sample to $\sim$ 1.5 R$_e$ and one third to 2.5 R$_e$. The MaNGA target selection is described in detail in Wake et al. (2017).

The raw data are processed with the MaNGA Data Reduction Pipeline (DRP) (Law et al. 2016). An individual row-by-row algorithm is used to extract the fiber flux and derive inverse variance spectra from each exposure, which are then wavelength calibrated, flat-fielded and sky subtracted. We use the MaNGA sample and data products

drawn from the MaNGA Product Launch-9 (MPL-9) and Data Release 16 (DR16, Ahumada et al. 2020). We use spectral measurements and other analyses carried out by MaNGA Data Analysis Pipeline (DAP), specifically version 2.3.0. The data we use here are based on DAP analysis of each spaxel in the MaNGA datacubes. The DAP first fits the stellar continuum of each spaxel to determine the stellar kinematics using the Penalised Pixel-fitting algorithm `pPXF` (Cappellari & Emsellem 2004; Cappellari 2017) and templates based on the MILES stellar library (Falcón-Barroso et al. 2011). The templates are a hierarchically clustered distillation of the full MILES stellar library into 49 templates. This small set of templates provide statistically equivalent fits to those that use the full library of 985 spectra in the MILES stellar library. The emission-line regions are masked during this fit. The DAP then subtracts the result of the stellar continuum modeling to provide a (nearly) continuum-free spectrum that is used to fit the nebular emission lines. This version of the DAP treated each line independently, fitting each for its flux, Doppler shift, and width, assuming a Gaussian profile shape. The final output from the DAP are gas and stellar kinematics, emission line properties and stellar absorption indices. All the spatially resolved 2D maps shown in the paper are outputs from the DAP with hybrid binning scheme. An overview of the DAP used for DR15 and its products is described by Westfall et al. (2019), and assessments of its emission-line fitting approach is described by Belfiore et al. (2019).

We use ancillary data drawn from the NASA-Sloan Atlas[2] (NSA) catalog which reanalyzes images and derives morphological parameters for local galaxies observed in

[2] http://www.nsatlas.org

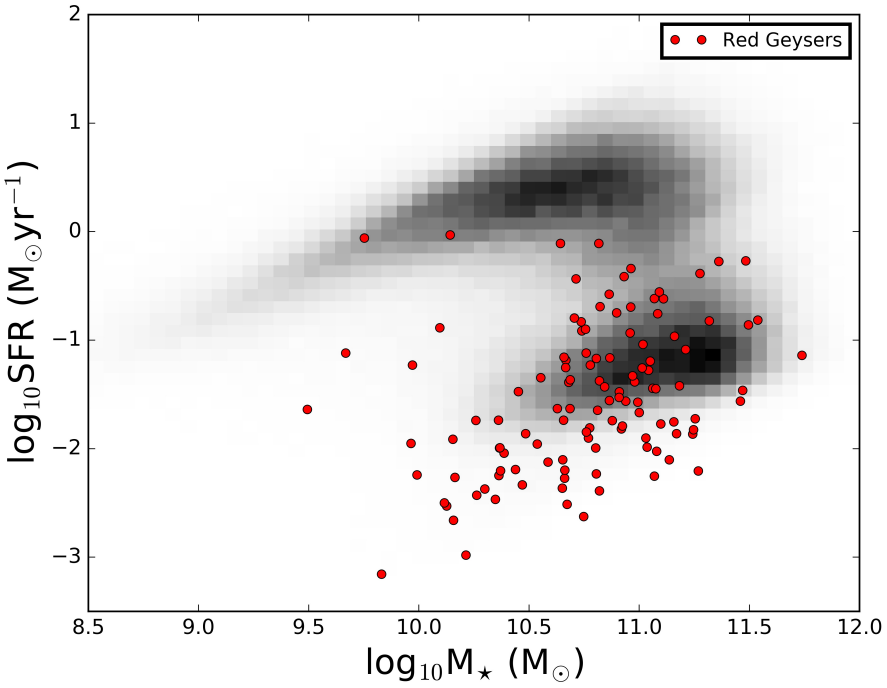

Figure 5.1: The figure shows the log SFR vs log $M_\star$ as obtained from GALEX+SDSS+WISE catalog of Salim et al. (2016). The gray 2D histogram shows all the MaNGA galaxies in the catalog with $0.01 < z < 0.1$. The red circles signifies red geyser galaxies. Most of the galaxies in our chosen geyser sample have a low log SFR value, with an average of ~ 0.01 $M_\odot yr^{-1}$.

Sloan Digital Sky Survey imaging. It compiles spectroscopic redshifts, UV photometry (from GALEX; Martin et al. 2005), stellar masses, and structural parameters. We have specifically used spectroscopic redshifts and stellar masses from the NSA catalog.

5.2.2 Sample definitions

Red Geysers are early type galaxies (ETGs) lying in the red sequence (NUV − r > 5) which have little-to-no ongoing star formation activity. Fig. 5.1 shows the star formation rates (SFR) of the red geyser sample (red circles) compared to all MaNGA

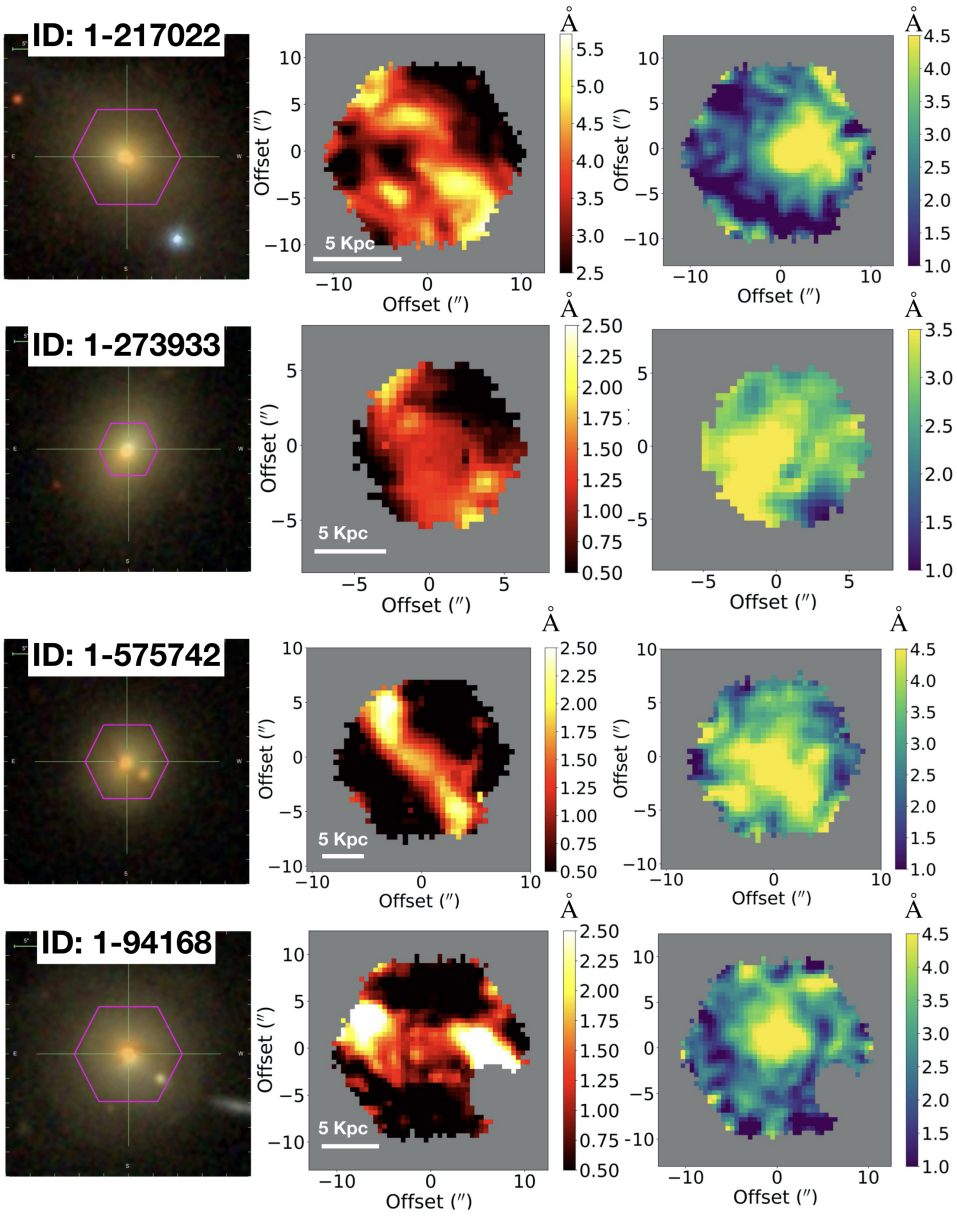

Figure 5.2: The spatially resolved emission and absorption line properties of 4 example red geysers (MaNGAID-1-217022, 1-273933, 1-575742 and 1-94168) from SDSS-IV MaNGA. The left panels show the optical images of the galaxies from SDSS with the MaNGA IFU overlaid on top in magenta. The on-sky diameter of the IFU fibers shown here range from 12″ to 22″ corresponding to physical size of roughly 10−20 Kpc. The middle panels show the Hα Equivalent width (EW) maps (observed-frame units in Å) showing the signature bi-symmetric pattern identifying the red geyser class, and the right panels show the EW map of NaD absorption (in Å) which includes both stellar and cool ISM gas component.

galaxies (grey) from Salim et al. (2016) catalogue. This catalog derives SFR from ultra-violet/optical spectral energy distribution (SED) fitting with additional constraints from mid-infrared data using GALEX-SDSS-WISE. The typical value of SFR for the red geysers is ~ 0.01 $M_{\odot}$ yr^{-1}. The sample of red geysers used here is derived from MaNGA Product Launch 9 (MPL-9) and consists of 140 galaxies which accounts for $\approx 6-8\%$ of the local quiescent galaxy population observed by MaNGA. The red geyser sample is visually selected based on their characteristic features, as described in detail in Cheung et al. (2016); Roy et al. (2018, 2021a). They are briefly outlined below:

- Spheroidal galaxies with no disk component as observed by SDSS and low star formation rate.
- Bi-symmetric feature in spatially resolved EW map of strong emission lines like Hα, [NII] and [OIII].
- Rough alignment of the bi-symmetric feature with the ionized gas kinematic axis, but misalignment with stellar kinematic axis.
- High spatially resolved gas velocity values, typically reaching a maximum of $\pm$ 300 km s^{-1}, which are greater than the stellar velocity values by at least a factor of $4-5$.
- High gas velocity dispersion values, reaching about $\sim 220-250$ km s^{-1} in distinct parts of the galaxy.
- Predominantly showing LINER or Seyfert type line ratios in the spatially resolved

BPT diagrams.

Four example red geysers are shown in Fig. 5.2. The optical images (left panels) from SDSS show spheroidal morphologies typical of these galaxies. The middle panels show the characteristic bi-symmetric feature in the Hα EW map. The right panels show the NaD EW map obtained using MaNGA-DAP (see §10 in Westfall et al. (2019) for details). The DAP performs the spectral index measurements after first subtracting the best-fit emission-line model from the observed spectrum. It does not perform any stellar continuum subtraction on the NaD feature, hence the observed EW shows the presence of both the stellar and the ISM component. However the NaD maps show highly anisotropic and clumpy spatial morphology, indicating that a major portion of the observed NaD absorption is likely contributed by ISM gas. We also find that the regions with high NaD EW are spatially offset from the bi-symmetric feature observed in Hα map suggesting the presence of multiphase gas components tracing different activities in these galaxies.

Roy et al. (2018) cross-matched the red geyser sample with VLA-FIRST catalog to identify the radio detected red geysers. For the latest sample from MPL-9, we have an updated list of radio detected red geysers consisting of 30 galaxies.

We construct a control sample of spheroidal quiescent galaxies which are matched in global properties, namely stellar mass, color, redshift and axis ratio, but do not show the resolved geyser-like features as described previously. For each red geyser, we match up to four quiescent galaxies (having NUV $-$ r $>$ 5) with the following

criteria:

- $\log M_{\star,\text{red geyser}}/M_{\star,\text{control}} < 0.2$ dex
- $z_{\text{red geyser}}$ - $z_{\text{control}} < 0.01$
- $b/a_{\text{red geyser}}$ - $b/a_{\text{control}} < 0.1$

where $M_\star$ is the stellar mass, z is the spectroscopic redshift, and b/a is the axis ratio from the NSA catalog. This technique results in 458 unique control galaxies with 65 of them detected in FIRST. These constitute the radio-detected control sample.

5.3 Data Analysis

5.3.1 Stellar continuum fitting

The sodium doublet feature can arise from photospheric transitions in evolved cool stars, as well as from cool neutral gas in the ISM. Since our samples consist of red and quiescent galaxies with evolved stellar populations, the presence of K-M type stars throughout the galaxy are likely to make up a major fraction of the spectral NaD profile (Jacoby et al. 1984; Tyson & Rich 1991) with the residual absorption attributed to the ISM component. On the other hand, since the primary contribution in the Magnesium triplet MgIλ5167,5173,5184 Å (Mg b) absorption is from the stars, studies of star-forming galaxies have found a linear relation between the EW of Mg b and NaD from the stellar component alone (Alatalo et al. 2016). Inspite of the observed scatter around

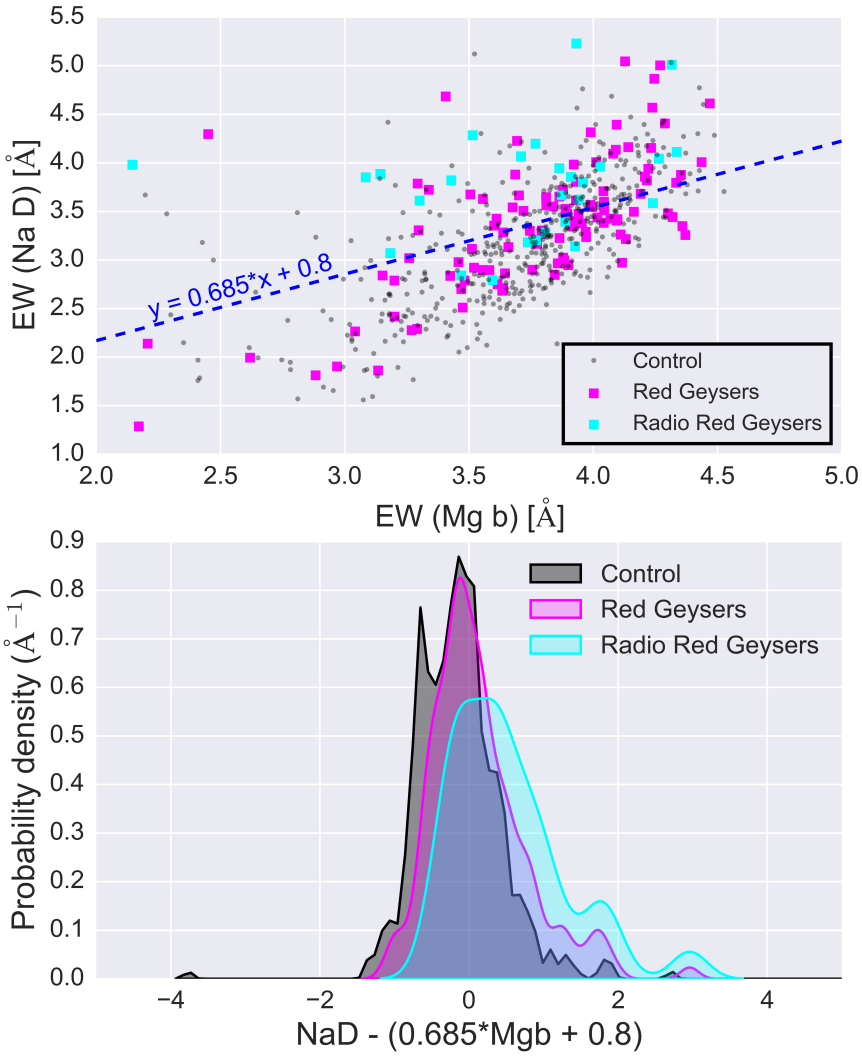

Figure 5.3: [Upper panel] Equivalent widths EW(NaD) vs. EW(Mg b) of the red geysers (magenta squares) and control sample (grey circles). The FIRST-detected radio red geysers are marked in cyan. The dashed blue line represents the empirical relation from stellar component only found in Alatalo et al. (2016) for star-forming galaxies. Any object above the relation is expected to have a dominant ISM contribution in NaD. [Lower panel] Probability density functions for the Na I D EW, measured with respect to the mean Alatalo et al. (2016) relation: EW(Na D) = 0.685*EW(Mg b)+0.8 (indicated by blue dashed line in the upper panel) for the different subsamples. The radio-detected red geysers (cyan) show a clear departure from the other two distributions, with a large fraction of objects showing excess NaD compared to their Mgb.

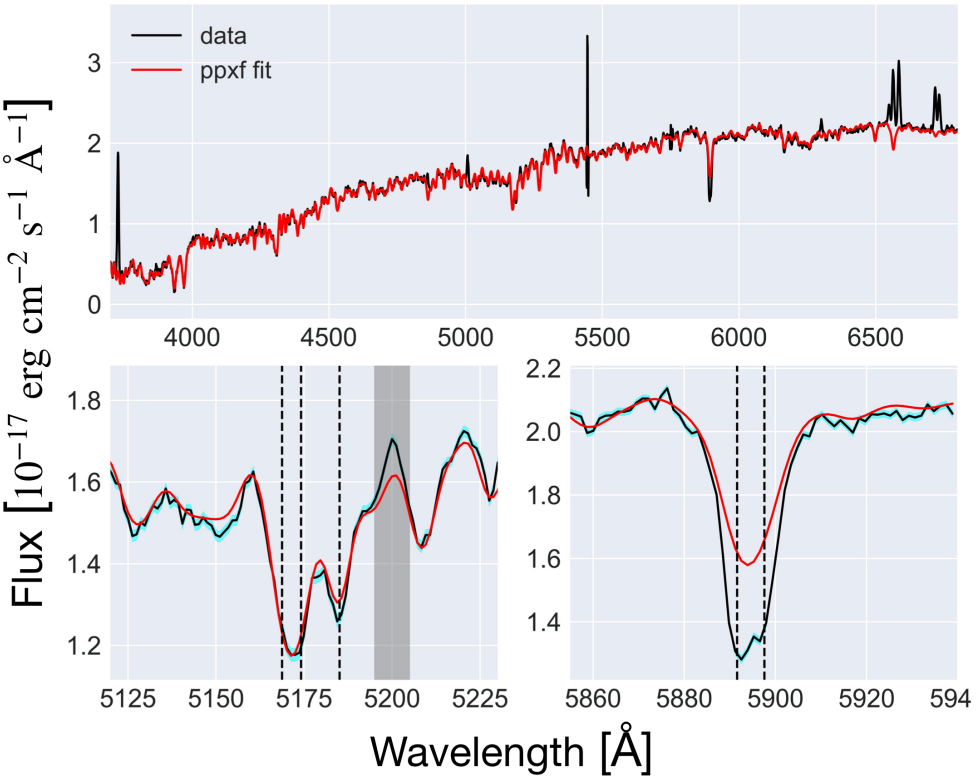

Figure 5.4: The top panel shows an example MaNGA spectrum in black. The best fit stellar continuum obtained from ppXF fit using MIUSCAT stellar population models, as described in §5.3.1, is overplotted in red. The result of the continuum fit around Magnesium triplet (Mg b) and Sodium doublet (NaD) absorption lines are shown in the left and right subplots in the bottom panel respectively. 1-σ errors in the observed spectra are shown in the bottom panels in cyan. The gray shaded region in the lower left panel highlight the [NI] emission line at 5200 Å.

the empirical relation in Alatalo et al. (2016), any enhancement in NaD compared to Mgb beyond the relation likely indicates the ISM contribution.

Fig. 5.3 (upper panel) compares the EW of NaD and Mgb of red geysers (in cyan and magenta squares, representing radio-detected and non-radio-detected galaxies from FIRST survey respectively) and the control sample (in grey circles), obtained by averaging the EW measured by the MaNGA DAP (that includes NaD absorption from both stellar and ISM component) over all spaxels within one effective radius. The figure shows that a large fraction of the galaxies in the radio-detected red geyser sample have a considerable excess in NaD lying above the Alatalo et al. (2016) empirical relation (blue dashed line).

This is further confirmed by the lower panel in Fig. 5.3, which shows the probability density function (PDF) of the deviation of NaD EW distribution with respect to the Alatalo et al. (2016) relation. We find that a large fraction of radio-detected red geysers show an excess amount of NaD, as indicated by the clear positive wing in the distribution, compared to the other two samples. Infact, 75% of the radio-red geyser sample lie above the relation, which compares to 51% in non-radio detected red geysers and only 32% in the control sample. This indicates an elevated abundance of cool gas within radio-detected red geysers and a possible correlation with the presence of radio-detected AGNs that we will return to below.

It is to be noted from Fig. 5.3 that there exist a notable amount of NaD deficit at low Mgb particularly for the control galaxies. This is likely caused by the in-filling of the resonant NaD emission line which has been previously detected in integrated,

stacked as well as spatially resolved NaD spectrum (Alatalo et al. 2016; Chen et al. 2010; Rupke et al. 2021). The non-radio detected red geysers, on the other hand, show roughly an equal fraction of galaxies with NaD deficit (at low Mgb) and excess (at high Mgb) with a rather symmetric distribution overall.

The next step is to accurately model out the stellar continuum contribution to the NaD absorption in order to extract the residual gaseous component. First, we mask spaxels with low or no spectral coverage, low signal-to-noise and having foreground stars, unreliable fits or noisy observations as flagged by MaNGA under the mask-bit names `NOCOV, LOWCOV, FORESTAR, UNRELIABLE` and `DONOTUSE`. Then, following Rubin et al. (in prep), we bin and stack the spectra in $2'' \times 2''$ spatial bins (or spaxels) to acquire a good continuum signal to noise (S/N>10 per dispersion element) per bin throughout the galaxy.

We then fit the stellar continuum for each spatial bin with ppxf (Penalized Pixel Fitting, Cappellari & Emsellem 2004; Cappellari 2017) which fits a linear combination of simple stellar population (SSP) model templates. Here, we make use of the MIUSCAT SSP (Vazdekis et al. 2012), although a detailed comparison with other SSP models is presented later. Strong emission line regions are masked during the fit. We also mask the region around the NaD transition, as we assume that the doublet is a result of stellar + ISM contribution and hence should not be fit by the model. We also mask the red half of the He I emission line at 5875.67 Å, which is close enough to the NaD line that it could affect the residual profile. An example spectrum and its continuum fit is shown in Fig. 5.4. The stellar continuum model shows a satisfactory fit, with minimal residuals

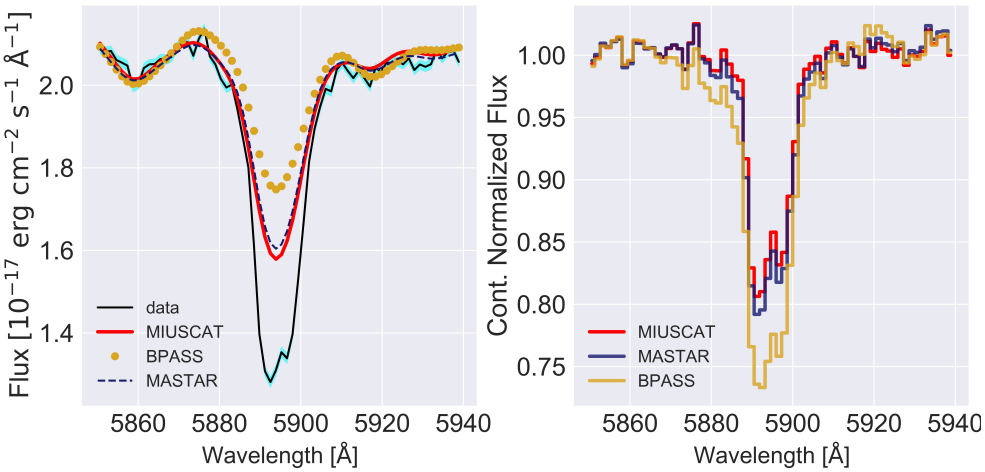

Figure 5.5: Left panel shows the modeled stellar continuum obtained by using three different stellar population models (MIUSCAT, BPASS and MASTAR) in different colors and line styles, overplotted on the observed NaD absorption spectra in black. 1-σ error of the observed NaD spectrum is shown in cyan. Right panel shows the corresponding continuum normalized residual NaD indicating contribution from the ISM.

around Mg b and an excess around NaD, which hints at the presence of ISM gas.

To remove the stellar continuum and isolate the ISM component, the spectrum in each bin is divided by the best corresponding continuum fit. We additionally fit a first-order polynomial to the continuum-normalized spectrum in the wavelength range immediately (20 Å) blueward and redward of the NaD profile and divide the residual by the polynomial fit. This is to account for any systematic errors in continuum fitting that might give rise to artificial residuals.

We now examine the robustness of our stellar continuum modeling to the assumed stellar library. We repeat the above continuum fitting process for 10 galaxies in each of red geyser and control sample across every spatial bin using two additional libraries, namely MaStar (Yan et al. 2019), an empirical library constructed using the

MaNGA instrumentation, and BPASS (Eldridge et al. 2017), a theoretical template library. The BPASS SSP models are drawn from the v2.2.1 release that adopted the default BPASS initial mass function [3]. SSPs over a range of log age (in Gyr) from -1.2 to 1.1, with stellar metallicity mass fractions Z=0.008, 0.02, and 0.03, are included. The BPASS fitting will be described in full in Parker et al. (in prep).

An example of the variation of the stellar contribution owing to the different stellar population models is shown in the left panel of Fig 5.5. The different colors indicate the SSPs used to construct the stellar model. The right panel shows the continuum normalized NaD spectra using those same SSPs. We find that the fractional difference in NaD EW of the continuum-normalized spectra, computed using the MASTAR and the MIUSCAT models, range between 5-15 % in the ten red geyser galaxies studied. However, the BPASS model can change the estimated EW by about 25-30%, compared to the other two models. The BPASS is the result of combining theoretical model spectra with as few empirical inputs as possible. Hence this differs largely from the two other stellar models (MIUSCAT and MASTAR) which are based on empirical libraries. Preliminary work has revealed that the BPASS continuum model may be under-predicting the amount of NaD coming from stellar atmospheres (Parker et al. in prep). On the other hand, the stellar models from MIUSCAT and the MASTAR models, drawing on empirical libraries, likely contain some interstellar NaI absorption from the Milky Way, overpredicting NaD absorption from stars. Thus, the three models are different and are shown to explore a broad range of parameter space in stellar continuum modeling and

[3]These are freely available at https://bpass.auckland.ac.nz/9.html

their effect in our analyses.

Although the equivalent width value of the continuum normalized NaD spectra changes owing to the different stellar models, the velocity difference is negligible ($<$ 5 km s^{-1}), as shown by the example in Fig 5.5. Among the three libraries we tested, we use the MIUSCAT SSPs in what follows because this particular set of models yields the most conservative (lowest) value of inferred NaD ISM contribution.

5.3.2 Equivalent Width Calculation

Once the spectrum is continuum-normalized, the strength of the NaD absorption arising from the ISM is quantified by the equivalent width (EW). EW is measured as follows:

$$\mathrm{W} = \mathrm{h}_\lambda \sum_{\mathrm{j}=1}^{\mathrm{M}} \left[1 - \frac{\mathrm{F_j}}{\mathrm{F_c}} \right] \tag{5.1}$$

where h_λ denotes the dispersion in wavelength in Å/pixel, M is the number of individual pixels that together constitute the desired wavelength interval which includes 20 Å immediately blueward and redward surrounding and including the NaD absorption feature, and $\mathrm{F_j}/F_\mathrm{c}$ is the continuum normalized flux for each of those pixels.

5.3.3 NaD line fitting using Bayesian inference

After continuum-normalizing the spectra as discussed in §5.3.1, we want to determine the kinematics of the neutral gas present in our galaxy samples. We perform a "detection" test for every spaxel to determine the significance of the ISM component

in the NaD spectra with the following criteria:

1. The depth of the absorption trough in the residual spectra must be at least $\sim 10\%$ of the continuum level.

2. The equivalent width measured from the residual ISM component must be > 0.3 Å.

3. The S/N of each spectrum > 10 per dispersion element.

The primary reason behind taking such restrictive criteria is to prevent biases from low signal-to-noise (S/N) spectra with extremely small inferred residuals which would provide inaccurate kinematic estimates from erroneous model fits. As discussed later, input spectrum with S/N < 10 gives an error of up to ~ 20 km s^{-1} in measured velocities which can be marginally close to the observed velocity amplitudes we wish to investigate. Requiring spectra with S/N > 10 ensures that the velocity errors remain within acceptable limits.

The NaD spectral feature in the spaxels which satisfy all the requirements are then modelled with an analytical function (Rupke et al. 2005), which takes the following form:

$$I(\lambda) = 1 - \mathrm{C_f} + \mathrm{C_f} \times \mathrm{e}^{-\tau_\mathrm{B}(\lambda) - \tau_\mathrm{R}(\lambda)} \tag{5.2}$$

where C_f is the velocity-independent covering factor, and $\tau_\mathrm{B}(\lambda)$ and $\tau_\mathrm{R}(\lambda)$ are the optical depths of the Na I λ 5891 Å and Na I λ 5897 Å (vacuum wavelength) lines, respectively. The optical depth of the line, $\tau(\lambda)$, can be expressed as:

$$\tau(\lambda) = \tau_0 \times \mathrm{e}^{-(\lambda-\lambda_0+\Delta\lambda_{\mathrm{offset}})^2/((\lambda_0+\Delta\lambda_{\mathrm{offset}})\mathrm{b_D/c})^2} \tag{5.3}$$

where τ_0 and λ_0 are the central optical depth and central wavelength of each line component, respectively, b_D is the Doppler line width, and c is the speed of light. The wavelength offset is converted from a velocity offset, given by $\Delta\lambda_{offset} = \Delta v\lambda_0/c$. For NaD, $\tau_{0,B}/\tau_{0,R} = 2$. The optical depth parameter can be derived from the column density of sodium described as :

$$N(\mathrm{NaI}) = \frac{\tau_0 \mathrm{b}}{1.497 \times 10^{-15}\lambda_0 \mathrm{f}} \tag{5.4}$$

where λ_0 and f are the rest frame wavelength (vacuum) and oscillator strength, respectively. Throughout this study we assume $\lambda_0 = 5897.55$Å and f = 0.318 (Morton 1991).

The absorption feature is fitted here using a single kinematic component. Fitting the neutral gas absorption with one component is certainly an over-simplification in a scenario where contributions from more than one gas cloud along the line of sight are embedded within a single line profile. However, this approach allows us to characterize the global kinematics obtained from the data. The absorption model is convolved with MaNGA's instrumental resolution ($\sim$ 65 km s^{-1}) before performing the fit.

In order to explore possible degeneracies, obtain unbiased fits, and estimate the errors, we wrap our fitting procedure in a Bayesian inference approach using the Dynamical Nested Sampling algorithm (Higson et al. 2019) as implemented in the Python

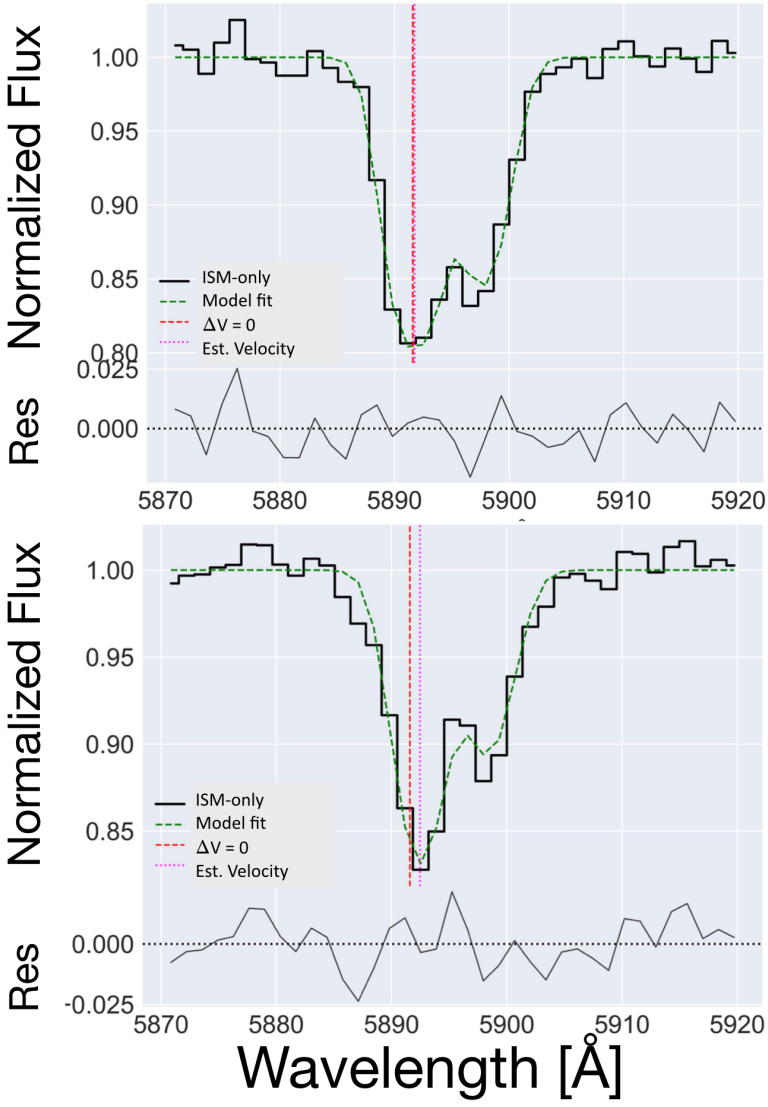

Figure 5.6: The two panels show the modeling of continuum-normalized NaD spectra using Rupke et al. (2005) absorption model for two different spaxels of a red geyser (MaNGA ID: 1-217022). The observed spectra are shown in black, the best fit models in green, and the wavelengths corresponding to the estimated velocities in magenta. The bottom subpanels below the main plots show the residuals of the fits.

package, `dynesty` (Speagle 2020). Nested Sampling (Skilling 2004) estimates both the Bayesian evidence and posterior distributions in an iterative fashion until the convergence criteria is met. The method has the flexibility to sample from complex, multi-modal distributions using adaptive sampling to maximise the accuracy and efficiency of the fitting process. The greater flexibility and the ability to compute Bayesian evidence (Z) on top of posteriors are advantages compared to traditional Marcov Chain Monte Carlo (MCMC) methods. The default stopping criterion for `dynesty` is used in our analyses with no limitation on the maximum number of iterations. We have set reasonable priors in our MCMC fitting routine: the line width is constrained within ± 100 km s^{-1} around the stellar line width obtained from the continuum model and the limits on the allowed velocity are set at ± 500 km s^{-1}. The covering fraction takes values within 0 and 1. No constraints are placed on the column density parameter. Fig. 5.6 shows two examples of model fits applied to two different spatial bins of a red geyser (MaNGA ID: 1-217022). The residuals vary from $2-5\%$, indicating an acceptable model fit.

For each input spectrum, our procedure delivers estimates of the column density, velocity, line width, and the covering fraction. The best fit velocity with respect to the systemic velocity is assigned to the kinematics of the neutral ISM at that location.

As a key aspect of this paper is a characterization of the global NaD kinematics in our red geyser sample, it is important to test the robustness of our velocity measurements for systematic biases. Such biases might be expected: we are fitting an asymmetric absorption doublet model to the spectral residual obtained after subtracting a broadened and possibly offset version (from the stellar continuum) of a similar

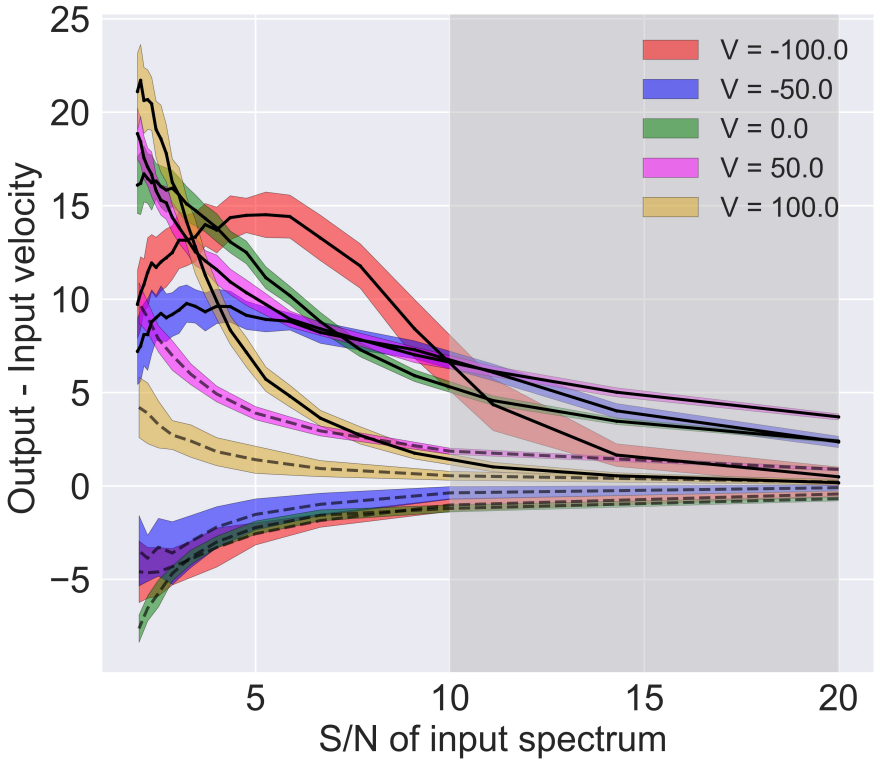

Figure 5.7: Difference between the input velocity (V) of the ISM component used to simulate the mock NaD absorption spectra and the retrieved velocity obtained with our velocity estimation analysis vs. the signal-to-noise ratio used in the mock simulation. Each color represents 'true' ISM velocities used for simulating the data. Colored shaded regions depict 1σ error regions on the difference. The solid lines are for realistic sodium doublet absorption profiles while dashed lines are for doublet profiles which are mirror images of the former. Grey shaded region indicates the S/N in our observed spectrum. This shows the bias in our velocity retrieval process.

doublet model.

We begin by generating a synthetic stellar NaD absorption spectra assuming a Gaussian stellar velocity profile of amplitude and width as observed from the stellar continuum model of our example galaxy with MaNGAID−1-217022. The mean of the Gaussian is set to the systemic velocity of the galaxy. We simulate the ISM component using the doublet absorption model of Rupke et al. (2005) with average values set for each parameter, namely, column density= 2.9×10^{13} cm^{-2}, line width (σ) = 150 km s^{-1} and covering fraction = 0.2. These parameter values were obtained by fitting the observed NaD-ISM spectra for the same galaxy with the same Rupke et al. (2005) model. Mock spectra are created for five assumed input velocity offsets (-100 km s^{-1}, -50 km s^{-1}, 0 km s^{-1}, 50 km s^{-1} & 100 km s^{-1}) relative to the systemic velocity. We convolve the resultant profile with the instrumental resolution of MaNGA and then add normally-distributed noise to the simulated spectra. We perform the above process for different signal-to-noise values ranging from 1 to 20 at each input velocity. We fit the resultant spectra and retrieve the model parameters according to the technique described above and in §5.3.1. The error estimates on the retrieved velocities are obtained by bootstrapping the simulated 'data'.

The difference in the retrieved versus input velocities for different values of signal-to-noise ratios are shown in the Fig. 5.7 via solid lines. Each colored line represents a different initial velocity offset value. The plot reveals systematic biases that result from our model fitting and velocity retrieval process. We see that a modest positive (redshifted) bias exist, but for at S/N >10 per dispersion element (grey shaded

region), similar to the noise level in the NaD spectra used in our analyses, the bias in all cases is less than ~ 5 km s^{-1}. As we show, this systematic error is roughly an order of magnitude smaller than the average velocity offsets we detect in our red geyser samples.

Such a bias probably arises due to the combination of the inherent shape of the subtracted stellar component as well as the interstellar component of the NaD doublet feature. To check that, we produce similar mock NaD spectra as before, but this time we reverse the shape of the doublet feature, while keeping the stellar absorption model same. We perform a similar velocity retrieval process and the results are shown in dashed lines. We see that the bias has now switched to the negative side for input velocities < 0 and show a much smaller positive bias compared to the previous exercise for positive velocities. Varying one or a combination of other parameters like column density, covering fraction or line width has no impact on the amplitude of the bias.

5.3.4 Stacking optical spectra and interpretation of stacked kinematics

In what follows, we will be interested in the average behavior of the NaD ISM component across various subsamples as a check on our model fits of spatially-binned spectra in individual galaxies. To compute spatially-integrated spectra per galaxy, we shift the spectra from each spaxel to the rest frame of the galaxy and continuum normalize them before coaddition to remove the stellar contribution by method discussed in §5.3.1. After generating a pure-ISM spectra from each spaxel, we construct a circular radius of $8''$ in each galaxy (which is roughly the angular scale corresponding to the average effective radii of our targets) and include only those spaxels within the radius

which satisfy the detection criteria. This is done to remove low signal-to-noise spaxels as well as spaxels near the extreme edge of the IFU. We co-add the spectra and perform weighted averages where the weights are the S/N of each spectrum used in the stacking. The spatially integrated velocity thus obtained represents the average kinematics from the particular galaxy. Once we obtain an integrated spectrum for each galaxy, we also compute a stacked spectrum across each galaxy sample.

5.4 Results

With the ISM component of the NaD absorption spectra extracted, we derive estimates of the equivalent width, column density, and kinematics to search for potential differences between red geysers and normal galaxies. Our four samples of interest include 30 radio-detected red geysers (radio-RG), 110 non-radio-detected red geysers (nonradio-RG), 65 radio-detected control sample galaxies (radio-CS) and 393 non-radio-detected control galaxies (nonradio-CS). We will compare these samples to investigate the frequency and strength of ISM NaD absorption in red geysers, both with and without radio AGN. Finally we will investigate the NaD kinematics.

5.4.1 Fractional contribution of Interstellar NaD absorption in red geysers

We begin by evaluating the fractional contribution of the ISM component to the total NaD absorption in our sample of 140 red geysers. After fitting the stellar continuum according to the method described in §5.3.1 we calculate the mean EW of

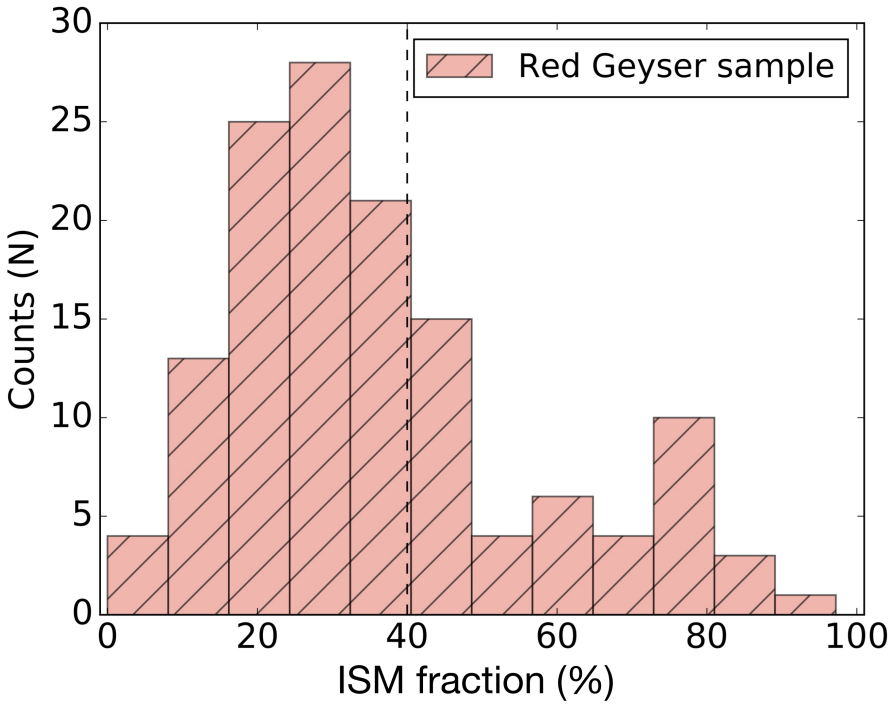

Figure 5.8: The distribution of mean percentage of ISM contribution in the NaD doublet absorption profile as observed in the red geyser galaxy sample. Dashed line separates red geyser galaxies with ISM fraction $> 40\%$, which is greater than twice the typical fraction observed in control galaxies.

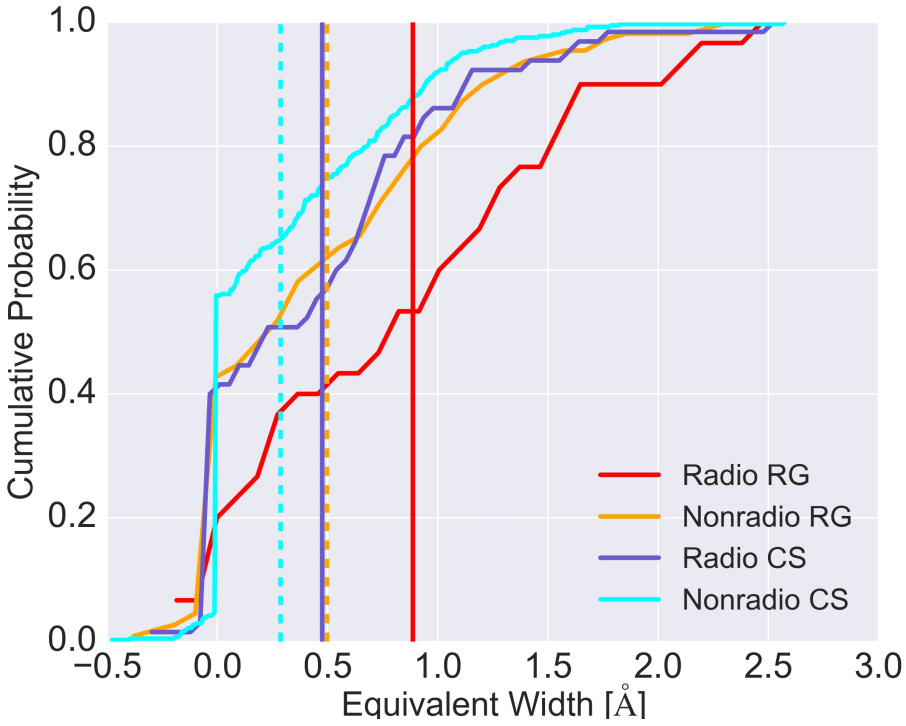

Figure 5.9: Cumulative distribution function showing the comparison of the distribution of mean NaD-ISM EW (computed by averaging over a circular radius of 8″) between four different samples - radio detected red geysers (red), non radio detected red gesyer (orange), radio detected control (blue) and non radio detected control (cyan) galaxies. The mean of each distribution is shown by same-colored solid (radio-detected galaxies) and dashed (non radio detected samples) lines. The radio detected red geyser shows the highest mean EW of = 0.9 Å and quite different distribution than control samples.

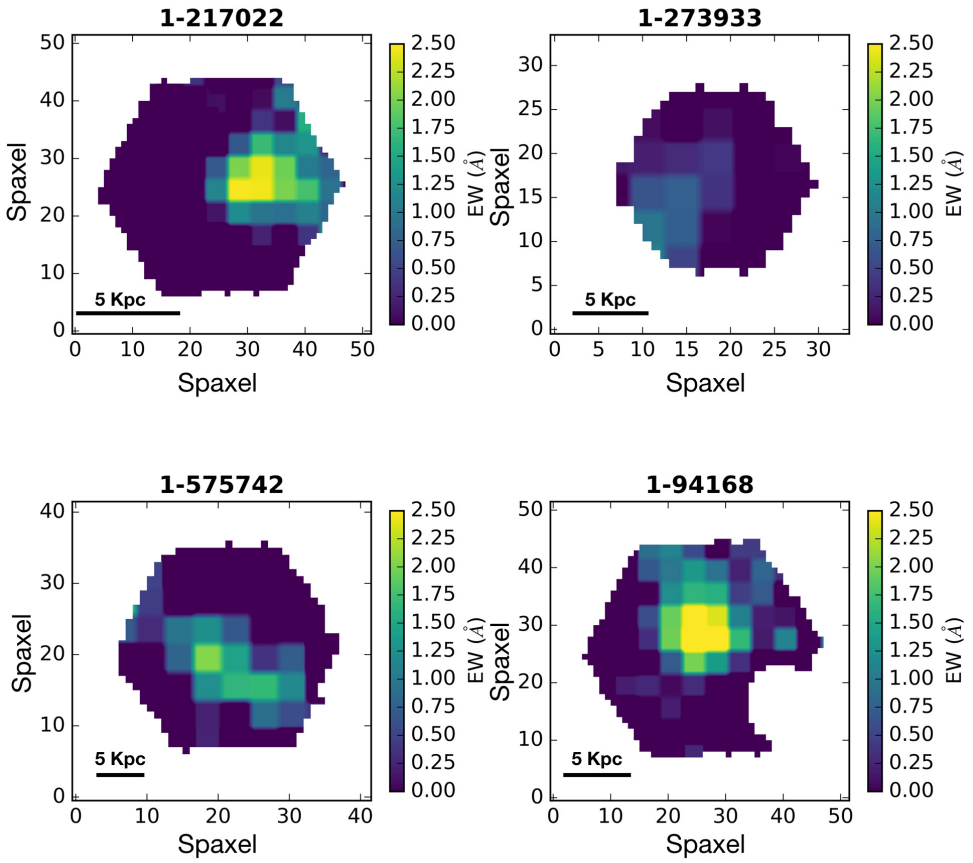

Figure 5.10: Spatially resolved NaD EW maps for four red geysers (MaNGA ID: 1-217022, 1-273933, 1-575742 and 1-94168) derived from the spaxel-wise continuum-normalized NaD spectra for each galaxy. Since the stellar continuum has been factored out, the displayed EW comes entirely from the ISM component. Out of the four red geysers shown here, three are radio detected (MaNGA ID: 1-217022, 1-273933, 1-94168).

the continuum normalized NaD-ISM spectra for each red geyser galaxy by averaging over those spaxels that satisfy the 'detection test' described in §5.3.3. We then compute the ratio of the NaD EW from the ISM component to the total EW derived from the original spectra. The distribution of this ratio for the entire red geyser sample is presented in Fig. 5.8.

Since passive early type galaxies are dominated by evolved stellar population which is the major contributor to the NaD absorption feature, the fraction of ISM component in the NaD EW is generally observed to be low. The fraction is $< 20\%$ in majority (80%) of the control galaxies. On the other hand, we find that in 50 out of 140 red geysers (i.e., 35% of the sample), the fractional ISM contribution is $> 40\%$, i.e. greater than twice the typical fraction observed in the control galaxies. 77 red geysers (i.e., 55% of the sample) have ISM fraction $> 30\%$. If we consider the spatially resolved map for each galaxy, roughly 56% of the red geyser sample show an appreciable presence of ISM gas(i.e., spaxels satisfies the detection criteria in §5.3.3) over a projected area of $\geq 5 \times 5$ kpc^2. The fraction increases to 78% if we consider only the radio detected red geyser sample. This compares to a mere 25% for the entire control sample and 41% for the radio detected control galaxies.

5.4.2 Comparison of mean EW in radio detected red geysers vs. control sample

Having shown that detections of substantial ISM components are 2–3 times more common among red geysers, we now investigate whether this implies that the total

amount of NaD-associated gas, as seen in absorption, is also greater. After removing the stellar contribution, we calculate the column density weighted mean NaD EW across all galaxies in the FIRST-detected radio-RG and nonradio-RG samples and compare them to radio-CS and nonradio-CS galaxies.

The comparison is shown as cumulative distribution functions in Fig. 5.9. The distribution of the NaD EW from the radio-RG galaxies appears to be different than both the radio detected and non-detected control samples. The nonradio RG, however, show a very similar distribution of NaD EW with the radio-CS sample. We perform a Kolmogorov-Smirnov (KS) test to measure the statistical significance of the differences of radio-RG sample with radio-CS and nonradio-CS samples and find that the null hypothesis that the said distributions are similar are rejected at a level $< 1\%$ with p values $= 0.008$ and 7×10^{-5} respectively. Additionally, the radio-red geysers have the highest mean with EW $= 0.9^{+0.31}_{-0.30}$ Å, greater by about 0.45 Å than the radio-CS sample which has a mean EW $= 0.46^{+0.29}_{-0.28}$ Å and more than the nonradio-CS (EW $= 0.27^{+0.41}_{-0.26}$ Å). The nonradio-RG also has a high NaD EW than both the control samples with a mean EW $= 0.51^{+0.35}_{-0.33}$ Å. This indicates a greater level of NaD-absorbing material in the ISM of the red geysers generally, but particularly so for the radio detected sample.

Fig. 5.10 shows the spatially-resolved NaD EW maps from the ISM components in four representative red geysers (MaNGA-ID: 1-217022, 1-273933, 1-575742, 1-94168) with ISM contributions $\frac{\mathrm{EW_{ISM}}}{\mathrm{EW_{tot}}} > 30 - 40\%$. While all four of them exhibit an ISM NaD enhancement, EW in two of them even exceed 2.5 Å in certain regions of these galaxies.

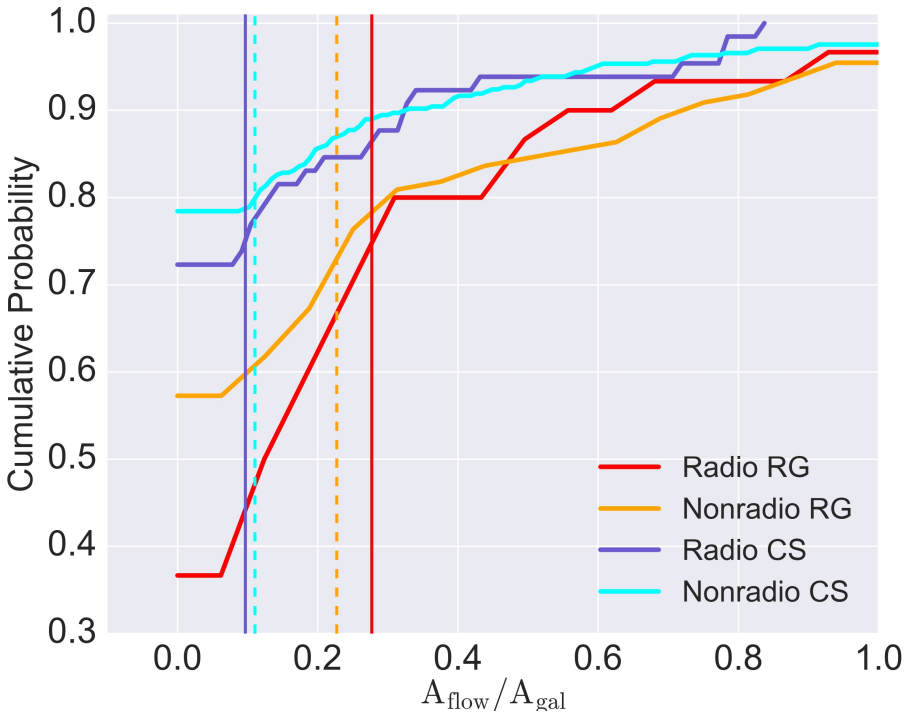

Figure 5.11: Cumulative distributions showing the fractional area of the galaxy comprising the cooler neutral ISM gas via NaD absorption for radio detected and not-detected red geysers (red and orange) and control samples (blue and cyan) galaxies respectively. Radio detected red geyser covers, on average, the highest fractional area of NaD absorption (red solid line), almost three times higher than that of the mean of radio detected control sample (blue solid line).

5.4.3 Spatial extent and morphology of the NaD feature

Fig. 5.10 illustrates several common features in the spatial morphology of the ISM NaD distributions observed within red geysers. These components typically have irregular shapes and are not smooth and symmetric, unlike what is typically expected from stellar distribution (similar to Cazzoli et al. 2014). These asymmetric spatial distributions reinforce the ISM origin of this enhanced NaD absorption.

We have shown that ISM-associated NaD absorption is more common and globally stronger in red geysers, but we can also characterize the typical density distributions of this absorption to distinguish between dense, but relatively concentrated components versus those that are more extended and diffuse. To quantify the spatial morphology and extent of the NaD absorption in each galaxy, we convert the number of spaxels comprising the NaD enhancements in each galaxy to the on-sky projected area using the following conversions:

$$\mathrm{A_{flow}} = \mathrm{A_{NaD}} = \mathrm{N} \times (\mathrm{S_p})^2 \tag{5.5}$$

$$\mathrm{A_{gal}} = \pi\ \mathrm{R_e^2}\ (\mathrm{b/a}) \tag{5.6}$$

where N is the number of spaxels, S_p is the pixel scale which is $0.5''$ for MaNGA, R_e indicates the effective radius of the galaxy and b/a gives the axis ratio.

Hence the quantity $\mathrm{A_{flow}/A_{gal}}$ gives the fractional area covered by the NaD ISM absorption compared to the on-sky projected area of the entire galaxy. Fig. 5.11 shows the cumulative distributions of this fraction for radio-RG, nonradio-RG, radio-CS and nonradio-CS galaxies. We see that when ISM NaD absorption above our threshold is detected, it covers a wider fractional area ($0.28^{+0.09}_{-0.07}$) within the average radio-detected red geyser sample compared to its areal fractions ($0.09^{+0.15}_{-0.09}$ and $0.1^{+0.1}_{-0.09}$) in the radio-detected and non-detected control samples respectively. This is consistent with Rupke et al. (2021) where the percentage of galaxy disk area showing inflows/outflows via

NaD signature is found to be within 10-25% for a sample of Seyfert galaxies. KS test reveals that the distribution of fractional area from radio-RG sample is similar to that of nonradio RG sample (p value = 0.161) but differ significantly from the radio-CS (p $= 5 \times 10^{-4}$) and nonradio CS (p $= 1 \times 10^{-5}$) galaxies. Here, p value < 0.01 indicates the null hypothesis of the distributions being similar are rejected at a level <1%. If we define a column density threshold of log N(Na I)/cm$^{-2} > 12.3$, which corresponds to the average NaD column density across the entire red geyser and control sample, we find that 63% of radio-RG show NaD absorption which covers at least > 10% of the on-sky projected area in the galaxy. This compares to 42% in non radio-RG sample, 27% and 21% in radio-CS and nonradio-CS galaxies respectively. Thus, the spatial extent of the cool gas present in the FIRST-detected radio enhanced red geysers far exceeds those from the other samples of galaxies.

5.4.4 Spatially resolved NaD kinematics

By a number of measures, the previous sections have illustrated that red geysers, and in particular radio-detected red geysers, feature more prominent levels of ISM-associated cool material as traced by NaD. We now turn to the kinematics of this material as a way to probe its physical origin and evolution. We first calculate the spatially-resolved kinematics of the cool neutral ISM in red geyser and control samples by measuring the doppler shift of the ISM component of the NaD absorption line with respect to the systemic velocity for each spaxel in every galaxy (see §5.4.2).

We calculate the mean doppler velocity offset within each galaxy after weight-

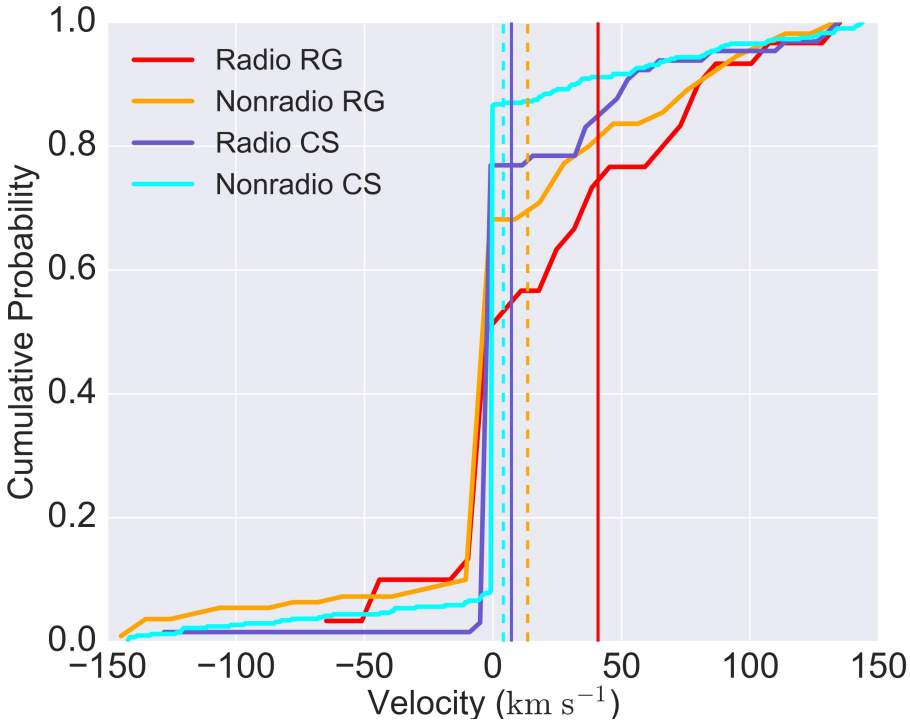

Figure 5.12: The cumulative distribution of mean velocities obtained from spatially resolved NaD kinematics for red geyser and control samples, split by radio detection. The color scheme is the same as Fig. 5.9. The mean velocities are calculated by computing the average of spatially resolved velocities over a circular radius of 8″. Both the radio detected and non-detected red geyser samples shows a clear excess in redshift or a positive velocity compared to control samples.

ing by the column density, similar to the computation of mean EW. The comparison between the mean velocity in radio detected and not-detected red geyser with control samples (split by radio detection) is shown in Fig. 5.12. The radio-RG sample shows an average positive (or redshifted) velocity V= 41 $\pm$ 14 km s^{-1}, with respect to the systemic velocity. The nonradio-RG sample also shows a positive velocity, though of lesser amplitude, with a mean value 13$\pm$9 km s^{-1}. The radio detected and non detected control galaxies, on the other hand, has average V= 8$\pm$12 km s^{-1} and 4$\pm$11 km s^{-1} respectively. Thus the radio red geyser sample shows more redshifted velocity on average. Looking at the statistics across the samples, we find that 86% of radio RG sample has V$\geq$ 0, while only 24% and 13% of radio-CS and nonradio-CS galaxies show a redshifted velocity. The radio RG sample show a statistically different distribution from radio-detected and non-radio detected control samples from KS test with p value= 0.009 and 6×10^{-4} respectively. The nonradio-RG however show similar distribution with radio-CS with p$>$ 0.01, but significant difference with nonradio-CS (p value = 1×10^{-3}.

Fig. 5.13 shows spatially resolved velocity maps of the NaD-ISM absorption spectra of the same four red geysers as Fig. 5.10 (MaNGA ID: 1-217022, 1-273933, 1-575742, 1-94168). Except for the galaxy in the lower left panel, the rest are radio-detected. The radio detected red geysers show significant redshifted spaxels, generally clustered on one side of the galaxy.

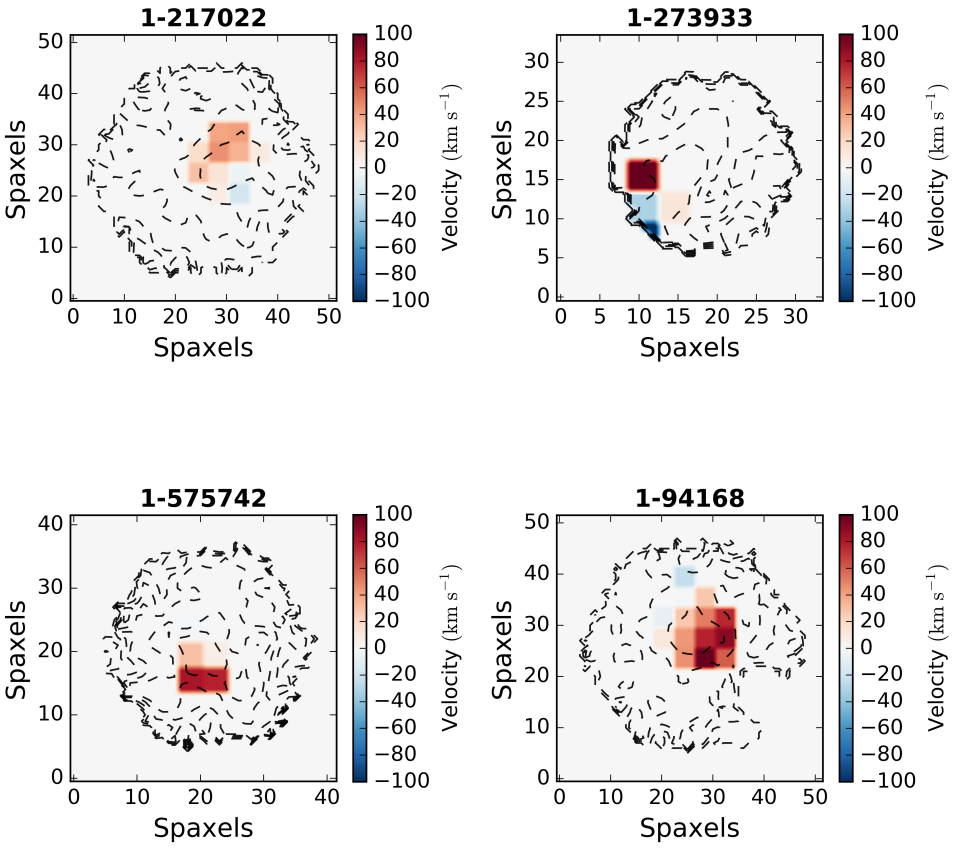

Figure 5.13: Spatially resolved NaD velocity maps of the same four red geysers as Fig. 5.10(MaNGA ID: 1-217022, 1-273933, 1-575742 and 1-94168). The velocities are extracted from modeling the NaD absorption spectra with Rupke et al. (2005) model, wrapped in an MCMC framework.

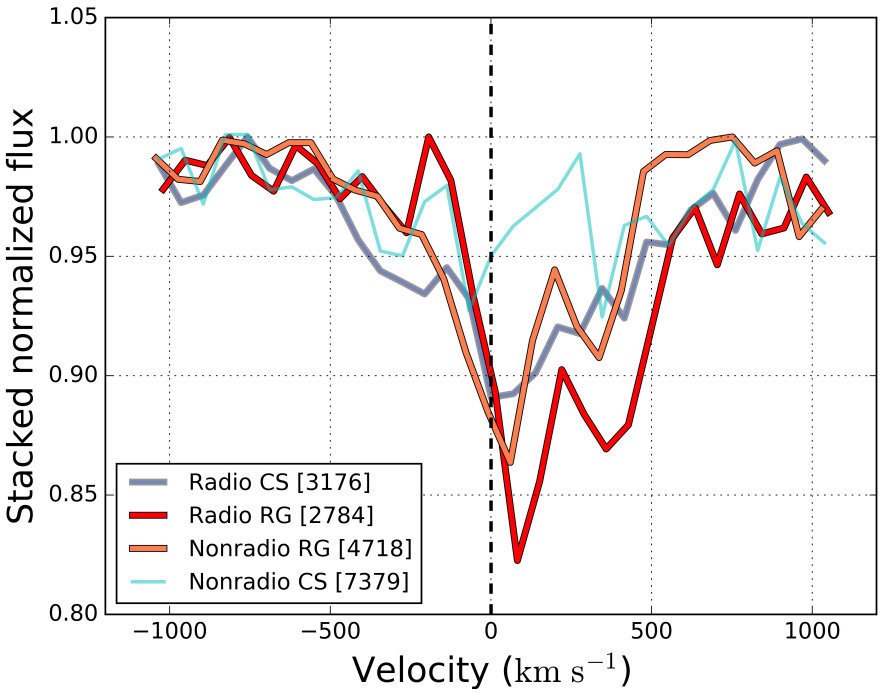

Figure 5.14: Stacked and normalized NaD spectra containing only the ISM component for radio detected and not-detected red geysers (red and orange) and control sample (blue and cyan) galaxies respectively. The total number of spaxels with detected NaD ISM used in the stacking for each of the galaxy sample is mentioned in the legend in square brackets. The radio detected red geyser sample show the highest positive velocity (or inflow) relative to the systemic velocity, closely followed by the non radio geysers. The control sample do not exhibit any visible redshift signature in the stacked sample.

5.4.5 Global stacked kinematics

We have found a clear, redshifted signature (positive velocity, V = 41 km s^{-1}) in the average of the spatially-resolved NaD offset velocity in the radio detected red geyser galaxies. However, to estimate these average velocities, we performed Bayesian fitting assuming a specific absorption model to each spaxel (§5.3.3) and computed the mean velocities after weighing by column density. We have shown in Fig. 5.7 that a small but positive bias ($\leq$ 5 km s^{-1} at S/N > 10 per dispersion element) can emerge from the fitting algorithm used for the kinematic analyses. Thus to ensure that the velocities we get do not arise due to artifacts of model fitting or averaging, we compute the kinematics of stacked NaD profiles from all four sample of galaxies to check if we see similar trends.

We only use spaxels that meet the criteria described in §5.3.3. Additionally we impose another constraint that the considered spaxels should have a measured EW of the total NaD feature (including both stellar and ISM contribution) to be > 2Å. This picks out the spaxels with an appreciable NaD signal in each galaxy and provides confidence in the measured equivalent width from the spectra. We then perform a spaxel wise stacking of the continuum normalised spectra around the NaD feature and over each sample. The stacked spectra for all four samples are shown in Fig. 5.14. The red geyser samples feature a positive velocity offset. The radio-detected red geysers show a higher redshifted velocity ($+53 \pm 6$ km s^{-1}) compared to non-radio-detected geysers (31 ± 5 km s^{-1}). The control samples do not show any significant redshift signature

Table 5.1: Summary of the NaD-ISM properties obtained for four galaxy samples

Sample	Mean EW [Å]	Fractional area on-sky	Mean resolved V [km s^{-1}]	Stacked V [km s^{-1}]
Radio-red geysers	$0.90^{+0.31}_{-0.30}$	$0.28^{+0.09}_{-0.07}$	40.86 ± 14.07	52.8 ± 6.27
Nonradio-red geysers	$0.51^{+0.35}_{-0.33}$	$0.22^{+0.15}_{-0.13}$	13.56 ± 9.21	31.0 ± 5.02
Radio control sample	$0.46^{+0.29}_{-0.28}$	$0.09^{+0.15}_{-0.09}$	8.13 ± 12.10	10.2 ± 7.78
Nonradio control sample	$0.27^{0.41}_{-0.26}$	$0.1^{+0.1}_{-0.09}$	4.00 ± 11.97	-28.1 ± 25.3

relative to the systemic velocity and show values within ±10 km s^{-1} with large errors (See Table 5.1, column 5). The errors quoted in Table 5.1 indicate mean 1-σ uncertainty over the whole sample. The stacked velocity values agree well with the average resolved kinematic measurements obtained in §5.4.4.

5.5 Discussion

We have examined the cool ISM properties as probed by NaD in four samples of interest: 30 radio-detected red geysers, 110 non-radio-detected red geysers, 65 radio-detected control sample galaxies and 393 non-radio-detected control sample galaxies. Table. 5.1 summarizes the main findings along with mean 1-σ error values calculated within each galaxy sample.

We find that the radio detected red geyser sample show the highest mean EW (0.9 Å) from the NaD ISM component, compared to the rest of the samples (Table. 5.1, column 2). Fig. 5.9 shows that the average EW in radio-RG sample is about 0.5 Å higher than the control galaxies, irrespective of radio detection. We also find that 78% of radio-RG sample possess an appreciable amount of cool gas detected over a projected area

$> 5 \times 5$ kpc^2, which is the largest compared to the other samples. The NaD in the radio detected red geysers also occupy a larger on-sky area on average, roughly 28% of the projected area of the galaxy (Fig. 5.11). These results imply that the red geyser galaxies, which host low luminosity radio AGNs, typically have an abundant supply of cool gas. A rough estimate of the mass of this detected cool gas is given in the later part of this discussion in §5.5.1.

Fig. 5.12 shows that the average doppler shift of NaD obtained from the spatially resolved kinematics in the radio RG sample is roughly 40 km s^{-1} with respect to the systemic velocity. The non-radio RG show a smaller positive velocity 13 km s^{-1}. The control galaxies, irrespective of radio detection, show an almost zero velocity within the uncertainties (Table. 5.1). This result very closely matches with the global stacked kinematics obtained by stacking all the galaxies in each of the four samples. We find that the radio detected red geysers show a strong redshift or positive velocity, of about 53 km s^{-1} compared to the other samples (Fig. 5.14, also see Table. 5.1). Redshift in absorption indicates gas inflowing towards the galaxy, away from the observer. The correlation with radio properties together with inflowing kinematics possibly indicate that the cool gas is fueling the central AGN in the radio detected red geyser galaxies, very similar to the prototypical red geyser in Cheung et al. (2016). It is interesting to note that the radio-detected control galaxy sample also displays a moderate amount of ISM-associated cool gas via NaD absorption (mean EW = 0.46 Å) but shows no inflowing signature as in the red geysers. Our interpretation in alignment with Roy et al. (2018) is that these radio detected control galaxies, which also host low-luminosity radio

AGNs, are not capable of driving energetic winds like the red geysers in present time but they might in the future. This detected cool gas may slowly accumulate over time and can eventually fuel the central AGN which can then trigger the red geyser winds.

5.5.1 Cool gas mass and inflow rates

In order to get a rough estimate for the implied mass inflow rate in red geysers, we adopt the following equation from Roberts-Borsani & Saintonge (2019):

$$\dot{M}_{out} = \Omega\ \mu\ m_H\ N(H)\ v\ r \tag{5.7}$$

where Ω is the solid angle subtended by the wind at its origin, m_H is the mean atomic weight (with a μ=1.4 correction for relative He abundance), N(H) is the column density of Hydrogen along the line of sight, v is the doppler velocity, and r is the extent of the NaD absorption in the galaxy with respect to the center.

Making the same assumptions as Rupke et al. (2005), the column density of hydrogen can be written as:

$$N(H) = \frac{N(Na\ I)}{\chi(Na\ I)\ d(Na\ I)\ Z(Na\ I)} \tag{5.8}$$

where N(Na I) is the sodium column density, χ(Na I)= N(Na I)/N(Na) is the assumed ionization fraction, d(Na I) is the fraction depletion onto dust, and Z(Na I) is the Na abundance. We assume a 90% ionization fraction (χ(Na I)=0.1), a Galactic value for the depletion onto dust (log d(Na I)=-0.95), and solar metallicity (Z_{solar}(Na I)=log[N(Na)/N(H)]=-5.69) similar to that assumed in Rupke et al. (2005). Putting the

log N(Na I) [cm^{-2}] values which range from 11.6 to 13.7 obtained from modeling the NaD absorption feature in radio detected red geyser sample, we obtain an average log $N(H)/cm^{-2} \sim 19.50-21.30$. This is roughly in agreement with the $\log N(H)/cm^{-2} \sim 21$ estimated according to Bohlin et al. (1978) from the average dust extinction in similar galaxies.

With these assumptions and setting Ωvr in Eq.5.7 equal to $C_f A_{\rm NaD}/t_{acc}$, where $A_{\rm NaD}$ is the on-sky projected area of the galaxy comprising NaD absorption from §5.4.3 and $t_{\rm acc}$ is the accretion timescale $\sim \frac{R_e}{v}$, we get:

$$\dot{M}_{\rm out} = \mu\ m_{\rm H}\ C_{\rm f}\ N(H)\ A_{\rm NaD}\ \frac{v}{R_e} \tag{5.9}$$

The total mass of the gas can be estimated by the assumption: $M_{\rm tot} = \dot{M}_{\rm out} \times t_{\rm acc}$.

$$M_{\rm tot} = \mu\ m_{\rm H}\ C_{\rm f}\ N(H)\ A_{\rm NaD} \tag{5.10}$$

The cloud covering factor C_f is taken to be 0.4, the average value obtained from our model fits. For the radio-detected red geysers, the NaD velocity (v) varies from 10 km s^{-1} – 100 km s^{-1} (Figure. 5.12) with a mean of $\sim$ 45 km s^{-1} (Table. 5.1, column 4 and 5). The estimated total mass ranges from $M_{\rm cool} \sim 0.1 \times 10^7\ M_\odot - 5. \times 10^8\ M_\odot$ within the radio-detected red geyser sample while the mass inflow rate spans a large range $\sim 0.02-5\ M_\odot\ yr^{-1}$. The estimated hydrogen column density, mass flow rates and the mass of the gas for each galaxy in the radio RG sample is given in Table. 5.2 along

with their 1-σ uncertainties. The 1-σ errors in the column density are derived from MCMC fitting of the absorption line model (§5.3.3) to the observed NaD spectrum in each spaxel, satisfying the detection criteria, within a galaxy and adding them in quadrature. The corresponding errors in flow rate and gas mass are obtained from simple error propagation.

A few galaxies show negative velocity (or blueshift) indicating possible outflowing gas and the outflow rate, estimated from the same eqn. 5.9, is given with a negative sign in the table. As expected, the majority of radio-detected red geysers show inflowing gas. Those galaxies with no NaD ISM component detected in any spaxels (following §5.3.3) are tabulated as having zero inflow rate and M_{tot} although there may be cool gas present below our detection level.

5.5.2 Origin of inflowing gas

Infalling gas in red geysers at the estimated accretion rates can come from a variety of sources:

- Accretion from outside the galaxy and its halo. Galaxy mergers, specifically minor mergers, present an obvious mechanism (Sanders et al. 1988; Weston et al. 2017; Kaviraj 2014; Pace & Salim 2014; Martin et al. 2018).

- A completely internal source, such as gas injected into the interstellar medium during stellar mass loss (Conroy et al. 2015) which undergoes cooling and condensation, perhaps eventually feeding an AGN (Ciotti & Ostriker 1997; Ciotti &

Ostriker 2001; Ciotti & Ostriker 2007).

- Fountain scenario where the warm ionized outflowing gas, driven out by the central AGN from earlier geyser episodes, rises into the halo, cools and condenses as it expands, and then falls back onto the galaxy (e.g., Shapiro & Field 1976; Bregman 1980; Norman & Ikeuchi 1989; Tremblay et al. 2016, 2018; Voit et al. 2017).

Numerous observations have measured the merger rates in nearby galaxies (see Ellison et al. 2015, and references therein) and several authors have emphasized widespread merger activity when observational evidence sensitive to long timescales and low mass ratios is scrutinized (e.g. van Dokkum 2005; Sancisi et al. 2008). For galaxies with stellar masses between $10^{10.5} - 10^{12}$ $M_\odot$, the average predicted merger rate per galaxy (assuming typical mass ratio of minor mergers $\sim 1:10$) from semi-empirical models and hydrodynamical simulations is roughly ~ 0.1 Gyr^{-1} (Hopkins et al. 2010; O'Leary et al. 2021). Thus galaxy mergers with a 1:10 (or greater) mass ratio can generate an M_* accretion rate of $\frac{0.1\times0.1\times1.\times10^{11}\ M_\odot}{10^9\ yr} = 1\ M_\odot\ yr^{-1}$ on average. If 10% of this value lies in cold gas, the estimated accretion rate is roughly 0.1 $M_\odot$ yr^{-1}. This is similar to the accretion rates quoted in Capelo et al. (2015) which performed detailed simulations by exploring a wide merger parameter space including different initial mass ratios, orbital configurations and gas fractions with high spatial and temporal resolution. The average cool gas inflow rate we estimate from NaD in red geysers is similar to the accretion rate implied by minor mergers. Merging gas-rich dwarfs may therefore be an important sources of the infalling gas. The apparently higher detection rate of NaD-

associated inflows in red geysers compared to control sample galaxies may be telling us that red geysers are a signpost of accretion activity. Indeed, some red geysers in our sample with accretion rate ~ 5 $M_\odot$ yr^{-1} may be signaling a peak in the instantaneous accretion rate during a merger event.

In addition to mergers, Ciotti et al. (1991); Ciotti & Ostriker (2007) predicted that a significant amount of gas, $\sim 20-30\%$ of the initial stellar mass of the galaxy, is donated throughout the galaxy over the course of stellar evolution and supernova explosions. This gas can be accreted onto an AGN. The radiative cooling time of this warm gas in typical elliptical galaxies is roughly $\sim 10^{7.5-8}$yr. Ciotti & Ostriker (2007) quoted a mass return rate of $\sim 5-10$ $M_\odot$ yr^{-1} from the stellar populations over the cooling timescale, which exceeds the cool gas inflow rates we observe in red geysers. Moreover, some fraction of warm ionized gas ($M_{warm} \sim 10^{5-6}$ $M_\odot$), ejected by the red geyser winds, may also accumulate within the ISM or the CGM of the galaxies over time. After cooling and condensation, this material might also become a source for the observed inflows.

Considering the different sources of infalling gas discussed above, we have found from visual inspection that most of radio-detected red geysers show a spatially irregular and clumpy NaD distribution (see Fig. 5.10). Additionally, we see from Fig 5.11 that the average fractional area occupied by the NaD absorption is around $\sim 30\%$ of the projected area of the entire galaxy for the radio red geyser sample, which implies a concentrated, lumpy distribution of gas confined in a small region. The recycled gas from the fountain scenario might be expected to present a more diffuse and smooth

component than is observed here.

Cooling ISM gas originating from stellar winds and supernovae might also be expected to cover a larger area of the whole galaxy. Moreover, the cool gas originating from stars might show greater correlations with the stellar kinematics which is not observed here.

It is also interesting to consider the relatively short timescales of dust enshrouded cool gas. As discussed in Rowlands et al. (2012), dust in early type galaxies get destroyed on relatively short timescales, ranging from 50 - 500 Myr, due to thermal sputtering from the hot X-ray halo surrounding the ISM or from shocks generated from Type 1a supernova. The signatures of clumpy, dust-associated NaD gas are likely short-lived, suggesting stochastic inflow episodes from merging systems over a more continuous 'rain' of recycled material.

Finally, we note that the detected cool gas in red geysers, with masses ranging from $10^7 - 10^8$ $M_\odot$ and average accretion rates $\sim 0.1 - 5$ $M_\odot$ yr^{-1}, might be expected to trigger a star formation rate of at least 1 $M_\odot$ yr^{-1}. However, the observed average star formation rate ($\sim 10^{-2}$ $M_\odot$ yr^{-1}) is several orders of magnitude lower, as evident from Fig. 5.1. This again is suggestive of active feedback mechanisms, perhaps related to the red geyser winds themselves, that are effective in suppressing star formation in these galaxies.

Table 5.2: Estimated mass and inflow rate of cool gas for the radio detected red geyser galaxies

ID	L_R $[10^{22}$ W Hz$^{-1}]$	log(N(H)) [cm^{-2}]	Inflow [$M_\odot$ yr^{-1}]	Gas mass [10^8 $M_\odot$]
1-352569	8.79	20.45±1.51	0.19±0.02	2.4±0.21
1-23958	0.32	20.89±0.45	0.47±0.03	1.3±0.10
1-113668	5.92	20.38±2.12	−0.41±0.04	3.5 ±0.36
1-595166	3.19	20.52±1.99	−0.78±0.04	2.5 ±0.13
1-550578	7.81	20.28±1.73	−0.23±0.01	0.96 ±0.10
1-634825	1.26	21.20±0.28	1.71±0.22	4.3 ±0.26
1-37036	0.12	20.03±2.07	$0.02\pm2\times10^{-3}$	$0.03\pm5\times10^{-3}$
1-43718	1.15	20.32±1.20	$0.05\pm9\times10^{-3}$	0.13 ±0.02
1-218116	2.06	0.0	0.0	0.0
1-217022	0.16	21.27±0.14	0.46±0.12	2.4 ±0.18
1-256446	2.29	20.81±0.60	1.80±0.10	1.9 ±0.22
1-94168	0.52	21.11±0.27	1.22±0.08	3.7 ±0.24
1-209926	3.36	20.68±0.24	0.78±0.07	5.1 ±0.48
1-273933	2.46	20.47±0.96	−0.03±0.02	0.3 ±0.04
1-245451	5.78	21.07±0.14	5.67±0.22	5.9 ±0.62
1-198182	1.30	0.0	0.0	0.0

1-210863	0.95	19.48±5.46	$0.01\pm5\times10^{-3}$	$0.01\pm3\times10^{-3}$
1-289864	77.52	0.0	0.0	0.0
1-24104	0.36	20.53±1.54	0.38±0.02	0.7 ±0.02
1-378770	45.32	20.49±0.51	0.88±0.06	3.3 ±0.42
1-279073	0.54	20.04±1.05	$0.01\pm3\times10^{-3}$	$0.02\pm5\times10^{-3}$
1-188530	8.37	20.37±0.93	3.21±0.2	3.9 ±0.05
1-209772	23.84	20.10±3.99	2.8±0.5	3.2 ±0.66
1-268789	6.51	20.19±0.81	0.04±0.01	1.0 ±0.02
1-567948	0.13	19.90±2.32	0.4±0.1	2.1 ±0.3
1-96290	6.22	20.27±1.50	0.27±0.03	2.0 ±0.24
1-37440	0.06	20.9±0.55	2.38±0.01	1.1 ±0.04
1-321221	0.25	0.0	0.0	0.0
1-322336	5.64	20.62±0.31	0.35±0.06	2.3 ±0.40
1-627331	0.91	0.0	0.0	0.0

5.6 Conclusion

We have performed a set of analyses of the sodium doublet absorption feature as a tracer of cool ISM gas in red geyser galaxies and a matched control sample using spatially-resolved data from the SDSS IV-MaNGA survey. After carefully subtracting the stellar contribution, we have found an excess in NaD absorption which we ascribe to the presence of cool material in the ISM. We study the properties of this gas in our radio-detected red geyser sample (30 galaxies) and compare to several other samples

- namely, 110 non-radio detected red geysers, 65 radio-detected and 393 non radio detected control samples.

We measure the kinematic behavior of the cool gas by computing the average velocity offsets in spatially resolved maps, integrated offsets per galaxy, and stacked kinematics of ISM NaD spectra across all four galaxy samples. We find that the NaD in the radio-detected red geysers shows a clear redshift ($40 - 50$ km s^{-1}) with respect to the systemic velocity. We interpret this result as an indication that the cool gas is inflowing into the galaxy center. The non-radio-detected sample of red geysers also show a similar redshift, but of slightly smaller amplitude on average ($\sim 15 - 30$ km s^{-1}). The control samples however show average velocity offsets around zero or slightly negative (< 10 km s^{-1}).

In order to check that the observed redshift is robust due to the systematics of the fitting technique itself, we tested our fitting approach using simulated spectra of varying signal-to-noise and different input velocities (Fig. 5.7). We find that at the signal-to-noise of our observation (> 10 per dispersion element), there exist a modest systematic bias of ≤ 5 km s^{-1} which is, however, much smaller than the velocity inflow values we observe.

The accretion of cool gas inflowing into the center coupled with the radio enhancement in the radio red geyser sample indicates that the central low luminosity radio AGN is possibly fueled by the cool neutral gas clouds in the ISM. Both external sources (like mergers) and internal processes (stellar mass loss, accumulation of gas from relic geyser winds) can explain the observed accretion rates, which span a vast range

$\sim 0.02 - 5$ $M_\odot$ yr^{-1} with a estimated total mass of the cool gas to be $\sim 10^7 - 10^8$ $M_\odot$. Although this gas is capable of triggering an easily detectable level of star formation (~ 1 $M_\odot$ yr^{-1}), the observed quiescent nature of the red geysers with a SFR almost 2 orders of magnitude lower indicates evidence of maintenance-mode feedback in action and possibly associated with red geyser phenomenon itself.

Chapter 6

Conclusions

The main focus of my thesis has been studying maintenance mode feedback in low redshift (z<0.1) universe in the context of "red geyser" galaxies. In this chapter, I summarize the key results presented in this thesis about these relatively new but common class of galaxies and discuss their possible connection with the proposed AGN maintenance mode. I also outline future work that will help address some of the questions that still remain unanswered.

6.1 A Brief Summary

AGN radio/maintenance mode feedback is the most widely accepted theory to explain the global shutdown of star formation in massive quiescent galaxies with stellar masses greater than $\sim 10^{10}$ $M_{\odot}$. This feedback is thought to manifest itself primarily via radio-AGN jets, which often drive multi-phase gas outflows. Detailed understanding of this feedback mechanism is essential to gain insight on the evolution and fate of galaxies.

However, direct detection of "caught-in-the-act" feedback signatures has always been challenging and limited to only a handful of galaxy groups and clusters via radio jets and ionized/molecular outflows (Morganti et al. 2005; McNamara & Nulsen 2007; Nesvadba et al. 2008; Fabian 2012). In this thesis, I have discovered valuable evidence in nearby red sequence galaxies that may suggest ongoing radio mode feedback in action. I leveraged the spatially resolved optical spectroscopic data from SDSS IV-MaNGA survey along with multi-wavelength datasets (Roy et al. 2018, 2021a,c,b) to identify and study the red geyser galaxy population, comprising of 140 early type galaxies. The previous chapters of this thesis present the gas, stellar and the black hole properties of these galaxies. In this concluding chapter, I synthesize these results and discuss their physical interpretation.

Red geyser galaxies are red and dead galaxies with red optical color and very little ongoing star formation (log SFR < -2 $M_\odot$ yr^{-1}). However, they host ample amount of diffuse ionized gas across the surface with line emission closely tracing the stellar light profile. Their line emission resembles LIER galaxies with the primary ionization source being post-asymptotic giant branch stars (Belfiore et al. 2016). On top of this diffuse LIER emission, red geysers show an additional enhanced bi-symmetric feature in their spatially resolved emission maps that stretches across the MaNGA fiber field of view. The gas kinematic major axis roughly aligns with this feature and shows signatures consistent with large scale ($\sim$ 10 kpc) but weak ionized outflows.

Additional kinematic arguments, discussed in Chapter 4, confirmed that these are indeed centrally driven winds (Roy et al. 2021a) and not gas in rotation. Higher

spectral resolution (R$\sim$ 8000) followup observations of a few red geysers using Keck ESI slit spectra revealed broad winged velocity profiles with distinct asymmetry features – indicative of a broad conical outflow projected along the line of sight (Roy et al. 2021a). This is consistent with the wind interpretation proposed by (Cheung et al. 2016) for the prototypical red geyser 'Akira', based on extremely turbulent ionized gas kinematics detected from MaNGA data. The average estimated wind kinetic power is approximately $\sim 10^{39}$ erg s^{-1}. The wind has sufficient energy to balance gas cooling and prevent any further star formation, if efficiently coupled to the ambient medium.

The next question is what drives these outflows? One of the key findings of this thesis is that red geysers exhibit enhanced radio AGN activity compared to similar non-red geyser quiescent galaxies. As shown in Chapter 2, this is evident from increased radio flux obtained from stacking VLA FIRST radio images at 1.4 GHz frequency. Red geysers host low luminosity radio AGNs ($L_{1.4GHz} \sim 10^{22}$ W Hz^{-1}) which act as the central powerhouse driving those observed ionized winds that signal red geyser phenomenon.

The AGNs are radiatively inefficient with an advection dominated accretion flow (Eddington scaled accretion rate $\lambda \sim 10^{-4}$) and their primary mode of energy output is mechanical energy via radio jets. The best fit linear relation between the radio power and the jet mechanical energy from Heckman & Best (2014) gives an estimate of the mechanical energy that can be supplied by the AGNs, assuming there is a small-scale radio jet underneath the unresolved compact radio source. The inferred mechanical energy $\sim 10^{41}$ erg s^{-1} can easily counterbalance the gas cooling rate ($\sim 10^{39}$ erg s^{-1})

inferred from X-ray gas (Best et al. 2005) and thus quench star formation if deposited efficiently.

The AGNs in the red geysers are low-luminosity sources and almost all of them appear compact through the FIRST radio images with 5″ resolution. It has been pointed out by numerous studies that compact radio sources play a strong role in triggering fast ionized outflows and form a crucial feedback mechanism (Holt et al. 2008; Riffel et al. 2014; Santoro et al. 2018; Jarvis et al. 2019; Husemann et al. 2019). This is because their mechanical energy is confined predominantly to the size-scales of the host galaxy halo within the inner few kpc. Majority ($\sim$ 60 %) of the red geysers show a compact radio morphology even with higher resolution (2.5″) radio images from high frequency ($\sim$ 2−4 GHz) VLA Sky Survey and with more sensitive observations at lower frequency (144 MHz) from LOFAR Two Meter Sky Survey (Roy et al. 2021b). Their observed characteristics are very similar to the low power compact radio galaxies, sometimes called the 'FR0' class (Baldi et al. 2021; Capetti et al. 2020) and the 'radio-quiet quasars' (Jarvis et al. 2019, 2021). Higher resolution ($<$ 1″) followup radio observations are required to detect the small scale 'frustrated' radio jets within these compact sources and determine their morphology with more accuracy. This is one of the key future goals to be addressed later.

This work has also revealed three massive double-lobed red geysers, with radio jets extending to $>$ 30 kpc. These large extended radio sources show considerably lower specific star formation rates (i.e. star formation rate per unit stellar mass) than compact radio red geysers. This could mean that the extended radio sources are more massive

and evolved than the compact ones. One possibility is that the compact 'FR0' class red geysers would eventually evolve into FRI/FRII sources with large radio jets. Red geysers exhibit a range of radio morphology - compact, slightly extended, one sided lobe/bubble, double-sided radio lobes and irregular structures (Roy et al. 2021b). This large range of radio morphologies may represent the various stages of this transition from compact FR0 to massive FRI/FRII class. A comprehensive discussion about the radio morphology and the AGN properties are presented in Chapter 3.

The kinematics from MaNGA data and the detailed velocity profiles from higher spectral resolution Keck ESI spectra in Chapter 4 place constraints on the major axis, opening angle and inclination of the putative ionized wind cones. On the other hand, low frequency (144 MHz) sensitive LOFAR radio data reveal the radio morphology of the radio detected red geyser sample. It is difficult to spatially map out the degree of alignment between the radio jets and large scale ionized wind in all red geysers, since 60% of the sample show compact and/or unresolved radio images. However, among those that have an extended morphology, the large-scale radio lobes extending to the circumgalactic medium (at scales > 30 kpc) often lie roughly parpendicular with the ionized winds, extending to ~ 10 kpc (Roy et al. 2021b). This is similar to the observations by Venturi et al. (2021), who found increased line widths perpendicular to radio jets. Similarly, at smaller spatial scales closer to the center (within the inner 2 kpc at 500 pc resolution), the ionized wind kinematics from Gemini GMOS spectra show considerable difference in orientation from the wind geometry from larger scale ($\sim$ 10kpc) MaNGA observations (Riffel et al. 2019). The observations are interpreted to

be signatures of jet precession, changing the wind orientation by about tens of degrees from the nucleus of the galaxy to kpc scales on a timescale of 10^7 years.

Widespread detection of ionized gas in the form of bisymmetric enhancements in emission line maps suggest that red geysers possess an abundant fuel supply inspite of being red and dead. An approximate estimate of the mass of this warm (T $\sim 10^4$ K) ionized gas phase is $\sim 10^5 - 10^6$ $M_\odot$. An even greater reservoir of cooler neutral gas of M $\sim 10^8$ $M_\odot$ is detected in the red geyser sample via NaD absorption lines using MaNGA data (Roy et al. 2021c). This cold gas lies spatially offset from the ionized outflow and is often clumpy and irregular in nature. A large fraction of this gas is observed to be inflowing towards the center with a moderate inflow rate ($\sim 0.02-5$ $M_\odot$ yr^{-1}), contrary to what is being observed in the ionized gas phase. Interestingly, the amount of infalling cool gas detected is particularly enhanced in the radio detected red geysers which host fairly bright AGNs in their center. Red geysers also show an enhanced 21 cm-HI neutral gas content compared to similar non red geyser quiescent galaxies (Frank et al. 2022 submitted). This implies that these cold gas must have a connection with the central radio mode AGNs.

One possibility is that this gas flows towards the center and feeds the central low luminosity AGNs, keeping it active and enabling it to trigger the red geyser winds. On the other hand, a fraction of the warm ionized outflowing gas, driven out by the central AGN from earlier geyser episodes can cool, condense and fall back down into the galaxy forming a galactic fountain scenario and thus constantly replenishing the gas supply (e.g., Shapiro & Field 1976; Bregman 1980; Norman & Ikeuchi 1989; Tremblay

et al. 2016, 2018). Additional minor mergers at an average predicted rate of ~ 0.1 Gyr^{-1} per galaxy (Hopkins et al. 2010) can also supply a bulk of the cold gas with an estimated accretion rate of ~ 0.1 M$_\odot$ yr^{-1}.

The average wind velocity $V_{wind} = 300$ km s^{-1} and the spatial extent of the winds derived from the MaNGA maps lead to a rough characteristic wind timescale of 10^7 yr, very similar to other AGN phenomena (e.g., Hopkins et al. 2005; Ciotti & Ostriker 2007). Given this relatively short wind timescale and the fact that red geyser galaxies do not stand out in terms of other global properties like stellar mass, optical morphology and environment, it seems likely that the phenomenon is episodic with a duty cycle that results in 5–10% of red galaxies experiencing a red geyser episode at any given time. This would suggest that such episodes are triggered every 0.5–1 Gyr, perhaps as a result of minor mergers which replenish cold gas reservoir and turn on the central AGN.

The amount of detected gas is expected to trigger a star formation rate of at least a few M$_\odot$ yr^{-1}. However, the observed average star formation rate (~ 0.01 M$_\odot$ yr^{-1}) is several orders of magnitude lower. This suggests an active feedback mechanism is at play, perhaps related to the detected red geyser winds. But how does the wind energy couple to the ISM? Is it via shock generation or dynamical interactions like turbulence? I leave some of these questions for future work.

6.2 Future Work

As evident from the previous section, red geysers have emerged as an exciting population of galaxies who possibly exhibit direct signatures of maintenance mode feedback in red sequence galaxies. The analyses of this thesis confirm that they host radio-mode AGNs, drive large scale winds in ionized gas phase and also show suppressed star formation activity inspite of having no dearth of star forming fuel. Occuring at a relatively common rate, the episodic nature of the red geyser phenomenon can explain quiescence in typical passive galaxies in the red sequence. This result is very timely, considering the rapid progress recently in both theoretical and observational aspects to understand how AGN feedback mechanism suppresses star formation. Clearly, the immediate next step is followup of the current red geyser sample with higher spatial resolution data in multiple wavelength channels to constrain the feedback mechanism near the very center and address how the feedback energy efficiently couples to the surrounding ISM. The other crucial task is to determine the completeness of the current red geyser sample in the local universe and search for higher redshift counterparts.

6.2.1 High resolution radio observations to trace small scale radio jets

The first step to directly detect maintenance mode feedback signatures is studying the interaction between the radio jet and the surrounding ISM in the host galaxies. To perform this study, the radio jet morphology, alignment and spatial extent need to be accurately determined. Chapter 3 (Roy et al. 2021b) makes an initial at-

tempt to detect and characterize the morphology of the radio AGNs associated with the red geysers. However the study is greatly limited by the spatial resolution of the radio observations available. With a resolution of $6''$ for the LOFAR observations, a majority of the sources appear compact with no features visible in smaller scale (< 5 kpc). This is unfortunate, since the radio properties of the red geysers are consistent with galaxies hosting low-power < 1 kpc radio jets, which is beyond the resolution limit of our datasets (Baldi et al. 2018; Capetti et al. 2020; Jarvis et al. 2019). As noted by Jarvis et al. (2019), objects possessing small-scale jets in higher resolution (sub-arcsec scale) VLA and e- MERLIN images exhibit compact morphology when observed in low spatial resolution ($> 3''$).

Chapter 3 presents results that demonstrate that if the radio morphology of the compact jets can be constrained with better resolution data, their alignment with the outflowing wind cones and the associated ionized gas kinematics of the surrounding region can reveal whether there is ongoing feedback. Thankfully, further progress is now possible with the availability of sub-arcsecond imaging with the LOFAR telescope (Morabito et al. 2022). With additional processing and calibration techniques, a new reduction pipeline software is now able to achieve sub-arcsecond resolution from existing LOFAR data at frequencies below 200 MHz (Morabito et al. 2022; Jackson et al. 2022). Running the red geyser LOFAR images through this new set of reduction tools will reveal many smaller scale structures. The main goal will be to study whether they show signatures of small scale 'frustrated' jets trapped in the dense ISM. Mapping the ISM conditions in and around the jet region will determine the direct role of these AGNs in

affecting the host galaxy conditions.

6.2.2 Infrared tracers to detect shocks

What makes red geysers unique is the bisymmetric enhancement in the maps of strong emission lines, especially Hα, on top of the diffuse LIER-like emission. Does the extra emission result from shocks generated from interactions of high velocity gas along the wind axis? Can shocks be a possible mechanism by which feedback energy couple to the ISM? Detection and mapping of the spatial locations of shocks is thus a crucial step in our understanding of these sources.

Optical BPT parameter space occupied by shocks, AGN and LI(N)ERs are greatly overlapping, which can be further complicated by dust attenuation and MaNGA's low spatial resolution. Our initial attempt to separate shocks from other ionization sources has not been fruitful using optical emission line ratios from MaNGA. As shown in Fig. 6.1, [SII] 6717, 6731 BPT diagram [upper right and lower right panel], line ratios extracted from locations along the putative wind cone (shown by black circles) are broadly consistent with shock models [orange and blue lines], but are not distinct from the other spaxels.

Infrared (IR) line ratios, on the other hand, are very efficient in decoupling shocks from other ionization sources like AGN, LI(N)ERs and starbursts since they are well separated in their IR parameter space. Shock heating can produce ample amount of warm molecular H_2 emitting gas, the amount of which can provide an estimate of the total energy injected into the ISM due to shock-heating. The line ratios between

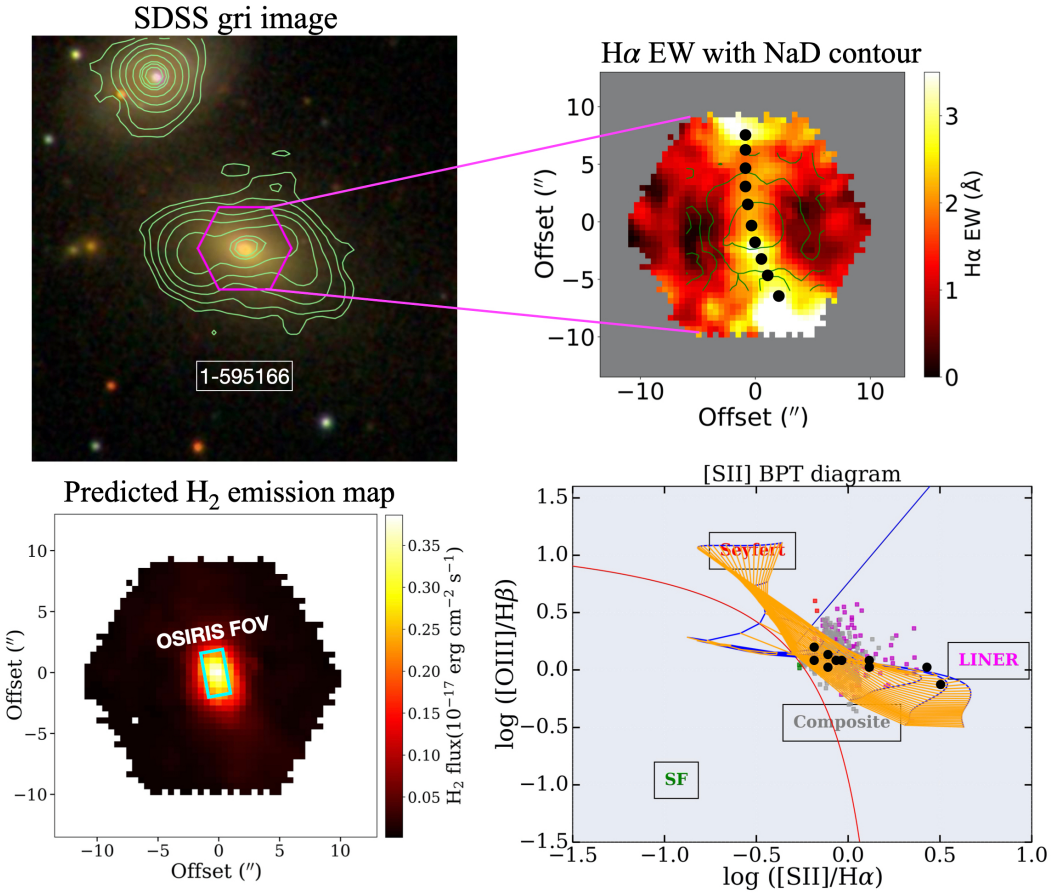

Figure 6.1: [Top left] SDSS gri color image with LOFAR radio contour overlaid of a porposed OSIRIS target (ID: 1-595166, z=0.045). [Top right] MaNGA Hα equivalent width map. [Bottom left] The predicted H2 intensity map. [Bottom right] The [SII] 6717,6731 BPT diagram of all spaxels, with the black points representing the locations along the wind cone within the Hα EW pattern. The optical line ratios are consistent with shock models, but can't be well constrained due to overlapping AGN and LINER-like emission sources.

the ro-vibrational transition lines of H_2 and the ionized gas tracers like Paβ and Brγ are critical to disentangle the multiple ionization sources like shocks, star formation, LINERs and AGNs. These lines are all detected in J, H and K band in the NIR.

Majority of the red geysers are predicted to host compact radio jets with a physical scale of $<$ 3kpc. These jets ultimately drive the large scale outflows detected in Hα. Thus, NIR line ratios with higher angular resolution ($\sim$ 100 pc) are particularly required near the very center where the small scale jets first encounter the ambient medium. I have submitted a Keck OSIRIS proposal in the K band ($1.96 - 2.38\mu$m) to conduct a short pilot study of a few red geysers. The spatially resolved spectroscopic observations in the infrared window with OSIRIS, coupled with adaptive optics capabilities will immensely boost the spatial resolution ($<$ 100 pc) compared to the MaNGA observations (1 - 2 kpc). The goal here is to understand the nature of energy injection via ISM shock heating in the central regions. The infrared tracers of ionized gas and their line ratios with the different H_2 lines (predicted flux map of H_2 is shown in Fig. 6.1 lower left panel) can provide clear separation between the ionization sources, much better than optical BPT. This work will set the stage for James Webb Space Telescope (JWST) observations that will immensely add to the infrared spectroscopic database, extending all the way upto far infrared.

6.2.3 Completeness of the red geyser sample

The current red geyser sample consists of 140 galaxies, which was derived from MaNGA Product Launch (MPL) 9. The total number of early type galaxies released

as part of MPL-9 were $\sim$ 2500. As of December 2021, MaNGA has now completed its survey by observing 10,010 galaxies, with nearly $\sim$ 5000 early type galaxies. It is crucial to inspect the rest of the red sequence galaxies to expand the red geyser galaxies and lead to a more complete sample in the local universe. Red geysers show a current occurance rate of $5 - 8\%$ in the local red sequence population, as confirmed by MaNGA data. Question remains whether they are equally prevalent in the higher redshift universe when the star formation and quasar activities reach their peak. JWST will be crucial to detect higher redshift counterparts of the red geyser phenomenon. The NIRSpec integral field unit mode and the MIRI medium resolution spectrometer (MRS) will provide high signal-to-noise spatially resolved spectra over the rest frame optical infrared window for z>1.

However unlike low z observations, detailed spatially resolved spectroscopic studies at high redshift are challenging to achieve for a statistically large sample of galaxies. Some initial pre-selection of red geyser candidates are needed possibly from integrated spectra, to ensure a methodical search and further followup via IFS studies. Our preliminary effort to perform dynamical modeling of the spatially resolved gas and stellar kinematics in the local red geysers using JAM models (Cappellari 2017) will be crucial to predict red geyser wind signatures from integrated high z observations. The combined criteria of a minimum threshold of radio luminosity, ionized gas content, gas velocity and rest frame optical color will be critical to extract geyser candidates at high redshift. Identifying such a huge and diverse sample of red geysers will better probe maintenance mode feedback over a wide range of stellar mass, cosmic epoch and

environments.

Appendix A

Supplementary information for kinematic modeling of Red geysers

A.1 Recovering the inclination using Jeans Anisotropic Modeling (JAM)

In order to construct the wind model for the second target galaxy, we recover the inclination using Jeans Anisotropic Modelling (JAM) method, detailed in Cappellari (2008) and implemented in the `jampy` package. This method approximates the stellar potential from the surface brightness distribution using Multi-Gaussian Expansion (MGE). In this instance, our observations of the surface brightness distribution comes from R-band DESI Legacy Survey imaging Dey et al. (2019) as this survey is deeper than the SDSS. We utilise the Python implementation of the method described in Cappellari (2002), `mgefit`. When constructing the MGE approximation, the flattest

Table A.1: The parameters of the best fit MGE. Total Counts refer to the counts under each component, σ is the width of each component in pixels, and q_{obs} is the projected axial ratio of each component.

Total Counts	σ	q_{obs}
272.886	2.47831	0.95
432.696	10.7368	0.95
165.534	21.1834	0.95
476.804	23.2103	1.0
1109.95	58.3299	1.0

gaussian in the best fit is found to be overly restrictive in the JAM modelling process, as it defines the minimum inclination which can be modelled. This is inherent to the JAM method and doesn't reflect a physical limitation on the inclination. We minimise this restriction while retaining suitable accuracy using the method in Scott et al. (2013). Here a limit is placed on the minimum axial ratio allowed in the MGE fit, and this limit is increased until the mean absolute deviation of the fit increases by 10%. Using this method we found the parameters which best fit the image, whilst maximising the inclination range available. The parameters are presented in Table A.1.

We perform an MCMC simulation to find the best fit parameters for the JAM model to match the v_{RMS} map from the MaNGA data. We decide that a simple JAM model neglecting dark matter is adequate for measuring the inclination, as in Cappellari et al. (2013). The free parameters which are allowed to vary are the orbital anisotropy β, the inclination $\cos i$, and the dynamical mass to light ratio M/L. Both β and M/L are

assumed to be constant across the galaxy. Note that M/L contains components from the stellar mass-to-light ratio and the presence of dark matter, and the contribution of each of these cannot be determined by this model. We use uniform priors on each of the parameters within the bounds below:

- β is allowed to vary between 0 and 0.75. Restricting $\beta > 0$ is required to break the known degeneracy between anisotropy and inclination, and is observationally motivated for fast rotators (see Section 3.1.1 of Cappellari et al. 2013) as the red geyser population are found to be.

- $\cos i$ is allowed to vary between 0 and $\cos i_{min}$, which is the minimum inclination imposed by the flattest component in the MGE approximation

- M/L is allowed between 0 and 10

- $\log f$ is an extra parameter added to quantify any underestimation of the errors, and is assumed to have a uniform prior within range -5 and 1

We find our best fit model with $\chi^2/DoF = 2.68$. The predicted v_{rms} (v_{zz}) from the best model is shown in comparison with the observed v_{rms} in Figure A.1, alongside the residuals. The measured parameters are presented in Table A.2. It is noted that the best fit inclination is close to the boundary on the prior, with artificially small errors. As such, it is believed that the true inclination may lie below the limit imposed by the MGE axial ratio.

Therefore, we use an inclination of 20° to construct our wind model. The

Table A.2: The parameters of the best fit JAM model. The inclination should be interpreted as an upper limit.

Inclination (°)	β	M/L
$19.58^{+0.070}_{-0.057}$	$0.216^{+0.025}_{-0.029}$	$6.921^{+0.019}_{-0.021}$

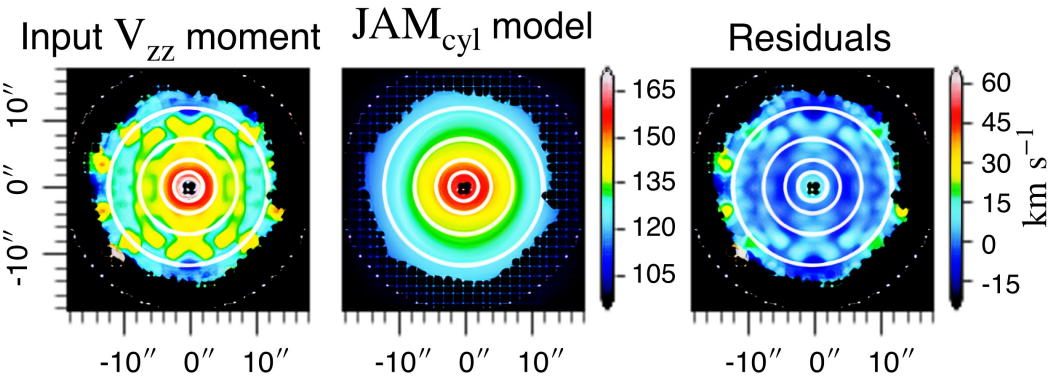

Figure A.1: Left: The symmetrised v_{rms} field for the galaxy which is input to JAM, Centre: The output from the best fit JAM model, Right: The residuals of the model and data. The white contours on all trace the surface brightness of the MGE. Black dots denote masked pixels. The unit of the color bars shown is km s^{-1}.

intrinsic 3D axis ratio is estimated from the inclination and observed axis ratio from Equation 1, Weijmans et al. (2014).

A.2 Parameters of individual velocity components of Hα and [NII] emission lines

The best fit parameters obtained from fitting the Hα and [N II] λ6584 Å emission lines from ESI at different slit positions for both targets are shown in Table A.3 - A.6. The different rows in each table indicate different Keck spaxels (or spatial locations) along each slit position. If the double gaussian model is preferred for an emission

line in a particular spaxel, V_1 and V_2 gives the primary and secondary velocity components while σ_1 and σ_2 are the corresponding dispersions. If the single component model is preferred, the velocities and dispersions are quoted as V_1 and σ_1 respectively, while keeping the other two columns empty.

Table A.3: Best fit model kinematic parameters for Hα and [NII] emission lines from ESI for slit 1 position of the first target galaxy (in km s^{-1} units).

Spaxel No.	$V_1 \pm \Delta V_1$	$V_2 \pm \Delta V_2$	$\sigma_1 \pm \Delta\sigma_1$	$\sigma_2 \pm \Delta\sigma_2$
No. 1 (Hα)	-242.99±0.54	-129.28±4.06	50.71±3.89	72.88±0.54
No. 1 (NII)	-232.49±1.19	-129.92±5.01	55.02±4.92	59.97±1.19
No. 2 (Hα)	-187.46±1.59	-44.06±10.59	75.09±3.29	129.57±1.58
No. 2 (NII)	-218.99±1.72	-48.57±1.00	83.84±6.84	131.94±1.72
No. 3 (Hα)	-146.59±2.96	-17.67±1.86	96.97±6	140.33±2.96
No. 3 (NII)	-176.29±1.55	-27.29±7.10	87.67±6.43	110.11±1.55
No. 4 (Hα)	-132.44±2.73	20.27±1.23	84.10±2.95	113.93±2.73
No. 4 (NII)	-105.67±1.27	4.50±14.96	104.90±4.83	143.41±1.27
No. 5 (Hα)	-43.41±3.50	—-	117.20±3.18	—-
No. 5 (NII)	-32.20±3.10	—-	132,10±2.31	—-
No. 6 (Hα)	-6.93±0.39	—-	124.28±5.16	—-

No. 6 (NII)	-25.25±1.76	13.10±5.77	102.63±5.23	164.10±1.76
No. 7 (Hα)	62.34±4.34	-126.16±13.82	108.73±4.93	276.80±4.34
No. 7 (NII)	31.20±1.70	82.55±17.48	88.76±6.66	219.95±1.70
No. 8 (Hα)	108.87±5.49	92.73±3.50	93.15±4.87	278.01±5.49
No. 8 (NII)	114.40±7.42	119.99±22.49	80.37±1.34	253.94±7.42
No. 9 (Hα)	140.16±3.94	-51.87±9.35	89.37±4.56	277.89±3.95
No. 9 (NII)	61.46±8.06	232.90±8.42	79.12±5.09	79.78±8.06

Table A.4: Best fit model parameters for Hα and [NII] emission lines from ESI for slit 2 position of the first target galaxy (in km s^{-1} units).

Spaxel No.	$V_1 \pm \Delta V_1$	$V_2 \pm \Delta V_2$	$\sigma_1 \pm \Delta\sigma_1$	$\sigma_2 \pm \Delta\sigma_2$
No. 1 (Hα)	-173.12±1.24	21.84±4.17	34.40±4.31	103.68±1.24
No. 1 (NII)	-136.19±3.80	54.99±8.83	159.15±3.59	184.52±3.80
No. 2 (Hα)	48.02±6.07	230.44±8.67	95.61±7.73	38.40±6.07
No. 2 (NII)	41.76±1.88	-39.63±4.73	135.75±9.72	102.11±18.83
No. 3 (Hα)	111.79±16.51	92.17±7.53	92.12±8.44	79.78±1.65
No. 3 (NII)	-42.28±9.21	146.24±11.89	100.06±7.51	112.64±9.21
No. 4 (Hα)	45.41±1.05	—-	123.75±4.95	—-

No. 4 (NII)	-37.18±1.04	82.60±3.92	130.70±4.61	137.55±10.40
No. 5 (Hα)	-8.29±1.96	—-	1.3967±2.11	—-
No. 5 (NII)	-1.71±0.53	—-	145.40±8.79	—-
No. 6 (Hα)	-41.84±1.65	—-	151.02±7.35	—-
No. 6 (NII)	-33.84±1.50	—-	140.20±7.27	—-
No. 7 (Hα)	-64.86±8.12	—-	146.77±6.73	—-
No. 7 (NII)	-41.25±4.55	—-	139.69±3.81	—-
No. 8 (Hα)	39.96±4.77	-151.19±9.21	51.80±4.09	271.33±4.77
No. 8 (NII)	-137.07±4.43	52.81±9.85	1.95.55±9.33	115.53±4.43
No. 9 (Hα)	46.26±3.46	189.63±11.97	127.02±19.58	50.51±14.66
No. 9 (NII)	1.18±3.80	-136.73±67.85	43.03±10.15	263.34±3.80

Table A.5: Best fit model parameters for Hα and [NII] emission lines from ESI for slit 3 position of the first target galaxy (in km s^{-1} units).

Spaxel No.	$V_1 \pm \Delta V_1$	$V_2 \pm \Delta V_2$	$\sigma_1 \pm \Delta\sigma_1$	$\sigma_2 \pm \Delta\sigma_2$
No. 1 (Hα)	-242.78±0.33	115.84±3.80	63.00±3.20	82.60±0.33
No. 1 (NII)	-219.22±2.02	-100.54±10.67	67.73±7.41	94.44±2.02
No. 2 (Hα)	-228.87±0.59	-60.39±4.79	68.89±5.45	90.11±0.59

No. 2 (NII)	176.52±1.70	5.75±9.39	93.44±5.57	128.30±1.71
No. 3 (Hα)	-136.26±5.24	20.39±1.59	89.23±3.99	119.42±5.24
No. 3 (NII)	151.17±3.78	17.82±7.20	89.01±3.94	105.79±3.78
No. 4 (Hα)	-41.16±0.38	—-	139.24±3.26	—-
No. 4 (NII)	-47.89±5.90	143.07±15.01	116.24±3.60	80.71±5.90
No. 5 (Hα)	-19.98±2.74	—-	138.34±2.19	—-
No. 5 (NII)	-57.41±5.27	48.12±1.57	119.26±2.90	133.11±5.27
No. 6 (Hα)	26.92±1.33	-171.21±2.21	117.79±1.62	279.54±1.33
No. 6 (NII)	-9.25±0.74	124.43±4.54	114.98±3.48	127.23±7.47
No. 7 (Hα)	77.83±1.80	117.47±5.88	107.12±2.29	279.48±1.87
No. 7 (NII)	66.36±2.86	-125.50±8.55	97.00±2.82	232.33±2.86
No. 8 (Hα)	150.62±4.20	89.54±8.43	119.33±15.36	69.79±4.20
No. 8 (NII)	90.88±17.56	96.00±9.07	113.29±9.74	81.11±17.56
No. 9 (Hα)	195.31±4.15	86.16±11.18	104.25±18.22	105.42±4.15
No. 9 (NII)	217.90±11.40	55.42±2.74	81.27±6.90	121.58±11.40

Table A.6: Best fit model parameters for Hα and [NII] emission lines from ESI for the second target galaxy (in km s^{-1} units).

SpaxelNo.	$V_1 \pm \Delta V_1$	$V_2 \pm \Delta V_2$	$\sigma_1 \pm \Delta\sigma_1$	$\sigma_2 \pm \Delta\sigma_2$
No. 1 (Hα)	-2.7671±1.14	-2.0153±5.28	3.603±5.40	3.878± 1.14
No. 1 (NII)	238.34±1.33	208.225±9.18	44.54±1.05	74.47±1.35
No. 2 (Hα)	-220.52±1.72	-113.65±15.92	34.95±4.19	90.50±1.72
No. 2 (NII)	-242.04±5.73	-170.61±10.42	48.34±1.53	38.85±5.73
No. 3 (Hα)	-248.59±1.50	-140.43±7.74	66.76±15.01	69.92±1.50
No. 3 (NII)	-252.36±1.98	-175.73±12.18	35.82±5.18	47.31±1.98
No. 4 (Hα)	-278.44±3.16	-196.77±6.57	200.93±4.51	73.13±3.16
No. 4 (NII)	-267.96±4.07	-176.50±2.13	82.67±4.51	58.05±1.64
No. 5 (Hα)	-291.78±2.10	—-	122.62 ±4.62	—-
No. 5 (NII)	-251.27±0.98	-58.79 ± 6.48	5.085 ± 4.07	1.3221 ±0.98
No. 6 (Hα)	-73.24±4.35	88.08±2.37	193.27±8.75	276.89±4.35
No. 6 (NII)	-263.89 ±9.87	-73.19±1.17	78.04±8.41	118.16±9.87
No. 7 (Hα)	132.66±7.47	313.36±5.72	93.72±6.07	46.42±7.47
No. 7 (NII)	-14.07±1.67	22.35±3.09	202.62±2.47	274.48±16.43
No. 8 (Hα)	228.31±14.59	120.40±5.19	57.39±1.03	73.28±1.45

No. 8 (NII)	300.75±6.15	117.76±10.83	66.50±6.06	136.84±6.15
No. 9 (Hα)	277.58±19.22	113.62±2.13	84.19±1.35	72.06±1.92
No. 9 (NII)	287.129±4.40	130.03±8.94	32.69±2.67	66.05±4.40

A.3 Rotation curves and spatially resolved velocity maps from disk model

Using the KINMSpy package, we construct a thin disk model defined by turnover radius, thickness of the disk, maximum velocity attained by the rotation curve and the scale radius associated with the assumed surface brightness profile for each of our target galaxies. The set of parameters chosen to best represent the observed target galaxies (see §4.5 for details) are decided based on the qualitative match between the modelled rotation curve and the observed velocity curve from ESI. The comparison between the ESI data (magenta circles) and that obtained from the model (yellow contours) is shown in Fig. A.2. The fair match between the rotation curves confirm the best possible choice of the disk parameters in an attempt to reproduce the data. Fig. A.3 shows the corresponding 2D spatially resolved velocity map of the modelled gas particles obtained from the thin disk model using the chosen set of parameters. The observed 2D velocity fields are harder to reproduce using disk model for both galaxies.

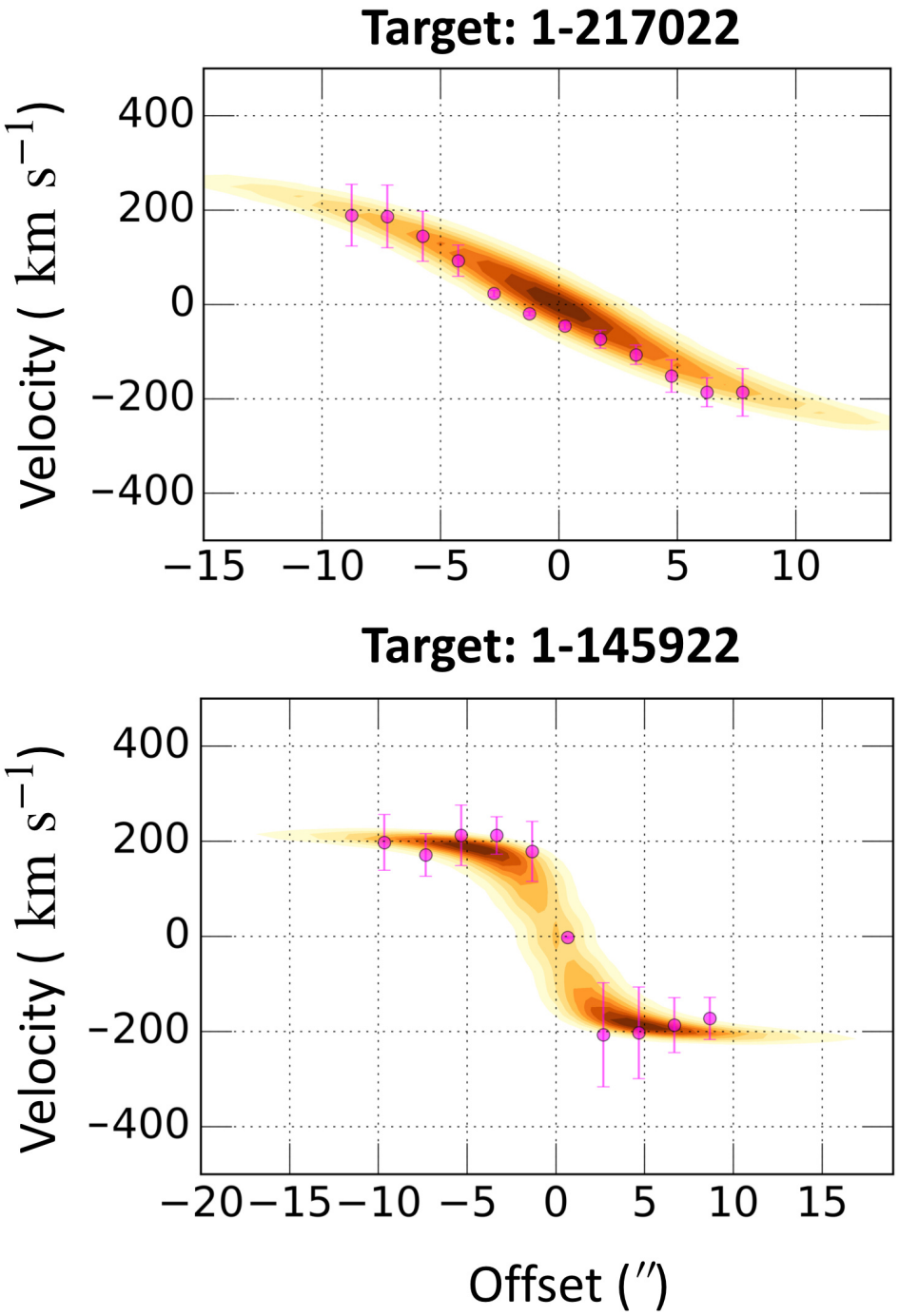

Figure A.2: The position-velocity curve from the ESI data in magenta circles overplotted on the best matched rotation curve assuming a disk model (details in §4.5) in yellow contours for both target galaxies. The parameters of the disk model are chosen based on this qualitative match.

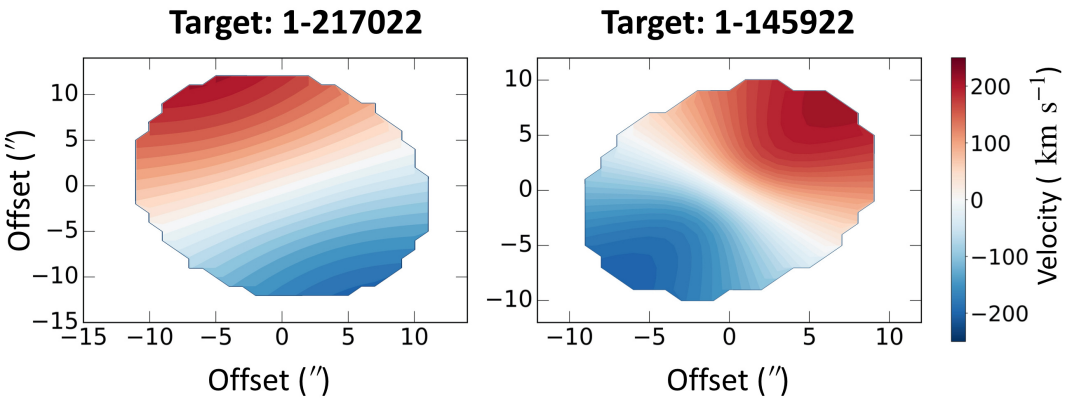

Figure A.3: The spatially resolved 2D gas velocity map obtained from the best matched disk model for the first (left panel) and second (right panel) target galaxies.

Bibliography

Abazajian, K. N., Adelman-McCarthy, J. K., Agüeros, M. A., et al. 2009, ApJS, 182, 543

Abolfathi, B., Aguado, D. S., Aguilar, G., et al. 2018, ApJS, 235, 42

Adelman-McCarthy, J. K., Agüeros, M. A., Allam, S. S., et al. 2008, ApJS, 175, 297

Aguado, D. S., Ahumada, R., Almeida, A., et al. 2019, ApJS, 240, 23

Ahumada, R., Prieto, C. A., Almeida, A., et al. 2020, ApJS, 249, 3

Al Yazeedi, A., Katkov, I. Y., Gelfand, J. D., et al. 2021, ApJ, 916, 102

Alatalo, K., Cales, S. L., Rich, J. A., et al. 2016, ApJS, 224, 38

Albareti, F. D., Allende Prieto, C., Almeida, A., et al. 2017, ApJS, 233, 25

Alexander, D. M., & Hickox, R. C. 2012, New A Rev., 56, 93

Alexandroff, R., Strauss, M. A., Greene, J. E., et al. 2013, MNRAS, 435, 3306

Allen, J. T., Hewett, P. C., Maddox, N., Richards, G. T., & Belokurov, V. 2011, MNRAS, 410, 860

An, T., & Baan, W. A. 2012, ApJ, 760, 77

Arribas, S., Colina, L., Bellocchi, E., Maiolino, R., & Villar-Martín, M. 2014, A&A, 568, A14

Baldi, R. D., Capetti, A., & Giovannini, G. 2015, A&A, 576, A38

Baldi, R. D., Capetti, A., & Massaro, F. 2018, A&A, 609, A1

Baldi, R. D., Williams, D. R. A., McHardy, I. M., et al. 2021, MNRAS, 500, 4749

Baldry, I. K., Glazebrook, K., Brinkmann, J., et al. 2004, ApJ, 600, 681

Baldwin, J. A., Phillips, M. M., & Terlevich, R. 1981, PASP, 93, 5

Balogh, M. L., Baldry, I. K., Nichol, R., et al. 2004, ApJ, 615, L101

Barnes, J. E. 1992, ApJ, 393, 484

Becker, R. H., White, R. L., & Helfand, D. J. 1995, ApJ, 450, 559

Begelman, M. C., Blandford, R. D., & Rees, M. J. 1984, Reviews of Modern Physics, 56, 255

Belfiore, F., Maiolino, R., Maraston, C., et al. 2016, MNRAS, 461, 3111

Belfiore, F., Maiolino, R., Maraston, C., et al. 2016, MNRAS, 466, 2570

Belfiore, F., Westfall, K. B., Schaefer, A., et al. 2019, AJ, 158, 160

Bell, E. F., Wolf, C., Meisenheimer, K., et al. 2004, ApJ, 608, 752

Benson, A. J., Bower, R. G., Frenk, C. S., et al. 2003, ApJ, 599, 38

Best, P. N. 2009, Astronomische Nachrichten, 330, 184

Best, P. N., & Heckman, T. M. 2012, MNRAS, 421, 1569

Best, P. N., Kaiser, C. R., Heckman, T. M., & Kauffmann, G. 2006, MNRAS, 368, L67

Best, P. N., Kauffmann, G., Heckman, T. M., et al. 2005, MNRAS, 362, 25

Bicknell, G. V. 1995, ApJS, 101, 29

Bicknell, G. V., Mukherjee, D., Wagner, A. Y., Sutherland, R. S., & Nesvadba, N. P. H. 2018, MNRAS, 475, 3493

Binette, L., Magris, C. G., Stasińska, G., & Bruzual, A. G. 1994, A&A, 292, 13

Binney, J. 1977, ApJ, 215, 483

Binney, J., & Tabor, G. 1995, MNRAS, 276, 663

Blanton, M. R., Kazin, E., Muna, D., Weaver, B. A., & Price-Whelan, A. 2011, AJ, 142, 31

Blanton, M. R., & Roweis, S. 2007, AJ, 133, 734

Blanton, M. R., Hogg, D. W., Bahcall, N. A., et al. 2003, ApJ, 594, 186

Blanton, M. R., Schlegel, D. J., Strauss, M. A., et al. 2005, AJ, 129, 2562

Blanton, M. R., Bershady, M. A., Abolfathi, B., et al. 2017, AJ, 154, 28

Blumenthal, G. R., Faber, S. M., Primack, J. R., & Rees, M. J. 1984, Nature, 311, 517

Bock, D. C. J., Large, M. I., & Sadler, E. M. 1999, AJ, 117, 1578

Bohlin, R. C., Savage, B. D., & Drake, J. F. 1978, ApJ, 224, 132

Bower, R. G., Benson, A. J., Malbon, R., et al. 2006, MNRAS, 370, 645

Bregman, J. N. 1980, ApJ, 236, 577

Brown, M. J. I., Moustakas, J., Kennicutt, R. C., et al. 2017, ApJ, 847, 136

Bryant, J. J., Croom, S. M., van de Sande, J., et al. 2019, MNRAS, 483, 458

Bundy, K., Ellis, R. S., Conselice, C. J., et al. 2006, ApJ, 651, 120

Bundy, K., Bershady, M. A., Law, D. R., et al. 2015, ApJ, 798, 7

Burkert, A., Förster Schreiber, N. M., Genzel, R., et al. 2016, ApJ, 826, 214

Buson, L. M., Sadler, E. M., Zeilinger, W. W., et al. 1993, A&A, 280, 409

Calzetti, D. 2001, PASP, 113, 1449

Cano-Díaz, M., Maiolino, R., Marconi, A., et al. 2012, A&A, 537, L8

Capelo, P. R., Volonteri, M., Dotti, M., et al. 2015, MNRAS, 447, 2123

Capetti, A., Baldi, R. D., Brienza, M., Morganti, R., & Giovannini, G. 2019, A&A, 631, A176

Capetti, A., Massaro, F., & Baldi, R. D. 2017, A&A, 601, A81

Capetti, A., Brienza, M., Baldi, R. D., et al. 2020, A&A, 642, A107

Cappellari, M. 2002, MNRAS, 333, 400

Cappellari, M. 2008, MNRAS, 390, 71

Cappellari, M. 2017, MNRAS, 466, 798

Cappellari, M., & Emsellem, E. 2004, PASP, 116, 138

Cappellari, M., Scott, N., Alatalo, K., et al. 2013, MNRAS, 432, 1709

Cattaneo, A., Faber, S. M., Binney, J., et al. 2009, Nature, 460, 213

Cavagnolo, K. W., McNamara, B. R., Wise, M. W., et al. 2011, ApJ, 732, 71

Cazzoli, S., Arribas, S., Colina, L., et al. 2014, A&A, 569, A14

Cazzoli, S., Arribas, S., Maiolino, R., & Colina, L. 2016, A&A, 590, A125

Chang, Y.-Y., van der Wel, A., da Cunha, E., & Rix, H.-W. 2015, ApJS, 219, 8

Chen, Y.-M., Tremonti, C. A., Heckman, T. M., et al. 2010, AJ, 140, 445

Chen, Y.-M., Shi, Y., Tremonti, C. A., et al. 2016, Nature Communications, 7, 13269

Cheung, E., Bundy, K., Cappellari, M., et al. 2016, Nature, 533, 504

Choi, E., Ostriker, J. P., Naab, T., et al. 2017, ApJ, 844, 31

Choi, J., Conroy, C., Moustakas, J., et al. 2014, ApJ, 792, 95

Ciotti, L., D'Ercole, A., Pellegrini, S., & Renzini, A. 1991, ApJ, 376, 380

Ciotti, L., & Ostriker, J. P. 1997, ApJ, 487, L105

Ciotti, L., & Ostriker, J. P. 2001, ApJ, 551, 131

Ciotti, L., & Ostriker, J. P. 2007, ApJ, 665, 1038

Ciotti, L., Ostriker, J. P., & Proga, D. 2010, ApJ, 717, 708

Circosta, C., Mainieri, V., Padovani, P., et al. 2018, A&A, 620, A82

Coil, A. L., Weiner, B. J., Holz, D. E., et al. 2011, ApJ, 743, 46

Cole, S., Lacey, C. G., Baugh, C. M., & Frenk, C. S. 2000, MNRAS, 319, 168

Combes, F., García-Burillo, S., Casasola, V., et al. 2014, A&A, 564, C1

Condon, J. J. 1984, ApJ, 287, 461

Condon, J. J., Cotton, W. D., & Broderick, J. J. 2002, AJ, 124, 675

Condon, J. J., Cotton, W. D., Greisen, E. W., et al. 1998, AJ, 115, 1693

Conroy, C., Graves, G. J., & van Dokkum, P. G. 2014, ApJ, 780, 33

Conroy, C., van Dokkum, P. G., & Kravtsov, A. 2015, ApJ, 803, 77

Couto, G. S., Storchi-Bergmann, T., Axon, D. J., et al. 2013, MNRAS, 435, 2982

Couto, G. S., Storchi-Bergmann, T., & Schnorr-Müller, A. 2017, MNRAS, 469, 1573

Crenshaw, D. M., Kraemer, S. B., Gabel, J. R., et al. 2003, ApJ, 594, 116

Croston, J. H., Hardcastle, M. J., Kharb, P., Kraft, R. P., & Hota, A. 2008, ApJ, 688, 190

Croston, J. H., Ineson, J., & Hardcastle, M. J. 2018, MNRAS, 476, 1614

Croton, D. J., Springel, V., White, S. D. M., et al. 2006, MNRAS, 365, 11

Davé, R., Finlator, K., & Oppenheimer, B. D. 2012, MNRAS, 421, 98

Davies, R. I., Maciejewski, W., Hicks, E. K. S., et al. 2009, ApJ, 702, 114

Davis, T. A., & Bureau, M. 2016, MNRAS, 457, 272

Davis, T. A., Alatalo, K., Bureau, M., et al. 2013, MNRAS, 429, 534

Dekel, A., & Birnboim, Y. 2006, MNRAS, 368, 2

Dekel, A., & Silk, J. 1986, ApJ, 303, 39

Demoulin-Ulrich, M. H., Butcher, H. R., & Boksenberg, A. 1984, ApJ, 285, 527

Dey, A., Schlegel, D. J., Lang, D., et al. 2019, AJ, 157, 168

Di Matteo, T., Springel, V., & Hernquist, L. 2005, Nature, 433, 604

Drory, N., MacDonald, N., Bershady, M. A., et al. 2015, AJ, 149, 77

Duckworth, C., Starkenburg, T. K., Genel, S., et al. 2020, MNRAS, 495, 4542

Dunlop, J. S., & Peacock, J. A. 1990, MNRAS, 247, 19

Dunn, J. P., Bautista, M., Arav, N., et al. 2010, ApJ, 709, 611

Dunn, R. J. H., & Fabian, A. C. 2006, MNRAS, 373, 959

Duric, N., Irwin, J., & Bloemen, H. 1998, A&A, 331, 428

Eldridge, J. J., Stanway, E. R., Xiao, L., et al. 2017, PASA, 34, e058

Ellison, S. L., Patton, D. R., & Hickox, R. C. 2015, MNRAS, 451, L35

Epinat, B., Amram, P., Balkowski, C., & Marcelin, M. 2010, MNRAS, 401, 2113

Faber, S. M., Willmer, C. N. A., Wolf, C., et al. 2007, ApJ, 665, 265

Fabian, A. 2012, ARA&A, 50, 455

Fabian, A. C. 1994, ARA&A, 32, 277

Fabian, A. C., Sanders, J. S., Taylor, G. B., et al. 2006, MNRAS, 366, 417

Falcke, H., & Biermann, P. L. 1999, A&A, 342, 49

Falcón-Barroso, J., Sánchez-Blázquez, P., Vazdekis, A., et al. 2011, A&A, 532, A95

Falcó n-Barroso, J., Sánchez-Blázquez, P., Vazdekis, A., et al. 2011, A&A, 532, A95

Fall, S. M., & Efstathiou, G. 1980, MNRAS, 193, 189

Fanaroff, B. L., & Riley, J. M. 1974, MNRAS, 167, 31P

Feruglio, C., Maiolino, R., Piconcelli, E., et al. 2010, A&A, 518, L155

Fischer, T. C., Crenshaw, D. M., Kraemer, S. B., Schmitt, H. R., & Trippe, M. L. 2010, AJ, 140, 577

Fischer, T. C., Machuca, C., Diniz, M. R., et al. 2017, ApJ, 834, 30

Freitas, I. C., Riffel, R. A., Storchi-Bergmann, T., et al. 2018, MNRAS, 476, 2760

Gallimore, J. F., Axon, D. J., O'Dea, C. P., Baum, S. A., & Pedlar, A. 2006, AJ, 132, 546

Ganguly, R., & Brotherton, M. S. 2008, ApJ, 672, 102

Gioia, I. M., Gregorini, L., & Klein, U. 1982, A&A, 116, 164

Gitti, M., Brighenti, F., & McNamara, B. R. 2012, Advances in Astronomy, 2012, 950641

Gomes, J. M., Papaderos, P., Kehrig, C., et al. 2016, A&A, 588, A68

Graham, M. T., Cappellari, M., Li, H., et al. 2018, MNRAS, 477, 4711

Graves, G. J., & Schiavon, R. P. 2008, ApJS, 177, 446

Green, A. W., Glazebrook, K., McGregor, P. J., et al. 2014, MNRAS, 437, 1070

Greene, J. E., Zakamska, N. L., Ho, L. C., & Barth, A. J. 2011, ApJ, 732, 9

Gunn, J. E., Siegmund, W. A., Mannery, E. J., et al. 2006, AJ, 131, 2332

Gürkan, G., Hardcastle, M. J., Smith, D. J. B., et al. 2018, MNRAS, 475, 3010

Hardcastle, M. J., & Croston, J. H. 2020, New A Rev., 88, 101539

Hardcastle, M. J., & Krause, M. G. H. 2013, MNRAS, 430, 174

Hardcastle, M. J., Williams, W. L., Best, P. N., et al. 2019, A&A, 622, A12

Hardcastle, M. J., Shimwell, T. W., Tasse, C., et al. 2021, A&A, 648, A10

Harrison, C. M., Alexander, D. M., Mullaney, J. R., & Swinbank, A. M. 2014, MNRAS, 441, 3306

Harrison, C. M., Costa, T., Tadhunter, C. N., et al. 2018, Nature Astronomy, 2, 198

Harrison, C. M., Thomson, A. P., Alexander, D. M., et al. 2015, ApJ, 800, 45

Harrison, C. M., Alexander, D. M., Swinbank, A. M., et al. 2012, MNRAS, 426, 1073

Heckman, T. M., & Best, P. N. 2014, ARA&A, 52, 589

Heckman, T. M., Kauffmann, G., Brinchmann, J., et al. 2004, ApJ, 613, 109

Hernquist, L. 1990, ApJ, 356, 359

Hickox, R. C., Jones, C., Forman, W. R., et al. 2009, ApJ, 696, 891

Higson, E., Handley, W., Hobson, M., & Lasenby, A. 2019, Statistics and Computing, 29, 891

Holt, J., Tadhunter, C. N., & Morganti, R. 2006, Astronomische Nachrichten, 327, 147

Holt, J., Tadhunter, C. N., & Morganti, R. 2008, MNRAS, 387, 639

Hopkins, P. F., Bundy, K., Hernquist, L., & Ellis, R. S. 2007, ApJ, 659, 976

Hopkins, P. F., Hernquist, L., Cox, T. J., et al. 2005, ApJ, 630, 705

Hopkins, P. F., Quataert, E., & Murray, N. 2011, MNRAS, 417, 950

Hopkins, P. F., Bundy, K., Croton, D., et al. 2010, ApJ, 715, 202

Humire, P. K., Nagar, N. M., Finlez, C., et al. 2018, A&A, 614, A94

Husemann, B., Wisotzki, L., Sánchez, S. F., & Jahnke, K. 2013, A&A, 549, A43

Husemann, B., Bennert, V. N., Jahnke, K., et al. 2019, ApJ, 879, 75

Ilbert, O., Salvato, M., Le Floc'h, E., et al. 2010, ApJ, 709, 644

Ivezić, Ž., Menou, K., Knapp, G. R., et al. 2002, AJ, 124, 2364

Jackson, N., Badole, S., Morgan, J., et al. 2022, A&A, 658, A2

Jacoby, G. H., Hunter, D. A., & Christian, C. A. 1984, ApJS, 56, 257

Jarvis, M. E., Harrison, C. M., Thomson, A. P., et al. 2019, MNRAS, 485, 2710

Jarvis, M. E., Harrison, C. M., Mainieri, V., et al. 2021, MNRAS, 503, 1780

Jiang, Y.-F., Ciotti, L., Ostriker, J. P., & Spitkovsky, A. 2010, ApJ, 711, 125

Kauffmann, G., Heckman, T. M., & Best, P. N. 2008, MNRAS, 384, 953

Kauffmann, G., Heckman, T. M., White, S. D. M., et al. 2003, MNRAS, 341, 33

Kaviraj, S. 2014, MNRAS, 440, 2944

Kellermann, K. I., Sramek, R., Schmidt, M., Shaffer, D. B., & Green, R. 1989, AJ, 98, 1195

Kennicutt, Robert C., J., Hao, C.-N., Calzetti, D., et al. 2009, ApJ, 703, 1672

Kereš, D., Katz, N., Weinberg, D. H., & Davé, R. 2005, MNRAS, 363, 2

Kewley, L. J., Groves, B., Kauffmann, G., & Heckman, T. 2006, MNRAS, 372, 961

Kimball, A. E., Ivezić, Ž., Wiita, P. J., & Schneider, D. P. 2011, AJ, 141, 182

King, A., & Pounds, K. 2015, ARA&A, 53, 115

Klein, U., Lisenfeld, U., & Verley, S. 2018, A&A, 611, A55

Kroupa, P., & Weidner, C. 2003, ApJ, 598, 1076

Krug, H. B., Rupke, D. S. N., & Veilleux, S. 2010, ApJ, 708, 1145

Kukula, M. J., Dunlop, J. S., Hughes, D. H., & Rawlings, S. 1998, MNRAS, 297, 366

Labiano, A. 2008, A&A, 488, L59

Lacy, M., Baum, S. A., Chandler, C. J., et al. 2020, PASP, 132, 035001

Lagos, C. d. P., Davis, T. A., Lacey, C. G., et al. 2014, MNRAS, 443, 1002

Lagos, C. d. P., Crain, R. A., Schaye, J., et al. 2015, MNRAS, 452, 3815

Law, D. R., Yan, R., Bershady, M. A., et al. 2015, AJ, 150, 19

Law, D. R., Cherinka, B., Yan, R., et al. 2016, AJ, 152, 83

Law, D. R., Westfall, K. B., Bershady, M. A., et al. 2021, AJ, 161, 52

Lena, D., Robinson, A., Storchi-Bergman, T., et al. 2015, ApJ, 806, 84

Liao, M., & Gu, M. 2020, MNRAS, 491, 92

Liu, G., Zakamska, N. L., Greene, J. E., Nesvadba, N. P. H., & Liu, X. 2013, MNRAS, 436, 2576

Martig, M., Bournaud, F., Teyssier, R., & Dekel, A. 2009, ApJ, 707, 250

Martin, D. C., Fanson, J., Schiminovich, D., et al. 2005, ApJ, 619, L1

Martin, G., Kaviraj, S., Volonteri, M., et al. 2018, MNRAS, 476, 2801

Mathews, W. G., & Brighenti, F. 2003, ARA&A, 41, 191

Mauch, T., Murphy, T., Buttery, H. J., et al. 2003, MNRAS, 342, 1117

Mauch, T., & Sadler, E. M. 2007, MNRAS, 375, 931

McConnell, N. J., & Ma, C.-P. 2013, ApJ, 764, 184

McNamara, B. R., & Nulsen, P. E. J. 2007, ARA&A, 45, 117

McNamara, B. R., & Nulsen, P. E. J. 2012, New Journal of Physics, 14, 055023

McNamara, B. R., Wise, M., Nulsen, P. E. J., et al. 2000, ApJ, 534, L135

Mehdipour, M., & Costantini, E. 2019, A&A, 625, A25

Mingo, B., Hardcastle, M. J., Croston, J. H., et al. 2011, ApJ, 731, 21

Mingo, B., Croston, J. H., Hardcastle, M. J., et al. 2019, MNRAS, 488, 2701

Mingozzi, M., Cresci, G., Venturi, G., et al. 2019, A&A, 622, A146

Morabito, L. K., Jackson, N. J., Mooney, S., et al. 2022, A&A, 658, A1

Morganti, R. 2017, Frontiers in Astronomy and Space Sciences, 4, 42

Morganti, R. 2021, in Nuclear Activity in Galaxies Across Cosmic Time, ed. M. Pović, P. Marziani, J. Masegosa, H. Netzer, S. H. Negu, & S. B. Tessema, Vol. 356, 229–242

Morganti, R., Oosterloo, T., Oonk, J. B. R., Frieswijk, W., & Tadhunter, C. 2015, A&A, 580, A1

Morganti, R., Tadhunter, C. N., & Oosterloo, T. A. 2005, A&A, 444, L9

Morton, D. C. 1991, ApJS, 77, 119

Moustakas, J., Coil, A. L., Aird, J., et al. 2013, ApJ, 767, 50

Mukherjee, D., Bicknell, G. V., Sutherland, R., & Wagner, A. 2016, MNRAS, 461, 967

Mukherjee, D., Wagner, A. Y., Bicknell, G. V., et al. 2018, MNRAS, 476, 80

Mullaney, J. R., Alexander, D. M., Fine, S., et al. 2013, MNRAS, 433, 622

Narayan, R., Igumenshchev, I. V., & Abramowicz, M. A. 2000, ApJ, 539, 798

Narayan, R., Yi, I., & Mahadevan, R. 1995, Nature, 374, 623

Nesvadba, N. P. H., De Breuck, C., Lehnert, M. D., Best, P. N., & Collet, C. 2017, A&A, 599, A123

Nesvadba, N. P. H., Lehnert, M. D., De Breuck, C., Gilbert, A. M., & van Breugel, W. 2008, A&A, 491, 407

Nims, J., Quataert, E., & Faucher-Giguère, C.-A. 2015, MNRAS, 447, 3612

Norman, C. A., & Ikeuchi, S. 1989, ApJ, 345, 372

O'Dea, C. P. 1998, PASP, 110, 493

O'Dea, C. P., & Saikia, D. J. 2021, A&A Rev., 29, 3

O'Leary, J. A., Moster, B. P., Naab, T., & Somerville, R. S. 2021, MNRAS, 501, 3215

O'Sullivan, E., Forbes, D. A., & Ponman, T. J. 2001, MNRAS, 328, 461

Pace, C., & Salim, S. 2014, ApJ, 785, 66

Padmanabhan, N., Schlegel, D. J., Finkbeiner, D. P., et al. 2008, ApJ, 674, 1217

Padovani, P. 2016, A&A Rev., 24, 13

Panessa, F., Baldi, R. D., Laor, A., et al. 2019, Nature Astronomy, 3, 387

Peebles, P. J. E. 1982, ApJ, 257, 438

Perna, M., Brusa, M., Salvato, M., et al. 2015, A&A, 583, A72

Pierce, J. C. S., Tadhunter, C. N., & Morganti, R. 2020, MNRAS, 494, 2053

Proga, D., & Kallman, T. R. 2004, ApJ, 616, 688

Rees, M. J., & Ostriker, J. P. 1977, MNRAS, 179, 541

Rengelink, R. B., Tang, Y., de Bruyn, A. G., et al. 1997, A&AS, 124, 259

Riffel, R. A., Storchi-Bergmann, T., & Riffel, R. 2014, ApJ, 780, L24

Riffel, R. A., Storchi-Bergmann, T., & Riffel, R. 2015, in Galaxies in 3D across the Universe, ed. B. L. Ziegler, F. Combes, H. Dannerbauer, & M. Verdugo, Vol. 309, 339–339

Riffel, R. A., Nemmen, R. S., Ilha, G. S., et al. 2019, MNRAS, 485, 5590

Rizza, E., Loken, C., Bliton, M., et al. 2000, AJ, 119, 21

Roberts-Borsani, G. W., & Saintonge, A. 2019, MNRAS, 482, 4111

Roger, R. S., Costain, C. H., & Bridle, A. H. 1973, AJ, 78, 1030

Rowlands, K., Dunne, L., Maddox, S., et al. 2012, MNRAS, 419, 2545

Roy, N., Bundy, K., Cheung, E., et al. 2018, ApJ, 869, 117

Roy, N., Bundy, K., Nevin, R., et al. 2021a, ApJ, 913, 33

Roy, N., Moravec, E., Bundy, K., et al. 2021b, ApJ, 922, 230

Roy, N., Bundy, K., Rubin, K. H. R., et al. 2021c, ApJ, 919, 145

Rubin, K. H. R., Prochaska, J. X., Koo, D. C., & Phillips, A. C. 2012, ApJ, 747, L26

Rubin, K. H. R., Prochaska, J. X., Koo, D. C., et al. 2014, ApJ, 794, 156

Rupke, D. 2018, Galaxies, 6, 138

Rupke, D. S., Veilleux, S., & Sanders, D. B. 2005, ApJS, 160, 87

Rupke, D. S. N., Thomas, A. D., & Dopita, M. A. 2021, MNRAS, 503, 4748

Rupke, D. S. N., & Veilleux, S. 2013, ApJ, 775, L15

Sabater, J., Best, P. N., Hardcastle, M. J., et al. 2019, A&A, 622, A17

Sadler, E. M., Ekers, R. D., Mahony, E. K., Mauch, T., & Murphy, T. 2014, MNRAS, 438, 796

Salim, S., Charlot, S., Rich, R. M., et al. 2005, ApJ, 619, L39

Salim, S., Rich, R. M., Charlot, S., et al. 2007, ApJS, 173, 267

Salim, S., Dickinson, M., Michael Rich, R., et al. 2009, ApJ, 700, 161

Salim, S., Lee, J. C., Janowiecki, S., et al. 2016, ApJS, 227, 2

Sancisi, R., Fraternali, F., Oosterloo, T., & van der Hulst, T. 2008, A&A Rev., 15, 189

Sanders, D. B., Soifer, B. T., Elias, J. H., et al. 1988, ApJ, 325, 74

Santoro, F., Rose, M., Morganti, R., et al. 2018, A&A, 617, A139

Sarzi, M., Kaviraj, S., Nedelchev, B., et al. 2016, MNRAS, 456, L25

Sarzi, M., Falcón-Barroso, J., Davies, R. L., et al. 2006, MNRAS, 366, 1151

Sato, T., Martin, C. L., Noeske, K. G., Koo, D. C., & Lotz, J. M. 2009, ApJ, 696, 214

Schawinski, K., Khochfar, S., Kaviraj, S., et al. 2006, Nature, 442, 888

Scott, N., Cappellari, M., Davies, R. L., et al. 2013, MNRAS, 432, 1894

Shapiro, P. R., & Field, G. B. 1976, ApJ, 205, 762

Shimwell, T. W., Röttgering, H. J. A., Best, P. N., et al. 2017, A&A, 598, A104

Shimwell, T. W., Tasse, C., Hardcastle, M. J., et al. 2019, A&A, 622, A1

Sijacki, D., Springel, V., Di Matteo, T., & Hernquist, L. 2007, MNRAS, 380, 877

Skilling, J. 2004, in American Institute of Physics Conference Series, Vol. 735, Bayesian Inference and Maximum Entropy Methods in Science and Engineering: 24th International Workshop on Bayesian Inference and Maximum Entropy Methods in Science and Engineering, ed. R. Fischer, R. Preuss, & U. V. Toussaint, 395–405

Smee, S. A., Gunn, J. E., Uomoto, A., et al. 2013, AJ, 146, 32

Somerville, R. S., & Davé, R. 2015, ARA&A, 53, 51

Somerville, R. S., Hopkins, P. F., Cox, T. J., Robertson, B. E., & Hernquist, L. 2008, MNRAS, 391, 481

Soto-Pinto, P., Nagar, N. M., Finlez, C., et al. 2019, MNRAS, 489, 4111

Speagle, J. S. 2020, MNRAS, 493, 3132

Starkenburg, T. K., Sales, L. V., Genel, S., et al. 2019, ApJ, 878, 143

Storchi-Bergmann, T., Lopes, R. D. S., McGregor, P. J., et al. 2010, MNRAS, 402, 819

Strateva, I., Ivezić, Ž., Knapp, G. R., et al. 2001, AJ, 122, 1861

Sturm, E., González-Alfonso, E., Veilleux, S., et al. 2011, ApJ, 733, L16

Su, K.-Y., Hopkins, P. F., Hayward, C. C., et al. 2019, MNRAS, 487, 4393

Tadhunter, C., Marconi, A., Axon, D., et al. 2003, MNRAS, 342, 861

Tadhunter, C., Morganti, R., Rose, M., Oonk, J. B. R., & Oosterloo, T. 2014, Nature, 511, 440

Tchekhovskoy, A., & Bromberg, O. 2016, MNRAS, 461, L46

Thomas, D., Maraston, C., Bender, R., & Mendes de Oliveira, C. 2005, ApJ, 621, 673

Tinsley, B. M. 1979, ApJ, 229, 1046

Tombesi, F., Cappi, M., Reeves, J. N., et al. 2010, A&A, 521, A57

Trager, S. C., Faber, S. M., Worthey, G., & González, J. J. 2000, AJ, 120, 165

Tremblay, G. R., Oonk, J. B. R., Combes, F., et al. 2016, Nature, 534, 218

Tremblay, G. R., Combes, F., Oonk, J. B. R., et al. 2018, ApJ, 865, 13

Tyson, N. D., & Rich, R. M. 1991, ApJ, 367, 547

van Breugel, W., Heckman, T., Butcher, H., & Miley, G. 1984, ApJ, 277, 82

van de Voort, F., Davis, T. A., Kereš, D., et al. 2015, MNRAS, 451, 3269

van Dokkum, P. G. 2005, AJ, 130, 2647

Vayner, A., Wright, S. A., Murray, N., et al. 2017, ApJ, 851, 126

Vazdekis, A., Ricciardelli, E., Cenarro, A. J., et al. 2012, MNRAS, 424, 157

Veilleux, S., Cecil, G., & Bland-Hawthorn, J. 2005, ARA&A, 43, 769

Veilleux, S., Maiolino, R., Bolatto, A. D., & Aalto, S. 2020, A&A Rev., 28, 2

Venturi, G., Nardini, E., Marconi, A., et al. 2018, A&A, 619, A74

Venturi, G., Cresci, G., Marconi, A., et al. 2021, A&A, 648, A17

Voit, G. M., Meece, G., Li, Y., et al. 2017, ApJ, 845, 80

Wagner, A. Y., & Bicknell, G. V. 2011, ApJ, 728, 29

Wagner, A. Y., Bicknell, G. V., & Umemura, M. 2012, ApJ, 757, 136

Wake, D. A., Bundy, K., Diamond-Stanic, A. M., et al. 2017, AJ, 154, 86

Webster, B., Croston, J. H., Mingo, B., et al. 2021, MNRAS, 500, 4921

Weijmans, A.-M., de Zeeuw, P. T., Emsellem, E., et al. 2014, MNRAS, 444, 3340

Weinberger, R., Ehlert, K., Pfrommer, C., Pakmor, R., & Springel, V. 2017a, MNRAS, 470, 4530

Weinberger, R., Springel, V., Hernquist, L., et al. 2016, MNRAS, 465, 3291

Weinberger, R., Springel, V., Hernquist, L., et al. 2017b, MNRAS, 465, 3291

Weiner, B. J., Coil, A. L., Prochaska, J. X., et al. 2009, ApJ, 692, 187

Westfall, K. B., Cappellari, M., Bershady, M. A., et al. 2019, AJ, 158, 231

Weston, M. E., McIntosh, D. H., Brodwin, M., et al. 2017, MNRAS, 464, 3882

White, S. D. M., & Frenk, C. S. 1991, ApJ, 379, 52

Whittle, M. 1992, ApJS, 79, 49

Willott, C. J., Rawlings, S., Blundell, K. M., & Lacy, M. 1999, MNRAS, 309, 1017

Worthey, G., Faber, S. M., & Gonzalez, J. J. 1992, ApJ, 398, 69

Worthey, G., Tang, B., & Serven, J. 2014, ApJ, 783, 20

Wylezalek, D., Flores, A. M., Zakamska, N. L., Greene, J. E., & Riffel, R. A. 2020, MNRAS, 492, 4680

Wylezalek, D., & Zakamska, N. L. 2016, MNRAS, 461, 3724

Xu, C., Livio, M., & Baum, S. 1999, AJ, 118, 1169

Yan, L., Donoso, E., Tsai, C.-W., et al. 2013, AJ, 145, 55

Yan, R., & Blanton, M. R. 2012, ApJ, 747, 61

Yan, R., Bundy, K., Law, D. R., et al. 2016, AJ, 152, 197

Yan, R., Chen, Y., Lazarz, D., et al. 2019, ApJ, 883, 175

Yesuf, H. M., Koo, D. C., Faber, S. M., et al. 2017, ApJ, 841, 83

York, D. G., Adelman, J., Anderson, John E., J., et al. 2000, AJ, 120, 1579

Yuan, F., & Narayan, R. 2014, ARA&A, 52, 529

Zakamska, N. L., & Greene, J. E. 2014, MNRAS, 442, 784

Zakamska, N. L., Lampayan, K., Petric, A., et al. 2016, MNRAS, 455, 4191

Zensus, J. A. 1997, ARA&A, 35, 607

Zheng, Y., Peek, J. E. G., Werk, J. K., & Putman, M. E. 2017, ApJ, 834, 179